



DISSERTATION

**Scattering in Complex Media:
Coherent Transport at the Cross-over
to Anderson Localization**

ausgeführt zum Zwecke der Erlangung des akademischen Grades
eines Doktors der technischen Wissenschaften

unter der Leitung von
Prof.Dr. Stefan Rotter
Institut für Theoretische Physik (136)

und mitbetreut durch
Univ.-Ass.Dr. Florian Libisch
Institut für Theoretische Physik (136)

eingereicht an der Technischen Universität Wien
Fakultät für Physik

von

Dipl.-Ing. Adrian Girschik
Matrikelnummer 0442533
Bahnhofstraße 64-68/3
A-3430 Tulln

Ort,Datum

Unterschrift

Streuung in komplexen Medien: Kohärenter Transport an der Schwelle zur Anderson-Lokalisierung

Abstract in German - Deutsche Kurzfassung

Anderson-Lokalisierung ist ein Wellenphänomen, welches exponentielle Lokalisierung von elektronischen Wellenfunktionen oder klassischen Wellen in stark ungeordneten Medien vorhersagt. Dieses Fehlen von Diffusion begründet erstaunliche Eigenschaften lokalisierter Systeme, die Physiker seit der Entdeckung des Effekts durch P.W. Anderson im Jahr 1958 in Atem hält.

Eine dieser Eigenschaften ist das Auftreten des sogenannten Ein-Kanal Transport-Regimes, welches wir numerisch und, in Zusammenarbeit mit der Universität von San Antonio (Texas), auch experimentell untersuchen. Das Erkennungsmerkmal des genannten Regimes ist die Konzentration des Transports auf nur einen einzigen der zur Verfügung stehenden Transmissionskanäle in einem ungeordneten Wellenleiter. Das Auftreten von Ein-Kanal-Transport wird durch die Analyse der Transport-Statistik sowie der Intensitätsverteilung innerhalb des ungeordneten Mediums gezeigt. Insbesondere verifizieren wir die Existenz sogenannter “necklace states” sowie deren Zusammenhang mit den internen Moden des offenen Systems.

Während das Ein-Kanal-Regime eine direkte Folge von Anderson Lokalisierung darstellt, haben jüngste Forschungen gezeigt, dass bestimmte Systeme sehr robust gegen Lokalisierung sind. Solche “topologische Isolatoren” besitzen Randzustände mit genau dieser Eigenschaft. Darüberhinausgehend können diese Zustände nicht nur der Unordnung trotzen sondern sogar erst durch sie erzeugt werden. Dieses Phänomen, welches “topologischer Anderson-Isolator” (TAI) genannt wird, untersuchen wir für den Fall eines räumlich korrelierten Potentials. Unsere numerischen Simulationen zeigen, dass solch eine Korrelation den Übergang in die TAI-Phase unterdrücken kann, was die Existenz des Phänomens in echten elektronischen Systemen in Frage stellt. Im Zuge dessen erweitern wir die bestehende analytische Theorie für den TAI auf den Fall räumlich korrelierter Potentiale.

Unsere zweite Studie zum Thema TAI befasst sich mit dem neuerlichen Verschwinden der TAI-Phase bei sehr starker Unordnung, welche zuvor mit einer Delokalisierung der Volumen-Zustände (also jener Zustände, die nicht entlang des

Randes laufen) in Verbindung gebracht werden konnte. Wir zeigen, dass sowohl die Entstehung als auch das Abklingen der TAI-Phase in enger Verbindung mit sogenannten Perkulations-Zuständen steht, welche um die Hügel und Täler des Unordnungspotentials laufen. Weiters befindet sich in dieser Arbeit ein Vorschlag für die Realisierung eines Mach-Zehnder Interferometers in einem System topologischer Isolatoren. Ein solches könnte in Zukunft Anwendungen als Spin-Transistor finden.

Neben Lokalisierung befassen wir uns auch mit einem zweiten fundamentalen Wellenphänomen genannt “branched flow”. Dieser Effekt tritt für Wellen auf, welche durch ein langreichweitiges und schwaches Potential laufen. Dabei verteilt sich ihre Intensität in verästelter Weise anstatt sich gleichmäßig im System auszubreiten. In solchen Systeme, die in der Physik von der Nanoelektronik bis zu Monsterwellen im Ozean zu finden sind, führt der Effekt zur Bildung von Ästen konzentrierter Intensität (“branches”) entlang welcher sich die Welle über große Distanzen ausbreiten kann. Wir befassen uns mit der Frage, inwieweit diese natürliche Eigenschaft zur Wellenkontrolle genutzt werden kann und Fokussieren durch ein ungeordnetes Medium ermöglicht. Unsere Methoden, die durch die Fortschritte in der Technologie mittlerweile auch schon im Experiment zugänglich sind, zeigen, dass durch gezielten Einschuss einzelne “branches” selektiert werden können.

Neben den physikalischen Anwendungen befasst sich diese Arbeit auch mit der erforderlichen Numerik, welche die Grundlage für die Erforschung der Transport- und Streueigenschaften ungeordneter Medien bildet. Die herkömmlichen Berechnungen verwenden die sogenannte “modular-rekursive Greensfunktions-Methode”, welche sehr effizient den numerischen Rechenaufwand minimiert. In dieser Arbeit konzentrieren wir uns hauptsächlich auf eine noch effizientere Parallelisierung der bekannten Algorithmen und erreichen eine signifikante Leistungssteigerung. Eine solche Verbesserung der Numerik erlaubt den Zugang zu größeren und stärker ungeordneten Systemen. Zusätzlich stellen wir einen Algorithmus namens “parallel permutation algorithm” (PPA) vor, welcher die Grundlage für die parallele Berechnung von Wellenfunktionsbildern, lokaler Zustandsdichten und ungeordneten Superzell-Strukturen ist. Es werden für alle drei dieser Anwendungen Algorithmen implementiert, die hochparallelisierte Berechnungen ermöglichen und somit noch tieferen Einblick in die Streu- und Transporteigenschaften ungeordneter Systeme bieten - ein vielversprechender Ausgangspunkt für zukünftige Entwicklungen.

Contents

Introduction	9
1. Classical waves in disordered media	11
1.1. The scattering problem	11
1.2. The single-channel regime of transport	13
1.3. Controlling branched flow	28
2. Two-dimensional topological insulators	41
2.1. Introduction	41
2.2. Model	42
2.3. Topological insulator in the presence of spatially correlated disorder	43
2.4. Percolating states in the topological Anderson insulator	55
2.5. Additional Hamiltonian corrections	66
2.6. Topological insulator in a magnetic field	70
2.6.1. Perpendicular magnetic field	71
2.6.2. In-plane magnetic field in a plane lead	73
2.6.3. In-plane magnetic field for a cylindrical lead	76
2.7. A topological Mach-Zehnder interferometer	78
3. Numerical methods and improvements	91
3.1. Finite differences method	91
3.2. Band structures	94
3.3. Green's functions and the Dyson equation	96
3.4. Improving the modular recursive Green's function method	100
3.5. The parallel permutation algorithm	106
3.6. Calculating scattering wave functions faster	111
3.7. Computing the local density of states	120
3.8. Super-cell band structures	127
3.9. Super-cell Bloch functions	133
Summary and outlook	137
A. Numerical Implementation of the BHZ model	141
A.1. Unperturbed BHZ model	141

A.2. Including Rashba coupling and Bulk inversion asymmetry	145
B. Implementation of a magnetic field	149
B.1. The Peierls substitution	149
B.1.1. General numerical formalism for the Peierls substitution . . .	151
B.1.2. Implementation on a finite-difference square grid	152
B.1.3. Perpendicular magnetic field	155
B.1.4. Magnetic field in x -direction for a plane lead	156
B.1.5. Magnetic field in x -direction for a cylindrical lead	157
B.1.6. Unit conversions	158
Bibliography	159
Acknowledgements	173
Curriculum vitae	175
Education	175
List of Publications	175

List of Acronyms

- BHZ** Bernevig-Hughes-Zhang. 43, 65–67, 82, 141, 155, 158
- BIA** bulk inversion asymmetry. 66–69, 72–75, 77, 78, 82, 145, 146
- BS** beam splitter. 79, 80
- BZ** Brillouin zone. 61–63, 65
- DOS** density of states. 120, 124, 125
- GF** Green’s function. 97–103, 105–109, 111–117, 119, 122–124, 127, 130–134, 139
- LDOS** local density of states. 58, 59, 121–126, 130
- MG** modulation gate. 79
- MRGF** modular recursive Green’s function method. 100
- MUMPS** Multifrontal Massively Parallel sparse direct Solver. 100, 113
- MZI** Mach-Zehnder interferometer. 78–81, 83–85, 87–89
- PARPACK** Parallel Arnoldi Package. 121
- PDA** parallel Dyson algorithm. 101, 103–106, 108–111, 118, 119, 139
- PPA** parallel permutation algorithm. 106, 107, 109–111, 114–120, 122–125, 139
- QPC** quantum point contact. 79–81, 83, 84, 87, 88, 138
- QSH** quantum spin Hall. 41, 45–47, 50, 52, 53, 55
- QW** quantum well. 67, 68, 70, 72–75, 77, 78, 133, 146
- SCBA** self-consistent Born approximation. 46, 52
- TAI** topological Anderson insulator. 9, 10, 41–43, 45–50, 52, 53, 55, 56, 58, 63–65, 135, 138

TI topological insulator. 50

TRS time-reversal symmetry. 70, 71

VSC Vienna Scientific Cluster. 103, 104, 106, 118–120, 125

Introduction

Anderson localization is a general wave phenomenon that predicts exponential localization of electronic wave functions or classical wave intensities in strongly disordered media. This absence of diffusion is accompanied by many intriguing features that have occupied physicists since the effect's discovery by P.W. Anderson in 1958 [1].

One of these features is the onset of a regime that we refer to as the „single-channel regime of transport“ [2] which we study here numerically in two dimensions. This regime is hallmarked by the entire transmission being carried by only a single of the many available channels through a randomly disordered medium. In this work the cross-over to the single-channel regime is explored by transport statistics as well as by the analysis of intensity patterns inside the disordered medium. In a collaboration with the University of Texas at San Antonio the universality of this transition is investigated by comparison of our numerical data to experimental data in microwave experiments. In addition, we investigate the evolution of so-called “necklace states” proposed by Pendry in 1987 [3]. In particular, we clarify the link between these states, the single transmission channel that dominates in this regime and, what we call, the internal modes of the system.

While the aforementioned regime is a direct consequence of Anderson localization, we also study here physical systems that are very robust against disorder and the effects of localization in transport. In particular, we are dealing with the recently discovered materials called topological insulators that feature edge states, whose robustness against disorder makes these media promising candidates for various applications in nano-electronics [4–6]. In this work we suggest one such application in the form of a topological Mach-Zehnder interferometer that could serve as a spin transistor.

Not only are the edge states of a topological insulator robust against disorder, they can even be evoked by the presence of disorder. This counter-intuitive topological phase was named topological Anderson insulator (TAI) and was discovered in numerical studies [7, 8]. In this work, we investigate a more realistic ansatz for the disorder potential by making it spatially correlated. The impact of these correlations on the TAI is investigated and the underlying theoretical framework is adapted to this more general case [9]. Additionally, we study the presence of percolating states in disordered two-dimensional topological insulators. The decay of the TAI phase could previously be connected to a delocalization of bulk states

with increasing disorder strength. During the course of this work, we investigate the connection between percolating states and the evolution and the decay of the TAI phase [10].

Besides localization another general wave phenomenon called branched flow [11] is explored in this thesis. Waves travelling through a random, long-ranged and weak disorder potential show branching behavior instead of a smooth spreading of flow. In such systems, that may range from nano-electronics to ocean acoustics, this branching effect leads to the formation of surprisingly focused branches in the disordered medium along which the waves propagate over large distances. We address the question, if and how wave front shaping techniques may allow us to use this effect for improved focusing through the medium.

Apart from the physical aspects, this work is also concerned with the numerics that are used to investigate the scattering and transport properties of random media. These numerics rely on the modular recursive Green's function method [12–16]. While the above method is very efficient in terms of minimizing the calculation effort, we improve the method in particular by proposing a more efficient parallelization. This effort is crucial for the future as it will allow to access even larger and more strongly disordered systems. Moreover, we develop an algorithm that efficiently allows a parallel evaluation of a scattering region in such a way that a number of tasks are simplified. These tasks are the parallel computation of scattering wave functions, the local density of states and disordered super-cell structures. For these three applications we implement new algorithms that represent a solid and efficient foundation for future research in this field.

Chapter 1.

Classical waves in disordered media

1.1. The scattering problem

In Fig. 1.1 we show the prototype of a scattering problem in two dimensions that we are concerned with in all our studies. We assume a scattering region that can

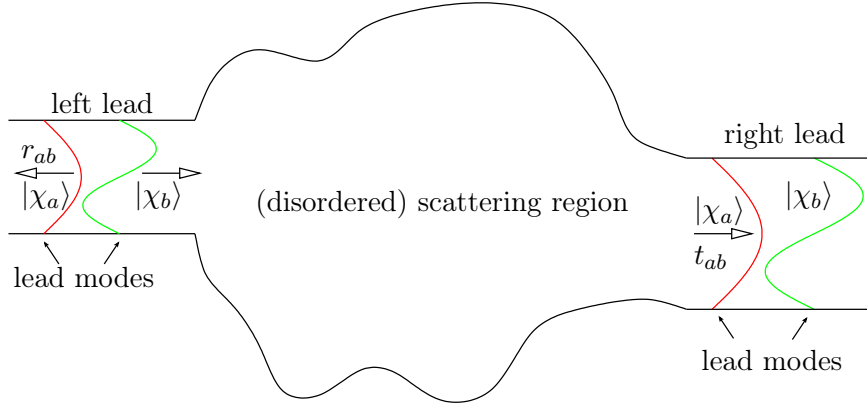


Figure 1.1.: Sketch of a prototype scattering problem. A disordered region is connected to two semi-infinite and clean leads on the left and on the right. The leads feature propagating modes $|\chi_i\rangle$ through which the wave enters and leaves the system. Black arrows indicate an exemplary injection of a lead mode $|\chi_b\rangle$ in the left lead. The complex number t_{ab} is the transmission amplitude of this injected mode coming out in the right lead in lead mode $|\chi_a\rangle$. Analogously, r_{ab} represents the reflection amplitude for the wave coming back travelling to the left in the left lead in lead mode $|\chi_a\rangle$.

contain disorder and is connected to two semi-infinite but clean leads on the left and

on the right. These leads feature a finite number of propagating lead modes $|\chi_i\rangle$ through which the wave can enter and leave the disordered system. The underlying equation of our studies is usually the stationary Schrödinger equation governed by a Hamiltonian \hat{H} :

$$\hat{H}\psi(\vec{r}) = E\psi(\vec{r})$$

evaluated at some scattering energy E and with the wave function being labelled by $\psi(\vec{r})$. In some of our studies we also consider optical systems in two dimensions which obey the scalar Helmholtz equation

$$[\Delta + k^2 n^2(\vec{r})] \psi(\vec{r}) = 0 \quad . \quad (1.1)$$

In this case $\psi(\vec{r})$ represents the out-of-plane z -component of the electric field and scattering occurs at a fixed incoming wave number $k = \omega/c$. Fortunately, this equation can be reordered to read

$$\left[-\frac{\Delta}{2} + \frac{k^2}{2} (1 - n^2(\vec{r})) \right] \psi(\vec{r}) = \frac{k^2}{2} \psi(\vec{r}) \quad , \quad (1.2)$$

which is equivalent to the electronic stationary Schrödinger equation in atomic units ($\hbar = 1, m_e = 1$):

$$\left[-\frac{\Delta}{2} + V(\vec{r}) \right] \psi(\vec{r}) = E\psi(\vec{r}) \quad .$$

With this knowledge, we can treat the Helmholtz equation 1.1 as a Schrödinger equation with energy

$$E = \frac{k^2}{2}$$

and an energy-dependent potential

$$V(\vec{r}) = E (1 - n^2(\vec{r})) \quad .$$

While this energy-dependence is problematic for solving an eigenvalue problem (as the Hamiltonian depends on the eigenvalue E), a scattering problem governed by the Helmholtz equation can be straight-forwardly solved like in the case of the Schrödinger equation since the energy E is a fixed parameter. For a detailed description of the numerics that we are using see chapter 3.

The entire information on how the scattering inside the disordered region manifests in its transport behavior is included in the so-called scattering matrix

$$S = \begin{pmatrix} r & t' \\ t & r' \end{pmatrix} \quad . \quad (1.3)$$

The matrices t and r are called the transmission and reflection matrix, respectively. The individual elements of t (r) are the complex transmission (reflection) amplitudes

t_{ab} (r_{ab}) describing transmission (reflection) from mode b incoming through the left lead to mode a leaving through the right (left) lead. The primed quantities t' and r' are the analogues of t and r for injection from the right.

All the above quantities can be numerically evaluated in the basis of open lead modes $|\chi_i\rangle$ according to Eqs. (3.20)-(3.23) and the descriptions in section 3.3. Mind that these quantities such as the transmission matrix t can be very large objects when there is a large number of incoming and outgoing modes as is the case in optical systems. Nowadays, however, the task of measuring large parts of this matrix has almost been completed [17–21] in optical system and entirely fulfilled in microwave systems [22]. Due to these achievements the methods of wave control do no longer rely on numerical simulations alone (as, e.g., Ref. [23]) but are ready to be implemented in real physical systems in the laboratory. As part of this upcoming search for applications, fundamental knowledge about transport through random systems is of critical importance. Our research in the next two sections goes into this direction.

1.2. The single-channel regime of transport

The effects of disorder are of basic interest for developing applications concerned with imaging and focusing of light through random media [18]. Additionally the concepts are applicable for many different materials of natural or artificial origin. The corresponding theoretical framework allows for the description of a range of physical systems reaching from mechanical waves over classical electromagnetic waves to matter waves in nano-structures governed by quantum mechanics. In the previous section 1.1 (see also Fig. 1.1) we already introduced the prototype of a scattering problem that can be approached by a variety of theories such as random-matrix theory [24] or, as in our case, by methods of mesoscopic transport theory. A fundamental quantity in this theory is the transmission matrix t that was introduced in the previous section 1.1. Numerically, this matrix is usually evaluated in the basis of incoming and outgoing lead modes. However, a switch of basis reveals interesting information about the effects of disorder. This new basis is spanned by the eigenvectors (called transmission eigenchannels) of the $t^\dagger t$ -matrix. The corresponding eigenvalues τ_n are referred to as transmission eigenvalues. The statistics of the latter are closely connected to Anderson localization. As long as transport is diffusive (i.e., for small sample length L compared to the localization length ξ), a finite number $M \approx \xi/L$ out of the N existing transmission eigenchannels show a corresponding transmission eigenvalue τ_n that is close to 1. Apart from these, the remaining channels are closed manifesting in their τ_n being exponentially small [25, 26]. When the sample is elongated, the ratio ξ/L decreases and so does the number M of open transmission eigenchannels. Moreover, when the localized regime,

i.e., $L > \xi$, is entered, this decrease manifests in an effect that is referred to as the “crystallization of transmission eigenvalues” [27]. Not only does the number of open channels, on average, go down, also the distribution of transmission eigenvalues $P(\tau_n)$ is significantly altered in the localized regime showing a peaked structure. The effect is hallmarked by the increasing separation of these peaks in $P(\tau_n)$ and has also been verified experimentally [22]. As this crystallization of transmission eigenvalues occurs on a logarithmic scale, we expect that in the deeply localized regime where $L \ll \xi$, only the largest transmission eigenvalue τ_1 has a value that is not negligibly small¹. In this regime, that we will call “the single-channel regime of transport”, the total transmission $T = \sum_n \tau_n \approx \tau_1$ through the disordered sample occurs through only the first transmission eigenchannel and decreases exponentially due to Anderson localization [1, 28].

The considerations above show, that the deeply localized limit actually simplifies transmission behavior through a long and strongly disordered system by eliminating the contribution of all but one transmission eigenchannel. This simple picture inspired the idea that other fundamental properties in the complicated world of transport through disordered systems can be more intuitively observed and established in this regime. A hint into this direction comes from a recent observation reported in Refs. [22, 29]: Measurements of the output intensity profile of microwaves sent through a disordered medium revealed that in the localized regime the intensity profile (speckle pattern) is literally frozen. This means, that the output profile does not depend on the input at all. While in strict contrast to the diffusive regime, where the output depends strongly on the input, this observation is a clear sign of a single channel dominating transmission [22].

However, the difficulty in exploring the single-channel regime lies in the fact that it is hard to access numerically as well as experimentally. From the numerical point of view this is because the systems have to be long ($L \ll \xi$), wide (to reach a large number N of open lead modes) and the strong disorder requires an even better resolution at the same time. In the microwave experiment all measurements in the localized limit feature small signals. Additionally these signals suffer from absorption which is inevitably present in photonic systems resulting in a low signal-to-noise ratio. By overcoming these challenges, this work reveals several fundamental properties of strongly disordered systems.

This study is a collaborative work between our group and the group of Prof. Andrey Chabanov in San Antonio, Texas, USA. In this thesis, I decided to describe in detail all the results that emerged from this fruitful cooperation in order to present a well-rounded picture of all the physics and to clarify the importance of our results. However, we clarify here that my contribution mainly consisted of producing the

¹ Conventionally, the τ_n are always arranged in descending order of their magnitude, i.e., $\tau_1 > \tau_2 > \dots > \tau_N$.

numerical results and the corresponding statistical analysis of this data, while the experimental data was measured and analyzed by Abe Peña, who was at that time a PhD student in Andrey Chabanov's group.

To verify the onset of the single-channel regime, we employ numerical simulations on planar disordered waveguides of width W and length L attached to clean semi-infinite leads on the left and right. We modeled the disorder by randomly placing non-absorbing dielectric scatterers of diameter $0.041W$ and refractive index 3.14 into the middle portion of the waveguide at a filling fraction of 0.125, keeping a minimum distance of $0.0205W$ between the scatterers. The width W of the waveguides is chosen such that there are $N = 15$ lead modes open and hence in total also 15 transmission eigenchannels present. For a more detailed description of the numerics see chapter 3. We calculated transmission spectra for 100 random disorder configurations at a sample length of $L = 5W = 3.29\xi$. For each disorder realization the transmission matrix was evaluated in a frequency window with altogether 2397 equally spaced frequency points. A small portion of such a spectrum is shown in Fig. 1.2(a). For this spectrum we check explicitly that the total transmission T is indeed dominated by only the largest transmission eigenvalue τ_1 . For this purpose we diagonalized the $t^\dagger t$ matrix at each frequency point and find that the second largest transmission eigenvalue τ_2 is indeed negligibly small ($\tau_2 < 0.01$ throughout the entire frequency range). This finding ensures that we have indeed pushed far enough into the deeply localized regime to reach the expected single-channel regime.

While the transmission eigenvalues are a good indicator for the onset of the single-channel regime, we now focus on the question how these channels are formed inside our randomly disordered waveguide. Such knowledge could in principle be extracted from the singular value decomposition of the transmission matrix [30], we choose, however, to refer to what we will call the “internal modes” in the following. The picture of such internal modes also allows for a very intuitive approach to the phenomenon of Anderson localization as put forward by Thouless [31]. In this framework the so-called Thouless number, $\delta \equiv \delta\nu/\Delta\nu$, can be used as a parameter to observe localization [32]. Since $\delta\nu$ in the above formula stands for the typical spectral width of the modes in the disordered medium and $\Delta\nu$ is the average spacing between neighboring modes, the Thouless number δ measures to which extent the internal modes in a sample overlap. Intuitively, this degree of overlap is characteristic for the corresponding transport regime: While in the diffusive regime, the overlap between modes is large ($\delta > 1$), the modes become more and more isolated when entering the localized regime ($\delta < 1$). The latter statement is also reflected in the shape of the typical spectrum in the localized regime featuring sharp, isolated peaks as shown in Fig. 1.2(a).

For the calculation of internal modes, we impose constant-flux outgoing boundary conditions [33] at the left and right edges of our disordered waveguides at which the leads are attached in the scattering problem. Then we solve the eigenvalue prob-

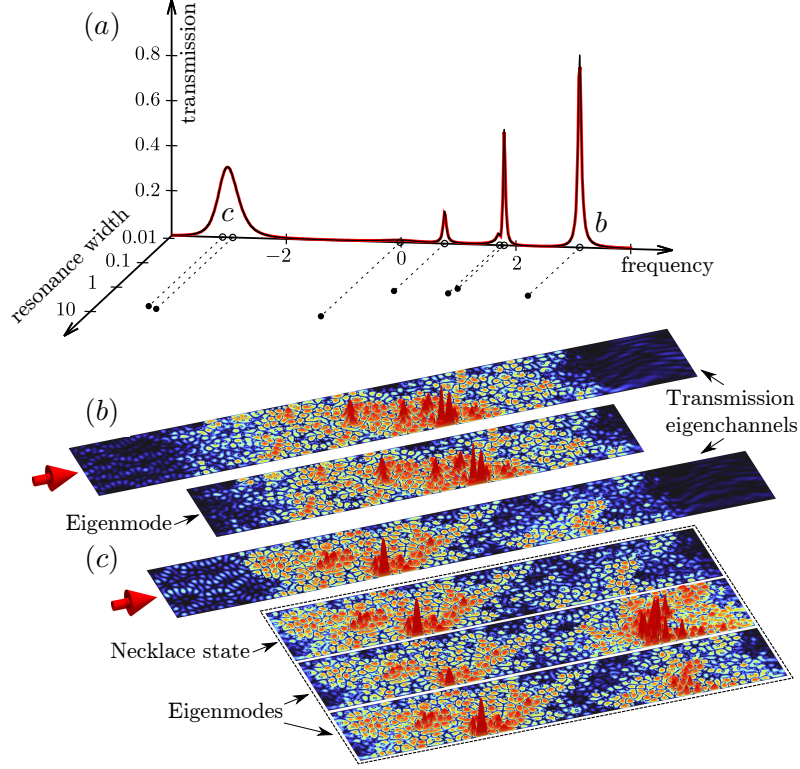


Figure 1.2.: (a) Numerically calculated transmittance T (red line) versus detuning ν from the mid-frequency of the localization band, normalized by the average mode spacing $\Delta\nu$, in a disordered planar waveguide of $L/\xi = 3.29$. The black line on top of the red curve shows the result of a fit of the transmittance, using the real $[\text{Re } \nu_m]$ and imaginary $[\text{Im } \nu_m]$ parts of the eigenfrequencies ν_m of the internal modes of the disordered region as fixed parameters (see empty and solid circles, respectively). Isolated eigenfrequencies represent individual localized modes (b), whereas closely spaced eigenfrequencies correspond to spectrally overlapping modes identified as necklace states (c). A spectral separation between the neighboring necklace states of about $5\Delta\nu$ can be noticed. (b) Spatial intensity pattern of the scattering state of the transmission eigenchannel (upper panel) and of the individual localized mode (lower panel) at the resonance peak b . (c) Spatial intensity profile of the scattering state of the transmission eigenchannel (upper panel) and of the two-mode necklace state (top panel in the framed box) at the resonance peak c . The lower two panels in the framed box display the two eigenmodes of the two-mode superposition. Figure and caption were adapted from our collaborative work Ref. [2].

lem for the resulting non-hermitian Hamiltonian that consequently yields complex frequency-eigenvalues ν_m . We expect that the real parts of these eigenfrequencies indicate the position of transmission resonances while the imaginary part is related to the resonance width Γ_m by $\Gamma_m = -2\text{Im } \nu_m$. These relations are very nicely confirmed by the comparison of the spectrum (red curve) in Fig. 1.2(a) and the real (empty circles) and imaginary (filled circles) parts of the eigenfrequencies ν_m . As expected, a nice correspondence between the resonance positions and the real parts of the ν_m as well as a correlation between the resonance widths and the imaginary parts of ν_m can be at least qualitatively perceived. In order to verify this agreement on a quantitative level, we formulate the total transmission $T(\nu)$ in the internal mode picture as a sum of Lorentzian curves,

$$T(\nu) = \left| \sum_{m=1}^N C_m \frac{\Gamma_m/2}{\Gamma_m/2 + i(\nu - k_m)} \right|^2, \quad (1.4)$$

with the real and imaginary parts of ν_m entering the formulation via

$$\begin{aligned} k_m &= \text{Re } \nu_m \quad \text{and} \\ \Gamma_m &= -2\text{Im } \nu_m. \end{aligned}$$

We fit this ansatz to the numerically calculated spectra $T(\nu)$. The comparison of the red and the black curve in Fig. 3(a) reflects the excellent fit that this ansatz yields. While the validity of such a description has been confirmed before [23, 29] we only used the complex amplitudes C_m of each mode as fit parameters. This perfect agreement allows us to draw the conclusion that the total transmission can indeed be expressed by a superposition of internal modes that contribute. Moreover, the positions and widths of the transmission resonances are indisputably included in the complex eigenfrequencies ν_m . As we found before that the total transmission is carried by only a single channel in the single-channel regime, we assess that also the dominant transmission eigenchannel is formed by a unique such internal mode or a combination of few modes that are spectrally overlapping.

To go further, we investigated these two distinct cases in panels (b) and (c) of Fig. 1.2, respectively. For the resonance on the right of the spectrum in Fig. 1.2(a) we find that only one internal mode is spectrally close to (as indicated by the single open black circle underneath it). In this simpler case, the single transmission eigenchannel is hence formed by only this single internal mode. While this correspondence has just been proven on the level of the total transmission, we should also be able to verify it having a look inside the disordered sample. More precisely, we expect the transmission eigenchannel to have a similar internal shape as this internal mode. This correspondence is shown in panel (b) of Fig. 1.2 where we show the scattering wave function belonging to the first transmission eigenchannel on top

and the intensity profile of the corresponding internal mode underneath. As easily visible, these two patterns are astonishingly similar throughout the entire sample. The only visible deviations occur close to the attachment of the left lead and can be attributed to the incoming flux that is included in the scattering problem but not in the boundary conditions for the internal modes. On the other hand, the wave functions inside the disordered sample are insensitive to a change of the boundary condition which is another hallmark of Anderson localization [31].

For the other case of a resonance that consists of two spectrally overlapping modes [labelled b in Fig. 1.2(a)], we want to find a similar correspondence as previously. As shown at the bottom of Fig. 1.2(c), the two internal modes do not resemble the scattering wave function of the first transmission eigenchannel (shown at the top of the same panel, marked by a red arrow). Due to mode hybridization [34, 35] they do show, however, a reasonable degree of spatial correlation with each other. We find that the resemblance of the transmission eigenchannel can be achieved by superimposing these two internal modes by the use of the corresponding coefficients C_m from the fit performed for the total transmission using Eq. (1.4) as convincingly presented in Fig. 1.2(c) (labelled by "Necklace state"). This striking correspondence establishes a link between transmission eigenchannels and internal modes. Mind, however, that although multiple modes contribute to its formation, it is still only a *single* dominating channel that carries transmission through the sample. This insight allows for the identification of such a composed channel as a so-called "necklace state" [3, 36]. In an intuitive physical picture, we can imagine the situation as follows: In the single-channel regime the entire transmission is carried by only a single transmission eigenchannel throughout the whole spectrum. While in most cases this channel is formed by a single internal mode, it can happen that two or more modes spectrally overlap. In this situation, the internal modes merge into a single channel that can be imagined as a necklace of connected internal and localized modes that allow for transmission through the disordered region.

In a next step we want to investigate the single-channel regime on a statistical basis. In order to do so, we introduce three quantities that can all be calculated from the elements t_{ab} of the transmission matrix t . The first of these is the modal transmission

$$T_{ab} = |t_{ab}|^2 \quad (1.5)$$

that is just the absolute values squared of an individual transmission matrix element. Furthermore, there is the total modal transmission

$$T_a = \sum_{b=1}^N |t_{ab}|^2 \quad (1.6)$$

that represents the transmission through the sample for only one specific incident mode a . As used already in the previous considerations, we will again refer to the

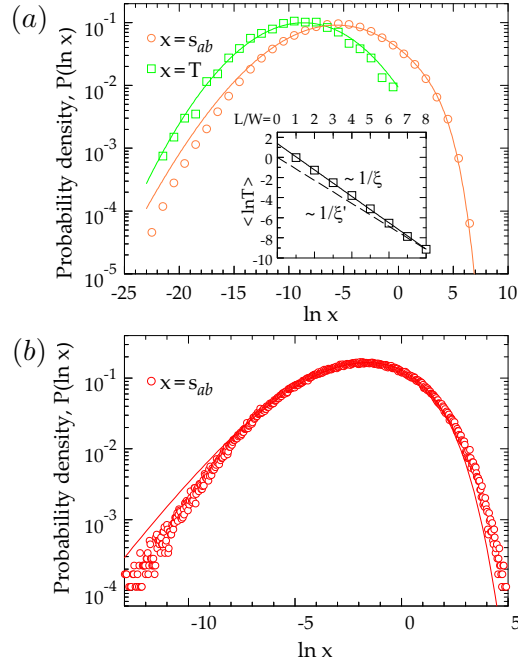


Figure 1.3.: (a) Probability density distributions $P(\ln T)$ (squares) and $P(\ln s_{ab})$ (circles) from the numerical data for a planar waveguide of $L/\xi = 5.25$. The solid lines plotted through the data are the predictions from Eqs. (1.9) and (1.10), respectively, with $L/\xi' = -\langle \ln T \rangle / 2 = 4.57$. Inset: $\langle \ln T \rangle$ versus L/W in the planar waveguides of eight different lengths (squares). The solid line is the best linear fit to the data, which yields the localization length $\xi = 1.52W$. The broken line is $\langle \ln T \rangle = -2L/\xi'$ for the planar waveguide of $L = 8W$, furnishing the renormalized localization length $\xi' = 1.74W$. (b) Experimental results and prediction for $P(\ln s_{ab})$ in the quasi-1D system of $L/\xi = 2.52$ (Sample *D*). Here, $L/\xi' = 1.25$ is obtained from fitting the bulk of the measured distribution (circles) with $P(\ln s_{ab})$ from Eq. (1.10) (solid line). Figure and caption were adapted from our collaborative work Ref. [2].

total transmission

$$T = \sum_{a,b=1}^N |t_{ab}|^2 = \sum_{a=1}^N T_a, \quad (1.7)$$

which is in some contexts in the literature also often called transmittance or dimensionless conductance g [37, 38].

As we want to do statistics, it has proven more convenient to also define three analogous quantities (labelled by the letter s) that just include a normalization by the disorder average (denoted by $\langle \dots \rangle$). These renormalized transmission quantities hence read

$$\begin{aligned} s_{ab} &= \frac{T_{ab}}{\langle T_{ab} \rangle} \quad , \\ s_a &= \frac{T_a}{\langle T_a \rangle} \quad , \\ s &= \frac{T}{\langle T \rangle} \quad . \end{aligned}$$

In addition we will in this part for the first time also substantiate our results by the use of a microwave experiment that was carried out by our collaborators in this project. In these experiments, microwaves are sent through long copper tubes of 4.4 cm in diameter. To mimic the disorder, these tubes are filled with a random arrangement of alumina (Al_2O_3) spheres. In order to lower the filling fraction of these spheres, they were coated with Styrofoam which is essentially transparent for microwaves. For insight into the statistics, many different configurations of disorder (i.e., arrangements of alumina spheres) have to be evaluated. This is achieved by rotating the tube and thereby making the spheres randomly fall in different places. For even more experimental details, see the methods section of our joint publication Ref. [2].

For the description of transmission statistics in the single-channel regime, one would ideally wish for an analytical expression. To get an intuition, we first establish that our strongly disordered system in the single-channel shows similarities with a one-dimensional sample. While in a one-dimensional system transport is due to the lack of a transverse degree of freedom naturally restricted to a single channel, localization is in our multi-dimensional and disordered systems responsible for limiting transport to a single channel. The difference is that for a one-dimensional system, the transmission statistics, i.e., the probability density $P(T)$, are known analytically [28, 39, 40]. The main finding in our following results is, that the same one-dimensional analytic theory can be applied to our multi-dimensional samples in the single-channel regime. The only adjustment that has to be made is a renormalization of the localization length ξ . In other words, our single-channel samples can be described as one-dimensional samples with an effective localization length

ξ' . This enlargement of the localization length accounts for the fact that the multi-dimensional samples first undergo a diffusive regime before localization sets in. Such a regime is entirely absent in a purely one-dimensional disordered system [41].

How this mapping to a one-dimensional system works in detail will be elaborated in the following. Usually in our numerics, the localization length ξ is determined by plotting the disorder-averaged logarithmic total transmission $\langle \ln T \rangle$ as a function of the system length L . As the transmission drops exponentially with system length due to Anderson localization, we can fit this curve by a straight line the slope of which is proportional to the inverse localization length, specifically $-2/\xi$, which allows for an easy calculation of ξ . An exemplary such fit is also shown by the solid line in the inset of Fig. 1.3(a). The effective localization length ξ' on the other hand is determined by assuming that even for zero length L there is only a single channel for propagation through the sample, i.e., $\langle \ln T \rangle(L=0) = 0$. Analogously, ξ' is calculated from the slope of the straight line that is connecting the origin to the particular point of $\langle \ln T \rangle$ at some length L [as shown by the dashed lines in the inset of Fig. 1.3(a)]. This leads to the relation

$$\xi' = -2L / \langle \ln T \rangle(L) . \quad (1.8)$$

Note that, while the pure localization length is universal for all lengths L of a sample, the effective localization length ξ' still depends on L .

To explicitly test whether the above renormalization of the localization length allows us to analytically describe the statistics of a strongly disordered sample in the single-channel regime, we compare both our numerical and experimental results to predictions for the probability density of transmission of a theory that was originally put forward for only one dimension [42]. The only thing that we change in the formula for the probability density distribution $P(T)$, is replacing ξ by the renormalized ξ' :

$$P(T) = C \frac{\sqrt{\text{arccosh}(T^{-1/2})}}{T^{3/2}(1-T)^{1/4}} \exp\left[-\frac{\xi'}{2L} \text{arccosh}^2(T^{-1/2})\right] , \quad (1.9)$$

where C is a normalization constant. Using this formula, we derived an expression also for $P(s_a)$ and $P(s_{ab})$ reading

$$\begin{aligned} P(s_a) &= \int_0^\infty \frac{ds}{s} P(s) \exp(-s_a/s) , \\ P(s_{ab}) &= 2 \int_0^\infty \frac{ds}{s} P(s) K_0(2\sqrt{s_{ab}/s}) , \end{aligned} \quad (1.10)$$

where $K_0(x)$ is a modified Bessel function of the second kind. This derivation involves the relations between the statistical moments of the normalized transmissions, i.e.,

$$\langle s_{ab}^n \rangle = n! \langle s_a^n \rangle = (n!)^2 \langle s^n \rangle ,$$

and so-called moment generating functions [43]. The comparison of our results and the prediction from Eq. (1.9) is shown in Fig. 1.3. As indicated by the comparison of the red and green lines with the numerical data represented as squares and circles of the corresponding color in panel (a), our results show excellent agreement for the statistics of T as well as s_{ab} . Importantly, this agreement is not achieved from a fit of any kind but by a real match of prediction and numerical data. Such a fit is only necessary for the experimental results of panel (b) since measuring the total transmission is not possible in our experiment. Still, for the experimental data we also find that Eq. (1.9) fits nicely the results [as shown in Fig. 1.3(b)] with ξ' now a fit parameter that is also in this case found to be larger than the actual localization length ξ . The only discrepancy in this fit occurs in the tails of the experimental distribution and can be attributed to subdominant transmission eigenchannels and/or the small signals due to the ever-present absorption in the experiments.

Overall, these results allow for an analytical model of the statistics of strongly disordered systems. This was achieved by a mapping of our system on an effective one-dimensional system featuring a renormalized localization length $\xi' > \xi$. We also found that this approach is valid in our numerics as well as the experiments. This universality is astonishing given that the numerics are carried out for two-dimensional systems that neglect the vectorial character of the microwaves in our three-dimensional experiment.

In the following we will see that not only this mapping is a universal property of localized disordered systems, also the cross-over to the single-channel regime itself happens in a universal manner and can be charted by statistical means.

For this purpose, it will be useful to find a parameter that reflects the entrance into the single-channel regime. In addition, this parameter should be experimentally (and also numerically) accessible. To find such a quantity, we look at the singular value decomposition of the transmission matrix

$$t = u \cdot \text{diag}(\sqrt{\tau_n}) \cdot v \ ,$$

which involves the two unitary matrices u and v . As in the single-channel regime we can neglect all the τ_m for $m > 1$, we find that

$$T_{ab} = |u_{a1}|^2 \tau_1 |v_{1b}|^2 \ ,$$

$$T_a = |u_{a1}|^2 \tau_1 \ ,$$

and of course also $T = \tau_1$. Since T_a is independent of the input mode b , this formula also reveals an intuitive explanation for the frozen speckle patterns observed in the experiment [22, 29]. According to Refs. [24, 43], $|u_{a1}|^2$ and $|v_{1b}|^2$ obey negative exponential statistics leading to the relation

$$\langle |u_{a1}|^{2n} \rangle / \langle |u_{a1}|^2 \rangle^n = \langle |v_{1b}|^{2n} \rangle / \langle |v_{1b}|^2 \rangle^n = n! \ .$$

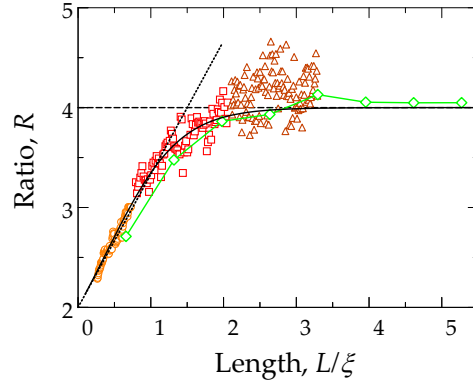


Figure 1.4.: The crossover to the single-channel regime is charted in terms of the ratio R of the statistical moments of the normalized transmitted intensity $s_{ab} = T_{ab}/\langle T_{ab} \rangle$ and the normalized transmittance $s = T/\langle T \rangle$, $R = \langle s_{ab}^2 \rangle / \langle s^2 \rangle$, as a function of L/ξ . From the microwave experiment, R was obtained in Sample *A* (orange circles), *C* (red squares), and *D* (brown triangles). The data points of the same color and style correspond to different frequencies in samples of the same filling fraction and length. In the numerical simulations, planar disordered waveguides of eight different lengths were considered at a single scattering frequency (green line-connected diamonds). Both the experimental and numerical data agree well with exact non-perturbative calculations of R for a quasi-1D geometry shown by the black solid line. The black dotted line represents the perturbative limit of R , for $L/\xi \ll 1$, $R = 2 + 4L/3\xi$, and the black dashed line represents the single-channel value $R = 4$ in the deeply localized limit. Figure and caption were adapted from our work collaborative Ref. [2].

This leads to an equation for the statistical moments of the normalized transmission quantities,

$$\langle s_{ab}^n \rangle = n! \langle s_a^n \rangle = (n!)^2 \langle s^n \rangle \quad .$$

Evaluated for the second moments ($n = 2$), this inspired us to define a ratio

$$R = \langle s_{ab}^2 \rangle / \langle s^2 \rangle \quad , \quad (1.11)$$

that will in case of single-channel transport show a unique value of $R \approx 4$. In the diffusive limit ($L \ll \xi$), however, we perturbatively find for $N \gg 1$ the equations [44, 45]

$$\begin{aligned} \langle s^2 \rangle &= \langle T^2 \rangle / \langle T \rangle^2 \approx 1 + 2L^2 / (15\xi^2), \\ \langle s_{ab}^2 \rangle &\approx 2 + 4L / (3\xi) \quad \text{and} \\ \langle s^2 \rangle &\approx 1 + 2L^2 / 15\xi^2 \quad . \end{aligned}$$

Plugging this into the definition of R from Eq. (1.11) leads to the result $R \approx 2 + 4L/(3\xi)$ which lets us expect a value of $R \approx 2$ for vanishing system length L . The above considerations show that the quantity R should allow us to chart the cross-over from diffusive transport into the single-channel regime as these regimes feature distinct values of $R \approx 2$ and $R \approx 4$, respectively. The results for R in these two limits are shown in Fig. 1.4 as the black dotted lines.

In order to find an analytical approach to the ratio R , we utilize the results of exact and non-perturbative calculations of Ref. [46] to express $\langle T \rangle$ and $\langle T^2 \rangle$. In addition we took the relations $\langle s_{ab}^2 \rangle = 2\langle s_a^2 \rangle$ and $\langle s_a^2 \rangle = 1 + \text{var}s_a = -(\xi/\langle T \rangle^2) \partial \langle g \rangle / \partial L$ from the literature [47, 48]. This analytic result for R is shown as the black solid line in Fig. 1.4 and shows a monotonic cross-over from $R = 2$ in the diffusive limit to $R = 4$ in the single-channel regime with increasing L/ξ . In order to verify these predictions, we also calculate R as a function of L in units of ξ numerically in our two-dimensional planar and disordered waveguides. As a starting point, ξ can be determined from the slope of the linearly decaying average logarithmic conductance $\langle \ln T \rangle$ as discussed before already. We numerically calculate the full transmission matrix t for 2000 random disorder realizations at 8 different values of L leading to a determination of $\xi = 1.52W$. From this data it is also possible to calculate R as a function of L/ξ for which the results are shown as line-connected green diamonds in Fig. 1.4. This data agrees very well with the analytical prediction for R . We emphasize that especially at large L/ξ the convergence of R to an approximate value of 4 is nicely confirmed by our numerical simulations. For further substantiation of the universality of this cross-over, our collaborators in San Antonio also measured R as a function of L/ξ in the microwave experiment. For this purpose, we used 4 different samples: A (alumina filling fraction, $f = 0.064$, and $L = 30.5$ cm), B ($f = 0.064$, $L = 45.7$ cm), C ($f = 0.064$, $L = 91.4$ cm) and D ($f = 0.125$, $L = 45.7$ cm). In order to determine R one needs to measure the second moment $\langle s^2 \rangle$ of the normalized total transmission s . Since the total transmission cannot be measured in the experiment, this challenge has to be overcome by using the relation [44, 49] $\langle s^2 \rangle = \langle s_{ab}s_{a'b'} \rangle_{a \neq a', b \neq b'}$. In this way the second moment can be expressed as a correlator of normalized modal transmissions s_{ab} and $s_{a'b'}$ that can be measured by rotating simultaneously both the emitting and receiving microwave antennas by 90° . As the number N of transmission channels in the experiment is directly proportional to the cross-section area of the copper tube, we find that N varies from 24 to 32 in the frequency range considered. We investigated 15000 different disorder configurations to have good statistics. The ratio R is plotted versus L/ξ in Fig. 1, represented by the unlinked data points. These points are gathered from a variation of frequencies and their color and style varies with the sample in use: Sample A is represented by the orange circles, B by red squares and D by brown triangles. We find that these data points are falling on the same curve predicted by analytic theory and numerics. This is astonishing, in particular when

considering that three different samples with varying filling fractions and lengths at different frequencies were used. The strong variations in the data occurring at larger $L/\xi \geq 2.5$ are caused by small signals that emerge from the increasing absorption in those strongly localized systems. Note that the cross-over to the single-channel regime in terms of the ratio R is not even distorted by the fact that the experiment is done with vector waves while the numerical waves are scalar.

However, we have to mention that the numerical and the experimental systems are still both quasi-one-dimensional. For this reason, samples with a slab geometry [50, 51] may require a theoretical treatment that reaches beyond the quasi-one-dimensionality considered here. The reason for this is that the behavior of R relies intrinsically on the negative exponential statistics of $|u_{an}|^2$ and of $|v_{nb}|^2$ which might not be guaranteed without quasi-one-dimensionality. A hint in the opposite direction can be found in Refs. [52, 53] where the distribution $P(s_{ab})$ measured in three-dimensional setups were found to agree nicely with a quasi-one-dimensional theoretical prediction. Also the eigenvalue distribution of the disordered system should not be very sensitive to the shape of the disordered sample [54]. Testing the cross-over to the single-channel regime also under this circumstances would be an interesting task for the future.

In the last part of this study we also investigate the time-response and thereby the dynamics of the single-channel regime. For this purpose, we evaluate the time-dependent transmission amplitudes $t_{ab}(t)$ by multiplying the spectrum with a Gaussian shaped envelope of width σ . This is done in the same way with the stationary experimental data as well as numerical data. We also again employ the statistical ratio $R(t)$ but now as a function of time delay t . As in the stationary case, we expect to be able to identify single-channel transport by finding $R(t) \approx 4$.

Following the arguments from the discussion of Fig. 1.2, we already assessed that in the single-channel regime the dominant transmission eigenchannel is formed by either a localized internal mode or a necklace state. From this we conclude, that the bandwidth of the eigenchannel is equal to the width of the transmission resonance. For a pulsed excitation of the disordered sample this leads us to the intuitive expectation that for a pulse bandwidth σ that is much smaller than the average mode spacing $\Delta\nu$ (average spectral distance of the resonances), the waves will transmit only through a single eigenchannel. On the other hand a broader pulse with bandwidth much larger than this spacing will occupy multiple eigenchannels on its way through the disordered region. In such a situation, one would observe a non-exponential decay of transmission in time and spreading of the signal due to modal dispersion [55].

As a starting point, the red line in Fig. 1.5(a) shows $R(t)$ as a function of time delay t in a microwave experiment of sample D ($L/\xi = 2.9$) for a pulse bandwidth that is smaller than the average mode spacing $\Delta\nu$ ($\sigma = 0.5\Delta\nu$) but still significantly larger than the average resonance width $\delta\nu$ ($\sigma = 5\delta\nu$). A comparison of this data

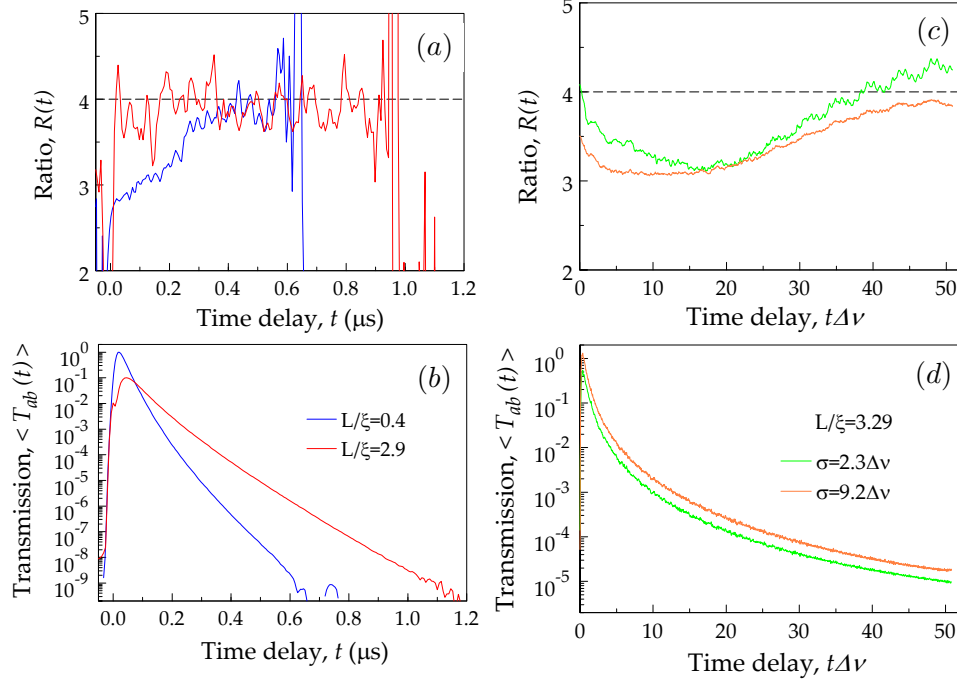


Figure 1.5.: Time-dependent ratio $R(t)$ in random quasi-1D [(a) experiment] and planar 2D [(c) numerics] waveguide systems following a Gaussian pulsed excitation of bandwidth σ . The horizontal dashed lines indicate $R = 4$ of the single-channel regime. The experimental data in (a) are for a localized sample of $L/\xi = 2.9$ (Sample D, red line) and for a diffusive sample of $L/\xi = 0.4$ (Sample D, blue line), using a pulse bandwidth of $\sigma = 5\delta\nu = 0.5\Delta\nu$ and $\sigma = 1.8\delta\nu = 3.9\Delta\nu$, respectively. Note that for the localized sample a single transmission eigenchannel dominates the pulsed transmission for all times, whereas a crossover to the single-channel regime with increasing time delay can be noticed in the diffusive system. The numerical data in (c) are for a localized sample of $L/\xi = 3.29$, using a bandwidth $\sigma = 2.3\Delta\nu$ (green line) and $\sigma = 9.2\Delta\nu$ (brown line). Note that for both cases we have $\sigma > \Delta\nu$, for which the single-channel regime sets in at long time delays. In addition, for the case where σ is less than the average separation between neighboring necklace-state resonances of $5\Delta\nu$, the single-channel regime can be realized by transmission through a necklace state at short time delays (see the green line at $R = 4$ for small t). For all cases, the average pulsed transmission, $\langle T_{ab}(t) \rangle$, is shown in (b) (experiment) and (d) (numerics). The experimental transmission curves were normalized to have a peak of unity and the curve for the localized system was displaced by a decade for clarity of presentation. Figure and caption were adapted from our collaborative work Ref. [2].

with the associated average modal transmission $\langle T_{ab}(t) \rangle$ [see red line in Fig. 1.5(b)] reveals that the onset of the single-channel regime (hallmarked again by $R \approx 4$) occurs right after the maximum of the modal transmission. This observation just perfectly fulfills the expectation that for $\sigma < \Delta\nu$ the pulse is typically transmitted through a single channel.

The contrasting case of a pulse bandwidth that is larger than the average mode spacing is investigated experimentally by the blue lines in Fig. 1.5(a) and (b). (sample *B*, $L/\xi = 0.4$ and $\sigma = 1.8\delta\nu = 3.9\Delta\nu$). As observed there, $R(t)$ starts out from a stationary value of 2.8 before monotonically crossing over to and saturating at a value of $R \approx 4$. Again, the comparison to the average modal transmission in the time-domain allows the conclusion that in this case the cross-over to the single-channel regime occurs at way larger values of t and considerably long after most of the intensity had leaked out of the sample. Also this observation is in line with our expectations: At short times most of the intensity transmits through the sample by the use of multiple channels because such a spectrally broad pulse collectively excites several of them at the same time. However, there are obviously also strongly localized, spectrally sharp resonances that are long-lived and transmit intensity only after a significantly larger amount of time. Such modes are called pre-localized modes in the literature [56] and can be held responsible for the occurrence of the single-channel regime also under these circumstances but at much later times than in the case of narrow pulses. These results are further numerically corroborated by the calculation of $R(t)$ for two-dimensional waveguides with $L/\xi = 3.29$ and charted by the green and brown lines in Fig. 1.5(c).

Comparing these two lines that are featuring a different pulse band width σ even reveals further information. As opposed to a single localized internal mode, a necklace state is characterized by a short lifetime [23]. Consequently we can hope for seeing signs of necklace states at small time-delays. Such a sign can be found for the green line in Fig. 1.5(c) that clearly starts out from a value of $R \approx 4$ at very short time-delays. The bandwidth of $\sigma = 2.3\Delta\nu$ in this calculation is larger than the average mode spacing and hence multiple resonances are excited. However, at this value of σ we can still expect that only one necklace resonance is excited by a single pulse as typically the spectral distance between two necklace states is larger than the average mode spacing $\Delta\nu$. This latter argument is supported by a look at Fig. 1.2(a) where one finds the two necklace resonances (those resonances with 2 internal modes underneath) are about $5\Delta\nu$ apart. In order to further check on the above considerations, we also excite a pulse of bandwidth $\sigma = 9.2\Delta\nu$ [see the brown line in Fig. 1.5(c)] which is so broad that we can expect it to also excite multiple necklace states. Indeed we find, that $R(t)$ in this case does not quite reach the value of 4 at very short times. For larger times, the green and the brown line again behave similarly: After the necklace resonances have leaked out of the sample, transport is for intermediate times dominated by multiple localized internal modes resulting

in multiple channels and a drop in $R(t)$. Only for very large times, single-channel transport is revived by pre-localized modes with very long life times (as discussed in the previous paragraph).

1.3. Controlling branched flow

Although wave scattering has been studied for several decades now already, the fundamental phenomenon of branched flow has only been discovered not much longer than a decade ago for electrons in semiconductor heterostructures [11]. The density of electrons injected through a quantum point contact into these two-dimensional systems shows clear branched patterns instead of the expected fan-like spreading into the system. This behavior could be attributed to the weak and smooth background potential that is always present in such structures [57]. Soon afterwards it was shown that this phenomenon can be largely explained in a classical way by the formation of caustics due to the smooth disorder potential acting like imperfect lenses [58]. This focussing effect leads to the formation of branches in the flow of the electrons which can drastically alter transport properties [59–61]. Although first discovered as a nano-scale wave effect, branched flow in the following proved to have an impact on wave-phenomena over a wide range of length scales reaching up to the formation of freak-waves in the ocean [62–65].

While many previous studies focussed on the statistics of the phenomenon [58, 65, 66] as well as its classical [58, 67] or quantum [57, 68, 69] origin, there is, to our best knowledge, no study so far that addresses the question how branched flow can actually be used for wave control or focussing through disordered media. In this work we are developing methods that let us guide the waves' intensity flow along single branches in a disordered medium. We are turning towards an optical system since in such experiments methods of wave control are sufficiently advanced for a possible experimental realization of our proposed methods.

First results regarding this topic were produced by Andre Brandstötter during the course of his project thesis [70] that was carried out under Prof. Rotter's, Philipp Ambichl's and my supervision.

In a first step we define the system under consideration more precisely (see Fig. 1.6): We consider a rectangular scattering region of length L and width W that is attached to two clean semi-infinite leads of the same width W on the left and on the right. In transverse direction hard-wall boundary conditions are used. As branched flow is at least partially a classical phenomenon [67], we need to consider a preferably large number M of propagating open modes in the leads. In all the calculations we choose $M = 200$ and a fixed wavenumber $k = \frac{m\pi}{W}$ of the incoming light. In order to choose well-suited units in our system, we set $W = m = 200.01$ resulting in $k = \pi$. This choice ensures that a length of 1 in our system corresponds to

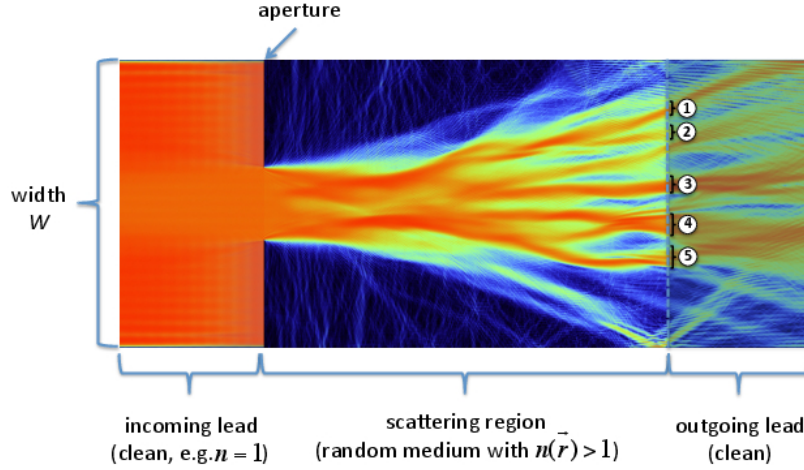


Figure 1.6.: Illustration of the setup under study. A cavity of length L and width W containing the smooth disorder potential as well as the aperture is attached to an incoming left and an outgoing right lead. The system parameters are all given in units of half a wave length and are the same in all figures if not stated otherwise. The width of the disordered region is $W = 200.01$, the length $L = 1.4W$. The aperture between left lead and scattering region is of height $d = 50.5$. The refractive index of the disorder varies smoothly between $n = 1.0$ and $n = 1.1$ with a correlation length of $\xi = 6.0$. Light at constant wavenumber $k = \pi$ is injected from the left lead one-by-one in the n -th transverse lead mode. The plotted intensity distribution shows the incoherent superposition of the corresponding scattering intensities of mode 1 to 25 injected through the left lead. The color code is logarithmic and high intensity regions are shown in red. The branched structure is clearly visible and 5 main branches are identified and marked by their respective numbers. Separating these branches exploiting techniques of wavefront shaping is the main goal of this study.

half a wavelength. Since historically branched flow has first been observed for electrons injected through a constriction (quantum point contact) into a high-mobility electron gas [11], we also include such a constriction in form of an aperture of width $d = 50.5$ between the left lead and the cavity in our geometry. The length of the cavity is typically chosen to be $L = 1.4W$.

The smooth long-ranged disorder necessary to observe branched flow is modelled by a spatially dependent index of refraction $n(\vec{r})$ throughout the whole scattering region. This disorder is chosen in such a way that it is characterized by its maximal refractive index $n_{\max} = 1.1$, while the minimal index of refraction is always kept at vacuum value $n_{\min} = 1$. The smoothness of the potential is guaranteed by a finite choice of correlation length $\xi = 6.0$ measuring the long-rangedness of the disorder. This length ξ is defined as the standard deviation of the Gaussian auto-correlation function

$$C(|\vec{r} - \vec{r}'|) = \langle (n^2(\vec{r}) - 1) \cdot (n^2(\vec{r}') - 1) \rangle \propto e^{-\frac{|\vec{r} - \vec{r}'|}{2\xi}}$$

We choose $\xi = 6$, which is of the order of the wave length $\lambda=2$. Discretizing the geometry on a square grid using finite differences, we solve the scattering problem of this 2-dimensional setup via the Helmholtz-equation (1.1) with $\psi(\vec{r})$ representing the out-of-plane z -component of the electric field and a fixed incoming wave number $k = \omega/c$. We use a discretization of 10 points per half-wavelength in all our calculations.

We employ the modular recursive Green's function technique [12] for the calculation of the scattering matrix Eq. (1.3). Our numerical method [13] also allows for calculating the intensity $|\psi(\vec{r})|^2$ of the electric field for arbitrary injection in the left lead (see also section 3.6 for a detailed explanation of the numerics).

In Fig. 1.6 we show an incoherent superposition² of the first 25 waveguide modes injected one-by-one through the left lead. In this way we can visualize the underlying branched structure caused by the smooth disorder potential. We are able to identify 5 main branches at the output that are marked by the corresponding numbers in Fig. 1.6.

The goal of this work is to separate these 5 main branches observed in Fig. 1.6 by finding suitable coherent superpositions of lead modes to inject from the left. Such purposeful excitations of single branches would be an interesting step forward in wave control in systems allowing for branched flow. The methods we are using in order to achieve this goal involve the scattering matrix S from Eq. (1.3) of which at least parts can already be measured in optical experiments thanks to recent technological developments of spatial light modulators. Such an approach in terms of S usually entails finding an operator that is able to separate the scattering states with respect to a physical quantity that is described by the operator's eigenvalues. From

² with incoherent we mean that the sum is taken over the absolute values squared of $\psi(\vec{r})$ and thus ignoring interferences.

an experimental point of view methods that are based on (parts of) the scattering matrix only, are of special interest since only asymptotic scattering amplitudes are available for measurement while full control of the wave inside the system is not possible. The most famous example of such an operator is the Wigner-Smith time-delay operator [71, 72]

$$Q = -iS^\dagger \frac{dS}{d\omega} \quad (1.12)$$

which measures the time-delay of an arbitrary injected superposition of lead modes in our optical system. Special eigenstates of Q , were so far used numerically to separate scattering states by their delay-times yielding particle-like scattering patterns inside the system (termed NOTES) [73].

In a first approach we try to use this exact method for the separation of branches. The left column of Fig. 1.7 shows those 5 eigenstates of Q_{11} that correspond to the smallest time delay eigenvalues of the system. One can clearly see, that the states excite branches with a similar path length through the medium but none of them cleanly excites only one single branch. It is also important to mention that due to the large number of $M = 200$ open modes, the scattering matrix contains a lot of information. In a possible experiment it will hence be hard to determine the full scattering matrix S and in optics it is so far only possible to measure (small) parts of it [17, 74].

However, a recent study proposed a method in case only a quadratic part s of size $N \times N$ with $N < 2M$ of the scattering matrix S is known [75]. In this case a reduced time-delay operator Q_s can be defined by

$$Q_s = -is^{-1} \frac{ds}{d\omega}. \quad (1.13)$$

This definition is almost analogous to Eq. (1.12) except that now the operator is calculated from the inverse s^{-1} instead of the hermitian conjugate S^\dagger . The only problem with this definition is, that the existence of the inverse of s is not guaranteed in any way and that s in general does not even have to be quadratic. For example if only the transmission matrix t is known, i.e., $s = t$, and the system under consideration features many modes that are hardly or not at all transmitted (like in our case due to the aperture), t is usually singular and Q_s thus not defined.

We overcome the aforementioned problem that may occur computing the inverse of s by projecting out the singular channels of s for the definition of an alternative operator \tilde{Q}_s . For this purpose we utilize the singular value decomposition (SVD) of s reading

$$s = U\Sigma V^\dagger,$$

with the unitary matrices U and V as well as a real diagonal matrix Σ consisting of the singular values σ_i of s ordered by $\sigma_1 > \sigma_2 > \dots > \sigma_N$. U and V contain in

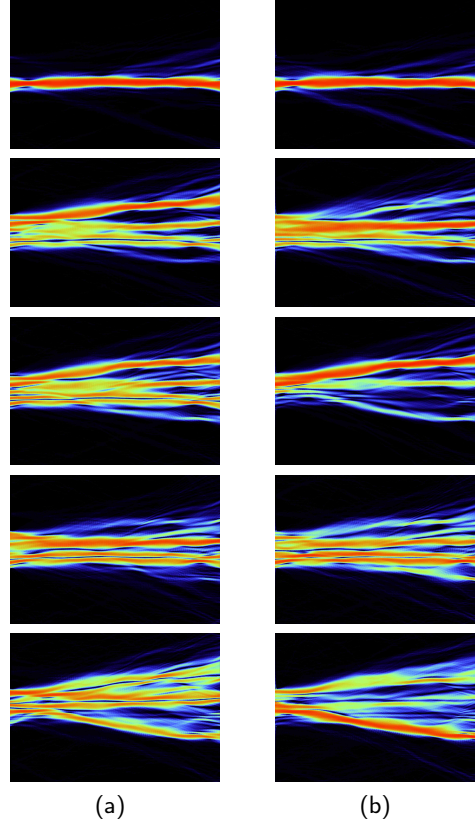


Figure 1.7.: Intensity distributions when injecting the 5 eigenstates of (a) Q_{11} [Eq. (1.12)] and (b) \tilde{Q}_t [Eq. (1.14)] that belong to the smallest time-delay eigenvalues of the corresponding operator. The derivative with respect to wavenumber k is for both operators approximated numerically by a symmetric difference quotient with a spacing of $\Delta k = \pi \cdot 10^{-8}$. The cutoff for singular values in the calculation of \tilde{Q}_t in (b) is set to $\epsilon = 0.1$.

their columns the left and right singular vectors, respectively. If s is singular or non-quadratic, some singular values will become zero. In order to guarantee regularity, we construct an alternative matrix \tilde{s} that includes only those \tilde{N} singular values of s that are larger than some small value ϵ . For this purpose we define

$$\tilde{\Sigma} = \tilde{U}^\dagger s \tilde{V}$$

with \tilde{U} and \tilde{V} deriving from U and V by truncation of all columns (all singular vectors) with index $j > \tilde{N}$. The inverse of s in the definition of Eq. (1.13) is in this way replaced by

$$s^{-1} \rightarrow \tilde{V} \tilde{\Sigma}^{-1} \tilde{U}^\dagger$$

and the wavenumber derivative in Eq. (1.13) is projected onto the subspace of the chosen singular values by the use of \tilde{U} and \tilde{V}

$$\frac{ds}{d\omega} \rightarrow \tilde{U} \tilde{U}^\dagger \frac{ds}{d\omega} \tilde{V} \tilde{V}^\dagger.$$

Overall we arrive at an alternative and always existing definition of a time-delay operator \tilde{Q}_s reading

$$\tilde{Q}_s = -i \tilde{V} \tilde{\Sigma}^{-1} \tilde{U}^\dagger \tilde{U} \tilde{U}^\dagger \frac{ds}{d\omega} \tilde{V} \tilde{V}^\dagger := -i \tilde{s}^{-1} \frac{d\tilde{s}}{d\omega} \quad (1.14)$$

with

$$\tilde{s}^{-1} = \tilde{V} \left(\tilde{U}^\dagger s \tilde{V} \right)^{-1} \tilde{U}^\dagger$$

and

$$\tilde{s} = \tilde{U} \tilde{U}^\dagger s \tilde{V} \tilde{V}^\dagger.$$

We tested the above method by assuming that only the transmission matrix t was known in the branched flow systems under consideration, i.e. $s = t$. This approach is also of special meaning for future experiments since it is in general easier to experimentally determine the transmission matrix t than the reflection matrix r . The 5 eigenstates belonging to the 5 smallest eigenvalues of \tilde{Q}_t for a cutoff value in the SVD of $\epsilon = 0.1$ are shown in the right column of Fig. 1.7. These states closely resemble the corresponding eigenstates of Q_{11} as can be seen by comparison to the left column of the same figure. Even more so it seems that the eigenstates of \tilde{Q}_t tend to even better emphasize single branches and are thus a step forward towards the final goal of clean branch separation. The reason for this is that \tilde{Q}_t is not as much affected by increased reflections as Q_{11} and is thus less sensitive to the scattering from the edges of the aperture. This result is astonishing when considering that only a quarter of the information was used for the calculation of \tilde{Q}_t than for the calculation of Q_{11} .

However, for the separation of branches there is still plenty of room for improvements. As it turned out, the delay time criterion is not sufficient for the clean separation of branches. This comes from the fact that many of the branches show very similar delay times making this property not unique for each single branch in the system. It is obvious though that spatial information at the outgoing right lead is unique to every main branch in the system. By this we mean that knowing the positions of the intensity maxima at the output and restricting ourselves to this section should in principle allow for a clean separation of branches.

For this purpose we have to transform the scattering matrix S (or only the transmission matrix t) from the lead mode basis to the space basis. One defines a transverse position operator

$$y_{mn} = \int_0^W \chi_m^*(y) y \chi_n(y) dy \quad (1.15)$$

where χ_n represents the y -dependent part of the n -th lead mode. With this operator we can define a transformation matrix Y that in its columns contains the eigenstates of y_{mn} . The i -th of these eigenstates is a well localized peak around a position y_i in the lead and converges to a delta-distribution $\delta(y - y_i)$ in the high frequency limit. These positions y_i divide the lead into M equally spaced parts. The transmission matrix t can then be transformed to the transmission matrix \bar{t} in transverse space basis via

$$\bar{t} = Y^\dagger t Y. \quad (1.16)$$

The i -th row of \bar{t} describes the transmission from the whole input lead to the i -th peak belonging to an eigenstate of y_{mn} at the output lead. At this point we want to mention, that this transformation is only an issue in a numerical approach. In a possible experiment all the measured parts of the scattering matrix will even be easier accessible in the space basis. In our calculations we aim at focussing just onto those parts of the output where a certain branch arrives. Thus we cut out the corresponding $N \times M$ -block from the matrix \bar{t} and we will call this block g in the following. In this case N represents the number of y_{mn} -eigenstates located in the region we want to consider at the output (while M is still the number of open lead modes). By calculating the eigenstates of $g^\dagger g$ with the largest eigenvalues we find those states that have the largest transmission into the selected region.

In more detail, when trying to separate a branch, we proceed as follows: First we calculate the scattering wave functions for different injections into our system and superimpose those incoherently. Further we plot the spatial overlap of these distributions with the eigenstates of y_{mn} that are centered at positions y_i . Such profiles at the output of our system for an incoherent superposition of the first 25 lead modes as well as a superposition of the 10 Q_{11} -eigenstates with smallest eigenvalue are shown in Fig. 1.8. In a next step, we pick a certain branch (corresponding to

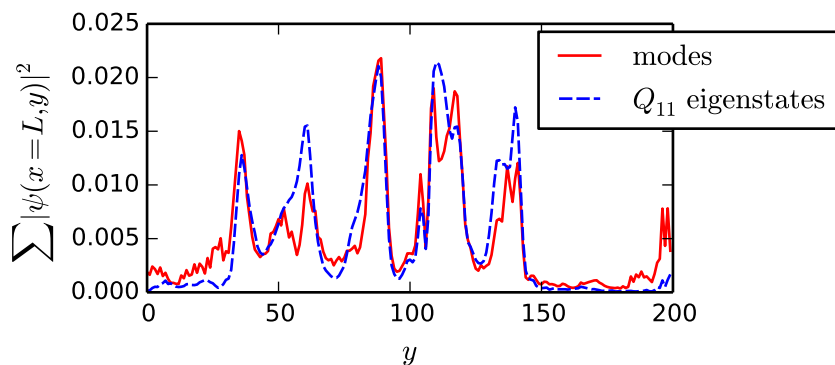


Figure 1.8.: Intensity output profiles as a function of central positions y_i of y_{mn} -eigenstates for an incoherent superposition of the first 25 lead modes (red solid line) and 10 Q_{11} eigenstates with smallest eigenvalues (blue dashed line). The maxima caused by the branched flow in the system are clearly visible. The regions where these maxima occur are used in our method to gain spatial information for the separation of branches.

a maximum in the output intensity) and choose a range of N such eigenstates that are located in the vicinity of the corresponding maximum at the output. Finally, we only keep those lines of \bar{t} that correspond to such an overlapping eigenstate. The resulting spatial transmission matrix g is then used for the calculation of the $g^\dagger g$ eigenstates. Experimentally this procedure would also be easily accessible: The output profiles can be determined by scanning the output facet measuring intensity and phase for injection through point sources at different positions. In this way g can be measured directly and can further be used for the procedure.

As an example we turn towards branch 5 in our system (see Fig. 1.6). We find that the intensity from this branch ends up mostly in the region between $y = 126$ and $y = 154$. We truncate \bar{t} by only keeping lines 126 to 154 yielding the desired spatial transmission matrix g . A singular value decomposition of g tells us that in fact 8 singular values are larger than 0.8 which lets us expect that many eigenstates of $g^\dagger g$ will transmit most of their intensity into the desired output region.

In Fig. 1.9(a) we show the first 5 such $g^\dagger g$ eigenstates for branch 5. We find that as expected these states very nicely transmit most of their intensity to the region between $y = 126$ and $y = 154$. In addition the eigenstate with the largest eigenvalue (largest transmission, top of the figure) already shows almost perfect excitation of only a single branch in our disordered cavity. Yet, a small contribution at the bottom can be seen that reflects from the boundary and is from there transmitted to the region at the output where also the main branch arrives. Such contributions

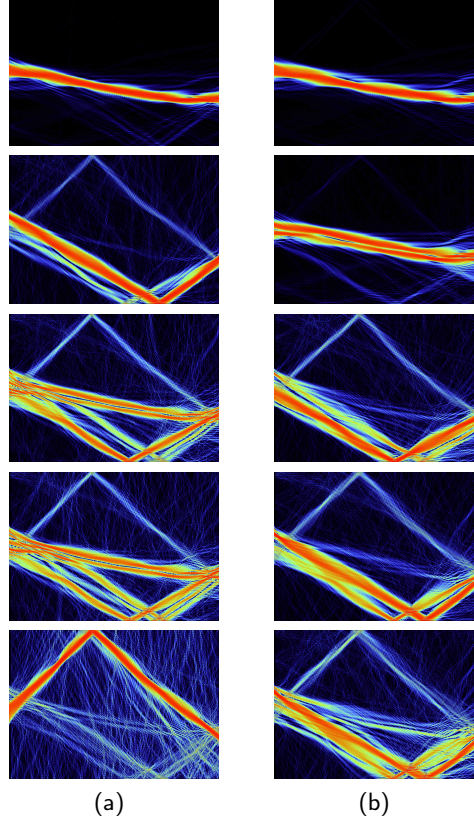


Figure 1.9.: Comparison of (a) eigenstates of $g^\dagger g$ with highest transmission eigenvalues and (b) eigenstates of \tilde{Q}_g with lowest time-delay eigenvalues. We restricted ourselves to the region from $y = 126$ to $y = 154$ in transverse direction at the outgoing lead. (a) The operator $g^\dagger g$ yields states that almost exclusively transmit into this region. States that bounce off the boundary several times are visible besides the clean main branches. (b) The \tilde{Q}_g operator is able to filter the subspace of $g^\dagger g$ for states that have similar delay times and thus leads to even cleaner separation of branches. All system parameters are the same as stated in the main text and the caption of Fig. 1.6.

with larger angles are in large number present in the other eigenstates of $g^\dagger g$ but still all of them arrive to a large extent in the desired region.

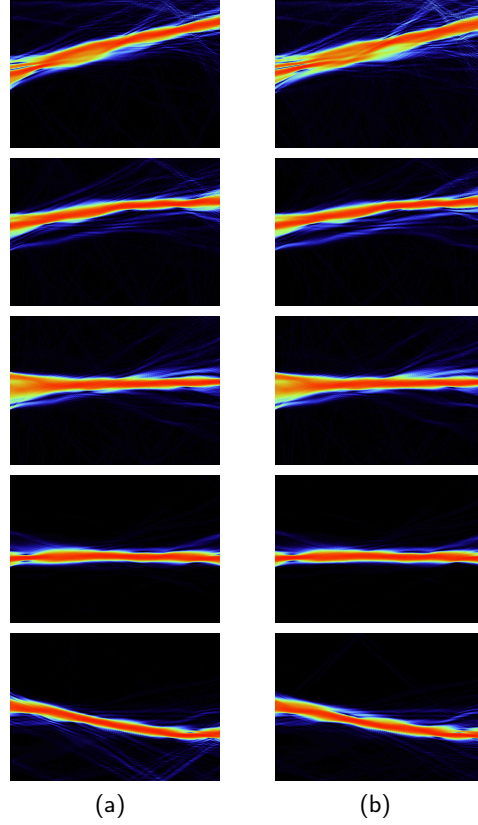


Figure 1.10.: We show the best states we were able to find for branches 1 to 5 of our system by considering (a) the $g^\dagger g$ eigenstates and (b) the \tilde{Q}_g eigenstates. One can see that both operators yield fairly similar results even though \tilde{Q}_g leads to a small improvement and elimination of larger angle contributions. The cutoff for accepted singular values in the calculation of \tilde{Q}_g is set to $\epsilon = 0.8$ for all 5 branches. All system parameters are the same as stated in the main text and the caption of Fig. 1.6.

We also applied this method to the other branches that were marked in Fig. 1.6. For every branch we show in Fig. 1.10(a) the eigenstate (of the respective $g^\dagger g$ -matrix) that resembles best a single branch. It is obvious that this method already works well as the desired main branches are almost exclusively excited in all 5 pictures. However, in some of the pictures we can still find small contributions from larger angles. In the following we will improve our results further by merging all the used

approaches into a single method.

Since the aforementioned large angle contributions have a longer way through the medium it can be expected that their time delay is significantly larger than for the main branch. It would be thus desirable to find an operator in the subspace of g that separates the $g^\dagger g$ eigenstates once more by time delay. Realizing that g is (in space basis) just a part of the full scattering matrix, we can additionally use our knowledge from the first section and interpret g as a partially known scattering matrix s as considered for the definition of a partial time-delay operator \tilde{Q}_s in Eq. (1.14). The only technical difference is the choice of the parameter ϵ that represents a minimal value for singular values of g (s) to be included in the calculation. Usually this value should be close to zero since it shall only guarantee regularity of \tilde{Q}_s but leave as many degrees of freedom as possible. However, in case of our time-delay operator \tilde{Q}_g it is essential that the states included have high transmission into a desired output region, i.e. have singular values close to 1. Still, choosing ϵ too close to 1 will remove degrees of freedom for the eigenstates of \tilde{Q}_g and impede clean separation of branches. In our calculations we find that choosing ϵ such that 5 to 10 $g^\dagger g$ -eigenstates are included (which is usually a value of $\epsilon \approx 0.8$ in our system) has proven to be a reasonable compromise. In Fig. 1.9(b) we show those 5 eigenstates of \tilde{Q}_g with smallest eigenvalue (again these results are calculated for branch 5 of our system as before for the $g^\dagger g$ -eigenstates). We find that especially the first eigenstate (on top of the panel) shows very clean excitation of a single branch and the high-angle contribution that was visible before [see top picture of Fig. 1.9(a)]. We can also see from the third row of Fig. 1.9 that the operator \tilde{Q}_g nicely eliminated the contribution of the main branch in the corresponding eigenstate of $g^\dagger g$. However, also in this state there are still contributions of two branches that reflect from the upper and lower boundary, respectively, but feature a very similar path length and thus a similar runtime. While this problem might be overcome by an additional operator separating this state with regard to the injection angle, it clearly does not occur for the main branches as these are not reflected from any of the boundaries.

As intended, the time-delay operator \tilde{Q}_g restricted in the subspace of large transmission to the region $126 \leq y \leq 154$ proved to be able to separate those states by delay time and finds a proper injection to exclusively excite the desired main branch. As shown in Fig. 1.10(b) we find that this way of exciting main branches works for all the branches that we identified in our system. We receive clean pictures of branches that almost show no diffraction and have over 90 percent of their intensity focussed on a small output region. These results show that our method leads to nice focussing through the disordered region as well as controlled branch flow.

One could argue that in this classical limit of many open modes single branches may be excited if one simply injects a state that corresponds to the classical angle in which the branch spreads. In order to check whether our own approach corresponds

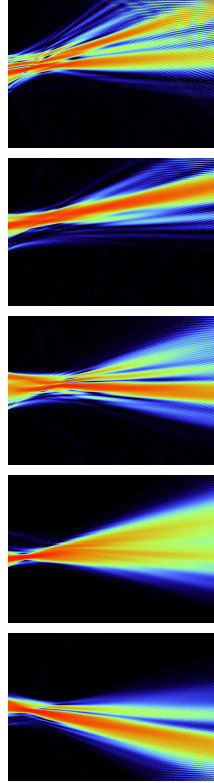


Figure 1.11.: Best single-branch \tilde{Q}_g -eigenstates injected into empty cavity. Removing the disorder potential leads to spreading of the states. All other system parameters are the same as stated in the main text and the caption of Fig. 1.6.

to this trivial strategy, we performed calculations where we injected the same superpositions of lead modes for which we found nice branch separation in Fig. 1.10(b) but now into an empty cavity. These results are shown in Fig. 1.11. One can clearly see that these states do not correspond just to a certain angle but rather spread widely in a clean region. This proves that our method does not yield trivial results and the disorder is mainly responsible for the nice collimation and focussing effects observed.

Another question that we turn towards is, how stable our results are with respect to injection frequency. For this purpose we increased the wavenumber k by up to 10 %. The results in Fig. 1.12 show that the excitation of branches hardly changes and only very slowly gets worse as a function of the incident wave's frequency (or wavenumber). Such an insensitivity to a frequency variation is a desirable feature for possible future experiments. This is because it allows for the injection of pulses

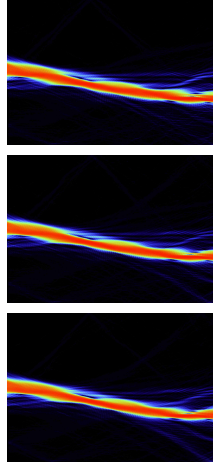


Figure 1.12.: Best \tilde{Q}_g -eigenstates of branch 5 with a variation of the wavenumber $k = 1.0\pi, 1.05\pi, 1.1\pi$, respectively. The superposition exciting the single branch that was previously calculated for $k = \pi$ proves to be very stable against variations of the wave number (frequency). All other system parameters are the same as stated in the main text and the caption of Fig. 1.6.

that naturally contain many frequency components. Since our single-branch states hardly change as a function of injection frequency we can expect that, in future experiments, one can also inject whole pulses which then propagate along single branches through the disordered system.

Overall we have shown that our methods allow for the selection of single branches in a disordered system with a smooth correlated disorder. These insight reveals the possibility of focussing waves through a disordered medium onto specific spots at the output, promising a broad range of future applications. One possible task that our methods could be helpful for is, e.g., the focussing of light through biological tissue which naturally features correlated disorder. Since the wave phenomenon of branch flow is not limited to optics but can be observed in all different kinds of wave systems, also steering electrical currents through nanostructures or even directing water waves in the ocean towards specific targets could, in principle, be realized.

Chapter 2.

Two-dimensional topological insulators

Topological insulators are recently discovered materials with promising electronic properties [4–6]. This chapter will be concerned with our research on this topic. Parts of this chapter are incorporated from our published papers Refs. [9] and [10].

2.1. Introduction

A two-dimensional topological insulator [4] features edge states similar to those of the quantum Hall effect with the difference that electrons of different spin move in the same direction at opposite edges. Accordingly, this so-called “quantum spin Hall” (QSH) effect [76] can be understood as two noninteracting copies of a quantum Hall system, one for each spin. These edge states are protected by time-reversal symmetry which forbids scattering into the counter-propagating edge state with opposite spin, strongly stabilizing them against non-magnetic disorder [77, 78]. These properties, which have recently attracted considerable attention [79–85], make topological insulators promising candidates for key components in future spin-tronic devices [86, 87].

In 2006 HgTe/CdTe quantum wells were proposed as suitable systems for a first experimental realization of the QSH effect [88] which was, indeed, achieved shortly thereafter [89, 90]. This experimental identification relied on observing the quantized conductance plateau hallmarking such disorder-insensitive conducting edge states.

As discovered in a successive numerical study [7], such edge states are not only immune from backscattering but can even be elicited by disorder in systems that have no topologically distinct properties in the clean limit. This disorder-induced topological phase was first believed to be caused by Anderson localization, and was thus named “topological Anderson insulator” (TAI). Meanwhile the TAI has been investigated numerically in a variety of different systems [91–95] including the case of a three-dimensional topological insulator [96].

In 2009 a theory was put forward [8] that lead to a detailed understanding of the TAI, showing that the phase boundaries at the transition from an ordinary insulator to the TAI can be explained by an effective medium theory. In this approach the

presence of disorder leads to a re-normalization of the medium parameters [8] in particular to the topological mass which pushes the system into the TAI phase. In this sense, the TAI appears due to a change of topology in the effective medium.

However, due to the challenges involved in controlling the disorder in a HgTe/CdTe quantum well, the TAI has not yet been realized experimentally. This problem can be overcome by employing photonic lattices that are fabricated in such a way that topologically induced edge states can be observed [97, 98]. In such a macroscopic system, the disorder can be controlled experimentally. Moreover, these systems are discrete which, for reasons to be explained below, makes them the most-promising candidates for an experimental observation of the TAI. Another system that could achieve this experimental observation are ultra-cold atomic gases in optical lattices [99]. In such a highly tunable model system the disorder could be introduced by an optical laser speckle potential [100, 101] which also has the advantage of being under external control. An important point to emphasize in this context is that both the speckle pattern for cold atomic gases as well as the disorder which naturally occurs in a quantum well are characterized by a finite spatial correlation length ξ .

2.2. Model

We proceed along the lines of previous studies, where an appropriate description of the two dimensional HgTe/CdTe quantum well was proposed in terms of an effective Hamiltonian [88]. This Hamiltonian which was derived based on the $\mathbf{k} \cdot \mathbf{p}$ perturbation theory and the six-band Kane-model takes the following form:

$$H_{\text{eff}}(k_x, k_y) = \begin{pmatrix} h(\vec{k}) & 0 \\ 0 & h^*(-\vec{k}) \end{pmatrix}, \quad (2.1)$$

with

$$\begin{aligned} h(\vec{k}) &= \mathbb{1}\epsilon(\vec{k}) + d_i(\vec{k})\sigma^i \\ \epsilon(\vec{k}) &= C - D(k_x^2 + k_y^2) \\ d_i &= \begin{pmatrix} Ak_x \\ -Ak_y \\ M(\vec{k}) \end{pmatrix} \\ M(\vec{k}) &= m - B(k_x^2 + k_y^2) \end{aligned} \quad (2.2)$$

and σ^i labeling the Pauli-matrices. The basis of this effective Hamiltonian consists of the s-like E1 and the p-like heavy-hole H1 quantum well sub-bands for spin up (+) and down (-). The ordering is chosen to be $|E1+\rangle, |H1+\rangle, |E1-\rangle, |H1-\rangle$. Details on the numerical implementation of this model Hamiltonian Eq. (2.1) can be found

in appendix A and in a similar form also in my diploma thesis [102]. A more detailed derivation of the model is given in the original paper [88] and also in my diploma thesis [102].

2.3. Topological insulator in the presence of spatially correlated disorder

An interesting feature of topological insulators is the so-called topological Anderson insulator (TAI) phase as mentioned already in the introduction. This phase is hallmarked by the fact that introducing disorder in the potential can actually introduce order in the electronic properties by causing unidirectional edge states that are typical of the Quantum Spin Hall effect [7]. Preliminary results on this topic can be found in my diploma thesis [102]. Parts of the following texts in this section are taken from our publication Ref. [9].

Here we ask the question, if a more realistic ansatz for the disorder potential including spatial correlations will have an effect on the appearance and decay of this phase. Since this correlation has been disregarded in all previous numerical studies of the TAI which we are aware of [7, 8, 95, 103, 104] the question was posed [104] how a finite correlation length ξ would influence the predictions for the appearance and for the stability of the TAI. In view of the fact that spatial correlations in the disorder have already been shown to play an important role in the context of various other scattering scenarios [73, 105–119] one may expect such correlations to be a relevant factor also for topological insulators. We address this topic by studying explicitly how a static and spatially correlated disorder influences the transport characteristics of topological insulators (Fig 2.1). As we will specify in detail below, our numerical results show marked deviations from conventional simulations with uncorrelated disorder.

For our calculations we use the Bernevig-Hughes-Zhang (BHZ) model Hamiltonian from Eq. (2.1). Since the spin-up and spin-down parts $h(\vec{k})$ and $h^*(-\vec{k})$, respectively, in the Hamiltonian are decoupled as a consequence of time reversal symmetry [120] it is sufficient for our calculations to only use the spin-up block $h(\vec{k})$ since the solution for the spin-down block follows from a time-reversal operation. The material-dependent constants A , B and D in the calculations of this section are set to realistic values $A = 364.5 \text{ meV nm}$, $B = -686 \text{ meV nm}^2$, $D = -512 \text{ meV nm}^2$ and $C = 0 \text{ meV}$ taken from Ref. [121]. The sign of the topological mass m has a strong impact on the system's transport behavior: for positive m the system behaves like an ordinary insulator with a band gap of $2|m|$, whereas if m is set to a negative value the system turns into a topological insulator featuring perfectly transmitting edge states for the Fermi energy E_F lying inside the bulk band gap $|E_F| < |m|$. To simulate such a system we use the experimentally determined value

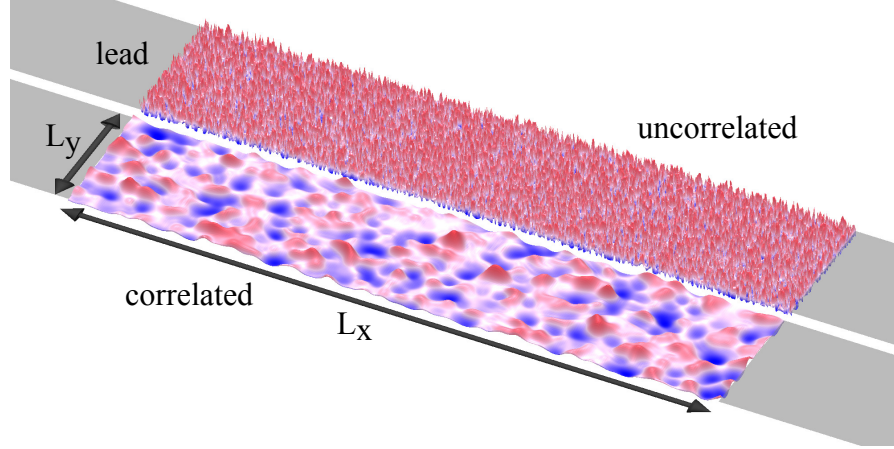


Figure 2.1.: Illustration of the scattering setup for the considered topological insulator: A rectangular disordered middle part of height L_y and width L_x is attached to two semi-infinite leads on the left and right. Random potentials with and without correlations between neighboring grid points in the underlying lattice discretization are shown in the bottom and top panel, respectively.

[121] of $m = -10$ meV. The scattering geometry which we consider consists of a rectangular disordered region of width L_x and height L_y attached to two clean, semi-infinite leads (see illustration in Fig. 2.1). We discretize the scattering region on a square lattice with grid constant a using the tight-binding approximation in the continuum limit for the implementation of the effective Hamiltonian. If not stated otherwise, the grid-constant a is set to 5 nm, in agreement with the value used in previous studies [7, 8, 103, 122, 123]. For simplicity, we consider the limit of vanishing temperature $T \rightarrow 0$ and infinitely small bias voltages $V \rightarrow 0$ applied between the two semi-infinite leads. According to the Landauer-Büttiker formalism the conductance G in this limit is proportional to the transmission probability T at the Fermi energy E_F ,

$$G = \frac{e^2}{h} T = \frac{e^2}{h} \sum_{n,m}^N |t_{nm}|^2 . \quad (2.3)$$

The indices n and m extend over all N lead modes and t_{nm} labels the transmission amplitude from mode n in the incoming lead to mode m in the outgoing lead. Since we consider both spins separately, every mode only contributes a single conductance quantum e^2/h . For the calculation of the transmission we employ the advanced modular recursive Green's function method [12, 13, 15] which incorporates the disorder by way of a static on-site energy value $V(\vec{x})$ imposed at every grid-point $\vec{x} = (x_i, y_j)$. In previous calculations the random on-site energies $V(\vec{x})$

were chosen to be uniformly distributed within a given energy interval $[-U/2, U/2]$, and each random sample from this distribution was drawn independently for each grid point. Since in this case the disorder value on each grid point has no correlation with the values on neighboring grid points we will refer to this type of disorder as “uncorrelated”. To go beyond this limitation and to account for the spatial correlations which naturally occur in realistic situations we choose our disorder potential such as to obey the Gaussian correlation function

$$C(\vec{r}) = \langle V(\vec{x}) \cdot V(\vec{x} + \vec{r}) \rangle \propto \exp\left(-\frac{r^2}{2\xi^2}\right) \quad (2.4)$$

where the brackets $\langle \dots \rangle$ stand for an average over all the grid points \vec{x} and many disorder realizations. The standard deviation of this Gaussian defines the correlation length ξ , which measures the spatial range of the correlations. The value of the disorder strength U is established by demanding

$$\begin{aligned} \langle V_{ij} \rangle &= 0 \quad , \\ \langle V_{ij}^2 \rangle &= \frac{U^2}{12} \quad . \end{aligned} \quad (2.5)$$

These values are chosen such as to agree with those of the uncorrelated disorder potential distributed within the interval $[-U/2, U/2]$. See Fig. 2.1 for an illustration of the disorder potentials with and without spatial correlations in the employed tight-binding grid. More details on the numerical construction of such a correlated disorder potential can be found in my diploma thesis [102].

We first consider the conductance through a disordered rectangular bar of width $L_x = 2000$ nm and height $L_y = 500$ nm for a negative and a positive value of the topological mass m ($m = -10$ meV and $m = +1$ meV), respectively. In the clean limit the system with $m < 0$ [see $U = 0$ in Fig. 2.2(a)] features quantized edge transport (green area) within the bulk band gap $|E_F| < |m|$, whereas conductance is entirely suppressed in the energy range $|E_F| < |m|$ for $m > 0$ [see $U = 0$ in Fig. 2.2(c)] [7]. Adding now an *uncorrelated* disorder to the clean systems with $m < 0$ and $m > 0$ gives rise to an unconventional conductance plateau [see $U > 0$ in Figs. 2.2(a) and 2.2(c) as well as Ref. [7]]. This so-called TAI phase of quantized transport emerges in the presence of strong uncorrelated disorder at energies at which no edge transport is present in the clean limit $U = 0$ [7]. In the case of $m < 0$ [Fig. 2.2(a)] this TAI phase extends the original QSH phase beyond the disorder-free limits, given by $|E_F| = |m|$. Note that our results from Figs. 2.2(a) and 2.2(c) agree very well with the literature [7, 8], thereby confirming the validity of our simulations.

In a next step we repeat this calculation for a *correlated* disorder potential. We choose the value of the correlation length $\xi = 23.45$ nm considerably larger than

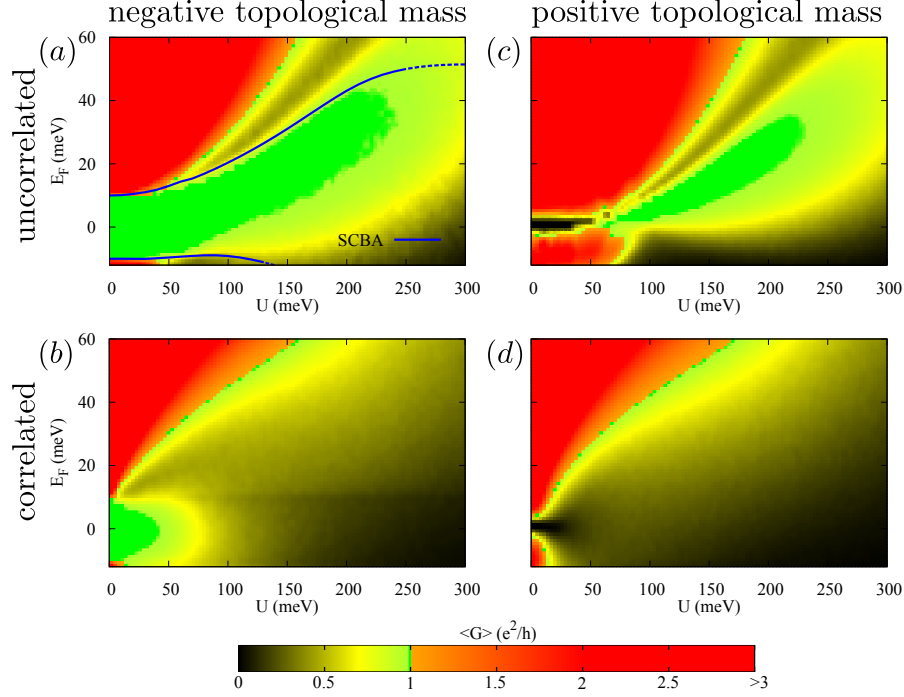


Figure 2.2.: Average conductance $\langle G \rangle$ as a function of disorder strength U and Fermi energy E_F for systems with negative $m = -10$ meV (left column) and with positive $m = 1$ meV (right column). The system length $L_x = 2000$ nm and the height $L_y = 500$ nm. The average is taken over 200 in (a) and 1000 disorder realizations in (b), (c) and (d). The green area shows where the average conductance $\langle G \rangle$ reaches a plateau at a single conductance quantum e^2/h originating from edge transport through the disordered system. Top row: For uncorrelated disorder the TAI phase appears in this green area for strong disorder at energies where no edge states exist for $U = 0$. The blue lines in (a) show the phase boundaries of the TAI predicted by the effective medium theory which is based on the self-consistent Born approximation (SCBA) shown in Eq. (2.6). Bottom row: Spatial correlations in the disorder with correlation length $\xi = 23.45$ nm destroy the TAI conductance plateau and for $m < 0$ also narrow the QSH plateau to an interval within the original bulk band gap. For positive topological mass (right column) the leads have been doped resulting in an energy offset of $\Delta = 20$ meV since otherwise no lead states would exist in the band gap.

the grid constant $a = 5$ nm but still much smaller than the height $L_y = 500$ nm of the sample. Our results for such a finite correlation length [see Fig. 2.2(b) and 2.2(d)] differ dramatically from the uncorrelated case [see Fig. 2.2(a) and 2.2(c)]: Apparently the chosen spatial correlations in the disorder lead to a total breakdown of the TAI conductance plateau. In the case of $m < 0$ we also observe an increased disorder-sensitivity as well as a narrowing of the conductance plateau corresponding to the original QSH phase in the clean limit. These results demonstrate that spatial correlations in the disorder add an important new component to the physics of topological insulators. Especially in view of the envisioned experiments that probe the physics of strongly disordered topological insulators, our results can apparently be expected to impose rather strict limits on the observability of the TAI phase. For such an experimental realization of the TAI we can certainly conclude that it is equally important to be able to control the correlation length ξ as it is to control the strength U of a disorder potential.

To check the influence of spatial correlations also for larger samples than the ones considered above we performed additional calculations. This is particularly important as finite-size effects in small samples due to a coupling of counter-propagating edge states can considerably distort the phase diagram of the TAI [103, 104, 120]. To determine these phase boundaries in extended samples we performed a scaling analysis following previous work in this direction [92, 122]. For this purpose a quadratic geometry of size $L = L_x = L_y$ is rolled up to a cylinder [8, 103, 122] using periodic boundary conditions in the y direction which eliminate the edge states in the sample. The disorder-averaged logarithmic conductance $\langle \ln G \rangle$ of the remaining bulk states is then calculated for three different sizes $L_1 < L_2 < L_3$ of the quadratic system as a function of the disorder strength U . This analysis allows us to estimate whether the bulk system in the limit of infinite size becomes conducting or insulating. For those values of U where $\langle \ln G \rangle$ increases with increasing system size L , bulk states also conduct in an infinite system and thus suppress any kind of TAI phase due to the coupling of the edge states via bulk states. In contrast, in those regions where $\langle \ln G \rangle$ decreases with increasing system size L the bulk is insulating in an infinitely large sample and clean edge transport can occur. The borders of these transitions between conducting and insulating bulk states can be estimated from the crossing points of $\langle \ln G \rangle$ [122, 123]. We calculated these phase transition points for an uncorrelated and for correlated potentials with different correlation length ξ in systems of three different sizes $L_1 = 500$ nm, $L_2 = 700$ nm and $L_3 = 1050$ nm. Due to the high numerical effort involved, we restrict ourselves to a single energy of $E_F = 16$ meV at which the TAI conductance plateau in the uncorrelated case is wide and well established [see Fig. 2.2(a)].

The results of our scaling analysis are shown in Fig. 2.3, where the uncorrelated case and two different correlation lengths ξ are considered. For each of these three cases the dependence of $\langle \ln G \rangle$ on the disorder amplitude U is shown. The phase

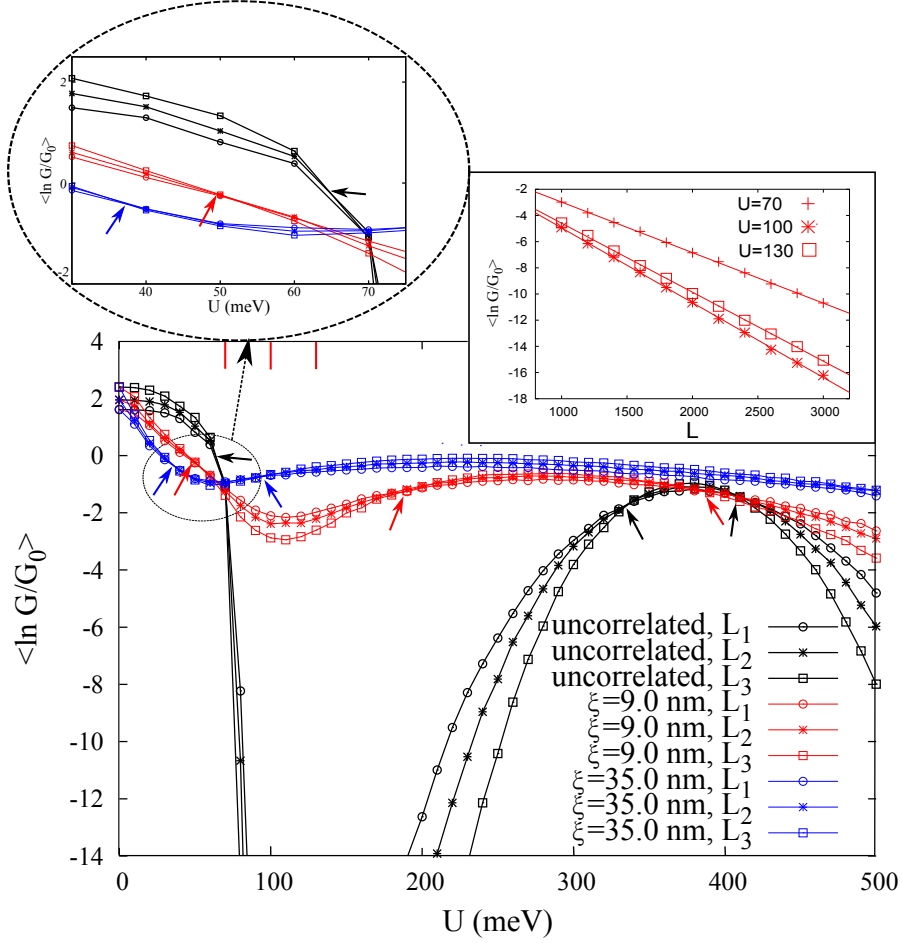


Figure 2.3.: (color online). Average logarithmic conductance $\langle \ln G \rangle$ through a rolled up quadratic topological insulator ($m = -10$ meV) of size $L_i \times L_i$ as a function of disorder strength U . We consider three different system sizes $L_1 = 500$ nm, $L_2 = 700$ nm and $L_3 = 1050$ nm for uncorrelated disorder (black) and for correlated disorder with correlation length $\xi = 9.0$ nm (red) and $\xi = 35.0$ nm (blue) at an energy of $E_F = 16$ meV (disorder average taken over 2000 configurations). The transitions into and out of the TAI phase occur at the crossing points of curves with equal color (their positions are marked by small arrows.) The TAI bulk band gap, present in the uncorrelated case in between the first and second crossing point, disappears for correlated potentials and the delocalization-localization region between second and third crossing point is broadened. The top right inset shows the behavior of $\langle \ln G \rangle$ as a function of the system length L with fixed system width $W = 500$ nm for $\xi = 9$ nm and for three values of disorder strength $U = 70, 100$ and 130 meV (see red vertical bars in the main panel). The localization length L_{loc} is calculated from the slope of the best linear fit of $\langle \ln G \rangle$: $L_{\text{loc}}(U = 70 \text{ meV}) = 518$ nm, $L_{\text{loc}}(U = 100 \text{ meV}) = 350$ nm and $L_{\text{loc}}(U = 130 \text{ meV}) = 379$ nm. The top left inset shows a closeup of some crossing points shown in the main panel.

transition points occurring at the crossing points of curves for different system sizes are marked by arrows. The top left inset of Fig. 2.3 shows a closeup of the crossing points. As found previously, the crossing points move slightly to lower values of U for increasing system size as a result of finite size effects [123]. We can thus expect the real phase transition point to be at lower values of U than our best estimate that we gain from the crossing points between the curves for L_2 and L_3 which are marked by the arrows in Fig. 2.3. Considering first the uncorrelated case studied already earlier (see black curves and arrows) we find that the lowest crossing point occurs at a value of the disorder strength $U \approx 65$ meV which fits well with the onset of the aforementioned TAI conductance plateau in Fig. 2.2(a) (see also Ref. [122]). This onset coincides here with the opening of a bulk band gap which is reflected in the scaling plots of Fig. 2.3 through a dramatic reduction of the conductance by more than ten orders of magnitude. The second and third crossing points, in turn, can be associated with the breakdown of the TAI phase observed in Fig. 2.2(a). The corresponding transition is, however, not induced by a band edge but rather by a mobility edge associated with those bulk states that fill the band gap when increasing the disorder strength beyond the first crossing point. These bulk states undergo a delocalization-localization transition at the second and third crossing point which destroys the conductance plateau as soon as the delocalized bulk states start coupling the edge states at opposite edges in the sample. Note that for this to happen it is already sufficient for individual rather than for all bulk states to delocalize such that finite size effects do play a role at this strong-disorder boundary of the TAI [122, 123].

When extending the above scaling analysis now to the case of correlated disorder with successively increasing correlation length ξ we find a behavior different from the uncorrelated case: Already for the case of very short-range correlations with $\xi = 9.0$ nm (red curves in Fig. 2.3) significant differences appear. We still find three crossing points as before, but the conductance no longer displays the very strong suppression associated with a bulk band gap. Instead, we find that the delocalization-localization region of bulk states, which was previously associated with the strong-disorder boundary of the TAI, widens for increasing correlation length ξ . Correspondingly, in the disorder interval between the first and the second crossing points (which are now also much closer together) the conductance is much less suppressed than in the uncorrelated case. This indicates that in the correlated case the bulk band gap disappeared and was filled with localized bulk states.

To prove this statement we investigate more closely the behavior of $\langle \ln G \rangle$ in the disordered cylinder with surface area $W \times L$. Keeping the circumference of the cylinder and the correlation length of the potential fixed at $W = 500$ nm, $\xi = 9.0$ nm, we vary the system length L and consider three different values of U within the region between the first and second crossing point where the bulk system is insulating in an infinitely large system. The results are shown in the top right

inset of Fig. 2.3. The bulk states are indeed localized as the averaged logarithmic conductance $\langle \ln G \rangle$ drops linearly with increasing length L . From the slope k_l of the fitted lines we determine the localization length $\xi = -2/k_l$ of the bulk states which ranges from 518 nm right after the first phase transition point ($U = 70$ meV) down to 349 nm in the middle of the "insulating" region ($U = 100$ meV). With the localization length ξ thus falling below the linear dimension $W = L$ of the quadratic disorder region considered in Fig. 2.3, we can understand that the reduced bulk conductance is here produced by the localization of bulk states, rather than by a band edge as in the uncorrelated case. We emphasize, however, that both a band gap as well as localized bulk states can give rise to a TAI, as was explicitly pointed out in a recent study [123]: In what was termed a TAI-I phase the coupling between edge states is prevented by a bulk band gap which eliminates all bulk states that would mediate such a coupling. In a system with negative topological mass $m < 0$ the TAI-I conductance plateau is joined with the original QSH plateau existing within the original bulk band gap $E_F < |m|$. A second TAI-II phase was characterized by a coexistence of localized bulk-states and extended edge-states. As long as the localization length of these bulk states remains smaller than the width of the sample, the coupling of edge states remains suppressed and the TAI persists. Following these arguments, the transition into the TAI phase can either occur at a band edge (for TAI-I) or at a mobility edge (for TAI-II). From this we conclude that the original band edge at the weak-disorder boundary of the TAI-I phase in the uncorrelated case gets replaced by a mobility edge as the new weak-disorder boundary of a TAI-II phase in the correlated case. The corresponding suppression of the TAI-I phase already at a rather small correlation length of $\xi = 9.0$ nm suggests that the TAI-II phase is more robust to spatial disorder correlation than the TAI-I phase. The TAI-II phase is, in turn, more sensitive to finite size effects due to *individual* localized bulk states which can couple counter-propagating edge states to each other. Correspondingly we can understand the absence of a TAI conductance plateau in Fig. 2.2(b) and Fig. 2.5 in between the first and second crossing points of our scaling analysis in Fig. 2.3 as a finite-size effect which may disappear for much larger samples than studied here. Further explicit calculations will be necessary to better understand the infinite-size limit for TIs with long-range correlations in the disorder. Our own results for the case of $\xi = 35$ nm (see the blue curves in Fig. 2.3) show that the widening of the delocalization-localization transition continues for increasing correlation length ξ . However, since the transition region for $\xi = 35$ nm is here already very wide, detailed statements on the phase boundaries in the infinite size limit are difficult to deduce from our finite-size calculations.

We may, however, get important insights into the nature of the localization-delocalization transition for correlated disorder potentials by explicitly studying the scattering wave functions close to this transition. In Fig. 2.4 we plot several such wave functions for increasing disorder strength U in our cylindrical system of

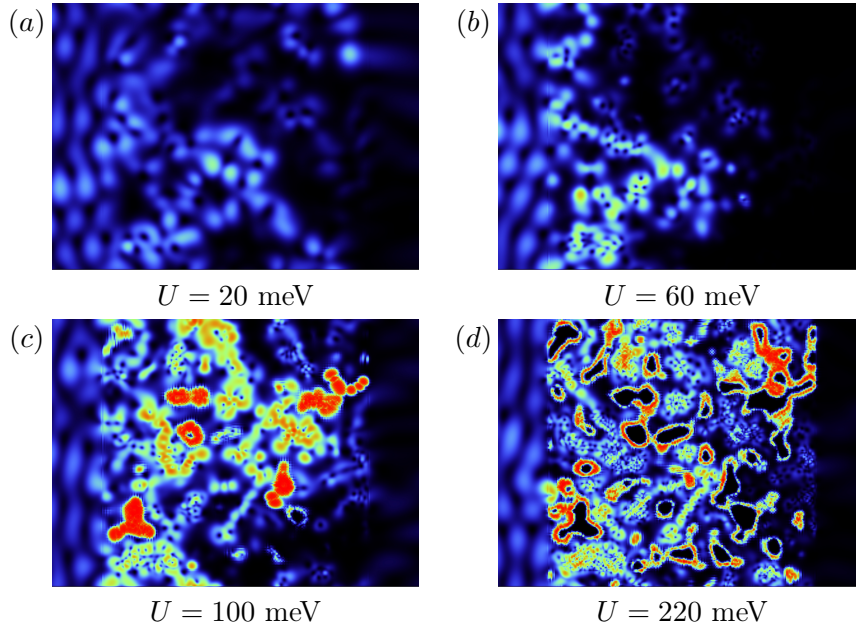


Figure 2.4.: Scattering wave functions $|\psi|^2$ in a cylindrical system of length $L = W = 1050$ nm, Fermi energy $E_F = 16$ meV in a random potential of correlation length $\xi = 35$ nm. The flux is incoming from the left and periodic boundary conditions are implemented on the top and bottom of the images. The disorder strength U for each of the pictures shown is indicated right below each panel. Note how the wave function turns into a percolating state when the localization-delocalization transition is approached for increasing disorder strength U (compare with blue curves in Fig. 2.3 and with experimental data from quantum Hall measurements as in Fig. 2.2 of Ref. [124]).

size $L = W = 1050$ nm and correlation length $\xi = 35$ nm (compare with blue curves in Fig. 2.3). These plots indicate that the observed localization-delocalization transition is, in fact, a percolation transition similar to the one in the quantum Hall effect [125]. At the percolation threshold which is realized at critical values of the system parameters (like the disorder strength U) localized bulk states turn into extended states which circumnavigate the hills and valleys of the disorder potential rather than being trapped by them. The wave functions shown in Fig. 2.4 indicate exactly such a behavior by displaying bulk states that propagate along the slopes of pronounced potential variations [see Fig. 2.4(d)] as observed in quantum Hall measurements (see Fig. 2 in Ref. [124]). This percolation explains the suppression of uni-directional edge transport quite intuitively since close to the percolation thresh-

old the bulk states which are otherwise localized may percolate from one edge to the opposite one and thereby couple the counter-propagating edge states. Note that our observation of the percolation transition fits well with earlier work [8] that found the critical exponent for this transition in the uncorrelated case to be consistent with the exponent from the quantum Hall universality class. The most closely related work to this paper which we could identify is by Shen *et al.* [126] who recently demonstrated that bound states in a quantum spin Hall anti-dot lattice feature a percolation transition *in the bulk band gap*. Since in the present system we observe the percolation transition at $E_F = 16$ meV, which is well outside the bulk band gap at $|E_F| < 10$ meV, a different mechanism seems to be at work here which we will discuss in section 2.4.

In the following we will present additional evidence to corroborate our arguments from above with respect to the suppression of the TAI-I phase due to correlations in the disorder. If these arguments are correct, the QSH phase (characterized by a negative topological mass and a chemical potential in the band gap, $|\mu| < |m|$) should border, in the correlated disorder case, directly on the surviving TAI-II phase (characterized by a negative topological mass and a chemical potential outside of the band gap, $|\mu| > |m|$). In the corresponding plot in Fig. 2.2(b) we see that the QSH conductance plateau (existing in the energy-range $-10 \text{ meV} < \mu < 10 \text{ meV}$ in the disorder-free sample) extends only to much smaller values of disorder strength U than in the uncorrelated case [compare with Fig. 2.2(a)]. Since for the above arguments the borders of this reduced QSH conductance plateau with the neighboring TAI-II phase are characterized by a band edge crossing, these borders should be describable in terms of a similar effective medium theory as has been developed for the uncorrelated case [8]. This theory maps the disordered system onto a disorder-free sample with a renormalized topological mass $\bar{m} = m + \delta m$ and chemical potential $\bar{\mu} = \mu + \delta \mu$. This renormalization was carried out in terms of the self-consistent Born approximation (SCBA) using an integral equation for the self-energy Σ :

$$\Sigma = \frac{U^2}{12} \left(\frac{a}{2\pi} \right)^2 \lim_{\kappa \rightarrow 0} \int_{-\frac{\pi}{a}}^{\frac{\pi}{a}} dk_x dk_y \left(E_F + i\kappa - H_0(\vec{k}) - \Sigma \right)^{-1} . \quad (2.6)$$

Whenever the renormalized chemical potential reaches the edge of the band gap ($|\bar{\mu}| = |\bar{m}|$) the border of the QSH (or TAI-I) phase has been reached. Since this indicator, as calculated through the above SCBA, is independent of the system size, the effective medium theory offers an insightful and practical tool to determine the boundaries of the QSH or possible TAI-I phases in the infinite-size limit.

In order to generalize the effective medium theory from above to the case of spatially correlated potentials we resort to recent theoretical work in which an extension of the coherent potential approximation to correlated disorder was proposed [127]. Following this line of work, one can conveniently include the disorder correlations

through an additional term in Eq. (2.6) which is given by the normalized Fourier transform of the disorder correlation function³, $\tilde{C}(\vec{k})$,

$$\Sigma = \frac{U^2}{12} \lim_{\kappa \rightarrow 0} \int_{-\frac{\pi}{a}}^{\frac{\pi}{a}} dk_x dk_y \tilde{C}(\vec{k}) \left(E_F + i\kappa - H_0(\vec{k}) - \Sigma \right)^{-1}. \quad (2.7)$$

Since in the present case of Gaussian disorder correlations [see Eq. (2.4)] the expression for $\tilde{C}(\vec{k})$ is a Gaussian itself (centered around $k = 0$), the effect of the disorder correlations is to smoothly cut off the above integral. The more long-range the correlations are (in real space), the sharper this cut-off is (in Fourier space).

To extract the corrections δm and $\delta \mu$ from the self-energy in Eq. (2.7), we proceed along the lines of the uncorrelated case [8] and decompose the self-energy into the Pauli matrices σ_i

$$\Sigma = \Sigma_0 \sigma_0 + \Sigma_x \sigma_x + \Sigma_y \sigma_y + \Sigma_z \sigma_z \quad (2.8)$$

with the help of

$$\begin{aligned} \delta m &= \text{Re } \Sigma_z, \\ \delta \mu &= -\text{Re } \Sigma_0. \end{aligned} \quad (2.9)$$

With the values extracted for the renormalized topological mass $\bar{m} = m + \delta m$ and chemical potential $\bar{\mu} = E_F + \delta \mu$, we can now estimate the boundaries of the QSH or TAI-I phase in the case of correlated disorder by determining the values of E_F and U for which the renormalized chemical potential $\bar{\mu}$ drops into the effective band gap at $\bar{\mu} = \pm \bar{m}$. We start by first testing our approach for the *uncorrelated* case, for which the weak disorder boundary of the TAI phase was estimated before. In this case the discrete Fourier transform of the correlation function $\tilde{C}(\vec{k})$ is constant. By normalizing this function in k -space to the volume $V = (2\pi)^2/a^2$ of the Brillouin zone, we exactly reobtain the expression for the self energy in the uncorrelated case, Eq. (2.6). If we determine with this approach the phase boundaries of the QSH and TAI-I phases in the *uncorrelated* case we obtain the blue curves in Fig. 2.2(a) which fit nicely to the conductance plateau of the QSH and TAI-I phases and to previous calculations [7, 8, 122]. Extending our calculations to the case of *correlated* disorder, the borders which we calculate through Eqs. (2.7) and (2.9) (see blue curves in Fig. 2.5) describe the boundaries of the QSH conductance plateau very well (without any adjustable parameters). The good agreement which we find for different correlation lengths ξ [see Fig. 2.5(a) and 2.5(b)] corroborates the validity of our approach. Note that, in contrast to the uncorrelated case, no TAI-I conductance plateau is observed for $|\mu| > |m|$ (i.e., outside of the energy region where the

³ Note that in our case the self-energy Σ is independent of \vec{k} , such that correlations between different \vec{k} -vectors as originally described in Eq. (27) of Ref. [127] reduce here to the simplified expression in Eq. (2.7)

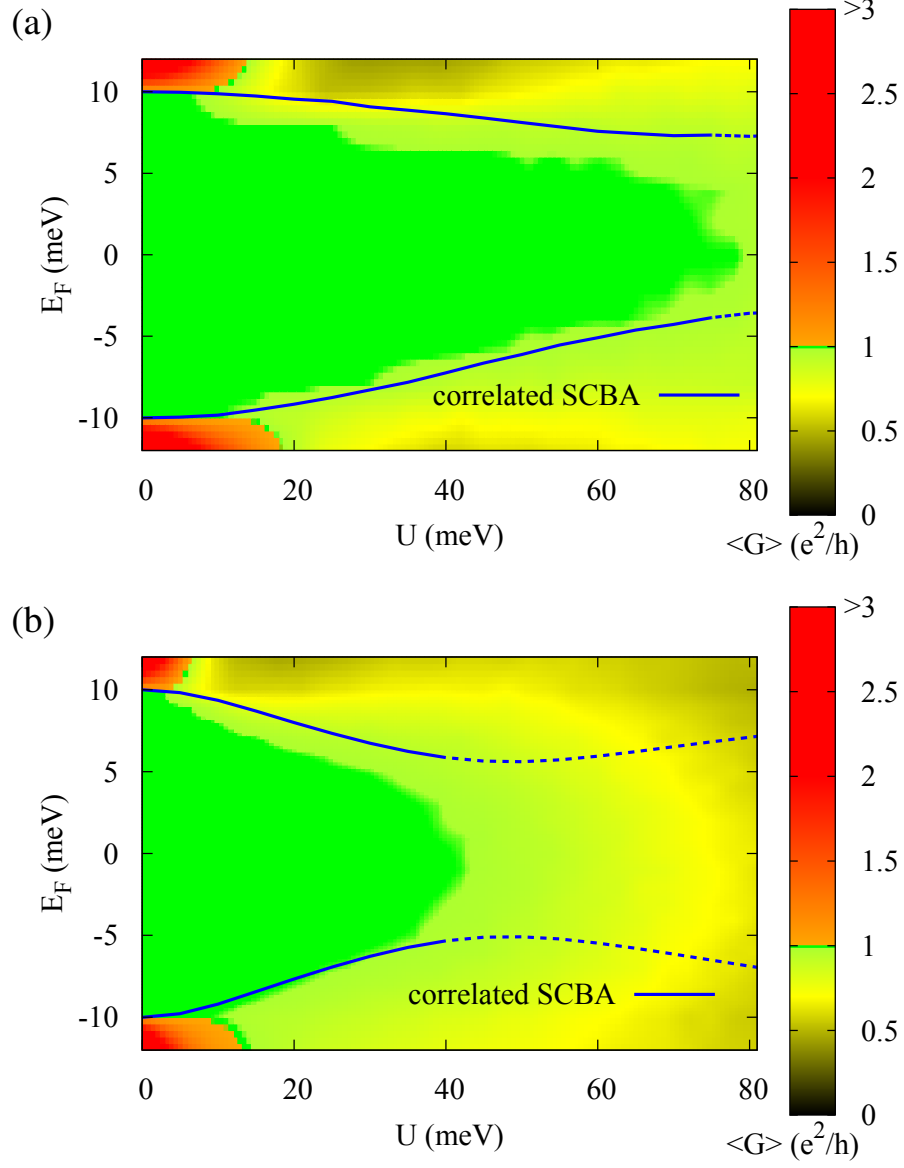


Figure 2.5.: The average conductance $\langle G \rangle$ as a function of Fermi energy E_F and disorder strength U is shown for the system considered in Fig. 2.2(b), here with correlation length (a) $\xi = 9$ nm and (b) $\xi = 23.45$ nm. The system is $L_x = 2000$ nm long and $L_y = 500$ nm high while the grid spacing $a = 5$ nm. The blue curves delineate the borders of the quantized conductance plateau as estimated by the effective medium theory for correlated potentials, Eq. (2.7). Note the very good agreement which we find with our numerical results.

QSH phase is present in the clean sample). An increasing disorder strength rather leads to a narrowing of the bulk band gap within which pure QSH edge transport can occur. This reduced band gap corresponds to positive corrections δm and $\delta \mu$ in the case of a correlated potential whereas in the uncorrelated case these corrections were shown to be negative. [8]. It is exactly these positive corrections which lead to the breakdown of the TAI-I phase that occurs in the uncorrelated case for $|\mu| > |m|$. Moreover, this narrowing of the region of pure edge-transport might be responsible for experimental difficulties in eliminating the bulk conductance in three-dimensional topological insulators [128].

2.4. Percolating states in the topological Anderson insulator

In this section (partially taken from our publication Ref. [10]) we investigate the presence of percolating states in disordered two-dimensional topological insulators. In particular, we investigate the connection between these states and the TAI phase. While the transition from an ordinary insulator to the TAI could be explained by an effective description [8] that we could also extend to spatially correlated potentials (see previous section 2.3 and Ref. [9]), the transition from the TAI phase back to an ordinary insulating phase at very strong disorder values proves more involved: the bulk states localize at intermediate disorder strength allowing for unimpeded edge-transport in the TAI phase, yet delocalize when disorder becomes even stronger [8, 91, 93]. So far, the resulting breakdown of the TAI phase could be attributed to the coupling of counter-propagating edge states on opposing edges through these delocalized bulk states, resulting in a suppression of the edge states' immunity from backscattering [103, 123]. This mechanism is responsible for an increased sensitivity to finite size effects [104, 122] making the transition hard to explore numerically and leaving the true nature of this counter-intuitive delocalization unclear. While first studies [92, 93, 122] interpreted the bulk delocalization as an intermediate metallic phase, a later study [123] considering larger systems pointed out that only a single bulk state is probably responsible for the delocalization and an intermediate metallic phase is not present. In addition, a spatially correlated potential and the associated pronounced bulk delocalization turn out to be able to destroy the TAI phase entirely as outlined in the previous section 2.3. In this section, we resolve the puzzle associated with these different observations by identifying the emergence of percolating states as the origin of the delocalization and by clarifying the general connection between such states and the TAI phase. Following Ref. [121], we use the same set of realistic quantum well parameters in this section as in the previous one 2.3: $A = 364.5 \text{ nm} \cdot \text{meV}$, $B = -686.0 \text{ nm}^2 \cdot \text{meV}$ and $D = -512.0 \text{ nm}^2 \cdot \text{meV}$. As before, the topology of the system is determined by the sign of the topological

mass m : For $m < 0$ the bulk band gap of size $2|m|$ is topologically non-trivial and thus filled with gap-less edge states characterizing a two-dimensional topological insulator. On the other hand, for $m > 0$, the bulk band gap is topologically trivial and does not contain any states leaving us with a system that is an ordinary insulator. Again we use the advanced modular recursive Green's function method [12, 13, 15] to calculate the conductance G through two-dimensional rectangular ribbons of HgTe/CdTe quantum wells discretized on a square grid with discretization constants Δx and Δy , width $W = (n_y + 1) \cdot \Delta y$ and length $L = n_x \cdot \Delta x$. In accordance with previous studies, [7–9, 93, 103, 104, 122, 123, 129] the discretization constants are set to $\Delta x = \Delta y = a = 5$ nm. Two clean semi-infinite leads are attached to the left and right end of the ribbon. Following the Landauer-Büttiker formalism Eq. (2.3), the conductance G in the limit of vanishing temperature is given by the total transmission T at the Fermi energy E_F . Our method also allows for a calculation of the scattering wave functions $\psi(x, y)$ as well as the density of states $\rho(E) = -\text{Tr} [\text{Im} G^r(\vec{x}, \vec{x}, E)] / \pi$ where G^r is the retarded Green's function. Details on the calculations of the density of states are provided in section 3.7. Disorder is modelled by static on-site energy values $V(x_i, y_i)$ at each grid point (x_i, y_i) randomly chosen from the interval $[-U/2, U/2]$ with U the disorder strength. In most studies [7, 8, 93, 103, 104, 122, 123, 129], the values of $V(x_i, y_i)$ are chosen without any spatial correlations between neighboring grid points [see Fig. 2.1]. Here, we also consider spatial correlations in $V(x, y)$ [see Fig. 2.1], characterized by a finite correlation length ξ , which can significantly affect the conduction properties (see previous section 2.3 and Ref. [9]).

In our simulations we first consider a quadratic region of width $W = L = 1000$ nm and an uncorrelated disorder potential (i.e., $\xi \rightarrow 0$). Two geometries will be studied that only differ in their boundary conditions: a ribbon for which hard wall boundary conditions along the edges are applied and a cylinder with periodic boundary conditions in y -direction. A comparison between the disorder-averaged conductance $\langle G \rangle$ through these two geometries has been used previously to distinguish between bulk and edge phenomena as the periodicity of the cylinder eliminates the edges of the geometry [103]. The results for $\langle G \rangle$ in a topological insulator with $m = -10$ meV at Fermi energy $E_F = 16$ meV are shown in Fig. 2.6(a) as a function of the disorder strength U for both geometries. The value of E_F is chosen such that for uncorrelated disorder the TAI conductance plateau with $\langle G \rangle = 1 e^2/h$ clearly appears in the ribbon [91, 103, 104, 123] for disorder strength $80 \text{ meV} \leq U \leq 280 \text{ meV}$ [see red curve in Fig. 2.6(a)]. In the cylinder this plateau is clearly absent, since no edge states can exist in this edge-less geometry. While for disorder values beyond this plateau the conductance drops monotonically in the ribbon, the conductance through the cylinder geometry [blue dashed curve in Fig. 2.6(a)] shows a renewed increase at the same disorder strength. This is the signature of the aforementioned bulk delocalization that has already been observed in uncorrelated potentials [8, 91, 93].

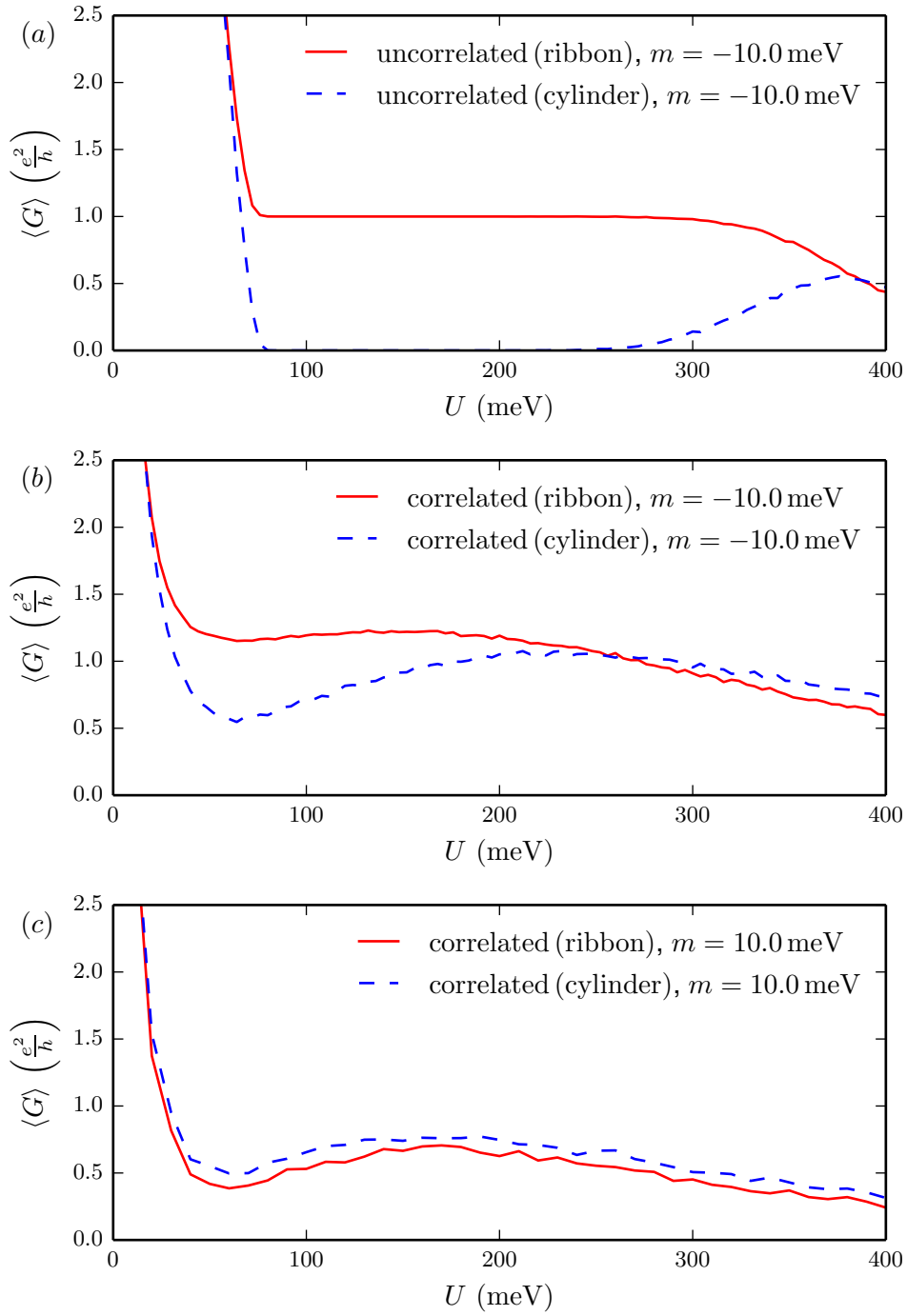


Figure 2.6.: Average conductance $\langle G \rangle$ as a function of disorder strength U through different HgTe/CdTe quantum wells. All systems are of width and length $W = L = 1000$ nm and the Fermi energy is set to $E_F = 16$ meV. [Caption continued on next page]

Figure 2.6.: [Continued caption from previous page] The ribbon geometries are shown by red solid curves while the cylinder geometries are shown by the blue dashed lines. (a) Average conductance through a system of topological mass $m = -10$ meV (topological insulator) in an uncorrelated potential. The disorder average is taken over 1000 configurations. The ribbon geometry features the TAI conductance plateau of $\langle G \rangle = 1e^2/h$ for $80 \text{ meV} \lesssim U \lesssim 280 \text{ meV}$. In this region the conductance through the cylinder is almost entirely suppressed followed by a delocalization transition of the bulk states starting at $U \approx 280 \text{ meV}$. (b) Average conductance through systems with the same parameters as in (a) but in a correlated potential with correlation length $\xi = 35 \text{ nm}$. The cylinder geometry (blue dashed curve) clearly shows the bulk delocalization transition, which occurs here for weaker disorder strengths U than in the uncorrelated case. (c) Average conductance through systems with positive topological mass $m = 10 \text{ meV}$ (ordinary insulator) in a correlated potential of correlation length $\xi = 35 \text{ nm}$. The disorder average is taken over 200 configurations. The cylinder geometry shows a less pronounced bulk delocalization transition than in (b), followed here also by the results for the ribbon due to the absence of edge states.

A physical intuition for this transition is, however, still lacking, but will become clear by considering disorder potentials that are spatially correlated (illustrations for uncorrelated and correlated disorder potentials are shown in Fig. 2.1).

In the previous section 2.3 we demonstrated that spatial correlations in the disorder potential can destroy the TAI phase entirely. Here we consider a situation, in which the correlations all but dissolve the plateau in the ribbon geometry [see the red curve in Fig. 2.6(b)]. While for the uncorrelated potentials [see Fig. 2.6(a)] the conductance plateau is a hallmark of the often-discussed TAI phase, the plateau for the correlated case [see Fig. 2.6(b)] is not caused by clean edge transport but by bulk states and its conductance close to unity is just a coincidence. This statement is verified in Fig. 2.7 where we show the local density of states (LDOS) for a disorder strength U within these plateaus in the uncorrelated [panel (a)] and the correlated [panel (b)] case. As clear from there, the uncorrelated potential allows for the existence of edge states in the disordered system as the LDOS shows states all located close to the edges of the geometry. In contrast, the LDOS in the correlated case shows states extended all over the entire bulk which proves that the large conductance observed in Fig. 2.6(b) must be attributed to bulk states.

Moreover, it is best visible for the parameter values chosen in Fig. 2.6, that the dissolution of the plateau is accompanied by a delocalization of bulk states. As can be seen by comparing the blue dashed curves in Fig. 2.6(a) and (b), this delocalization happens at much lower disorder values for correlated potentials than for uncorrelated ones. In both cases, however, these delocalized bulk states contribute to the conductance, but also suppress the edge conductance by coupling counter-propagating edge states with each other, thereby leading to a breakdown of the TAI

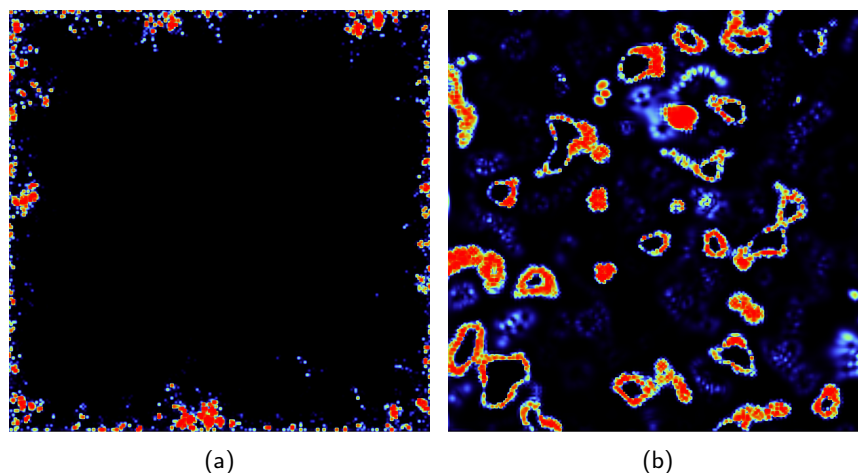


Figure 2.7.: Pictures of the local density of states (LDOS) at energy $E = 16$ meV in a two-dimensional topological insulator with topological mass $m = -10$ meV attached to two semi-infinite leads. In both panels, we consider a ribbon geometry. The disorder is entirely uncorrelated in (a) but correlated in (b) with a correlation length of $\xi = 35$ nm. This comparison shows the LDOS at the points of disorder strength $U = 150$ meV for the solid red lines in Fig. 2.6(a) and (b). It clarifies, that while for uncorrelated disorder the plateau results from states located close to the edges with only small strongly localized spots in the bulk, for a correlated potential the states are mainly situated in the bulk. Details on the calculation of the LDOS can be found in section 3.7.

conductance plateau.

To get a better insight into this scenario, we now consider the scattering wave functions $\psi(x_i, y_i)$ during this delocalization transition [see Fig. 2.8(a) and (c) for two such states at $U = 220$ meV]. A first optical inspection of these wave function images suggests that the associated flux is circumnavigating the hills of the underlying correlated potential [9], reminiscent of percolation states found in the Quantum Hall effect [124] and in antidot topological insulator lattices [126]. To make this first impression more quantitative, we analyze how the intensities of the wave functions $\psi(x_i, y_i)$ shown in Fig. 2.8 are correlated with the values $V(x_i, y_i)$ of the underlying potential landscape. For this purpose we compute the weighted probability $P(V)$ for a wave to encounter a potential value V with the weights of this probability distribution being given by the intensity $|\psi(x_i, y_i)|^2$ of the wave function at a grid-point (x_i, y_i) with potential value V . The distribution $P(V)$ resulting from an average over 1000 disorder realizations shows a surprisingly pronounced enhancement at positive disorder values V approximately situated between $V_{\min} \approx 25$ meV

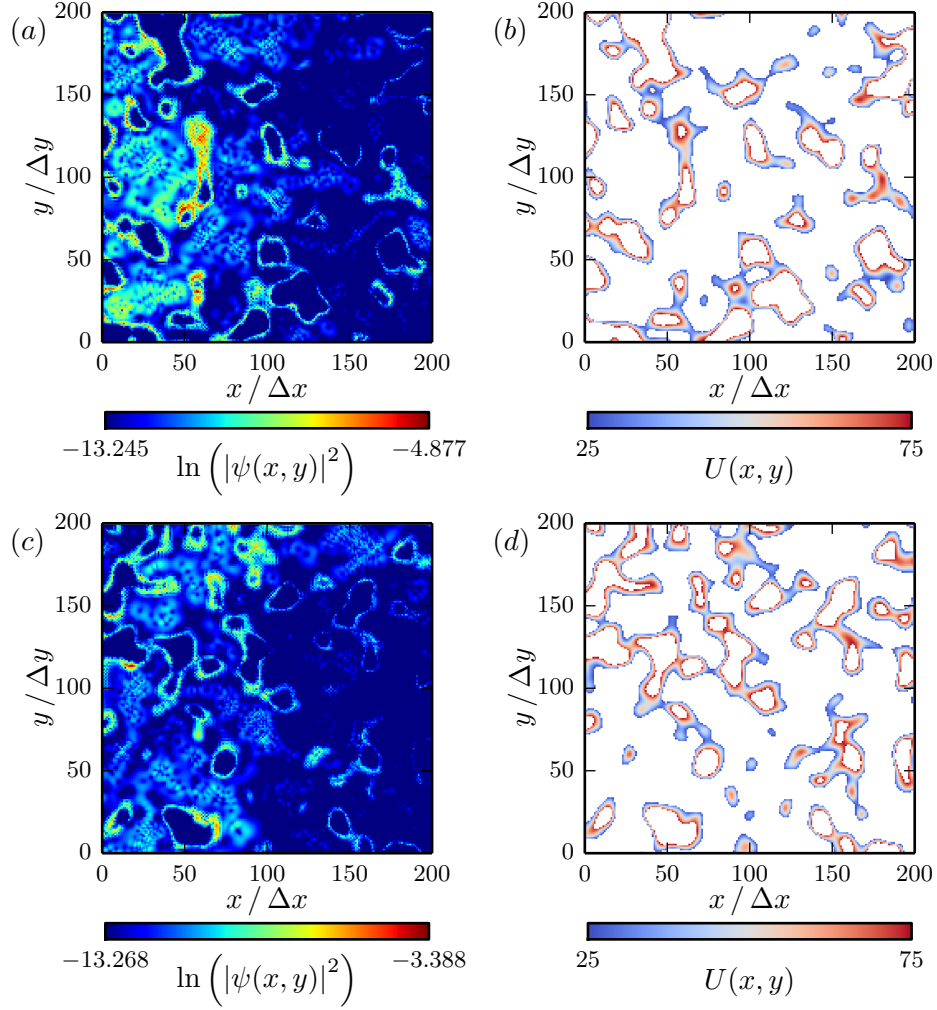


Figure 2.8.: Comparison of the scattering wave function $|\psi(x_i, y_i)|^2$ (shown on a logarithmic scale in the left column) and the potential itself (right column) at the delocalization transition ($U = 220$ meV) for systems with $W = L = 1000$ nm, $E_F = 16$ meV and $m = -10$ meV. We only colored the potential values between $26 \text{ meV} \leq V(x_i, y_i) \leq 78 \text{ meV}$ for which the Fermi energy is effectively shifted into the valence band of the clean band structure (the remaining potential values are left in white). Two different disorder configurations for cylinder and ribbon geometry are considered in the top and bottom row, respectively. The similarity of the wave functions and these truncated potentials illustrates that the delocalizing bulk states are percolating around the hills of the potential landscape and that these percolating states have their origin in the bulk band structure of the clean sample.

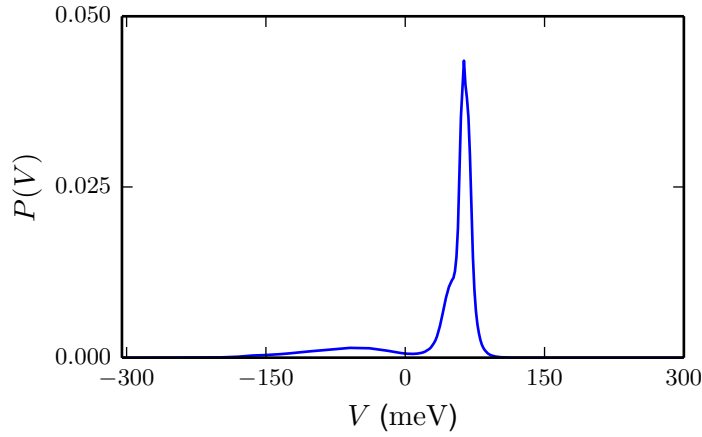


Figure 2.9.: Probability density distribution $P(V)$ for disorder values $V(x_i, y_i)$ at grid points (x_i, y_i) weighted by the absolute value $|\psi(x_i, y_i)|^2$ of the scattering wave function at $E_F = 16$ meV with injection in the first lead mode in a system of width and length $W = L = 1000$ nm and topological mass $m = -10$ meV. A disorder average is taken over 1000 configurations of random potentials with disorder strength $U = 220$ meV and correlation length $\xi = 35$ nm. The distribution shows an enhancement of the wave functions at disorder values V situated between $V_{\min} \approx 25$ meV and $V_{\max} \approx 75$ meV. These values correspond nicely to the distance of Fermi energy E_F to the flat valence bulk band states at the BZ edges.

and $V_{\max} \approx 75$ meV [see Fig. 2.9], suggesting that disorder values from this interval give rise to clearly enhanced wave function intensities. Apparently the states responsible for the bulk delocalization tend to reside primarily at relatively high values of the disorder potential, i.e., in a certain altitude interval of the hills in the correlated potential landscape. Correspondingly, we find that the wave function intensities shown in Fig. 2.8(a) and (c) strongly resemble contour plots of the associated disorder potential, when we truncate that latter to the interval $V \in [25, 75]$ meV [see Fig. 2.8(b) and (d)].

To identify the origin of this curious behavior, we first point to the fact that the above interval bounds, i.e., $V_{\min} \approx 25$ meV and $V_{\max} \approx 75$ meV, are astonishingly close to the minimal and maximal distances $E_{\min} = 26$ meV and $E_{\max} = 78$ meV of the Fermi energy $E_F = 16$ meV to the energy range $E_{\text{bulk}} = [-10, -62]$ meV in which the valence band states are situated in the clean system [see the band structure of Fig. 2.10(a)]. This observation suggests that the flux in our correlated potential is carried mostly by the disorder-analogues of these valence band states. Further evidence for this correspondence can be deduced when considering the rescaled

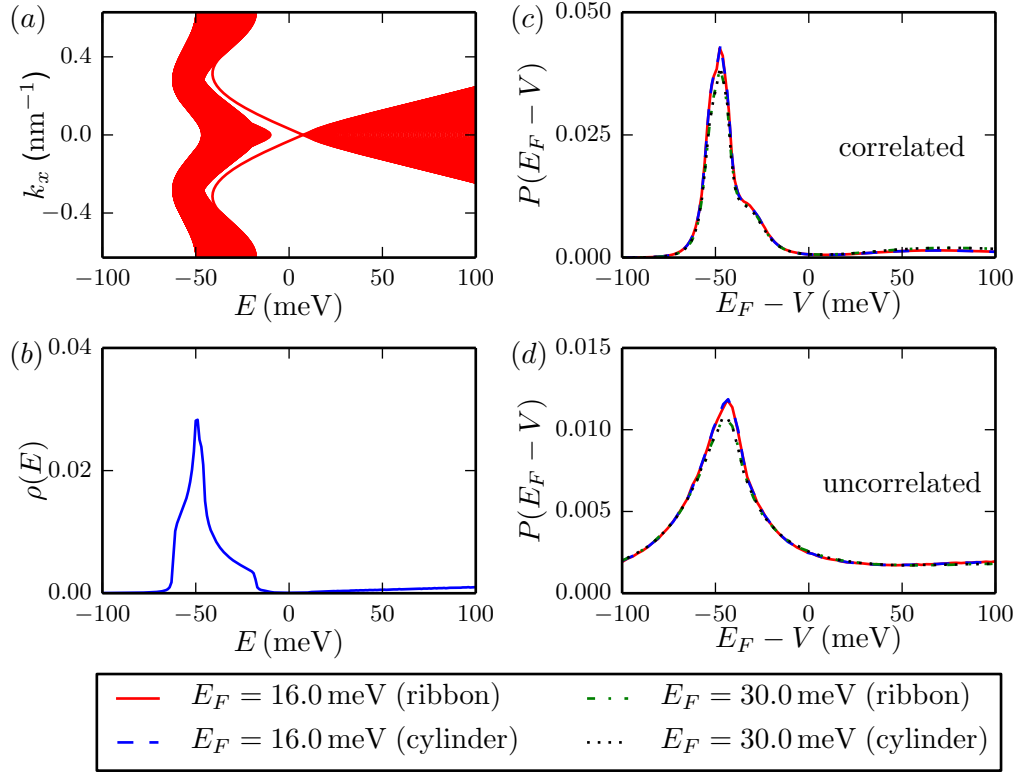


Figure 2.10.: (a) Band structure $E(k_x)$ of a system of width $W = 1000$ nm and topological mass $m = -10$ meV obtained by directly solving the Bloch-eigenvalue problem numerically for the Hamiltonian in Eq. (2.1). (b) Density of states $\rho(E)$ in a closed and clean system of width and length $W = L = 1000$ nm, topological mass $m = -10$ meV and cylindrical geometry. (c) Weighted probability density distribution $P(E_F - V)$ for systems with $m = -10$ meV, $W = L = 1000$ nm in a correlated potential of correlation length $\xi = 35$ nm. The wave functions are calculated in the region of the bulk delocalization at disorder strength $U = 220$ meV and for 1000 random disorder configurations. The red solid and blue dashed lines show $P(E_F - V)$ at $E_F = 16$ meV in the ribbon and the cylinder geometry. The green dash-dotted and black dotted lines represent $P(E_F - V)$ for ribbon and cylinder at $E_F = 30$ meV. The similarity of all four curves shows that the distribution is a very fundamental system property. The shape of the distributions closely resembles the density of states at the BZ boundary shown in (b). This indicates the bulk-like nature of the states responsible for the delocalization transition. (d) Weighted probability density distribution $P(E_F - V)$ with the same system parameters as in (c) but in an uncorrelated disorder potential. The pictures are again taken in the region of the bulk delocalization at disorder strength $U = 370$ meV and for 1000 disorder configurations.

probability distribution $P(E_F - V)$, which measures, as above, the probability for a scattering state to reside at a potential value V , but now shifted by the Fermi energy E_F . We find that this distribution, quite remarkably, stays almost invariant with respect to a change of the Fermi energy [see a comparison between two different values of E_F in Fig. 2.10(c)]. This observation reflects the fact that a change of E_F just shifts the corresponding wave functions to different disorder values, but that the origin of states in the valence bands stays unchanged. Furthermore, the density of states $\rho(E)$, shown in Fig. 2.10(b), and the distribution $P(E_F - V)$, shown in Fig. 2.10(c), are very similar - even the small kinks in $\rho(E)$ are clearly reproduced in $P(E_F - V)$. Such kinks in the density of states are nothing else but van-Hove-singularities resulting from the flat bands in the band structure. We may thus conclude that the flat valence band states especially at the Brillouin zone (BZ) edges [where the maximum of $P(E_F - V)$ is located] represent the most significant contribution to the intensity of the scattering wave functions. In addition, we find that the distribution $P(E_F - V)$ is not at all sensitive to the boundary conditions since it is almost exactly equal for the ribbon and for the cylinder (see Fig. 2.10(b)). The distribution $P(E_F - V)$ thus turns out to be quite fundamental in that it has its origin in basic system properties, which are given here by the band structure in Fig. 2.10(a) and by the flat band states contained in it.

These observations allow us to construct a comprehensive picture of the physics in the cylindrical geometry with a correlated potential [see blue dashed curve in Fig. 2.6(b)]: While in the clean limit pure bulk conduction is observed, the conductance drops down to a minimum at disorder strength of $U \approx 60$ meV due to the increasing localization of the bulk states [see Fig. 2.6(b)]. When at $U \approx 100$ meV the hills of the correlated potential are high enough to locally shift the Fermi energy into the valence band, the bulk is filled with localized states deriving from clean valence band bulk states spatially located around the hills of the underlying disorder potential. With growing disorder strength, these localized states connect with each other and go through a percolation threshold, which is responsible for the delocalization transition and the increased bulk conductance. Only at very strong disorder $U \approx 300$ meV the connection between these percolating states weakens and the conductance again decreases. This picture is also strongly supported by previous studies of the TAI in the uncorrelated case (see Refs. [94] and [129]): Considering the arithmetic and geometric average of the local density of states it was shown there that the states carrying the flux in the TAI are not single extended states throughout the whole TAI phase (as would be expected for edge states) but for very strong disorder rather formed by clusters of well localized states. Our percolating wave functions deriving from the valence band are perfect candidates for such linked, localized states. This picture is also corroborated by the flatness of the valence band states, which leads to the very small group velocity responsible for the wave function enhancements around the potential hills as seen in the examples of

Fig. 2.8(a) and (c).

The flatness of the states in the effective band structure is, in fact, also important for the theory put forward in the aforementioned studies [94, 129]: Considering disordered super-cell structures it was argued that flat and localized bands develop small sub-gaps that can be of topological non-trivial type. Hence these gaps have to be filled with edge states in the same way as the inverted band gap of a clean topological insulator is [88, 89, 121]. In this picture the TAI phase is thus characterized by edge states that appear in the energy gaps between localized bulk states and are consequently again immune from backscattering.

At this point the question arises how the above results can be reconciled with our own model, which so far does not contain any reference to edge states in the percolation transition. To investigate this issue in detail, we performed additional calculations for a system where no edge effects can be present due to a topological mass, which we choose to take on the positive value of $m = 10.0 \text{ meV}$. As shown in Fig. 2.6(c) this sign change of m significantly modifies the conductance properties. While previously for $m < 0$ and moderate disorder strength U the conductance in the ribbon was clearly enhanced in comparison to the cylinder [see Fig. 2.6(b)], the conductance of the ribbon for $m > 0$ is even smaller than in the cylinder [see Fig. 2.6(c)]. This behavior can be attributed to the absence of edge states at the sample edges for positive topological mass $m > 0$. In the cylindrical geometries we find that the delocalization transition is less pronounced for $m > 0$ than it was for $m < 0$ [compare blue dashed lines in Figs. 2.6(b) and (c)]. On the one hand the fact that the delocalization transition still exists for $m > 0$ supports our model of flat bulk states undergoing a percolation transition. On the other hand, however, the more pronounced nature of the transition for $m < 0$ suggests that edge states propagating along the edges of the potential hills provide an additional link between localized states leading to a larger conductance. This picture, indeed, agrees very well with the analyses of Refs. [94] and [129], since the connecting local edge states in our model can directly be identified with the edge states that were predicted to form in the non-trivial sub-gaps of the localized flat bands.

We would thus be in a perfect position to complement the theory of Refs. [94] and [129] with the intuitive explanation that these sub-gap edge states exist locally and connect bulk states localized around hills of the potential landscape to form a percolating network of internal bulk states that lead to the decay of the TAI phase. The missing piece to complete our argument is to show that the picture we derived for the case of correlated disorder holds also for the uncorrelated case considered in Refs. [94] and [129].

We check this point explicitly by verifying that our model can explain the appearance of the TAI as well as the observed delocalization-localization transition of the bulk states for the case of uncorrelated disorder. Consider, in this context, that the TAI conductance plateau in the ribbon geometry between $U \approx 80 \text{ meV}$ and

$U \approx 280$ meV [see red curve in Fig. 2.6(a)] is destroyed by the onset of the bulk delocalization at $U \approx 280$ meV in the cylinder [see blue dashed curve Fig. 2.6(a)] which happens for much larger U than in the correlated case. Still, when the delocalization transition is in full effect (at $U = 370$ meV) the corresponding scattering states show a similar weighted distribution $P(E_F - V)$ in the now spatially uncorrelated potential as already observed in the correlated case [see Fig. 2.10(d)]. Again the peak of this distribution fits nicely to the band structure of the clean limit, indicating that our picture of local edge states percolating around internal edges of strong disorder holds also for the uncorrelated case. Last but not least, we mention that such a percolating state corresponds exactly to the “single bulk state” that is held responsible for the delocalization in Ref. [123].

Our results suggest that the emergence as well as the decay of the TAI phase depend strongly on the energy offset and on the flatness of bulk valence bands in the clean limit. These flat bands feature an enhanced contribution to the density of states and occur in the center as well as at the boundaries of the BZ. Yet, the underlying BHZ model is only valid for small k_x close to the Γ -point and thus does not yield a good approximation for the valence bands at the BZ boundaries of a real HgTe/CdTe quantum well [88]. Correspondingly, we find that when changing the grid spacing a in our discretized lattice from the value conventionally used in the literature ($a = 5$ nm) to different values, the position of the BZ boundaries $k_x^{\text{BZ}} = \pm\pi/a$ and the energy offset of these states at the BZ boundaries also change significantly. We also verified that the flatness of the bands at the BZ boundary is a direct consequence of the discreteness of the underlying lattice used for the numerical solution of the transport problem (see also Refs. [7, 8, 103] where discretized models were first employed to describe the TAI). As a result, the localization-delocalization transition and possibly even the TAI phase itself associated with these states at the BZ boundary will not occur in real HgTe/CdTe quantum wells as the strong-disorder limit in these devices will be different from the predictions of the discretized model. Quite remarkably, however, realizations of topological insulators have recently also been considered based on photonic systems [97, 98]. These so-called Floquet topological insulators are based on a discretized lattice of sites, just like in the numerical model used above to approximate the physics in HgTe/CdTe quantum wells. The strong-disorder physics, which we have discussed here, have thus been realized in experiments based on effective model systems in optics [97, 98]. Similar proposals exist also in acoustics [130] and can in principle be developed in any other field where wave scattering parameters can be tuned appropriately.

2.5. Additional Hamiltonian corrections

So far in this work we have described the two-dimensional topological insulator by the very simple BHZ model given in Eq. (2.1) which we repeat here for easier readability:

$$H_{\text{eff}}(k_x, k_y) = \begin{pmatrix} h(\vec{k}) & 0 \\ 0 & h^*(-\vec{k}) \end{pmatrix} \quad (2.1 \text{ revisited})$$

with

$$\begin{aligned} h(\vec{k}) &= \mathbb{1}\epsilon(\vec{k}) + d_i(\vec{k})\sigma^i \\ \epsilon(\vec{k}) &= C - D(k_x^2 + k_y^2) \\ d_i &= \begin{pmatrix} Ak_x \\ -Ak_y \\ M(\vec{k}) \end{pmatrix} \\ M(\vec{k}) &= m - B(k_x^2 + k_y^2) . \end{aligned} \quad (2.2 \text{ revisited})$$

and σ^i labeling the Pauli-matrices. This original toy-model Hamiltonian for a two-dimensional topological insulator (HgTe/CdTe quantum well) was derived based on the $\mathbf{k} \cdot \mathbf{p}$ perturbation theory and the six-band Kane-model [88] resulting in the above compact form. The parameters A , B , D and m are material parameters taken from the literature as used in the previous calculations in sections 2.3 and 2.4. However, this model is still very simplified as many physical aspects in the system are neglected.

For the remaining considerations of this chapter, especially regarding the construction of a topological Mach-Zehnder interferometer (see section 2.7), this model is not sufficient anymore and needs to be extended. For example it has so far been intrinsically assumed that the crystal is bulk inversion symmetric which is clearly not the case for the zinc-blende lattice of HgTe and CdTe. To account for this, a correction can be implemented in the model by the addition of a bulk inversion asymmetry (BIA) term according to Ref. [121] which reads

$$H_{\text{BIA}} = \begin{pmatrix} 0 & 0 & -\Delta \\ 0 & \Delta & 0 \\ -\Delta & 0 & 0 \end{pmatrix} . \quad (2.10)$$

The strength of this correction is determined by the parameter Δ for which a realistic value of $\Delta = 1.6$ meV is taken from the literature [121]. This term is of basic importance for observed physics especially in the presence of a magnetic field (see section 2.6). It represents a coupling of the two spin components and hence the

spin is not a good quantum number. Due to this coupling [120] it is not sufficient anymore to use the spin-up block $h(\vec{k})$ Eq. (2.2) exclusively as done in all previous numerical calculations of sections 2.3 and 2.4. Additionally this term will open up a band gap between the edge states and lift the degeneracy at the Γ -point.

The second correction that is usually considered for an extension of the pure BHZ model from Eq. (2.1), is the Rashba coupling term derived in Ref. [131], which in the above 4-band basis reads:

$$H_{\text{RC}} = \begin{pmatrix} 0 & -iR_0k_- & 0 \\ iR_0k_+ & 0 & 0 \\ 0 & 0 & 0 \end{pmatrix} \quad (2.11)$$

with

$$k_{\pm} = k_x \pm ik_y \quad .$$

This term is linear in k and accounts for the coupling between the light-hole subbands that is described by an effective electric field [131]. The strength of the correction is determined by the Rashba coupling coefficient R_0 . The range of realistic values that are used for this correction is fairly large [131, 132]. For an electric field ϵ_z in z -direction, $R_0/(e\epsilon_z) = -15.6 \text{ nm}^2$ was found [131] with e the elementary charge. Another study performing simulations with similar QW parameters A , B , D and m that also we use in our calculations, takes $R_0 = 40 \text{ meV nm}$ [132]. Also old measurements in asymmetric (magnetic) quantum well structures [133] confirm a similar value of Rashba splittings up to 30 meV. In reality R_0 will also increase with the absolute value $|m|$ of the topological mass and thus with increasing quantum well thickness. This term splits the degenerate spin-up and spin-down states leading to different dispersion relations for the spins. While the Rashba correction is still linear in k there are also higher order corrections proportional to k_{\pm}^2 and k_{\pm}^3 which can still be approximately neglected for our calculations near the Γ -point [131]. Details on the numerical implementation of the Rashba coupling as well as the BIA term can be found in appendix A.2.

In a first step, we try to get a feeling for how a Rashba coupling together with the BIA changes the band structure of the two-dimensional topological insulator quantum well. In Fig. 2.11, we show band structures of a clean topological insulator lead of width $W = 500 \text{ nm}$ for different values of combinations of the BIA and Rashba corrections. The original band structure with both corrections set to zero is shown in red in all panels. As expected, we find that this BIA induces a band gap around the original Dirac point at $E_F \approx 7.1 \text{ meV}$ [compare red and blue lines in Fig. 2.11(a)]. For a Rashba coupling of $R_0 = 40 \text{ meV nm}$ we find in Fig. 2.11(b) that the effect of the spin splitting is still very small as it is hardly visible. When zooming in to a cutout around the Dirac point [see Fig. 2.11(c)] we find that as expected the

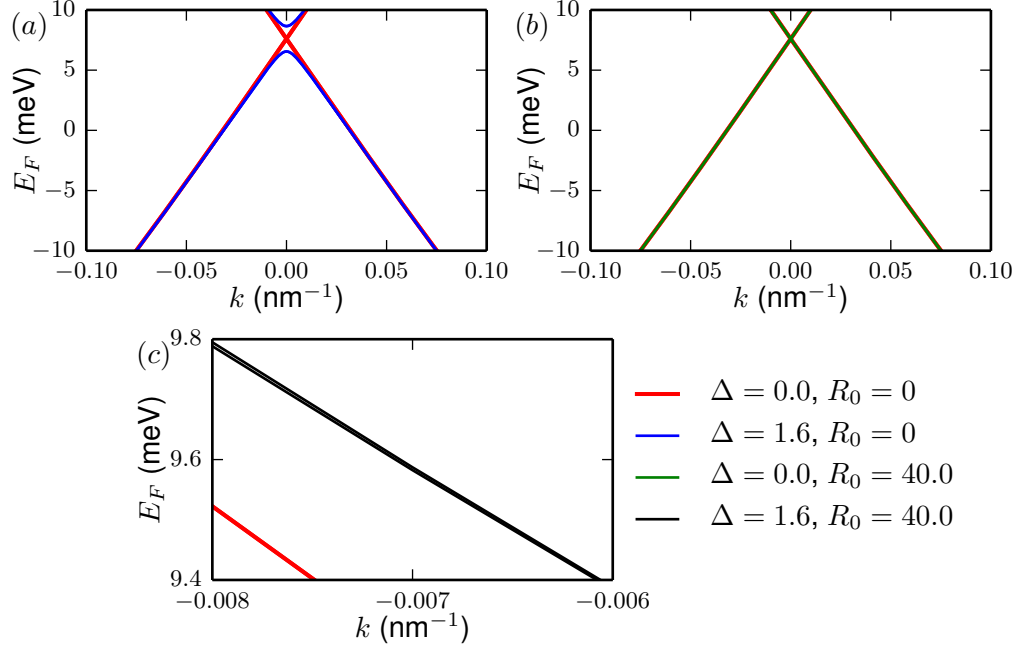


Figure 2.11.: Band structures of a QW with parameters $A = 365.0$ nm·meV, $B = -706.0$ nm²·meV, $D = -532.0$ nm²·meV, $m = -10.09$ meV, $R_0 = 40.0$ meV nm taken from Refs. [131] and [132] (and a realistic value of $\Delta = 1.6$ meV taken from Ref. [121]). The lead width $W = 500$ nm ($\Delta x = \Delta y = 5$ nm). The red lines in all panels show the original band structure with $\Delta = R_0 = 0$ meV nm. In (a) we investigate the Rashba term only and set $\Delta = 0$ meV. Panel (b) shows the BIA term $\Delta = 0$ meV and only the Rashba term $R_0 = 40$ meV nm being considered. In (c) both corrections are taken into consideration and a zoom close to the Γ -point at $k = 0$ nm⁻¹ is shown in order to be able to make the spin-splitting resulting from the Rashba term visible.

splitting of the spins depends on k and increases with increasing $|k|$. These results are in nice agreement with the literature [131, 132] and show the validity of our numerical approach. We find that close to the Γ -point the Rashba splitting is still negligibly small while the BIA inversion asymmetry opens a band gap. In addition the Rashba term has almost no effect on the edge states below the Dirac point at $E_F \lesssim 7.1$ meV.

In order to quantify this statement more precisely, we plot the spin splitting in terms of $\Delta k(E_F) = k_{x\uparrow}(E_F) - k_{x\downarrow}(E_F)$ defined as the difference between spin-up and spin-down wavenumbers at some fixed Fermi energy E_F . In Fig. 2.12 we show this quantity as a function of E_F inside the bulk band gap between $-|m| < E_F < |m|$ for the same quantum well parameters as in Fig. 2.11 but for different lead widths W . This energy range is of special interest since in section 2.7 we aim at using pure edge transport for interference experiments of edge states and possible future applications in spin-tronics. One can see that the splitting almost exclusively takes effect close to the conduction band above the degeneracy point of the original Dirac cone at $E \approx 7.1$ meV and is increasing with energy. This comes from the fact that the edge state above the Dirac point mostly derive from the $|E1\pm\rangle$ light-hole subbands of the quantum well which are coupled by the Rashba correction. In contrast, the edge states below the Dirac point mostly stem from the $|H1\pm\rangle$ heavy-hole subbands and are thus hardly affected by the correction. Another feature of this correction term can be seen from the comparison of the red and blue lines in Fig. 2.12 which show $\Delta k(E_F)$ for different lead widths $W = 500$ nm and $W = 200$ nm, respectively. The sudden decrease of Δk to zero for the small system (blue line) around the Dirac point comes from the fact that here the small size of the lead allows edge states to couple and induces a finite-size band gap. This absence of states in this small energy region causes also Δk to vanish. Still one notices that overall a smaller lead width W increases the spin splitting. At the maximally chosen value of $E_F = 10$ meV the splitting is approximately 11 times larger for the smaller lead than in the larger one. This indicates that the Rashba correction is fairly sensitive to finite size effects.

Overall these results show that the BIA term will be necessary to include when looking into edge state physics as it opens a significant band gap in the relevant region of pure edge transport. Additionally this term is also expected to be of fundamental importance when including a magnetic field as pointed out in Ref. [121]. Such a field will be investigated in the next section. The Rashba term on the other hand hardly has an effect on the band structure and the edge state physics in the bulk band gap between $-|m| < E_F < |m|$. For the approximately maximal energy inside the bulk band gap of $E = 10$ meV and for $W = 500$ nm we find a Rashba splitting of $\Delta k \approx 4 \cdot 10^{-4} \text{ nm}^{-1}$ which is still fairly small. Especially when considering those edge states below the Dirac point at Fermi energies $E_F \lesssim 7.1$ meV and additionally choose the lead width W large enough around 500 nm we can safely neglect this correction.

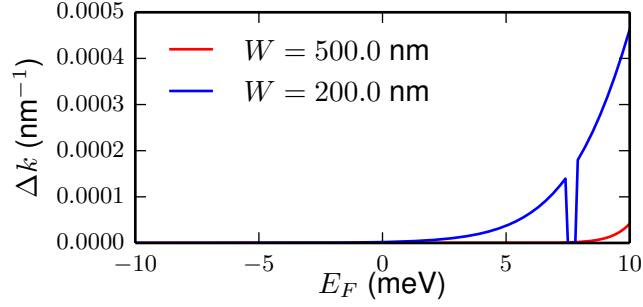


Figure 2.12.: Spin-splitting Δk as a function of Fermi energy E_F for a QW with parameters $A = 365.0 \text{ nm} \cdot \text{meV}$, $B = -706.0 \text{ nm}^2 \cdot \text{meV}$, $D = -532.0 \text{ nm}^2 \cdot \text{meV}$, $m = -10.09 \text{ meV}$, $R_0 = -15.6 \text{ meV nm}$ taken from Ref. [131] and $\Delta = 1.6 \text{ meV}$ taken from Ref. [121] ($n_y = 100$, $\Delta x = \Delta y = 5 \text{ nm}$). The red line shows the results for a lead width of $W = 500 \text{ nm}$ and the blue line shows $W = 200 \text{ nm}$. The difference between these results shows the sensitivity of the Rashba spin splitting to finite size effects.

2.6. Topological insulator in a magnetic field

Since the immunity of a topological insulator's edge states against backscattering fundamentally relies on the presence of time-reversal symmetry (TRS), it is essential to investigate their behavior when TRS is broken. The easiest way to break this symmetry is by considering the presence of a magnetic field \vec{B} . According to the literature [121] the impact of such a field on the transport properties of a two-dimensional topological insulator depends strongly on the field's direction with respect to the effective two-dimensional plane of the quantum well structure. While a perpendicular magnetic field causes strong deviations also for weak field strength, an in-plane magnetic field should not lead to strong changes as long as it is not too strong. For this reason we will verify these statements numerically and in this way also verify the correctness of our numerical approach. Apart from the above motivation, the inclusion of a magnetic field forms an important basis for the construction of a topological Mach-Zehnder interferometer, which we discuss in section 2.7. This is because the application of such a field and the associated breaking of TRS allow for using the device as a spin-transistor.

The field will be implemented in terms of the Peierls substitution which is described in detail in appendix B.1. Apart from this, an additional Zeeman term has to be added to the effective Hamiltonian from Eq. (2.1). This correction also depends on the field's direction and will thus be treated separately in the following subsections for out-of-plane and in-plane fields.

2.6.1. Perpendicular magnetic field

In this section we investigate the effect of a purely perpendicular magnetic field of strength B on the band structure of the HgTe/CdTe quantum well. For this purpose we need to modify the effective Hamiltonian Eq. (2.1) accordingly and introduce a Zeeman correction. This correction includes the Zeeman coupling due to the perpendicular magnetic field in first-order perturbation theory of the effective 4-band model [121]. This correction to the model Hamiltonian $H_{\text{eff}}(k_x, k_y)$ from Eq. (2.1) reads [121, 134]

$$H_{\text{ZM}} = \mu_B B \begin{pmatrix} g_{E\perp} & & & \\ & g_{H\perp} & & \\ & & -g_{E\perp} & \\ & & & -g_{H\perp} \end{pmatrix} \quad (2.12)$$

with the usual g-factor values of $g_{E\perp} = 22.7$ and $g_{H\perp} = -1.21$ which are used in all our calculations. The numerical implementation of this Zeeman terms, as well as the implementation of the magnetic field by means of the Peierls substitution are described in appendix B and more specifically in appendix B.1.3. Explicit conversions for the occurring constants such as μ_B into the correct units can be found in appendix B.1.6. Results for the band structure of a stripe of width $W = 500$ nm are shown in Fig. 2.13 for different field strengths B . The results especially for $B = 0.08$ T [see black line in panel (b)] look very similar to those of figure 4 in Ref. [134]. However, a strict quantitative comparison is hardly possible since no axis labels or ticks are provided there and no statement about the specific parameters used is given. As obvious from Fig. 2.13, the center of the bands structure is shifted to larger values of k_x . This shift is clearly visible as the band structures as a whole (see green and black lines) shift to the right with increasing field strength B as compared to the band structure at $B = 0$ Tesla that is in all panels shown in red for $\Delta = 0$ meV and in blue for $\Delta = 1.6$ meV. This behavior is clear as the magnetic field is implemented by the minimal substitution $\hat{k} \rightarrow \hat{k} - \frac{e}{\hbar} \vec{A}$ with \hat{k} the wavenumber operator and \vec{A} the magnetic vector potential. Also the breaking of TRS is reflected in this band structure shift since now for a state at wavenumber k_x one cannot automatically find a time-reversed partner at $-k_x$. When the field is turned on, the degeneracy between spin-up and spin-down is lifted and the edge states split up. The original degenerate Dirac cone now splits into two cones - one for each spin-polarization. The results also show that an inclusion of the bulk-inversion asymmetry correction Δ as described in section 2.5 opens a band gap in the vicinity of these Dirac points of the order of $|\Delta|$ (see comparison of red and blue lines in Fig. 2.13). As expected the changes in band structure are significant for a perpendicular component of the field. To check the correctness of our calculations, we also plot the band structure at a strong magnetic field of $B = 1$ T in Fig. 2.14

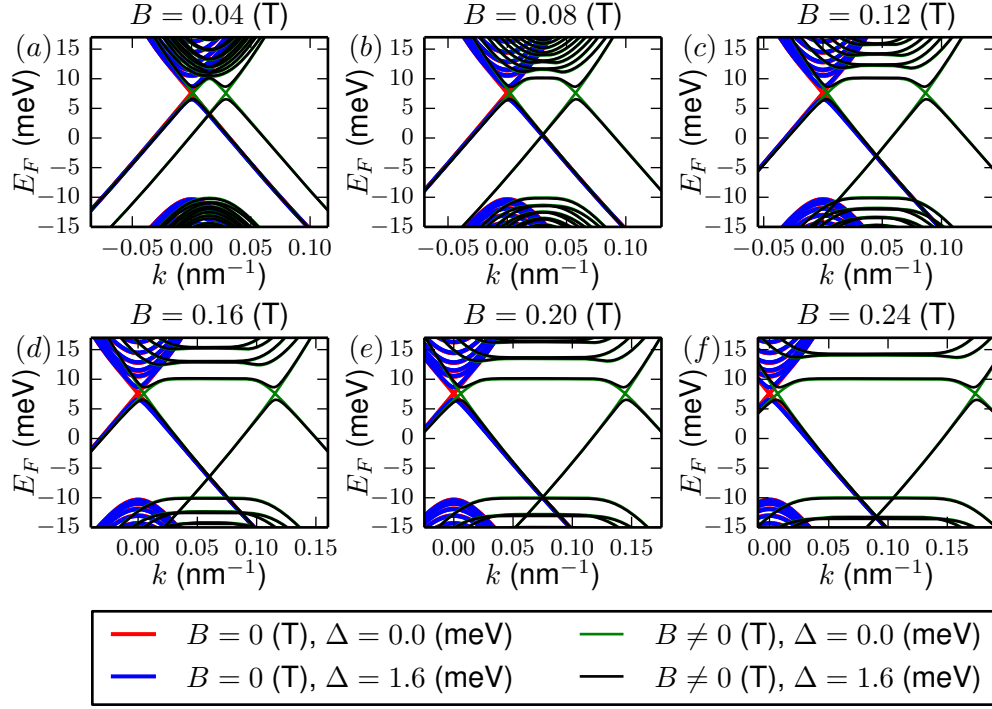


Figure 2.13.: Band structure of a stripe of width $W = 500$ nm for different perpendicular magnetic fields. The QW parameters taken from Ref. [121] are $A = 365.0$ nm \cdot meV, $B = -706.0$ nm 2 \cdot meV, $D = -532.0$ nm 2 \cdot meV, $m = -10.09$ meV. The red and blue lines show the band structures for zero field $B = 0$ T and a BIA term $\Delta = 0$ meV and $\Delta = 1.6$ meV in all panels, respectively. Likewise the green and black lines show the results for finite field B according to the panel's title again for the BIA term once ignored and once included. The grid constants in the numerics are set to $\Delta x = \Delta y = 5$ nm.

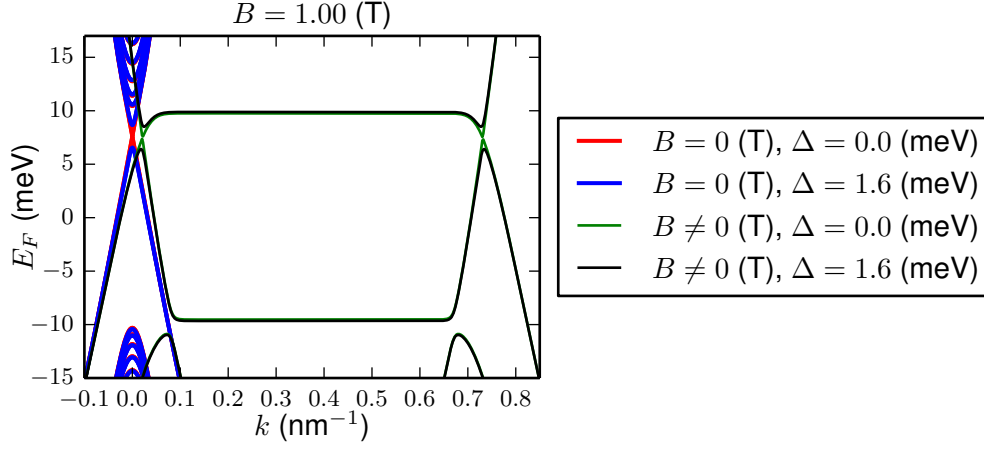


Figure 2.14.: Band structure of a stripe of width $W = 500$ nm for no field (red and blue) and a perpendicular magnetic field of strength $B = 1$ T (green and black). The QW parameters taken from Ref. [121] are $A = 365.0$ nm \cdot meV, $B = -706.0$ nm² \cdot meV, $D = -532.0$ nm² \cdot meV, $m = -10.09$ meV. The red and blue lines show the band structures at zero field $B = 0$ T and a BIA term $\Delta = 0$ meV and $\Delta = 1.6$ meV, respectively. Likewise the green and black lines show the results for finite field $B = 1$ T again for the BIA term again once neglected (green) and once included (black). The grid constants in the numerics are $\Delta x = \Delta y = 5$ nm.

(see green and black lines). In Ref. [121] a band gap of ≈ 3.1 meV is predicted when including a BIA term as well. This prediction is approximately confirmed also in our calculations where we find the band gap to be of size 2.0836 meV (see black line). However, these calculations are for sure very sensitive to finite-size effects and also Ref. [121] does not provide any numerical details of their calculations.

2.6.2. In-plane magnetic field in a plane lead

In contrast to the effects of a perpendicular field, an in-plane field is expected to have only little effect on the transport properties of a two-dimensional topological insulator [121]. To check this explicitly, we included the magnetic field in x -direction through the implementation of a parallel Zeeman term

$$H_{zm} = \mu_B B \begin{pmatrix} 0 & 0 & g_{\parallel} & 0 \\ 0 & 0 & 0 & g_{\parallel} \\ g_{\parallel} & 0 & 0 & 0 \\ 0 & g_{\parallel} & 0 & 0 \end{pmatrix} \quad (2.13)$$

with the value of $g_{\parallel} = -20.5$ taken from Ref. [121] and used in all our calculations. Details on the implementation of this correction and the corresponding Peierls phases can be found in appendix B.1.4 and the constant values are in detail derived in appendix B.1.6. Fig. 2.15 shows the band structures with such an in-plane magnetic field of up to 0.24 T (see green and black lines) compared to the band structures at no field (see red and blue lines). While a weak field of $B = 0.04$ T

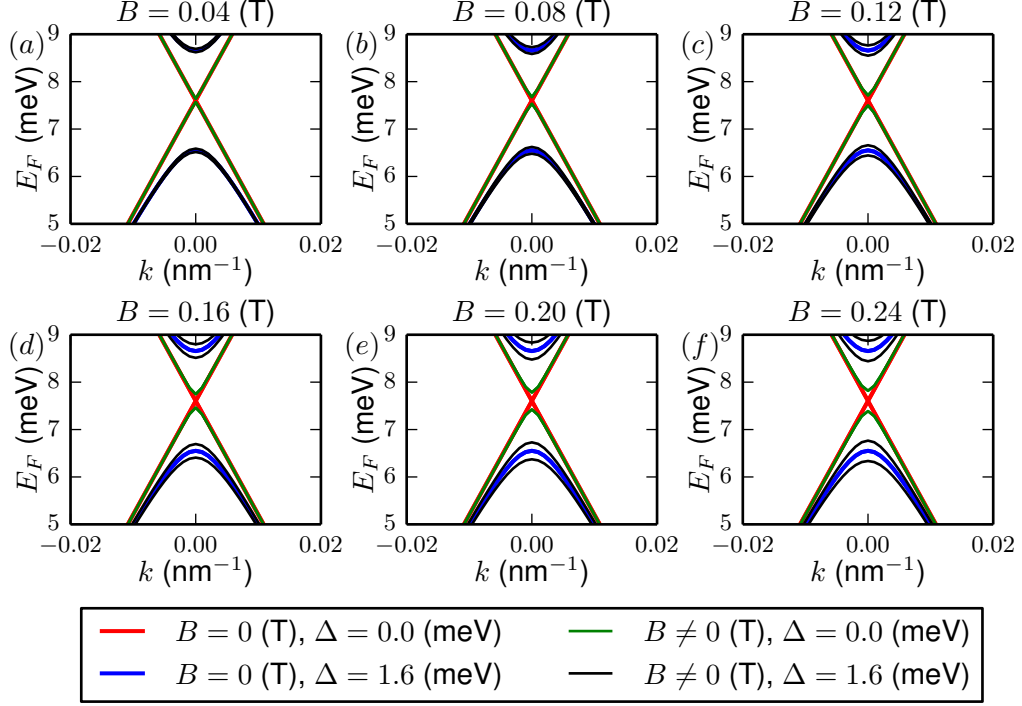


Figure 2.15.: Band structure of a plane rectangular stripe of width $W = 500$ nm for an in-plane magnetic field in x -direction of different strength B . The QW parameters taken from Ref. [121] are $A = 365.0$ nm \cdot meV, $B = -706.0$ nm² \cdot meV, $D = -532.0$ nm² \cdot meV, $m = -10.09$ meV. The red and blue lines show the band structures for zero field $B = 0$ T and a BIA term $\Delta = 0$ meV and $\Delta = 1.6$ meV in all panels, respectively. Analogously the green and black lines show the results for finite field B as indicated on top of each panel for the BIA term once ignored (green) and once included (black). The grid constants are $\Delta x = \Delta y = 5$ nm.

hardly changes the band structure [see panel (a)], an increasing field starts to open a gap even if no BIA term is included, i.e. $\Delta = 0$ meV [compare red and green lines in panels (b) to (f)]. If the BIA term $\Delta = 1.6$ meV is considered, the gap that already exists at zero field (see blue lines) is actually shrunk with increasing field

(see black lines). The BIA term causes the edge states of opposite spins to split with increasing field strength B close to the Dirac point at $k = 0 \text{ nm}^{-1}$. This is evident from the increasing splitting of the black lines as one goes to stronger magnetic fields from panel (a) to (f) while on the other hand the green data neglecting the BIA correction does not split and the edge states remain degenerate. This splitting

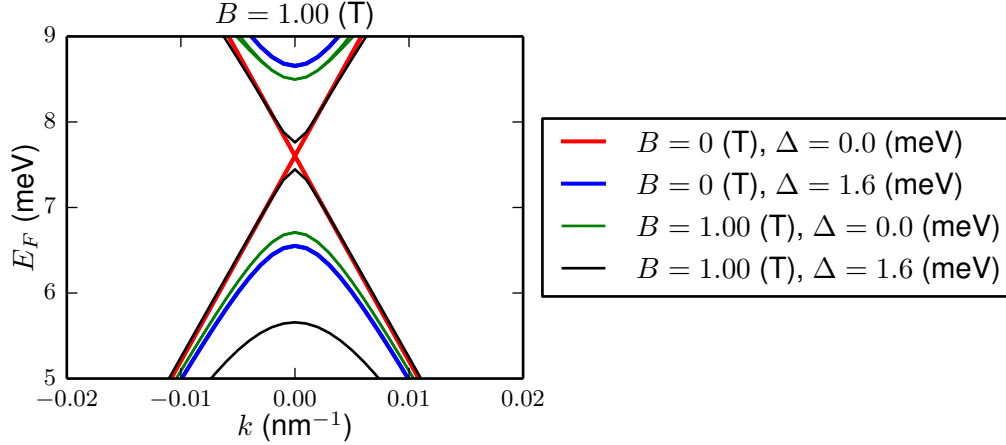


Figure 2.16.: Band structure of a plane rectangular stripe of width $W = 500 \text{ nm}$ for no field (red and blue) and an in-plane magnetic field in x -direction of strength $B = 1 \text{ T}$ (green and black lines). The QW parameters taken from Ref. [121] are $A = 365.0 \text{ nm} \cdot \text{meV}$, $B = -706.0 \text{ nm}^2 \cdot \text{meV}$, $D = -532.0 \text{ nm}^2 \cdot \text{meV}$, $m = -10.09 \text{ meV}$. The red and blue lines show the band structures at zero field $B = 0 \text{ T}$ and a BIA term $\Delta = 0 \text{ meV}$ and $\Delta = 1.6 \text{ meV}$, respectively. Likewise the green and black lines show the results for finite field $B = 1 \text{ T}$ for the BIA term again once neglected (green) and once included (black). The grid constants of the numerical finite-difference grid are $\Delta x = \Delta y = 5 \text{ nm}$.

explains the decrease of the gap size since one of the spins is pushed up in energy while the other spin polarization is pushed down. Accordingly, the gap is shrunk as states of a single spin-polarization penetrate into the original gap from both sides and hence diminish the gap as a result of the field. Again we are able to confirm the validity of our calculations by looking at the prediction of the band gap size in Ref. [121]. There it is found that such a parallel magnetic field of strength 1 T will induce a band gap of $\approx 0.3 \text{ meV}$. The value that we find (see black line in Fig. 2.16) is 0.31538 meV which is in good agreement. Overall we find that although some details in the band structure especially close to the Dirac point at $k = 0 \text{ nm}^{-1}$ are changing, the band structure as a whole does not change as much. Also edge states can be expected to exist and still be fairly stable with respect to disorder as also

observed even experimentally before [89].

2.6.3. In-plane magnetic field for a cylindrical lead

The following considerations are fundamental for our work, since the topological Mach-Zehnder interferometer that we propose in section 2.7, features leads that are cylindrically deformed as sketched in Fig. 2.17. In this figure we show the quantum well structure built in a cylindrical fashion and a lead that is cut off at $x = 0$ to make the layered structure visible. The effective two-dimensional plane that the electrons live in is the inner layer of HgTe that is shown in blue.

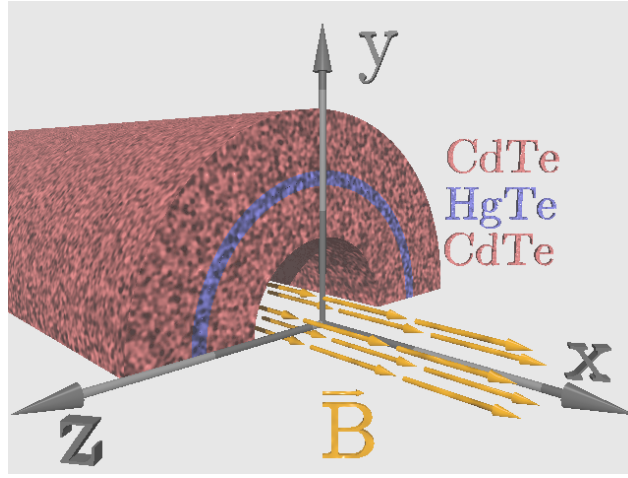


Figure 2.17.: 3-d sketch of a cylindrical lead exposed to a magnetic field \vec{B} in x -direction shown in orange. The quantum well layers are shown in red (CdTe) and blue (HgTe) sandwiching the effective two-dimensional system.

The question to answer is which consequences this lead shape brings along, especially when a magnetic field in x -direction is applied to it. While the Zeeman term Eq. (2.13) stays unchanged, further details of the numerical implementation are described in section B.1.5. As shown in Fig. 2.18 we find that the cylindrical shape of the lead has no visible impact on the band structure. The bands show the same behavior also for a plane lead with in-plane magnetic field as discussed in the previous section and shown in Fig. 2.15. The same shrinking of the band gap (compare blue and black curves in Fig. 2.18) as well as the separation of edge states with different spin-polarization close to the Dirac point (see splitting of black lines in the same figure) can be observed. Also for a very strong magnetic field (see Fig. 2.19) the band structure is the same as in the plane lead (compare to Fig. 2.16). These results indicate that a cylindrical lead does not have any impact on the edge states as long as the edges are not eliminated by closing the cylinder. For a lead

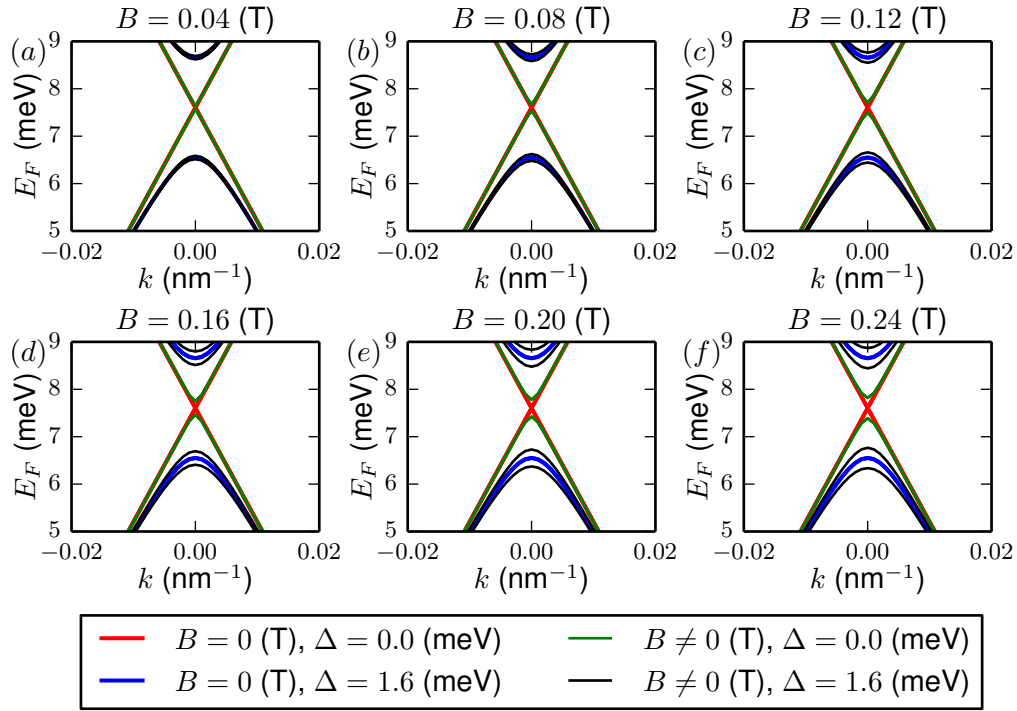


Figure 2.18.: Band structure of a cylindrical lead of width $W = 500$ nm for different parallel magnetic fields of different strength B . The radius of the cylinder is chosen such that the lead corresponds to exactly half a cylinder as sketched in Fig. 2.17. The QW parameters taken from Ref. [121] are $A = 365.0$ nm \cdot meV, $B = -706.0$ nm² \cdot meV, $D = -532.0$ nm² \cdot meV, $m = -10.09$ meV. The red and blue lines show the band structures for zero field $B = 0$ T and a BIA term $\Delta = 0$ meV and $\Delta = 1.6$ meV in all panels, respectively. The green and black lines show the results for finite field B given in the panel's title again for the BIA term once ignored (green) and once included (black). The grid constants in the numerics are $\Delta x = \Delta y = 5$ nm.

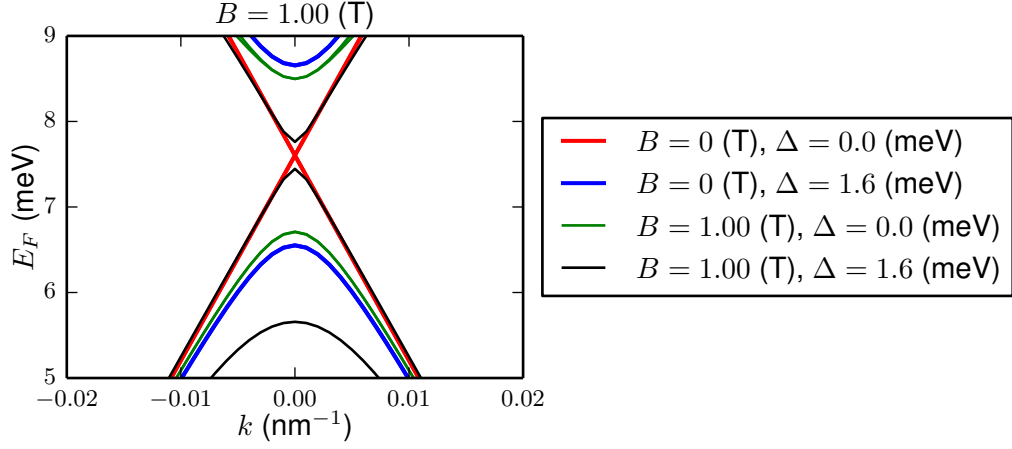


Figure 2.19.: Band structure of a plane rectangular stripe of width $W = 500$ nm for no field (red and blue) and an in-plane magnetic field in x -direction of strength $B = 1$ T (green and black lines). Again the radius of the cylinder is chosen such that the lead corresponds to exactly half a cylinder as sketched in Fig. 2.17. The QW parameters taken from Ref. [121] are $A = 365.0$ nm \cdot meV, $B = -706.0$ nm² \cdot meV, $D = -532.0$ nm² \cdot meV, $m = -10.09$ meV. The red and blue lines show the band structures at zero field $B = 0$ T and a BIA term $\Delta = 0$ meV and $\Delta = 1.6$ meV, respectively. Likewise the green and black lines show the results for finite field $B = 1$ T again for the BIA term again once neglected (green) and once included (black). The grid constants in the numerics are $\Delta x = \Delta y = 5$ nm.

that is half a cylinder our results show, that edge states still exist and are also rarely affected along the cylinder axis. This knowledge will be of special importance in the next section where we use such cylindrical leads as the in- and outputs of a spin-filter device in the form of a topological Mach-Zehnder interferometer.

2.7. A topological Mach-Zehnder interferometer

In this section we propose a setup that allows to use the edge states of topological insulators for interference experiments. Our setup mimics a Mach-Zehnder interferometer (MZI) as proposed for light already in the late 19th century [135, 136] and several years ago also realized for electronic edge states of the integer Quantum Hall phase [137]. For convenience, we choose here to explain the setup from scratch although the original idea was presented already in my diploma thesis [102] and in Alexander Fuß's bachelor thesis [138] that was supervised by Prof. Rotter and myself. In this work we go beyond the aforementioned studies by concretely exploring

possible applications of the topological MZI and in much more detail exploring the effects of a magnetic field applied to the device.

The functionality of a classical Mach-Zehnder interferometer is easily explained and illustrated in Fig. 2.20(a): An incoming beam B is split by a beam-splitter BS1 into two beams B1 and B2 taking different geometric paths. After being exposed to different physical conditions under which their phases evolve differently, these two beams are again brought together by reflection off two mirrors M1 and M2 and interfere at a second beam-splitter BS2. The two beams emerging from BS2 are detected by two detectors D1 and D2. Depending on the phase difference, which is in the original setup determined by the geometric path length difference Δl , the interference can be tuned between constructive and destructive and the light intensity measured in the detectors will oscillate as a function of Δl . The first electronic MZI [137] realized in semiconductor heterojunctions in high magnetic fields is sketched in Fig. 2.20(b). The unidirectional edge states caused by the integer Quantum Hall effect are the analogues of the light beams in the classical MZI. The quantum point contacts (QPCs) in this setup cause partial reflection of incoming edge states and thus mimic the beam splitters. In this case the phase difference depends on the strength of the applied perpendicular magnetic field and the enclosed area that the edge-states circumnavigate due to the Aharonov-Bohm effect. Additionally, the phase difference can in this setup be tuned by the two modulation gates MG1 and MG2. While the interference of edge states in these systems have already been realized [137], interference experiments with the edge states of two-dimensional topological insulators are missing up to this point. A device that enables experimentalists to observe such coherent interference would be a huge step with a potentially broad field of applications [87] possibly even at room temperature [86, 139]. For this purpose we propose a setup of a two-dimensional topological insulator such as a HgTe/CdTe quantum well that is realized in a cylindrical way as shown in a three-dimensional illustration in Fig. 2.20(d). A simplified two-dimensional sketch of the proposed geometry is shown in Fig. 2.20(c) where the cylindrical surfaces are unrolled into a two-dimensional picture that we also use for our numerical simulations. The zig-zag lines at the top and bottom of this figure indicate the periodic boundary conditions that are used for the simulation of the underlying cylindrical structure.

In contrast to the Quantum Hall effect, the edge states of a topological insulator do not rely on a strong and perpendicular magnetic field which would not be realizable for a cylindrical surface. In return our setup allows for the observation of edge state interference in only a two-terminal setup while any planar setup would at least require the use of three terminals as the case in the electronic MZI [137]. In this way the signals in D1 and D2 are proportional to the total reflection R and the total transmission T through our system respectively. According to the Landauer formula Eq. (2.3) the total transmission T is in this two-terminal setup directly

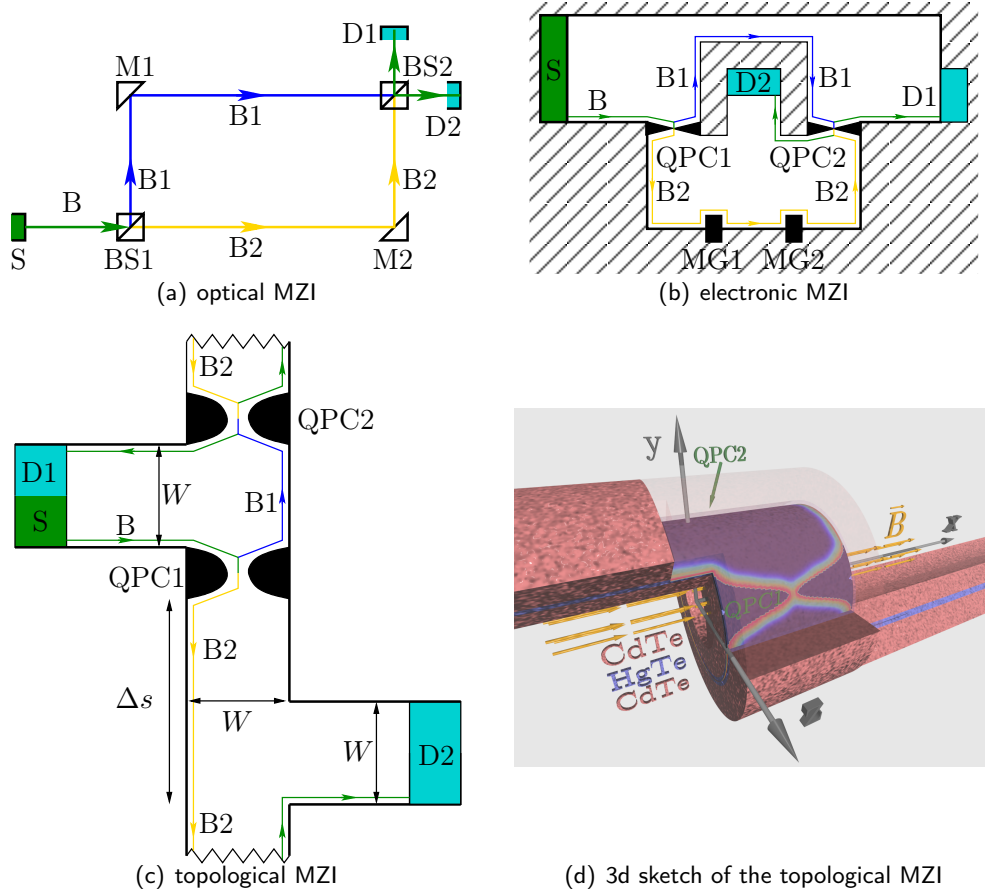


Figure 2.20.: Illustration of different types of MZIs. Light (electrons) are injected from the source S on the way B to the first beams splitter $BS1$. The beams propagate along two different ways $B1$ and $B2$ acquiring a phase difference of ϕ and are lead (after reflection at mirrors $M1$ and $M2$) back together at a second beam splitter $BS2$ where interference takes place. Measurements are performed at detectors $D1$ and $D2$. Illustration of (a) an optical MZI and (b) the first electronic MZI [137]. The beam splitters in this setup are replaced by quantum point contacts (QPCs) that partially reflect or transmit incoming electrons. (c) Setup of our topological MZI. The path length difference Δs is shown as well as the stripe width W which is the same in the leads as well as on the cylinder. (d) 3-d sketch of the topological MZI. The quantum well layers are shown in red (CdTe) and blue (HgTe) and are partially rendered transparent to leave a look at the exemplary electronic wave function on the cylinder surface. The QPCs are marked and the external magnetic field \vec{B} that can be applied in order to use the device as a spin filter is shown.

proportional to the conductance of the device in the limit of vanishing temperature.

As easily verifiable from Fig. 2.20(c) our geometry again features the same topology for the paths an electron can take as in the optical and the electronic MZI which is achieved by arranging the QPCs on top and beneath the incoming lead. When considering no coupling between the edge states of different spin, our setup can be viewed as two copies of an MZI, one for each spin-polarization since inter-spin scattering is in this case forbidden also at the QPCs' constrictions. In this case also, the transmission of spin-up and spin-down electrons is always equal since the taken paths are just time-reversed partners and thus the phase difference ϕ that determines the interference is always equal. As a result we can for now neglect the presence of a second spin-degree of freedom. The scattering at the QPCs is of fundamental importance for the functionality of our device. In the following we label the transmission and reflection amplitudes of an incoming edge state with given spin at the i^{th} QPC by $t_i^{\uparrow\downarrow}$ and $r_i^{\uparrow\downarrow}$, respectively. As the spin has no influence on the scattering amplitude for non-magnetic scattering and due to the use of symmetric Gaussian shaped QPCs one can assume $t_i^{\uparrow} = t_i^{\downarrow} = t_i$ and $r_i^{\uparrow} = r_i^{\downarrow}$. The total transmission of a single spin polarization through the i^{th} QPC is then given by $T_i^{\uparrow\downarrow} = |t_i|^2$. For an electron injected in a right-moving edge state of a specific spin-polarization into our setup, one can easily verify the following behavior: To be reflected to the source (D1) the electron must either be transmitted or reflected at both the QPCs ($t_1 t_2$ or $r_1 r_2$). On the other hand, to be transmitted through the whole geometry (i.e. to reach the outgoing lead D2) it must be once reflected and once transmitted ($t_1 r_2$ or $r_1 t_2$). Due to the cylindrical layout any electron that has reached the second QPC will leave the device and multiple scattering has not to be taken into account. This is a fundamental difference to other devices that were proposed for interference experiments before [134]. For simplicity we also choose the QPCs to be symmetric and of Gaussian shape with equal gap width g and thus the total transmission of a single edge-state with well-defined spin through either QPC is equal:

$$T_1^{\uparrow\downarrow} = T_2^{\uparrow\downarrow} = T_Q \quad .$$

In this case the total transmission and reflection of both right-moving edge states with opposite spin polarization can be expressed by

$$T = 4T_Q (1 - T_Q) [1 - \cos(\phi + \phi_0)] \quad , \quad (2.14)$$

$$R = 2 - 4T_Q (1 - T_Q) [1 - \cos(\phi + \phi_0)] \quad (2.15)$$

with ϕ representing the geometric phase difference that the electron picks up by propagating along paths $B1$ and $B2$ of different lengths. As an edge state is traveling at some constant wavenumber k along the edges of our geometry, $\phi = k\Delta s$ in terms of the path length difference Δs .

The HgTe/CdTe quantum well is described by the Bernevig-Hughes-Zhang (BHZ) model [88] in terms of the effective 4-band Hamiltonian from Eq. (2.1) including the BIA term Eq. (2.10) as discussed in section 2.5 and in appendices A. As worked out explicitly in section 2.5, we neglect the Rashba correction Eq. (2.11) as it has very little impact on the edge states, especially at energies below the Dirac point at $E_F \approx 7.1$ meV, which we will focus on in the following. Unless stated otherwise, realistic quantum well parameters [131] are chosen: $A = 365.0$ meV, $B = -706.0$ meV, $D = -532.0$ meV and $m = -10.09$ meV. A realistic value for the bulk-inversion asymmetry term is used by setting $\Delta = 1.6$ meV [121].

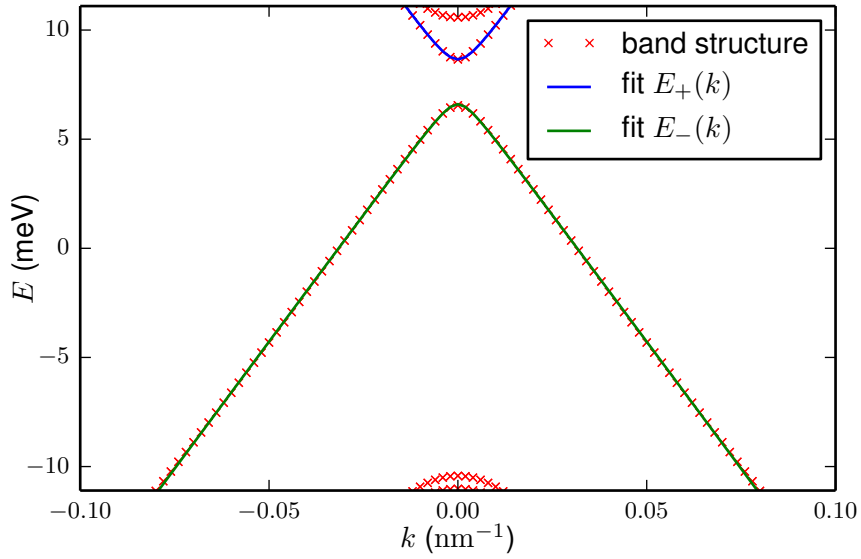


Figure 2.21.: The red crosses show the numerically calculated band structure of a clean waveguide of HgTe/CdTe quantum well with lead width $W = 500$ nm at zero magnetic field. Two hyperbolic functions $E_+(k)$ and $E_-(k)$ are fitted to these data points using Eq. (2.16) to obtain an analytic expression for the band structure in the bulk band gap region $-|m| < E_F < |m|$. The fit parameters are $a_+ = 1.2995$, $b_+ = 273.303$, $d_+ = 1.197$, $E_{0+} = 7.605$, $a_- = 1.472$, $b_- = 282.94$, $d_- = 0.976$ and $E_{0-} = 7.409$.

In a first numerical approach we are verifying the validity of the simple Eqs. (2.14) and (2.15) for the description of transport. Since interference is modulated by the wavenumber k of the corresponding edge state we expect to observe oscillations of T as a function of the Fermi energy E_F that we choose in the scattering problem. We are thus varying the Fermi energy in the energy interval $-|m| < E_F < |m|$ where the edge states exist exclusively without any contributing bulk conductance.

For this purpose we utilize a topological MZI as shown in Fig. 2.20(c) with lead width $W = 500$ nm and $\Delta s = W = 500$ nm. As the transmission Eq. (2.14) and the interference of edge states depend strongly on their wave number k , we need knowledge about the band structure $E(k)$ of the edge states. For this purpose we compute the band structure numerically within the desired energy region. These results are shown by the red crosses in Fig. 2.21. While without bulk inversion asymmetry corrections (i.e. $\Delta = 0$ meV) the edge states show a Dirac point at $k = 0$ nm⁻¹, choosing $\Delta = 1.6$ meV opens a band gap. We fit the band structure by hyperbolic functions

$$E_{\pm}(k) = E_{0\pm} \pm \sqrt{\frac{d_{\pm}^2 + b_{\pm}^2 k^2}{a_{\pm}}} \quad (2.16)$$

that show an almost perfect fit in the important energy region (see blue and green curves in Fig. 2.21).

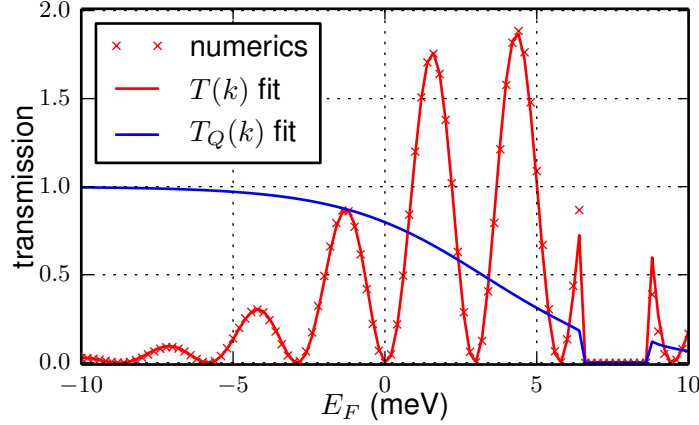


Figure 2.22.: Red crosses show the total transmission through a topological MZI with lead width $W = 500$ nm, QPC gap size $g = 30$ nm and path length difference $\Delta s = 500$ nm. We fit these data points using Eqs. (2.14) and (2.17). The blue curve shows the obtained fit for the total transmission T_Q through each of the two QPCs. The obtained fit parameters are $c = 0.9996$, $k_0 = -0.0177$, $f = 99.343$, $\phi_0 = 3.0914$ and $\Delta s = 498.526$.

For the transmission T_Q at a single quantum point contact we are using a Fermi function of the form

$$T_Q(k) = \frac{c}{1 + e^{-f(k-k_0)}} \quad (2.17)$$

with fit parameters c , f and k_0 . The total transmission T through the topological MZI that was computed numerically (see red crosses in Fig. 2.22) can thus be fitted

by the use of Eq. (2.14) (see red line in Fig. 2.22). These results confirm that even in the case of $\Delta \neq 0$ meV the inter-spin scattering can be neglected and Eq. (2.14) indeed holds. Being now able to describe analytically the transmission through our device as a function of E_F , we want to use this knowledge to propose basic interference experiments with topological insulator edge states and to make our device usable as a transistor. For this it is necessary to be able to observe both, entirely constructive (i.e., $T = 2$) and entirely destructive interference (i.e. $T = 0$) at the second QPC. It is evident from Eq. (2.14) that the maximal transmission value of $T = 2$ can only be reached when $T_Q = 0.5$, i.e. each QPC is set exactly to half transmission. This behavior is also reflected in Fig. 2.22.

From our fitted function Eq. (2.17) we find that $T_Q = 0.5$ can be achieved by tuning the Fermi energy to $E_F = E_{\text{on}} = 3.198$ meV. In order to reach $T = 2$ the interference must at this point be perfectly constructive corresponding to an overall phase difference $\phi + \phi_0 = k\Delta s + \phi_0$ of π for this given $k(E_F)$. For this purpose we tune Δs to yield $T = 2$ according to Eq. (2.14) using the fixed parameters from our fit in Fig. 2.22 and find a value close to $\Delta s = 350$ nm. Keeping Δs fixed at this value, the next minimum of transmission $T = 0$ is found at $E_F = E_{\text{off}} = 1.14$ meV. The scattering wave functions in panels (a) and (b) of Fig. 2.23 show that indeed for $E_F = E_{\text{on}}$ electrons are almost perfectly transmitted in both edge states, respectively. Also the MZI can be tuned to almost no transmission by choosing $E_F = E_{\text{off}}$ [see panels (c) and (d) in Fig. 2.23].

In an experiment such a switching between no and perfect transmission could also be achieved by tuning the gate voltage at the cylinder surface and by this the Fermi energy E_F . While in the numerics we then choose to tune the path length difference Δs , in an experiment this is hard to do since Δs depends on the sample. Instead one should there tune the gate voltages of the QPCs and thus the size of their constrictions which is impractical in the numerics since we are there limited by the discretization of the finite-difference square grid.

Our results indicate that it is not possible to filter one of the spin components since, due to time-reversal symmetry, the transmission for the spin-up and spin-down is always equal at any value of E_F . To achieve this, we have to break this symmetry which can in the easiest way be achieved by applying a weak magnetic field along the cylinder axis [i.e. the x -direction, see also Fig. 2.20(d)]. Alternatively also a ferromagnetic core in the cylinder's center could be used. In this way the lead states would not be influenced significantly and also pure edge transport should not be inhibited since the magnetic field is in-plane and very weak [121]. We implement such an in-plane magnetic field in x -direction by the use of the Peierls substitution (see appendix B) and the addition of a Zeeman correction Eq. (2.13) to the Hamiltonian Eq. (2.1) as we already discussed in section 2.6. There we have already convinced ourselves that we can safely use cylindrically shaped leads for the in- and output without destroying the edge states of the topological insulator, even in the

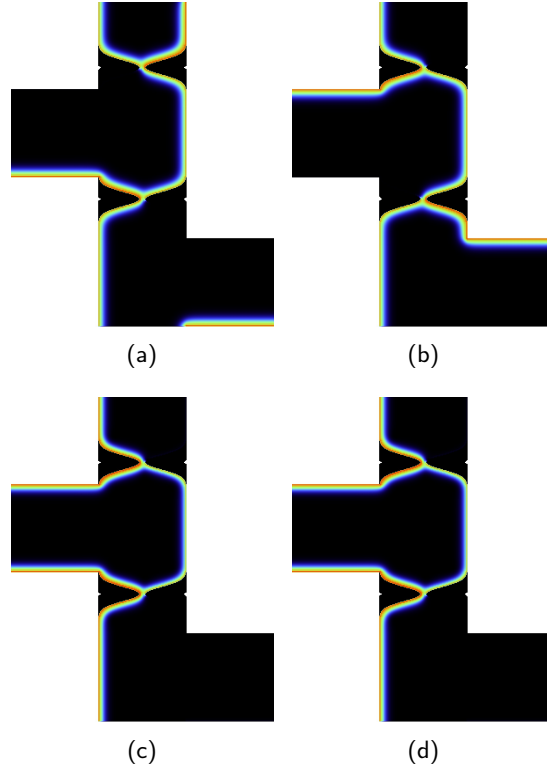


Figure 2.23.: Pictures of the electronic scattering wave function through a topological MZI with path length difference $\Delta s = 350$ nm and lead width $W = 500$ nm. Panels (a) and (b) show the patterns at energy $E_F = E_{\text{on}} = 3.198$ meV for injection of spin-up and spin-down right-moving edge states, respectively. The Fermi energy is chosen such, that full transmission of $T = 2$ can be achieved. The numerics show that the transmissions of each spin component are equal and sum up to a total transmission of $T = 1.99915$ which is very close to the expected value. Also the pictures reflect this almost perfect transmission. Panels (c) and (d) show the scattering wave functions at energy $E_F = E_{\text{off}} = 1.14$ meV again for spin-up and spin-down edge states, respectively. The Fermi energy is selected to reside at the expected transmission minimum of $T = 0$ meV corresponding to destructive interference in the MZI. The pictures show, that almost no intensity is transmitted to the right and the total transmission is indeed almost vanishing with $T = 0.0037$.

presence of a weak magnetic field along the cylinder's axis. The Zeeman coupling strength is in all our calculations set to $g_{\parallel} = -20.5$ [121]. By the application of a magnetic field we want to use the Aharonov-Bohm effect in order to filter one of the spin-components. This is possible since these additional phase differences ϕ_{AB} have opposite signs for spin-up and spin-down edge states since they are propagating in opposite directions. These phase differences

$$\phi_{AB}^{\uparrow\downarrow} = \pm \frac{e}{\hbar} A_{\text{cyl}} B \quad (2.18)$$

are proportional to the encircled magnetic flux enclosed by the cylinder with cross section A_{cyl} . At this point it is important to mention that it is not even necessary for the electrons to get in touch with the magnetic field since the Aharonov-Bohm phase is purely connected to the magnetic flux through the cylinder [140]. In this way it is sufficient to use, e.g., a ferromagnetic core in the center of the cylinder instead. Moreover one can see from Eq. (2.18) that a single flux quantum $\phi_0 = 2A_{\text{cyl}}B_0 = \frac{h}{2e}$ is sufficient to gather an Aharonov-Bohm phase of $\pm\pi$. We expect the total transmission for the individual spin components to be given by

$$T^{\uparrow\downarrow}(B) = 2T_Q(1 - T_Q) \left[1 - \cos \left(\phi_0 + k\Delta s \pm \frac{e}{\hbar} A_{\text{cyl}} B \right) \right]. \quad (2.19)$$

In order to realize a spin-switching device in our setup we again want to see transmission oscillations with maximal amplitude. For this purpose we set $E_F = E_{\text{on}} = 3.198$ meV which guarantees $T_Q = 0.5$. From Eq. (2.19) it is obvious that in order to observe spin filtering effects, we need to tune the field-independent phase $\phi_0 + k\Delta s$ such that it is an odd multiple of $\pi/2$ in order to achieve $T^{\uparrow}(B)$ and $T^{\downarrow}(B)$ to be out of phase as a function of the magnetic field. The reason for this behavior is that the cosine in Eq. (2.19) is odd around $\pi/2$ but even around zero which allows for both, in-phase and out-of-phase oscillations of T^{\uparrow} and T^{\downarrow} . The latter corresponds to tuning $\Delta s = 440$ nm such that $T(B = 0) = T^{\uparrow}(B = 0) + T^{\downarrow}(B = 0) = 1$ at energy $E_F = E_{\text{on}}$. We can then also expect that the total transmission T at this energy will yield a constant value of $T = 1$ for all values of B [see Eq. (2.19) when $T(B = 0) = 1$]. This result is confirmed by a nice match of the theoretical prediction and the numerical results for the total transmission in this setup shown by the red line and crosses in Fig. 2.24(b). In the same figure we also show that the transmissions of individual spin components are indeed out of phase (see the green and blue lines and arrows). We thus find that at values of $B = \pm B_0 = \pm \frac{\pi\hbar}{4eA_{\text{cyl}}} = \pm 0.003452$ T only one of the spin-components can fully transmit through the setup while the other one is entirely reflected. In this way a spin-filter can be achieved since the sign of the field of magnitude B_0 will determine the spin-polarization of the transmitted electrons.

However, it is still possible to also achieve almost full transmission $T = 2$ and no transmission $T = 0$ by once again tuning the Fermi energy such that at zero

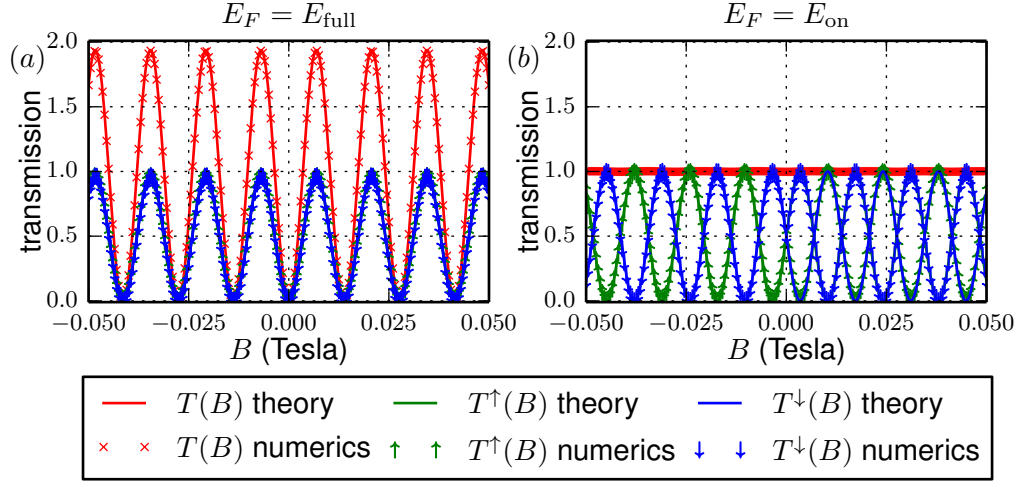


Figure 2.24.: In both panels red crosses show the total transmission T as a function of the magnetic field B through a topological MZI with lead width $W = 500$ nm, QPC gap size $g = 30$ nm and path length difference $\Delta s = 440$ nm from numerical calculations. The red lines show the total transmission predicted by simple theory for Aharonov-Bohm interference. Theoretical predictions for the transmissions $T^\uparrow(B)$ and $T^\downarrow(B)$ for the individual single spin-components are shown by the green and blue lines, respectively. Numerical results for $T^\uparrow(B)$ and $T^\downarrow(B)$ are marked by small arrows of the same colors. In panel (a) the Fermi energy is chosen at $E_F = E_{\text{full}} = 2.378$ meV such that at zero magnetic field the total transmission is in theory equal to $T = 0$. Numerics show for these parameter values that indeed $T = 0.00011$ close to zero. Expected full oscillations of T as a function of B are numerically verified with a maximal value of $T = 1.9333$ at $B = 2B_0 = 0.0069$. Also for the individual spin-components the numerical calculations and theoretical predictions show a perfect match as well as the equality of spin-up and spin-down transmissions at arbitrary field for this choice of E_F . Panel (b) shows the same quantities as above but for $E_F = E_{\text{on}} = 3.198$ meV. This value is tuned in such a way that at zero magnetic field the total transmission is in theory equal to $T = 1$. Numerics confirm this expectation by $T(B = 0) = 0.99987$. Theoretically we expect the total transmission to be constant $T = 1$ with respect to B which is numerically confirmed (see red crosses and line). The individual spin components on the other hand now show alternating transmission and points of pure spin-up and spin-down transmissions can be found at $B = \pm 0.00345$ T, respectively. Once again the numerics show the same behavior.

magnetic field $T = 0$. Using Eq. (2.14) this gives a value of $E_F = E_{\text{full}} = 2.378$ meV for which the total transmission T as well as the transmissions of spin-up and spin-down electrons are again shown in red, green and blue, respectively in Fig. 2.24 (the lines always show the theory, the crosses and arrows shown the numerical results). We numerically confirmed that for no magnetic field the device is blocked for any charge transfer at $T = 0.00011$ while almost perfect transmission of $T = 1.93314$ can again be achieved at $B = 2B_0$. The reason why T in this case does not exactly reach $T = 2$ is because at this value of E_F the transmission through a single QPC is $T_Q \neq 0.5$. This problem could be overcome by simultaneously tuning the gate voltages of the QPCs (their gap widths g) to again guarantee $T_Q = 0.5$. In addition the deviations from $T = 2$ will decrease when a larger MZI with a larger path length difference Δs is used since then the transmission maxima in energy are closer together.

Overall, this specific topological MZI with lead width $W = 500$ nm and path length difference $\Delta s = 440$ nm can serve as a spin-filter and spin-transistor in the following way: By setting the Fermi energy E_F to the value of $E_F = E_{\text{full}}$ the device can be used in reflection mode featuring almost no transmission. Applying a magnetic field along the cylinder axis of strength $B = 2B_0$ will transfer the device to transmission mode with total transmission close to $T = 2$. By then changing the Fermi energy to $E_F = E_{\text{on}}$ and halving the field strength to $B = B_0$ one ends up in pure spin-up transmission while spin-down electrons are entirely reflected. Inverting the magnetic field to $B = -B_0$ will also invert the spin of transmitted electrons propagating on the opposite edge and filtering now the spin-up component while spin-down is perfectly transmitted. Pictures of the device in these four possible configurations are shown in Fig. 2.25 for injection of an equally-weighted coherent superposition of right-moving spin-up and spin-down edge states. The desired behavior and the 4 possible settings of the spin-transistor can easily be verified by looking at the transmitted electronic wave functions in the right lead. In contrast, previous suggestions for devices featuring tunable spin and charge currents are relying on four-terminal measurements [139, 141–147]. Also in the most popular such device [141] the spin and charge conductances cannot be steered separately since pure spin-conductance is accompanied by vanishing charge conductance. In our two-terminal setup the charge transfer itself can be tuned to consist of a single spin-component only. In return we have to use a magnetic field which is, however, very weak and in-plane and thus is not destroying coherent edge transport or backscattering immunity. Moreover, this magnetic field does not necessarily need to act on the electrons themselves since it is sufficient to introduce an enclosed magnetic flux through the cylinder to achieve this filtering property [140]. Additionally, in the aforementioned suggested setup the interference is a combination of two distinct mechanisms, namely Fabry-Pérot and electrical Aharonov-Bohm interference showing complicated interplay [141]. In our setup the interference effects are of strict

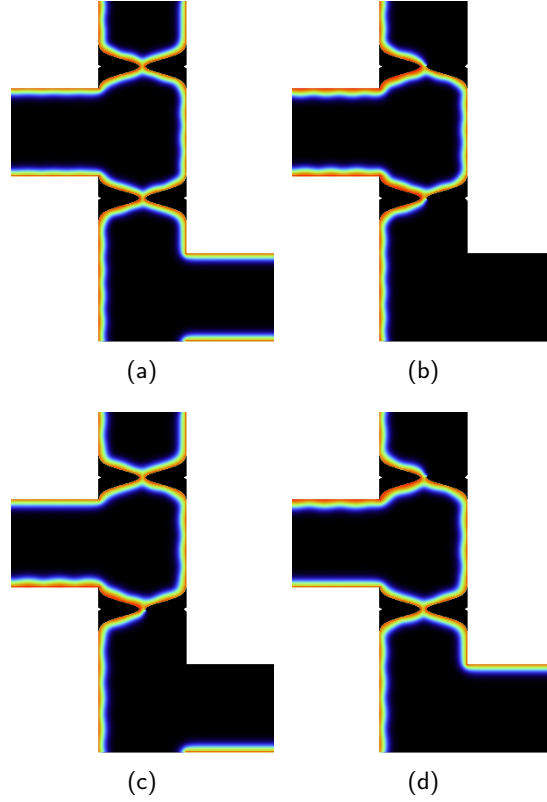


Figure 2.25.: Pictures of the electronic scattering wave function through a topological MZI with path length difference $\Delta s = 440$ nm and lead width $W = 500$ nm. Panels (a) and (b) show scattering wave functions at energy $E_F = E_{\text{full}} = 2.378$ meV for injection of a coherent and equally-weighted superposition of spin-up and spin-down right-moving edge states. In (a) the device at zero magnetic field $B = 0$ T is set to blocking status with $T = 0.000228$. Panel (b) shows the electronic wave function in the device in full transmission mode with $B = 2B_0$ and $T = 1.933$. Panels (c) and (d) show the scattering wave functions at energy $E_F = E_{\text{off}} = 1.14$ meV again for the same coherent superposition of spin-up and spin-down edge states. The Fermi energy is here chosen such that transmissions for spin-up and spin-down are out of phase yielding a constant value for their sum of $T = 1$ for arbitrary field B . In (c) the MZI is exposed to a magnetic field of strength $B = B_0$ resulting in pure spin-up transport $T = T^\uparrow = 0.99987$ while in (d) the field's direction is inverted, i.e. $B = -B_0$, leaving us with pure spin-down transmission $T = T^\downarrow = 0.99987$.

Mach-Zehnder type making them possibly more easily controllable. Other proposals for spin-transistors [140, 148] rely on more sophisticated descriptions and would thus need better control of material parameters in a real experiment. Furthermore these devices do not allow for spin filtering but rather spin switching and could serve as spin-transistors with 2 [140] or 3 [148] possible settings and do not rely on basic interference effects. Our device would allow for spin filtering and could be used as a spin-transistor with 4 possible settings. Further suggestions that point into a similar direction [149, 150] are well suited for spin-polarized single-electron or single-pair emission from a source but cannot serve as a spin-filter or spin-transistor.

Chapter 3.

Numerical methods and improvements

3.1. Finite differences method

In this chapter we give insight into the numerical model that is used in all our calculations focusing on quite a few improvements that we performed. The systems of interest can all be described by a Hamiltonian operator \hat{H} that is a differential operator of second order. In a numerical scheme the solution of the corresponding second order differential equation

$$\hat{H}\psi(x, y) = E\psi(x, y) \quad (3.1)$$

has to be mapped onto a discrete pattern in any form. The easiest way to do this, is to discretize the considered geometry on a rectangular grid featuring n_y points in y -direction and n_x points in x -direction with the corresponding grid spacings Δy and Δx as sketched in Fig. 3.1. The discretized geometry is then characterized by its coordinates (x_i, y_j) with $i = 1, \dots, n_x$ and $j = 1, \dots, n_y$. The solutions $\psi(x, y)$ of Eq. (3.1) are in this scheme represented by a vector of complex values $\psi(x_i, y_i) = \psi_{ij}$, one for every point of the geometry. The ordering of this vector ψ_{ij} is chosen such that the points are ordered column wise

$$\psi_{ij} = \begin{pmatrix} \psi_{11} \\ \psi_{12} \\ \vdots \\ \psi_{1n_y} \\ \psi_{21} \\ \vdots \\ \psi_{2n_y} \\ \vdots \\ \psi_{n_x n_y} \end{pmatrix} := \vec{\psi} \quad (3.2)$$

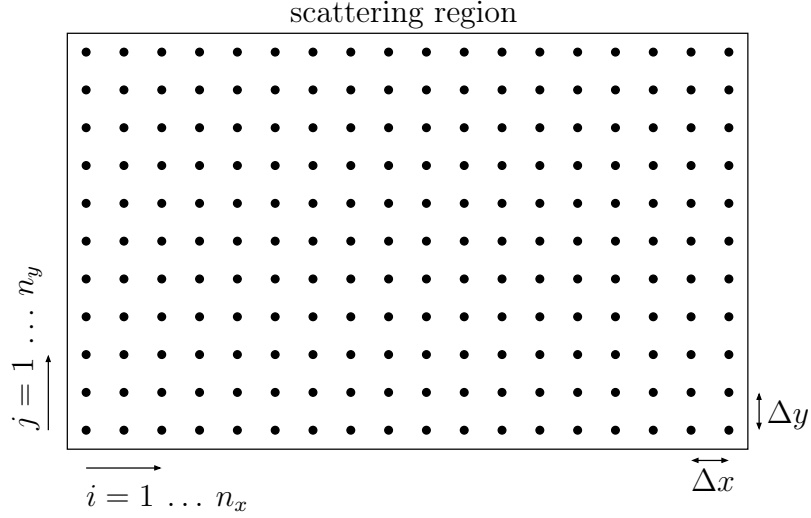


Figure 3.1.: Sketch of the discretization in our numerical scheme on a rectangular grid of $n_x \times n_y$ points. The grid spacings are Δx and Δy in x - and y -direction respectively. The points of the geometry (x_i, y_i) are labelled by their line index i and their column index j .

In this way the Hamilton operator \hat{H} can be written as a matrix H of dimension $n_x \cdot n_y \times n_x \cdot n_y$ taking a strictly tridiagonal block-form

$$H = \begin{pmatrix} H_0^{(1)} & H_I & 0 & \dots & \dots & 0 \\ H_I^\dagger & H_0^{(2)} & H_I & 0 & \dots & \vdots \\ 0 & \ddots & \ddots & \ddots & 0 & \vdots \\ \vdots & 0 & \ddots & \ddots & \ddots & 0 \\ \vdots & \dots & 0 & H_I^\dagger & H_0^{(n_x-1)} & H_I \\ 0 & \dots & \dots & 0 & H_I^\dagger & H_0^{(n_x)} \end{pmatrix}. \quad (3.3)$$

The $n_y \times n_y$ subblocks $H_0^{(i)}$ on the diagonal connect those wave function components with the same x -coordinate x_i . In this sense $H_0^{(i)}$ describes a single stripe of points at some constant x_i . The subblocks H_I and H_I^\dagger on the other hand describe the coupling between adjacent such stripes. For easier readability we assumed that H_I and H_I^\dagger do not depend on the position of the slices that they connect. For this reason we dropped the index i that they should in general depend on. Such a distinction would for example be necessary if n_y was not constant for all slices but varied with the slice position x_i . We will add this index when necessary; in most cases the final equations of our considerations remain essentially unchanged. The explicit form of

these matrices is found by approximating the derivatives with respect to x and y by the corresponding symmetric difference quotients

$$\frac{d\psi(x, y)}{dx} \rightarrow \frac{\frac{\psi_{i+1,j} - \psi_{i,j}}{\Delta x} + \frac{\psi_{i,j} - \psi_{i-1,j}}{\Delta x}}{2} = \frac{\psi_{i+1,j} - \psi_{i-1,j}}{2\Delta x} \quad (3.4)$$

$$\frac{d\psi(x, y)}{dy} \rightarrow \frac{\psi_{i,j+1} - \psi_{i,j-1}}{2\Delta y} . \quad (3.5)$$

In the same way the second derivatives are approximated by

$$\frac{d^2\psi(x, y)}{dx^2} \rightarrow \frac{\psi_{i+1,j} - 2\psi_{i,j} + \psi_{i-1,j}}{(\Delta x)^2} \quad (3.6)$$

$$\frac{d^2\psi(x, y)}{dy^2} \rightarrow \frac{\psi_{i,j+1} - 2\psi_{i,j} + \psi_{i,j-1}}{(\Delta y)^2} . \quad (3.7)$$

For example the Hamiltonian \hat{H} of a free electron is given by

$$\hat{H} = -\frac{\hbar^2}{2m_e} \left(\frac{d}{dx^2} + \frac{d}{dy^2} \right) . \quad (3.8)$$

In atomic units usually $\hbar = 1$ as well as the electron mass $m_e = 1$. Using (3.6) and (3.7) one finds that $H_0^{(i)} = H_0$ and H_I are in this simplest case given by (we also assume a square lattice here, i.e. $\Delta x = \Delta y$)

$$H_0 = -\frac{1}{\Delta y^2} \begin{pmatrix} -4 & 1 & 0 & \dots & \dots & 0 \\ 1 & -4 & 1 & 0 & \dots & \vdots \\ 0 & 1 & -4 & 1 & \ddots & \vdots \\ \vdots & \ddots & \ddots & \ddots & \ddots & \vdots \\ \vdots & \dots & 0 & 1 & -4 & 1 \\ 0 & \dots & \dots & 0 & 1 & -4 \end{pmatrix} , \quad (3.9)$$

$$H_I = -\frac{1}{\Delta x^2} \begin{pmatrix} 1 & 0 & \dots & \dots & \dots & 0 \\ 0 & 1 & 0 & \dots & \dots & \vdots \\ \vdots & 0 & 1 & 0 & \dots & \vdots \\ \vdots & \dots & \ddots & \ddots & \ddots & \vdots \\ \vdots & \dots & \dots & 0 & 1 & 0 \\ 0 & \dots & \dots & \dots & 0 & 1 \end{pmatrix} . \quad (3.10)$$

A static bulk disorder potential $V(x, y)$ described by a corresponding vector V_{ij} yielding the potential value at each grid point (x_i, y_j) will appear on the diagonal of $H_0^{(i)}$. The implementation of more complicated Hamiltonians works in the same way, e.g. two-dimensional topological insulators as described in appendix A.

3.2. Band structures

Consider an infinitely long waveguide of width W as sketched in Fig. 3.2. In a discretized scheme, this waveguide can be seen as a periodic sequence of equal slices each of which consists of n_y points in y -direction with $W = (n_y + 1)\Delta y$. One such slice is described by the Hamiltonian subblock H_0 . The connection between

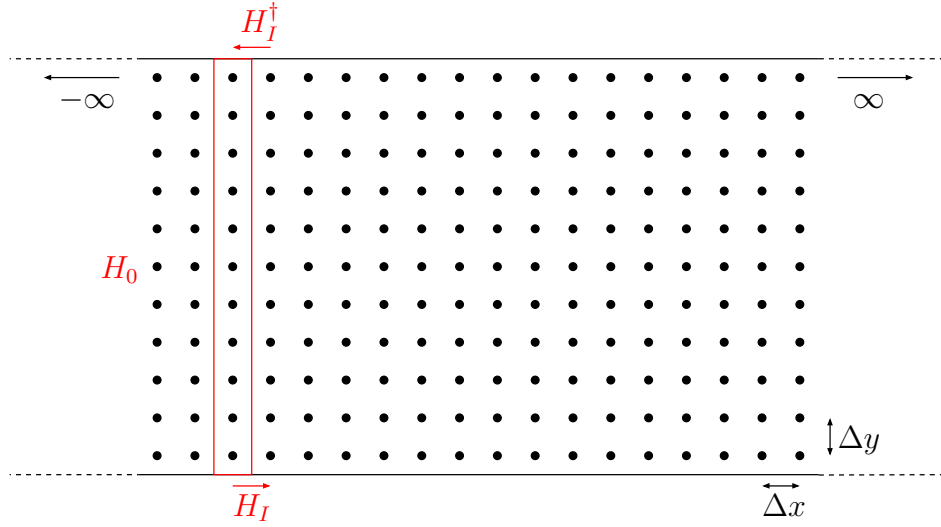


Figure 3.2.: Sketch of a discretized waveguide that is infinitely long and features, depending on the energy E , a certain number of open lead modes $\langle y | \chi_a \rangle$. A slice i is described by the Hamiltonian subblock H_0 . The coupling between adjacent slices is described by the matrices H_I and H_I^\dagger . The band structure and the lead modes can be calculated numerically from these matrices.

adjacent slices is described by the matrices H_I and H_I^\dagger . As the system can be viewed as periodic in x -direction we can use Bloch's theorem to decompose the real-space representation of the wave functions, $|\psi(x, y)\rangle$ into an x - and a y -dependent part:

$$\langle x, y | \psi_n \rangle = e^{ik_x n x} \langle y | \chi_n \rangle . \quad (3.11)$$

As the waveguide is infinitely extended in the longitudinal direction, the x -dependent part of the solution is just a plane wave with wave number k_x that can take continuous values between $-\pi/\Delta x$ and $\pi/\Delta x$. In transverse y -direction the waveguide

is finite leading to discrete solutions $|\chi_n\rangle$ to which a wave number $k_{y,n} = k_y$ can be assigned. The wave functions $\langle x, y | \psi_n \rangle$ from Eq. (3.11) are solutions of the Schrödinger equation

$$\hat{H}|\psi_n\rangle = E_n(k_x)|\psi_n\rangle . \quad (3.12)$$

The eigenvalues $E_n(k_x)$ are called the band structure of the waveguide.

In our discrete scheme, the ansatz Eq. (3.11) turns into

$$\langle r | \psi_n \rangle \rightarrow \begin{pmatrix} \vdots \\ e^{-ik_{x,n}\Delta x} \vec{\chi}_n \\ \vec{\chi}_n \\ e^{ik\Delta x} \vec{\chi}_n \\ \vdots \end{pmatrix} , \quad (3.13)$$

where we only show the components of the three slices around the position $x = 0$ of the (in theory) infinitely long vector. The Schrödinger equation from Eq. (3.12) in this discretized structure reads according to Eq. (3.3)

$$\left(e^{-ik_x\Delta x} H_I^\dagger + H_0 + e^{ik_x\Delta x} H_I \right) \vec{\chi}_n = E_n(k_x) \vec{\chi}_n . \quad (3.14)$$

Numerically, the band structure $E_n(k_x)$ can be easily determined by fixing k_x and solving the above eigenvalue problem. For the solution of a scattering problem the numerics prove a little more complicated. In such a computation the given quantity usually is the scattering energy E for which all possible solutions $\vec{\chi}_n$ have to be found. These solutions are usually referred to as lead modes and finding them requires solving Eq. (3.14) for fixed E instead of k_x . As in this case we are confronted with a quadratic eigenvalue problem, the solution requires doubling the dimension of the problem. This procedure leads to the equation

$$\begin{pmatrix} (H_I^\dagger)^{-1}(E - H_0) & -(H_I^\dagger)^{-1}H_I \\ \mathbf{1} & 0 \end{pmatrix} \begin{pmatrix} \vec{\zeta}_n \\ \vec{\chi}_n \end{pmatrix} = \beta_n \begin{pmatrix} \vec{\zeta}_n \\ \vec{\chi}_n \end{pmatrix} \quad (3.15)$$

with the definitions

$$\begin{aligned} \beta_n &= e^{-ik_{n,x}\Delta x}, \\ \vec{\zeta}_n &= \beta_n \vec{\chi}_n. \end{aligned}$$

The group velocity of a lead mode a that will be needed for the flux normalization of transmission and reflection amplitudes (see section 3.3) is given by [16, 151, 152]

$$v_n = i\Delta x \langle \chi_n | \left(H_I \beta_n^{-1} - H_I^\dagger \beta_n \right) | \chi_n \rangle . \quad (3.16)$$

More details on all the above relations and rigorous derivations can be found in Refs. [16] and [152].

3.3. Green's functions and the Dyson equation

In most of our simulations we are considering a scattering problem in two dimensions including one incoming and one outgoing lead. The common way of solving this numerically is by the use of retarded Green's functions [12, 14, 15, 153, 154]. This object, labelled here by $\hat{\mathcal{G}}$, is defined by the equation

$$(E - \hat{H})\hat{\mathcal{G}}(\vec{r}, \vec{r}', E) = \delta(\vec{r} - \vec{r}'). \quad (3.17)$$

It is the so called propagator since it connects the wave function $\psi(\vec{r})$ at some point \vec{r} to all the other points \vec{r}' in the system by

$$\psi(\vec{r}) = \int d^3r' \hat{\mathcal{G}}(\vec{r}, \vec{r}', E) \psi(\vec{r}'). \quad (3.18)$$

In the discrete two-dimensional geometry we consider in our numerics, the Green's function becomes a matrix of the dimension of the Hamiltonian H . The delta function in the definition Eq. (3.17) is in discrete systems represented by a unit matrix. Consequently the discrete Green's function (matrix) \mathcal{G} corresponds to the inverse of the Hamilton matrix H from Eq. (3.3):

$$\mathcal{G} = (E - H)^{-1}. \quad (3.19)$$

Although this expression looks very compact, it is not easy to calculate this object numerically since it requires the inversion of a matrix with $(n_x \cdot n_y)^2$ elements. However, for the majority of physical problems it is sufficient to compute parts of the Green's function matrix. In our scheme we are usually dealing with $n_y \times n_y$

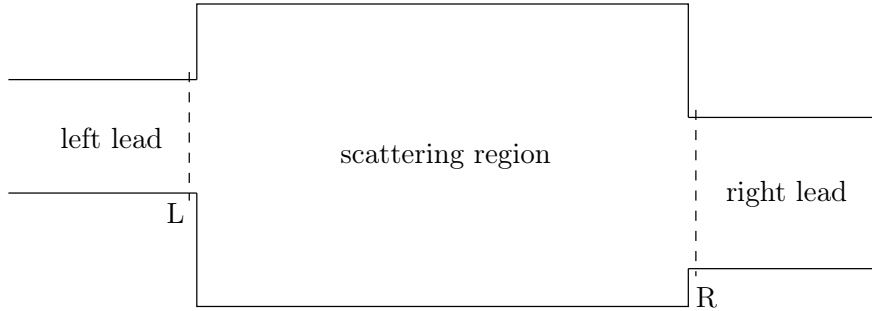


Figure 3.3.: Sketch of a scattering problem consisting of a scattering region and two attached semi-infinite leads to the left and to the right. The first and last slice of the left and the right lead are labelled by L and R, respectively.

blocks \mathcal{G}_{ij} denoting those parts of the matrix that connect slice j with slice i . Those

subblocks that connect the first and the last slice of the geometry are of special interest in transport. These 4 blocks are referred to as the surface Green's functions \mathcal{G}_{LL} , \mathcal{G}_{LR} , \mathcal{G}_{RL} and \mathcal{G}_{RR} , where “L” stands for the last slice of the left lead and “R” for the first slice of the right lead (with both leads attached to the scattering region, see also Fig. 3.3). The set of the above four surface GFs will in the following be denoted by $\{\mathcal{G}\}$. All the information about transport and the scattering matrix is contained in these objects. The transmission and reflection amplitudes (the elements of the scattering matrix), t_{ab} and r_{ab} respectively, can be calculated by the use of the surface GFs $\{\mathcal{G}\}$ using the following relations [16]:

$$t_{ab} = \sqrt{\frac{v_a^R}{v_b^L}} \langle \chi_a^R | \mathcal{G}_{RL} V^L | \chi_b^L \rangle , \quad (3.20)$$

$$r_{ab} = \sqrt{\frac{-v_a^L}{v_b^L}} \langle \chi_a^L | \mathcal{G}_{LL} V^L - \mathbb{1} | \chi_b^L \rangle , \quad (3.21)$$

$$t'_{ab} = \sqrt{\frac{v_a^L}{v_b^R}} \langle \chi_a^L | \mathcal{G}_{LR} V^R | \chi_b^R \rangle , \quad (3.22)$$

$$r'_{ab} = \sqrt{\frac{-v_a^R}{v_b^R}} \langle \chi_a^R | \mathcal{G}_{RR} V^R - \mathbb{1} | \chi_b^R \rangle . \quad (3.23)$$

The unprimed quantities t_{ab} and r_{ab} describe transmission and reflection of a lead mode b injected in the left lead to another lead mode a . The primed quantities t'_{ab} and r'_{ab} describe injection in the right lead. The lead modes have been previously calculated by the use of Eq. (3.15) and are here denoted by $|\chi_a^{R/L}\rangle$. The lower index represents the corresponding right-moving mode while a bar over this mode index indicates the left-moving mode. Analogously v_a and $v_{\bar{a}}$ denote the group velocities of the a^{th} right-moving and the a^{th} left-moving lead modes, respectively. These velocities are evaluated by the use of Eq. (3.16) and their occurrence as prefactors in Eqs. (3.20)-(3.23) accounts for the flux normalization of incoming and outgoing modes. The matrix V is a projection operator that in essence resembles the transformation between lead mode and space basis [16, 151, 152]. It can be easily calculated from the lead solutions Eq. (3.15) according to the appendix of Ref. [16]. The upper indices “L” or “R” in the lead modes, the group velocities and projection operators V distinguish between the left and the right lead, respectively.

While these lead modes $\tilde{\chi}_n$ and Bloch eigenvalues β_n are numerically fairly easy to calculate [see Eq. (3.15)], the challenging task is the computation of the set of surface Green's functions $\{\mathcal{G}\} = \{\mathcal{G}_{LL}, \mathcal{G}_{RL}, \mathcal{G}_{LR}, \mathcal{G}_{RR}\}$. Mind that these GFs labelled by the caligraphic \mathcal{G} include the attachments of the two semi-infinite leads. These connections to the waveguides can also be done numerically very efficiently since the surface GFs of the leads themselves are again given by the lead solutions $\tilde{\chi}_n$

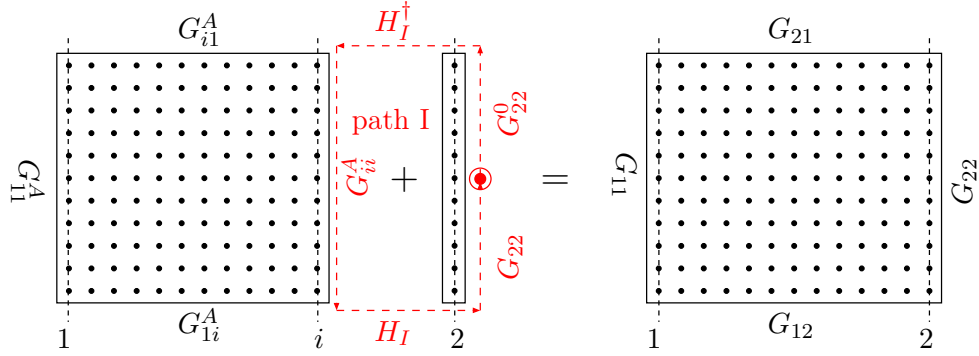


Figure 3.4.: Sketch of the numerical attachment of a single slice (labelled 2) to a module A of which the surface GFs $\{G^A\}$ are known. The interaction of slice 2 is mediated by the block matrices H_I and H_I^\dagger . As an example, the “path” that can be used to find Eq. 3.27 is shown in red and labelled “path I”. The contributions of each path segment are also shown in red. This illustrates how Dyson equations based on the Hamiltonian block matrices H_0 , H_I and H_I^\dagger can be established.

and Bloch eigenvalues β_n calculated from Eq. (3.15). The details of this procedure can, e.g., be found in Ref. [16].

Fortunately, there is a very useful tool which allows for an iterative calculation of the surface GFs alone. This tool is the so-called Dyson equation which represents a relation between the Green's function \hat{G}_0 of an unperturbed system and the Green's function \hat{G} of the system including a perturbation \hat{V} :

$$\hat{G} = \hat{G}_0 + \hat{G}_0 \hat{V} \hat{G} . \quad (3.24)$$

While this self-consistent operator equation is analytically not easy to solve, it numerically turns into a self-consistent matrix equation that can be solved by matrix multiplications and inversions. A possible approach used in the recursive Green's function method is to iteratively build up the surface GFs of the whole geometry slice by slice. In the following we will provide an idea of how this works in detail. To start the iteration, one considers only the first slice (labelled 1) of the geometry for which the total GF is by definition given by

$$G^{(1)} = (E - H_0^{(1)})^{-1} ,$$

with E the scattering energy. For this trivial module, all four surface GFs are equal to $G^{(1)}$. In every subsequent step $i + 1$, one already knows the surface GFs $\{G^A\}$ of the module A reaching from slice 1 to slice i as depicted in Fig. 3.4. To this structure we want to add the next slice labelled by 2. The matrix of the full GF G that we need for the use of the Dyson equation (3.24) is viewed as matrix consisting

of blocks of dimension $n_y \times n_y$ (where we for simplicity assume that the number n_y of points in y -direction is equal for all slices):

$$G = \begin{pmatrix} G_{11} & \cdots & G_{12} \\ \vdots & \ddots & \vdots \\ G_{21} & \cdots & G_{22} \end{pmatrix} . \quad (3.25)$$

In this notation we only labelled the blocks representing the surface GFs of the structure that we are finally interested in. The GF matrix G_0 of the unconnected structure where slice 2 is not yet attached reads

$$G_0 = \begin{pmatrix} G_{11}^A & \cdots & G_{1i}^A & 0 \\ \vdots & \ddots & \vdots & \vdots \\ G_{i1}^A & \cdots & G_{ii}^A & 0 \\ 0 & \cdots & 0 & G_{22}^0 \end{pmatrix} .$$

The blocks labelled by A are the surface GFs of module A known from the previous iteration and G_{22}^0 is the GF of the single slice 2 defined by

$$G_{22}^0 = (E\mathbf{1} - H_0^{(2)})^{-1} .$$

As a perturbation V we treat the connection between the last slice of A and slice 2. This connection is numerically represented by the subblocks H_I and H_I^\dagger of the Hamiltonian H [see Eq. (3.3)]. Thus V reads

$$V = \begin{pmatrix} 0 & \cdots & 0 & 0 \\ \vdots & \ddots & \vdots & \vdots \\ 0 & \cdots & 0 & H_I \\ 0 & \cdots & H_I^\dagger & 0 \end{pmatrix} .$$

These ingredients can be used for the discrete version of the Dyson equation

$$G = G_0 + G_0 V G . \quad (3.26)$$

Instead of always considering the full multiplications of these matrices it is convenient that the resulting equations for the subblocks (surface GFs) can be extracted in a diagrammatic way. As an example we are considering the calculation of the surface GF G_{22} . The corresponding Dyson equation can be found by following the “path” (which is labelled “path I ” and shown by red arrows in Fig. 3.4). This diagrammatic way of finding Dyson equations works as follows: As in this case we want to find an expression for the full GF G_{22} of the structure in which slice 2 is already attached, we need to start with the unperturbed G_{22} before slices 2 is

glued on, which is in this case the GF of the single slice 2, G_{22}^0 . In the following, we have to add the “path” across the site of fracture starting at the beginning slice (first index of the GF under consideration, in this case slice 2, marked by the red circle in Fig. 3.4) and follow the red arrows while writing down the corresponding contributions (shown next to the corresponding arrow in Fig. 3.4). The procedure ends, when the final slice (in this case slice 2) is reached and all possible paths (in this case there is only one) have been included. In the current example one finds for G_{22} :

$$G_{22} = G_{22}^0 + G_{22}^0 H_I^\dagger G_{ii}^A H_I G_{22} \quad . \quad (3.27)$$

Whenever a Dyson equation is used throughout this work, we endeavored to provide the corresponding sketch and all the contributions shown by similar arrows as in Fig. 3.4.

Solving this matrix Eq. (3.27) yields a compact expression for G_{22} that only requires the inversion of a $n_y \times n_y$ matrix and some multiplications of equally sized matrices:

$$G_{22} = (\mathbb{1}E - H_0^{(2)} - H_I^\dagger G_{ii}^A H_I)^{-1} \quad . \quad (3.28)$$

The remaining surface GFs and their respective Dyson equations are then obtained analogously and can be easily evaluated by multiplications of known matrices only:

$$G_{12} = G_{1i}^A H_I G_{22} \quad , \quad (3.29)$$

$$G_{21} = G_{22} H_I^\dagger G_{i1}^A \quad , \quad (3.30)$$

$$G_{11} = G_{11}^A + G_{1i}^A H_I G_{21} \quad . \quad (3.31)$$

In a very similar way also two modules A and B of which the surface GFs G^A and G^B are known can be glued together. We spare the details of these calculations for easier readability [151]. This modular treatment that the Dyson equation allows for is the basis of the modular recursive Green's function method (MRGF) [12, 13, 155].

3.4. Improving the modular recursive Green's function method

In the following we want to introduce an improved algorithm that we implemented in order to speed up the calculation of the surface GFs which by far takes most of the time in the numerical solution of our scattering problems. The crucial improvement in this algorithm is the fact that the whole parallelization of the code is done purely by hand while before the parallelization of the code was relying on numerical parallel inversion routines included from MUMPS [156, 157].

This new algorithm can be run on $n = 2^m$ cores (threads) with $m \in \mathbb{N}$ and relies on the automatic split-up of our scattering region into n equally sized submodules.

In the following we will explain the algorithm by using an example of a scattering region of which the desired set of surface GFs is labelled $\{G\}$. This example is also illustrated in Fig. 3.5.

In a first step, the scattering region is split into n equally sized modules that are in our example Fig. 3.5 labelled by Latin letters from A to H . Each such module is assigned to a core, e.g., core 0 is responsible for module A , core 1 for module B and so on. As a starting point, each core i calculates the surface GFs $\{G^X\}$ of its module X exclusively on its own. This is done by starting with the GFs of the first slice of the module and adding each slice iteratively using the Dyson equations (3.28)-(3.31). This procedure has been described towards the end of the previous section 3.3. We then distribute the surface GFs of these modules in such a way that the whole geometry can be glued together in the end by Dyson equations.

However, we still want to do this in an optimally parallel way. For this purpose the modules' surface GFs are distributed in such a way, that in the next step we can glue together the modules pairwise ending up with surface GFs $\{G^{AB}\}, \{G^{CD}\}, \{G^{EF}\}, \dots$. The communication process is indicated in Fig. 3.5 by the use of arrows. In our example we can see that in this case now cores 0, 3, 4 and 7 calculate these module pairs. Essentially from here on out this procedure is repeated: The surface GFs of the paired modules are distributed such that cores 0 and 7 can now calculate the surface GFs of 4 such modules, i.e. $\{G^{A \rightarrow D}\}$ and $\{G^{E \rightarrow H}\}$. Finally, core 7 provides his surface GFs for core 0 which completes the final step ending up with the surface GFs $\{G_{A \rightarrow H}\} = \{G\}$ of all the modules assembled together.

The big advantage of this algorithm, which we will call parallel Dyson algorithm (PDA) in the following, is, that all the parallelization is done by hand in an optimal way fitting the problem. The previously used algorithm relied on the parallelization of matrix inversion and factorization routines that are very efficient in principle, but less efficient for this particular problem of the iterative assembly of the surface GFs of a scattering region. This fact is illustrated convincingly in Fig. 3.6 where we compare the computation times of the old algorithm and the new PDA for quadratic scattering regions as a function of $N = n_y = n_x$.

We clearly find that our PDA is faster for all considered system sizes N . For the largest considered geometry the PDA is almost 6 times faster than the old algorithm. Additionally, we can estimate the PDA's runtime in a very precise way depending on n_x , n_y and the number of used cores c . We expect that the total computation time t consists of 2 main contributions: First, there is the time that is needed for every core to calculate the surface GFs of its own module. As this process requires inversion and multiplication of $n_y \times n_y$ -matrices, we expect it to scale with n_y^3 . The length of the module of each core is n_x/c , which is why we expect the total time t_1 for this first step to be

$$t_1 = a \frac{n_x}{c} n_y^3 .$$

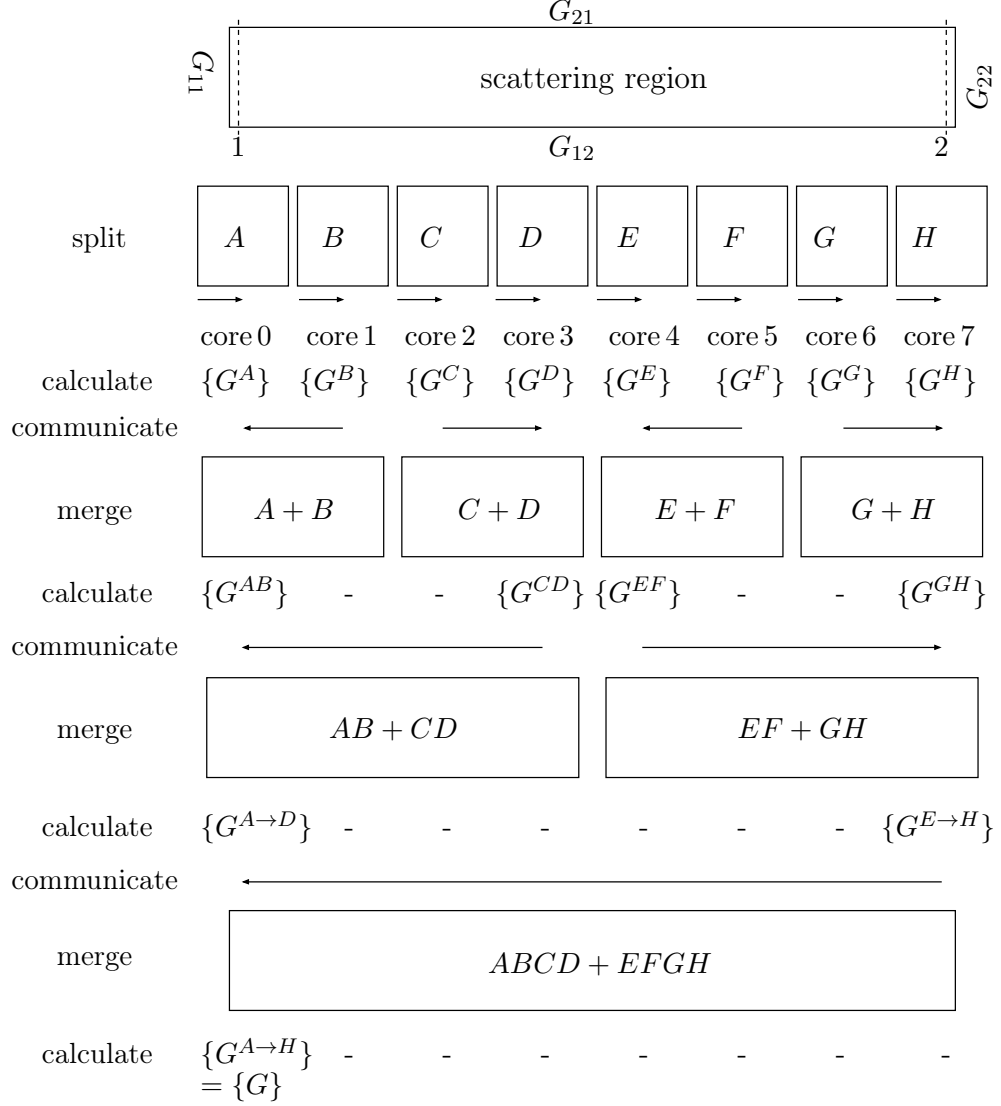


Figure 3.5.: Illustration of our improved recursive GF algorithm for the case of a parallel calculation on 8 cores. The goal is the calculation of the scattering region's surface GFs $\{G\} = \{G_{11}, G_{12}, G_{21}, G_{22}\}$, where 1 and 2 entitle the first and the last slice of the geometry, respectively. For this purpose, the geometry is split up in a first step such that each core calculates the surface GFs of an equally sized module labelled from A to H. This is done by putting together the module slice-by-slice in a recursive way. Afterwards, the necessary GFs of each module are sent to those cores that in the next step merge these modules together. This communication process is indicated by black arrows. During the further procedure, the surface GFs of the unified modules are calculated and communicated again in such a way that the algorithm ends with the first (master) core calculating the desired surface GFs $\{G\}$ in the last step. The procedure can be easily generalized to $n = 2^m$ cores where always m communication steps are required to build up the whole geometry.

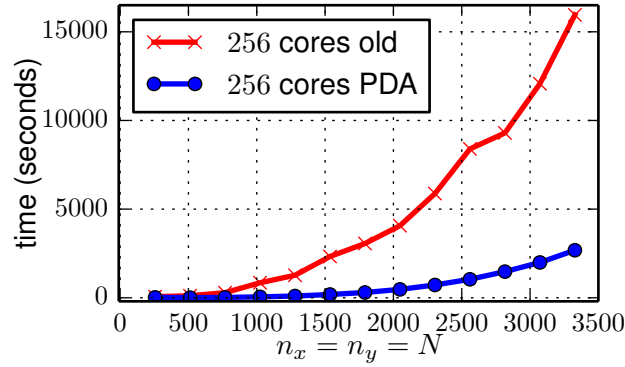


Figure 3.6.: Benchmark of the PDA (blue curve) in comparison to the old algorithm (red curve). We are calculating the surface GF of a quadratic structures of different size $N = n_x = n_y$. The new PDA algorithm shows significantly faster calculation than the old one. These benchmarks were performed on the Vienna Scientific cluster 3 (VSC-3).

The parameter a is hardware-specific and describes the time that appending a single slice to one core's own module takes.

The second contribution to t comes from the parallel assembly of the surface GFs of the whole geometry including data exchange. This procedure consists of $m = \log_2 c = \ln c / \ln 2$ steps each of which requires time for the assembly of 2 modules which we again expect to scale with n_y^3 . Mind, however, that this contribution t_2 is independent of n_x and we can write

$$t_2 = b \frac{\ln c}{\ln 2} n_y^3 ,$$

where again a free hardware-dependent parameter b is introduced.

The data exchange between the cores will scale with n_y^2 and can therefore be neglected for large n_y . Overall we get a total computation time that reads

$$t = t_1 + t_2 = a \frac{n_x}{c} n_y^3 + b \frac{\ln c}{\ln 2} n_y^3 . \quad (3.32)$$

For a quadratic geometry with $n_y = n_x = N$ this transforms to

$$t = a \frac{N^4}{c} + b \frac{\ln c}{\ln 2} N^3 . \quad (3.33)$$

In Fig. 3.7 we check this law on 2 different clusters, the Vienna Scientific Cluster 1 (VSC-1) and the Vienna Scientific Cluster 3 (VSC-3). We measured the computation time of the surface GFs of a quadratic geometry for different core numbers

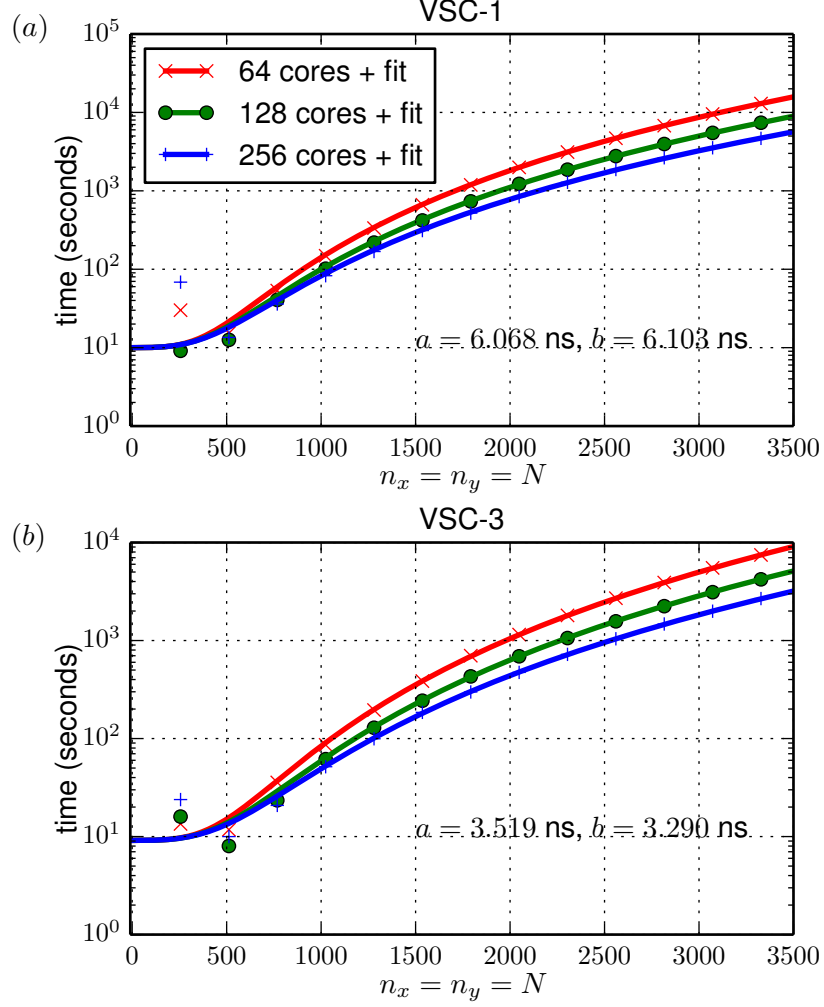


Figure 3.7.: Benchmarks of the PDA algorithm on (a) VSC-1 and (b) VSC-3. Quadratic geometries of size $N = n_x = n_y$ are evaluated on 64 (red crosses), 128 (green dots) and 256 (blue pluses) cores. The solid lines show a fit of the expected total computation time from Eq. (3.33) with fit parameters a and b . This fit is done simultaneously for all 3 curves in each panel. The resulting values for a and b are cluster-specific and are also shown in the corresponding panel. We find that the PDA obeys very nicely the expected time-scaling law Eq. (3.33).

c on both clusters. The measured times are indicated by the markers, while the fit according to Eq. (3.33) is shown by solid lines. Mind that on each cluster the fit is done simultaneously for all three curves with different core number. The inaccuracy of the fit for small system sizes can be entirely attributed to the fact that we neglected initialization times or quadratic contributions in n_y in our time law Eq. (3.33). The very good quality of the fit at large system sizes N shows that the computation time is in this case very well described by Eq. (3.33) and also that the code nicely scales in the expected way with the number of used cores.

These benchmarks show that our new algorithm is a major improvement regarding computation time and Eq. (3.33) provides us with a useful tool in order to estimate the runtime of a calculation. However, there is a small inefficiency that is left in the PDA: As also obvious from Fig. 3.5 during the $m = \log_2 c$ steps used for the parallel assembly of the surface GFs there are a number of cores inactive. More precisely, in step i there are only 2^{m-i} cores used in the computations. This inefficiency peaks at the very end of the algorithm, when only the master core assembles the whole surface GFs while the other $c - 1$ cores are inactive. It is possible to share the assembly of 2 modules between two cores which approximately halves the time needed for the assembly part of the algorithm. Actually this improvement is already included in the benchmarks from Figs. 3.6 and 3.7 but was for simplicity not included in the algorithm's scheme (see Fig. 3.5) and its description.

We chose to also explain one further improvement that can be implemented. As obvious from the Dyson equations (3.27)-(3.31) a lot of the matrix multiplications that have to be performed involve either H_I or H_I^\dagger . Usually, these matrices are composed of only few non-zero elements as, e.g., obvious in the case of free electrons in Eq. (3.10). Hence most of these multiplications can be executed a lot faster when sparse matrices and multiplications are used. Indeed, the implementation of such provides another significant boost for the computation time of our algorithm (Fig. 3.8). We find that the parameters a and b in our time law Eq. (3.33) are significantly lowered resulting in a tremendous speed boost by another factor of almost 2.

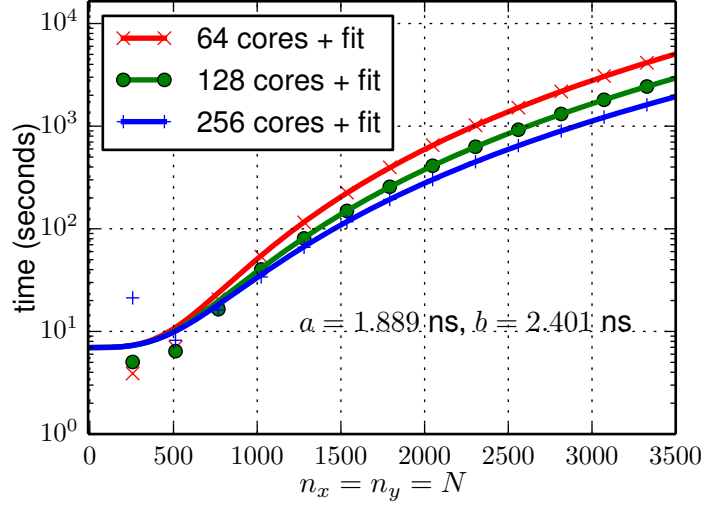


Figure 3.8.: Benchmarks of the PDA algorithm using sparse matrix multiplications executed on VSC-3. Quadratic geometries of size $N = n_x = n_y$ are evaluated on 64 (red crosses), 128 (green dots) and 256 (blue plusses) cores. The solid lines show a fit of the expected total computation time from Eq. (3.33) with fit parameters a and b . This fit is done simultaneously for all 3 curves in each panel. The resulting values for a and b are cluster-specific and are also shown in the corresponding panel. We find that sparse matrix multiplications significantly reduce the time consumed by the PDA.

3.5. The parallel permutation algorithm

The PDA algorithm is the fastest way to calculate the scattering matrix S since for this information only the final surface GFs of the entire geometry are required. As discussed before, there still is some unused computational power within the algorithm. When the assembly of the modules progresses further, not all cores can be used at all times.

However, there are other computations where additional information has to be calculated. For this purpose we will in the following develop an algorithm that fills the “white spaces” in the PDA and uses those to calculate data that will be very useful to improve the calculation of scattering wave functions (see section 3.6) or allows for the parallel calculation of the local density of states (see section 3.7). We will call this algorithm parallel permutation algorithm (PPA). The meaning of this name will become clear shortly.

As illustrated in Fig. 3.9 the algorithm starts out in the same way as the PDA: Each of the n cores is assigned an equally-sized part X of the scattering region of

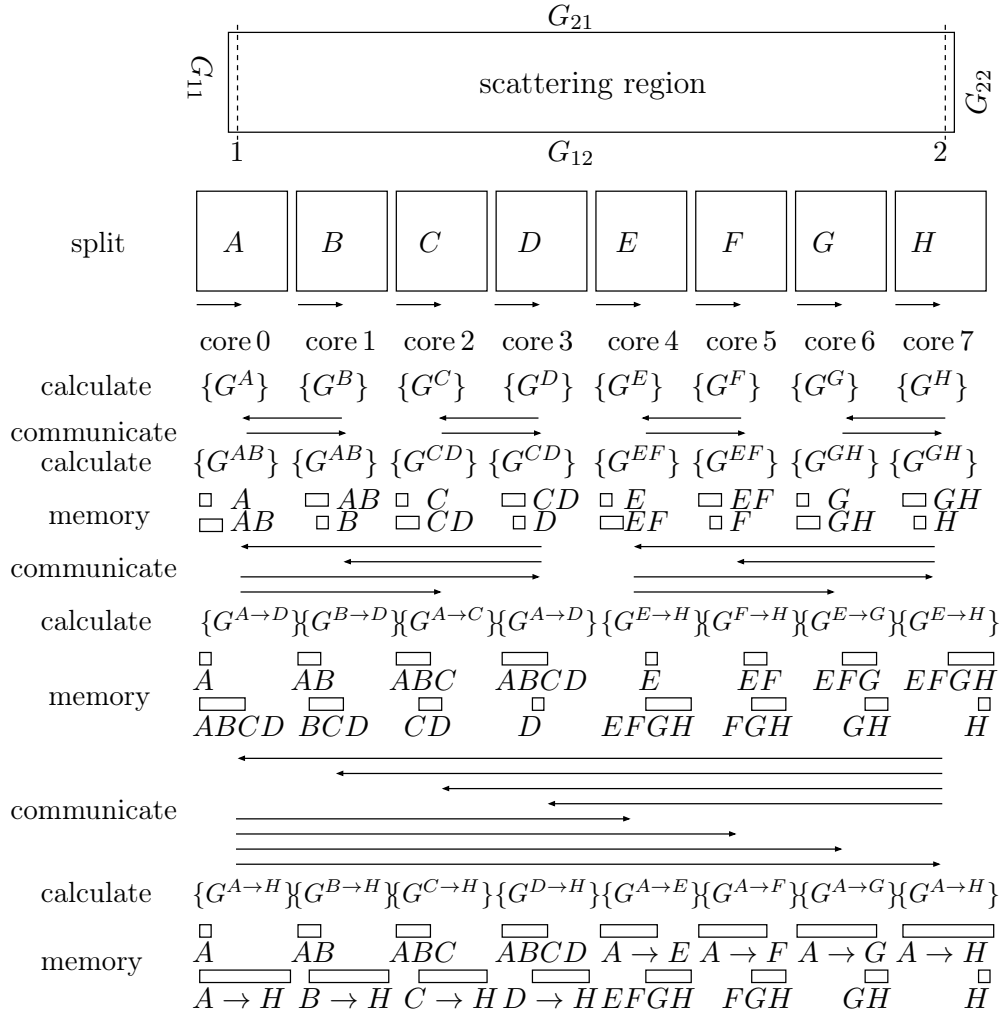


Figure 3.9.: Illustration of our parallel permutation algorithm (PPA) for the exemplary case of a calculation on $8 = 2^3$ cores. The geometry is again split into 8 parts labelled with the letters A to H . Each such module is assigned to a specific core, that calculates the surface GFs of this module in the first step. This is done by putting together the module slice-by-slice in a recursive way. In the following these surface GFs are distributed such that each core connects 2 modules in each step. This communication process is indicated by black arrows. The algorithm is divided into communication steps each of which consists of a sequence of communicate-calculate. In the lines labelled “memory” we sketch the parts of the structure of which the surface GFs are stored on each core. After the last step each core has calculated the surface GFs of the rectangles from the left end of the whole structure to the right end of its module and from the right end of the whole to the left end of its module. More details of the algorithm are provided in the text. The procedure can be easily generalized to $n = 2^m$ cores where always m communication steps are required to build up all these permutations of surface GFs.

which it calculates the surface GFs $\{G^X\}$ iteratively. Subsequently, just like in the PDA, $m = \log_2 n$ communication-calculation steps are employed. A fundamental difference with regard to the PDA is that now each core has to memorize 2 sets of surface GFs instead of 1. These 2 different sets we will call “left” and “right” surface GFs. In the initialization step where each core builds up its own module iteratively, the surface GFs of this module is stored into both, the “left” and the “right”, memory slots. In each following step i the cores are first divided into 2^{m-i} subgroups each of which consists of 2^i cores to set up correct communication. These subgroups are alternately called “lefties” and “righties”. The master core of the subgroups is for the lefties always the core with the lowest ID, for the righties always the core with the highest ID within the subgroup.

Communication at the beginning of each step works as follows: The master core of each leftie-subgroup provides his left set of surface GFs to all the members of the next rightie-subgroup. Likewise, the master core of each rightie-subgroup provides his right set of surface GFs to all the members of the previous leftie-subgroup. In the following, each leftie attaches the surface GFs that it just received to its right set of surface GFs and replaces those with the result. The righties proceed analogously and attach the surface GFs they have just received to their left set of surface GFs and replace those with the new left set of surface GFs. Then step i is completed and the process is repeated.

As an example, we illustrated the algorithm for a calculation on 8 cores in Fig. 3.9. The algorithm starts with preparation during which each core carries out the part of the structure assigned to it. During this step ($i = 0$, starting with the first “communicate” in Fig. 3.9) each core is a subgroup of its own. The cores 0,2,4 and 6 represent the leftie-subgroups and trivially are also the master cores of their respective subgroup. The cores 1, 3, 5 and 7 are the only members of all the rightie-subgroups and are thus also the rightie master cores. Hence, each leftie master core sends its left set of surface GFs (in this case the surface GFs of the own module) to all the righties in the next rightie-subgroup. This means core 0 sends $\{G^A\}$ to core 1, core 2 sends $\{G^C\}$ to core 3 and so on. The righties proceed analogously and send the surface GF of their own module to all the lefties in the previous subgroup, i.e. core 1 sends $\{G^B\}$ to core 0, core 3 sends $\{G^D\}$ to core 2 etc. The lefties and righties attach the received surface GFs to those in their right and left memory slot, respectively. This is illustrated in Fig. 3.9 where the state of the sets of surface GFs of each core is always sketched in the line labeled by “memory”. As shown there, core 0 now has the surface GFs of its own module A and the pair of modules A plus B , core 1 contains B and also A plus B , core 2 knows C and C plus D and so on.

With this, step 0 is complete and step 1 is entered. Now, each subgroup consists of 2 cores. This means now that core 0 and 1 are a leftie-subgroup with master core 0, core 2 and 3 are a rightie-subgroup with master core 3 and so on. Again, the information is sent in the described way: Core 0 as a left master sends his left surface

GFs (that is $\{G^{AB}\}$) to all the next righties, i.e. core 2 and 3. Core 3 as a right master core sends $\{G^{CD}\}$ to the previous leftie-subgroup, i.e. core 0 and 1. The other master cores 4 and 7 do the analogous. Again, the received modules are glued together and the procedure starts over. After the m^{th} and last step the situation is the following: Each core contains the surface GFs of its own module connect to all the other modules to the left (left surface GFs memory slot) and those of its own module connected to the rest of the modules to the right (right surface GFs memory slot). As a result, the first and the last core have calculated the surface GFs of the entire structure contained in their right and left slot, respectively. The other permutations of modules stored on the other cores can be used for other applications as will become clear in the following two sections.

We also need to mention, that while above we were talking about the surface GFs $\{G\}$ of the whole structure, a scattering problem actually requires knowledge about the surface GFs $\{\mathcal{G}\}$ of the structure including the leads. This can, however, be easily achieved by letting the first and the last core attach the leads [of which the surface GFs can be calculated from the lead solution of Eq. (3.15)] by treating those as an additional slice on the left or on the right during the assembly of the first and last module in the first step of the PPA.

In comparison to the PDA, the PPA is more efficient in the sense that no core is unemployed at any time. Also, in each step the actual calculation effort is the same as in the PDA, namely the connection of 2 modules only. However, the effort for the assembly of all the modules is a lot larger which is why we expect the PPA to be still slower than the PDA but scale equally well with the number of used cores and the system size. This additional effort can, in fact, be compensated for the applications that we will consider later since the additional surface GFs can be reused and their calculation within the PPA has been cheap since only a slight overhead is produced.

To verify the above statement, we show a benchmark of a quadratic structures of sizes $N = n_x = n_y$ for both algorithms in Fig. 3.10(a) where we again fitted the measured times using Eq. (3.33). This data shows that indeed the PPA produces a slight overhead (compare red and blue curves) but also that it still obeys the time laws from Eqs. (3.32) and (3.33). This overhead is about 12 % and 21 % at the largest investigated system size of $N = 1920$ on 64 and 128 cores, respectively. As expected, the overhead increases with increasing core number.

We observe however, that the overhead percentually decreases with increasing N as, e.g., at $N = 384$ the overheads are almost 51 and 46 % on 64 and 128 cores, respectively. Additionally, since the additional effort should not depend on n_x , we also benchmarked our algorithms as a function of n_x with n_y kept constant. Our benchmarks [see Fig. 3.10(b)] clarify on the one hand that indeed both algorithms scale almost linearly with n_x [see Eq. (3.32)] and on the other hand that in such elongated rectangular structures the overhead is indeed independent of n_y . The

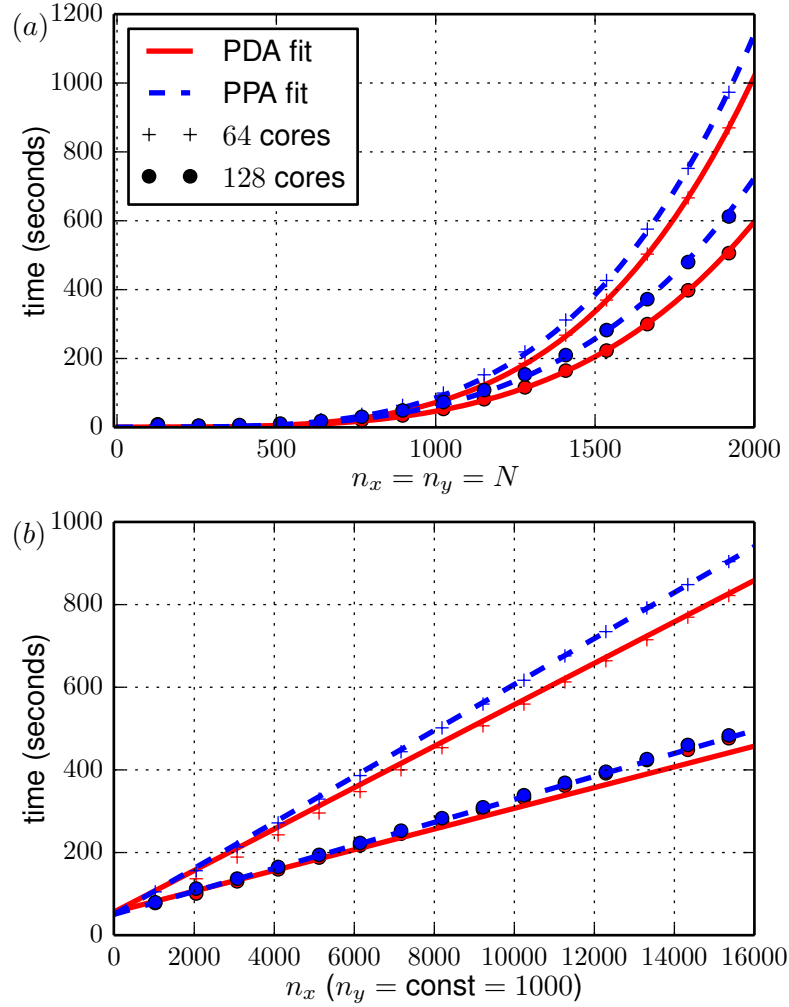


Figure 3.10.: Benchmarks of the PDA and the PPA algorithm for (a) quadratic systems as a function of system size $N = n_x = n_y$ and (b) rectangular geometries with fixed $n_y = 1000$ as a function of n_x . Plusses and dots show the measured calculation times on 64 and 128 cores, respectively. The red data is for the PDA while blue represents the PPA. Solid and dashed lines fit the calculation times using Eq. (3.33) in (a) and Eq. (3.32) in (b). We find that the PPA also nicely obeys the expected time-scaling laws.

latter statement is proven by the fact that in these benchmarks the additional time-consumption percentually stays almost constant at 10 and around 2 % on 64 and 128 cores, respectively. We find that although the PPA represents a computational time investment, it scales as well as the PDA and produces an overhead that is fairly small and does not diverge at least at accessible system sizes. In the next sections we will introduce some applications of the PPA where this overhead is compensated by the additional information the PPA calculates very efficiently.

3.6. Calculating scattering wave functions faster

While the calculation of the scattering matrix S only requires the surface GFs $\{\mathcal{G}\} = \{\mathcal{G}_{LL}, \mathcal{G}_{LR}, \mathcal{G}_{RL}, \mathcal{G}_{RR}\}$ according to Eqs. (3.20)-(3.23), other quantities depend on larger parts of the whole GF matrix. One of these are scattering wave functions (see, e.g., Figs. 2.4 or 2.8). The PPA allows explicit parallelization of this task in a much more efficient way than previously. We will first explain briefly how the calculation of a scattering wave function has been performed so far (see Ref. [16] for details). For this purpose we consider a scattering region labelled (i) that is attached to two semi-infinite leads which is the standard setup that is considered in most of our calculations and is sketched in Fig. 3.11. One injects from the left a superposition $|P\rangle$ of lead modes $|\chi_a\rangle$ characterized by some complex coefficients c_a . From now on, we denote these states by \vec{P} and $\vec{\chi}_a$ to emphasize their numerical representation as vectors of size n_g . The injected flux-normalized state \vec{P} is then given by

$$\vec{P} = V \sum_a \frac{c_a}{\sqrt{v_a}} \vec{\chi}_a \quad , \quad (3.34)$$

with v_a being the group velocity of a right-moving lead mode a in the left lead and V labelling the projection matrix that already occurred in Eqs. (3.20)-(3.23). The scattering wave function $\psi(x_j) = \vec{\psi}_j$ at some slice j can be expressed by

$$\vec{\psi}_j = \mathcal{G}_{j0} \vec{P} \quad (3.35)$$

with \mathcal{G}_{j0} representing the block of the full GF matrix (including both leads) connecting slice j with the last slice 0 of the incoming left lead. In order to calculate the full scattering wave function of the scattering region, we now need to know all the inner GFs \mathcal{G}_{j0} which is a much harder task than just calculating the four surface GFs. However, there is an elegant way to solve this problem. These GFs \mathcal{G}_{j0} can be expressed by the use of a Dyson equation in the following form:

$$\mathcal{G}_{j0} = G_{j1} H_I^{\dagger L} \mathcal{G}_{00} + G_{j2} H_I^{(i)} \mathcal{G}_{30} \quad . \quad (3.36)$$

The GFs G_{j1} and G_{j2} describe inner GFs of the scattering region (i) without the leads. Fig. 3.11 illustrates how this equation can be found. The two contributions

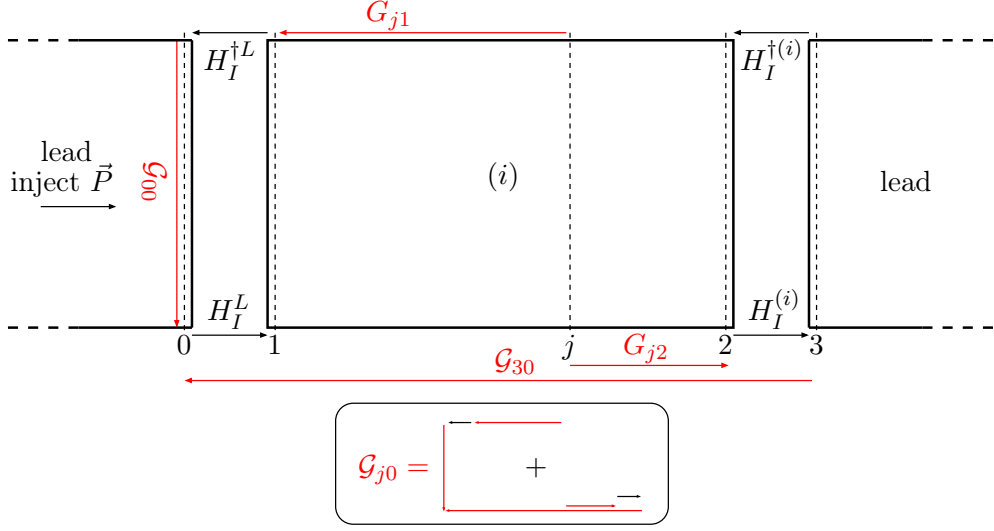


Figure 3.11.: Illustration of a setup for the standard wave function picture calculations. A scattering region called (i) is attached to two semi-infinite leads. Through the left lead, a superposition \vec{P} of propagating lead modes is injected into the system. To calculate scattering wave functions at some slice j , the relevant GF \mathcal{G}_{j0} has to be expressed by a Dyson equation (3.36). The occurring contributions in this equation are shown diagrammatically at the bottom of the figure. The corresponding GFs that contribute are highlighted in red.

result from one path that connects the left lead and one path that connects the right one. Mind, that now the surface GFs \mathcal{G}_{00} and \mathcal{G}_{30} , that probably have already been calculated for the computation of the scattering matrix, appear again. G_{j1} and G_{j2} are the only contributions that depend on j . Thus, when we plug Eq. (3.36) into Eq. (3.35) we find that the scattering wave function $\vec{\psi}_j$ at a specific slice j is given by

$$\vec{\psi}_j = G_{j1} H_I^{\dagger L} \mathcal{G}_{00} \vec{P} + G_{j2} H_I^{(i)} \mathcal{G}_{30} \vec{P} = G_{j1} \vec{\xi} + G_{j2} \vec{\eta} \quad , \quad (3.37)$$

where we introduced the definitions

$$\vec{\xi} = H_I^{\dagger L} \mathcal{G}_{00} \vec{P} \quad \text{and} \quad (3.38)$$

$$\vec{\eta} = H_I^{(i)} \mathcal{G}_{30} \vec{P} \quad . \quad (3.39)$$

These vectors $\vec{\xi}$ and $\vec{\eta}$ are independent of the specific slice j that we are interested in and furthermore contain quantities that we can calculate efficiently. As a result in Eq. (3.37) we have reduced the problem to the products of the inner GFs G_{j1} and G_{j2} of the disconnected module (i) with the once computed vectors $\vec{\xi}$ and $\vec{\eta}$, respectively. As these terms are only matrix-vector products it is not even necessary

to ever calculate G_{j1} and G_{j2} to their full extent as will be become clear shortly. Eq. (3.37) actually represents n_x equations as there is one for every slice j . We can thus for the full scattering wave function $\vec{\psi}$ write

$$\vec{\psi} = \begin{pmatrix} \vec{\psi}_1 \\ \vdots \\ \vec{\psi}_j \\ \vdots \\ \vec{\psi}_2 \end{pmatrix} = \begin{pmatrix} G_{11} \\ \vdots \\ G_{j1} \\ \vdots \\ G_{21} \end{pmatrix} \vec{\xi} + \begin{pmatrix} G_{12} \\ \vdots \\ G_{j2} \\ \vdots \\ G_{22} \end{pmatrix} \vec{\eta} , \quad (3.40)$$

where $\vec{\psi}$ consists of the wave function vectors of the individual slices. On the right-hand side all the inner GFs connecting the inner slices to the first and last slice of the scattering region are also denoted in vector form. This vectors of $n_y \times n_y$ -matrices can in terms of the full GF matrix G Eq. (3.25) be substituted in Eq. (3.40) in the following way:

$$\vec{\psi} = G \begin{pmatrix} \mathbb{1} \\ 0 \\ \vdots \\ 0 \end{pmatrix} \vec{\xi} + G \begin{pmatrix} 0 \\ \vdots \\ 0 \\ \mathbb{1} \end{pmatrix} \vec{\eta} . \quad (3.41)$$

According to the definition Eq. (3.19) this leads to

$$\vec{\psi} = (E - H)^{-1} \begin{pmatrix} \mathbb{1} \\ 0 \\ \vdots \\ 0 \end{pmatrix} \vec{\xi} + (E - H)^{-1} \begin{pmatrix} 0 \\ \vdots \\ 0 \\ \mathbb{1} \end{pmatrix} \vec{\eta} . \quad (3.42)$$

We can in the following bring the Hamiltonian H of the full geometry to the left-hand side in Eq. (3.42) and end up with

$$(E - H)\vec{\psi} = \begin{pmatrix} \vec{\xi} \\ 0 \\ \vdots \\ 0 \\ \vec{\eta} \end{pmatrix} . \quad (3.43)$$

This equation is numerically more efficiently solved as it represents an ordinary system of equations with an unknown solution $\vec{\psi}$. Moreover, the Hamiltonian H is usually a sparse matrix and also the right-hand side contains mostly zeroes. Therefore efficient numerical routines from MUMPS [156, 157] can be used in order to factorize the matrix $(E - H)$ and efficiently calculate $\vec{\psi}$ in a parallel manner.

However, this system of equations [Eq. (3.43)] can be huge as the vector $\vec{\psi}$ is $n_x \cdot n_y$ complex elements long. As we will see in the following, the PPA discussed in the previous section 3.5 will provide a handle to manually split the work between the individual cores in a way that simplifies the problem and speeds up the calculations. For this purpose, we consider a geometry for which the PPA has been executed on n cores (see Fig. 3.12). During the PPA, the geometry has been split into n modules

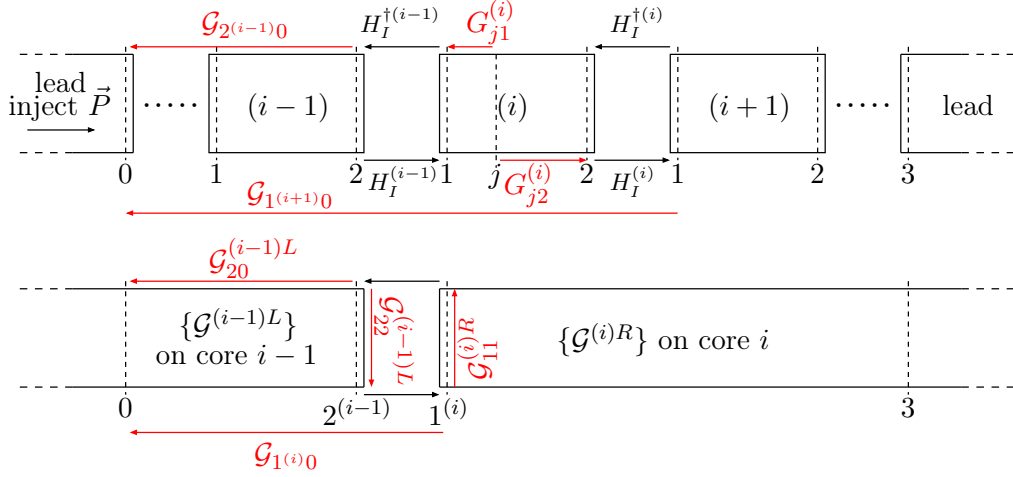


Figure 3.12.: Illustration of a multi-module setup for the parallel calculation of pictures. The scattering region is divided into n modules, labeled from (0) to $(n-1)$. We concentrate on some inner module (i) and its two neighbors $(i-1)$ and $(i+1)$. At the ends of the entire region, two semi-infinite leads are attached. Through the left lead, a superposition \vec{P} of propagating lead modes is injected into the system. To calculate scattering wave functions at some slice j within module (i) , the relevant GF $\mathcal{G}_{j(i)0}$ has to be expressed by a Dyson equation (3.45). In the lower panel we show the contributions to the Dyson equations (3.49) and (3.50). For these the sets of surface GFs $\{\mathcal{G}^{(i-1)L}\}$ and $\{\mathcal{G}^{(i)R}\}$ that are calculated by the PPA and the structures they describe are sketched in the lower part of this figure.

that we label for simplicity from (0) to $(n-1)$. In the first step of the PPA the surface GFs of module (i) have then been calculated by core i . After this initialization core 0 attaches the left lead and core $n-1$ attaches the right lead. The PPA ends with core i knowing the two sets of surface GFs $\{\mathcal{G}^{(i)L}\} = \{G_{00}^{(i)L}, G_{02}^{(i)L}, G_{20}^{(i)L}, G_{22}^{(i)L}\}$ and $\{\mathcal{G}^{(i)R}\} = \{G_{00}^{(i)R}, G_{02}^{(i)R}, G_{20}^{(i)R}, G_{22}^{(i)R}\}$. These describe the structure that is composed of all the modules from (0) to (i) including the left lead and the structure composed of all the modules from (i) to the last $(n-1)$ including the right lead, respectively. To evaluate the scattering wave function $\vec{\psi}_j^{(i)}$ at some slice j for some

injection \vec{P} inside module (i) one finds

$$\vec{\psi}_j^{(i)} = \mathcal{G}_{j(i)0} \vec{P} \quad , \quad (3.44)$$

with $\mathcal{G}_{j(i)0}$ denoting the internal GF of the full connected structure including the leads from slice j inside module (i) to slice 0 as depicted in Fig. 3.12. As before, we can decompose this GF using a Dyson equation (see contributions in Fig. 3.12)

$$\mathcal{G}_{j(i)0} = G_{j1}^{(i)} H_I^{\dagger(i-1)} \mathcal{G}_{2(i-1)0} + G_{j2}^{(i)} H_I^{(i)} \mathcal{G}_{1(i+1)0} \quad . \quad (3.45)$$

With the help of Eq. (3.44) we can write analogously to Eq. (3.37)

$$\vec{\psi}_j^{(i)} = G_{j1}^{(i)} H_I^{\dagger(i-1)} \mathcal{G}_{2(i-1)0} \vec{P} + G_{j2}^{(i)} H_I^{(i)} \mathcal{G}_{1(i+1)0} \vec{P} = G_{j1}^{(i)} \vec{\xi}^{(i)} + G_{j2}^{(i)} \vec{\eta}^{(i)} \quad , \quad (3.46)$$

where we introduced the vectors

$$\vec{\xi}^{(i)} = H_I^{\dagger(i-1)} \mathcal{G}_{2(i-1)0} \vec{P} \quad , \quad (3.47)$$

$$\vec{\eta}^{(i)} = H_I^{(i)} \mathcal{G}_{1(i+1)0} \vec{P} \quad . \quad (3.48)$$

With this the scattering wave contains contributions from the pure module GFs $G_{j1}^{(i)}$ and $G_{j2}^{(i)}$, which depend on the position of slice j while the other terms only depend on the module number under consideration. While before [Eqs. (3.38) and (3.39)] we found that the vectors $\vec{\xi}$ and $\vec{\eta}$ are unique (for a given injection) throughout the whole structure, we now can still define them to stay the same throughout each module (i). We will be able to use the information about the surface GFs of the partial structures calculated by the PPA in order to be able to calculate $\vec{\xi}^{(i)}$ and $\vec{\eta}^{(i)}$ in parallel for each module. For this purpose, we need to calculate the GFs $\mathcal{G}_{2(i-1)0}$ and $\mathcal{G}_{1(i+1)0}$ which are still complicated objects as they connect those slices right before and after our module (i) to the entrance at slice 0. Mind, that these are inner GFs of the full geometry. First concentrating on $\mathcal{G}_{2(i-1)0}$, we find the Dyson equation (see also lower panel in Fig. 3.12):

$$\mathcal{G}_{2(i-1)0} = \mathcal{G}_{20}^{(i-1)L} + \mathcal{G}_{22}^{(i-1)L} H_I^{(i-1)} \mathcal{G}_{1(i)0} \quad . \quad (3.49)$$

Note, that the GFs $\mathcal{G}_{20}^{(i-1)L}$ and $\mathcal{G}_{22}^{(i-1)L}$ are surface GFs of composed modules calculated by the PPA on core ($i-1$). We can here already see that some communication will be required in order to correctly distribute the GFs as information needed on core (i) is for now only stored on core ($i-1$). For the moment, we use another Dyson equation

$$\mathcal{G}_{1(i)0} = \mathcal{G}_{11}^{(i)R} H_I^{\dagger(i-1)} \mathcal{G}_{2(i-1)0} \quad (3.50)$$

into which we can plug Eq. (3.49) and solve for $\mathcal{G}_{1(i)0}$ yielding

$$\mathcal{G}_{1(i)0} = A_{(i)}^{-1} \mathcal{G}_{11}^{(i)R} H_I^{\dagger(i-1)} \mathcal{G}_{20}^{(i-1)L} , \quad (3.51)$$

with the definition of some matrix

$$A_{(i)} = \mathbb{1} - \mathcal{G}_{11}^{(i)R} H_I^{\dagger(i-1)} \mathcal{G}_{22}^{(i-1)L} H_I^{(i-1)} . \quad (3.52)$$

We strain that these Eqs. (3.51) and (3.52) only contain quantities that have been, thanks to the PPA, already computed. Hence, we already know that we can calculate our wave function pictures entirely in parallel. The problem that remains is to develop an algorithm that does that in an efficient way as the information is scattered over our cores. At first glance, the situation is confusing since when we look at our equations for $\vec{\xi}^{(i)}$ [Eq. (3.47)] and $\vec{\eta}^{(i)}$ [Eq. (3.48)], we find that some required data is located at core (i) , some at core $(i-1)$ and some even at core $(i+1)$. The deciding hint in unscrambling this puzzle comes by shifting our equation (3.47) for $\vec{\xi}^{(i)}$ to the next module, i.e. doing $i \rightarrow i+1$:

$$\vec{\xi}^{(i+1)} = H_I^{\dagger(i)} \mathcal{G}_{2(i)0} \vec{P} . \quad (3.53)$$

The required GF $\mathcal{G}_{2(i)0}$ can be found by applying the same trick to Eq. (3.49), giving

$$\mathcal{G}_{2(i)0} = \mathcal{G}_{20}^{(i)L} + \mathcal{G}_{22}^{(i)L} H_I^{(i)} \mathcal{G}_{1(i+1)0} , \quad (3.54)$$

and finally to Eq. (3.52) plugged into Eq. (3.51) with the result

$$\mathcal{G}_{1(i+1)0} = (\mathbb{1} - \mathcal{G}_{11}^{(i+1)R} H_I^{\dagger(i)} \mathcal{G}_{22}^{(i)L} H_I^{(i)})^{-1} \mathcal{G}_{11}^{(i+1)R} H_I^{\dagger(i)} \mathcal{G}_{20}^{(i)L} . \quad (3.55)$$

This last equation contains only a single GF that is not known on core (i) , namely $\mathcal{G}_{11}^{(i+1)R}$ stored on core $(i+1)$. This represents the minimal data exchange effort that we could have hoped for. Obviously, it makes sense to let each core (i) actually calculate $\vec{\xi}^{(i+1)}$ which will be needed on the next core. Even more so, when plugging Eq. (3.54) into Eq. (3.53) and using the abbreviations

$$\vec{a}^{(i)} = H_I^{\dagger(i)} \mathcal{G}_{20}^{(i)L} \vec{P} , \quad (3.56)$$

$$\vec{b}^{(i)} = \mathcal{G}_{1(i+1)0} \vec{P} \quad (3.57)$$

one finds that

$$\vec{\xi}^{(i+1)} = H_I^{\dagger(i)} \vec{a}^{(i)} + H_I^{\dagger(i)} \mathcal{G}_{22}^{(i)L} H_I^{(i)} \vec{b}^{(i)} = H_I^{\dagger(i)} \vec{a}^{(i)} + H_I^{\dagger(i)} \mathcal{G}_{22}^{(i)L} \vec{\eta}^{(i)} . \quad (3.58)$$

This shows, that the desired quantity $\vec{\eta}^{(i)}$ even comes along as an intermediate result in the calculation of $\vec{\xi}^{(i+1)}$ on core (i) .

Overall, the algorithm that we constructed works as follows: After running the PPA each core (i) starts out with calculating $\vec{a}^{(i)}$ according to Eq. (3.56) for which all data is present. Then it sends the single GF subblock $\mathcal{G}_{11}^{(i)R}$ to the previous core and receives $\mathcal{G}_{11}^{(i+1)R}$ from the next core. With this it can now calculate

$$A_{(i+1)} = \mathbb{1} - \mathcal{G}_{11}^{(i+1)R} H_I^{\dagger(i)} \mathcal{G}_{22}^{(i)L} H_I^{(i)} .$$

Plugging Eq. (3.55) into Eq. (3.57) yields after some rearrangements

$$A_{(i+1)} \vec{b}^{(i)} = G_{11}^{(i+1)R} \vec{a}^{(i)} , \quad (3.59)$$

which represents an ordinary system of n_y equations with the solution $\vec{b}^{(i)}$ that can be easily calculated numerically. In a next step

$$\vec{\eta}^{(i)} = H_I^{(i)} \vec{b}^{(i)}$$

is calculated [compare Eqs. (3.39) and (3.57)]. Finally $\vec{\xi}^{(i+1)}$ can be computed by the use of Eq. (3.58). This vector has to be sent to the next core, while the own vector $\vec{\xi}^{(i)}$ is received from the previous core. The only exception from these rules is the last core $n - 1$, which can simply use the surface GF of the whole geometry to calculate

$$\vec{\eta}^{(n-1)} = H_I^{(n-1)} \mathcal{G}_{30} \vec{P}$$

and therefore also saves time to calculate

$$\vec{\xi}^{(0)} = H_I^L \mathcal{G}_{00} \vec{P}$$

and send it to the first core 0, that would otherwise not receive its desired $\vec{\xi}^{(0)}$.

By the end of this procedure, the entire wave function $\vec{\psi}^{(i)}$ of each module can be calculated on the corresponding core autonomously and fully in parallel. This is because the derivation of Eq. (3.43) from the beginning of the section holds true with only slight modifications:

$$(E - H^{(i)}) \vec{\psi}^{(i)} = \begin{pmatrix} \vec{\xi}^{(i)} \\ 0 \\ \vdots \\ 0 \\ \vec{\eta}^{(i)} \end{pmatrix} . \quad (3.60)$$

Note that $H^{(i)}$ here only is the part of the full Hamiltonian matrix H that describes the single module (i) detached from the rest of the geometry and also $\vec{\psi}^{(i)}$ only contains as many elements as module (i) alone has grid points. In this way we can

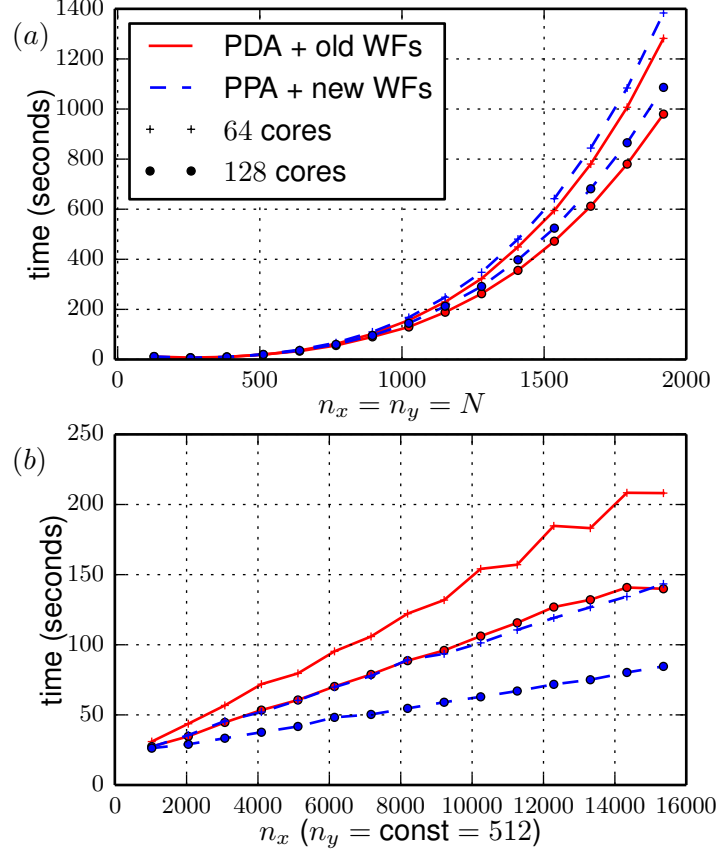


Figure 3.13.: Benchmarks of the old picture algorithm preceded by the PDA and the new picture algorithm after the PPA for (a) quadratic systems as a function of system size $N = n_x = n_y$ and (b) rectangular geometries with fixed $n_y = 512$ as a function of n_x . Plusses and dots show the measured calculation times on 64 and 128 cores, respectively. All calculations were performed on the VSC-3. The red data is for the PDA with the old wave function calculation while blue represents the PPA followed by the new wave function computations. All calculations only evaluate a single wave function picture for some injection \vec{P} . We find that the new algorithm might be slower in a quadratic system with only a single picture [see panel (a)]. However, for more pictures there will be a threshold where the new picture algorithm can make up for the lost time due to the overhead of the PPA with respect to the PDA. For fixed n_y and increasing n_x , the new picture algorithm is approximately twice as fast as the old one [see panel (b)].

instead of solving one huge system of equations (3.43), solve n systems of equations (3.60) on n cores almost perfectly in parallel. The communication effort is minimal and we expect the algorithm to be a lot faster than the original one.

To show this, we performed some benchmarks shown in Fig. 3.13. In panel (a) of this figure we present the times that computations of the scattering matrix and a subsequent calculation of a single scattering wave function take in a quadratic structure of size $N = n_x = n_y$. In red one can see the fastest possible calculation that is still using the old algorithm. As the latter does not rely on the PPA, we can in this case use a PDA in order to calculate the surface GFs of the structure. As the PDA is faster than the PPA (see previous section 3.5), we can see that the old algorithm combined with a PDA is still faster in such a quadratic region than the new one which relies on a preceding execution of the PPA.

However, these calculations only evaluated a single wave function picture (for only one injected superposition \vec{P} in the left lead). When we look at the pure times that our new algorithm alone takes without the disadvantage of the PPA's overhead compared to the PDA, we find, e.g., at $N = 1920$ [rightmost points in Fig. 3.13(a)] that the new picture algorithm only lasted 9 seconds as opposed to the 28 seconds of the old picture calculation. Unfortunately the PPA took 598 seconds, while the PDA was done after 462 seconds. Still, simple math tell us that when instead of only a single picture, we calculate 8 of them, the algorithms will be approximately equally fast. For a large number of pictures, as is often necessary (see, e.g., section 1.3) the new algorithm is for sure preferable.

Another issue in this comparison is that we expect our algorithm to scale a lot better with n_x . While the old algorithm relies on factorizing the full Hamiltonian matrix containing $(n_x n_y)^2$ elements, our new algorithm splits the task into factorizing $(\frac{n_x}{n} n_y)^2$ matrices in parallel on n cores. This comes with the downside that data has to be exchanged between the cores in the PPA and also later for the wave function calculations. The size of this data only depends quadratically on n_y . While the old picture algorithm does not make a difference between n_x and n_y , our new algorithm should almost scale linearly with n_x , but be more sensitive to n_y . This behavior can be clearly seen in the benchmark for rectangularly shaped structures where n_y is kept fix at a typical size of 512 and only n_x is varied [see Fig. 3.13(b)]. For such structures our new algorithm is clearly faster than the old one even for only a single picture. The improvement is almost 100 % as the new calculations on 64 cores are approximately as fast as the old ones on twice as many cores.

To emphasize the nice scaling behavior of the new algorithm even more, we performed a benchmark for even bigger rectangular structures with $n_y = 1000$ shown in Fig. 3.14. One can see that the computation time indeed increases linearly with n_x enabling us to compute very large structures in reasonable time. We also need to mention, that when trying to execute this benchmark with the old algorithm on the VSC-3, the calculations crashed due to a memory overflow at approximately

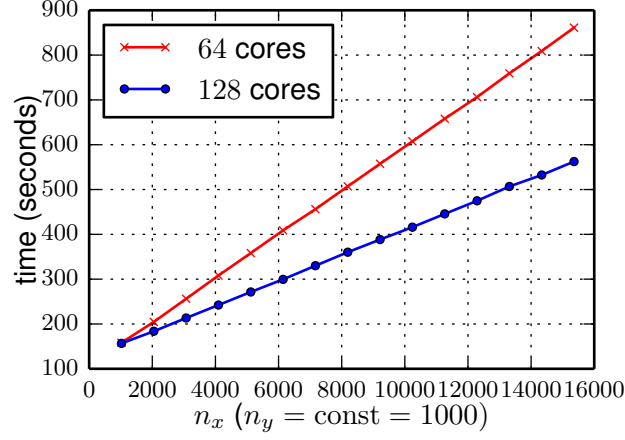


Figure 3.14.: Bigger benchmark of the new picture algorithm preceded by the PPA performed on 64 (red curve) and 128 cores (blue curve) performed on the VSC-3. Here n_y is fixed at $n_y = 1000$ and n_x is varied. Unlike before (see Fig. 3.13), we could in this benchmark not perform the old picture algorithm as it crashed on VSC-3 due to memory overflow in the 10th step of the benchmark. We find that the new algorithm scales almost perfectly linear with n_x as desired.

$n_x = 10000$. This also shows, that the new algorithm is also a lot more memory efficient since the full Hamiltonian of the entire structure (containing already close to 10^{14} elements at the mentioned crashing system size) never has to be constructed to its full extent.

Overall, we conclude that our new algorithm is vastly superior compared to the old one as it scales very well with n_x , scales well with the number of employed cores and needs less memory in most cases. Problems might only occur when n_y becomes larger than n_x . In such situations, when the structure is a lot higher than it is long, $n_y \gg n_x$, and only few wave function pictures are required, it might still pay off to use the old algorithm. In all the other cases, our new algorithm provides access to larger systems and many more scattering wave functions as before.

3.7. Computing the local density of states

The (local) density of states $\rho(E)$ (DOS) is an important quantity in physics in general and even more specifically in disordered electronic systems. It contains information about transport properties and governs whether a material is a conductor or insulator. A vanishing DOS at the Fermi energy E_F will suppress transport while a large one will leave opportunities for electrons to pass through the system. The

local density of states $\tilde{\rho}(\vec{r}, E)$ (LDOS) also contains information about where these states are located spatially within the system, or how localized such states at the Fermi energy are. The two aforementioned quantities are in general connected by the relation

$$\rho(E) = \int \tilde{\rho}(\vec{r}, E) d^3r . \quad (3.61)$$

In a closed system the LDOS is defined as

$$\tilde{\rho}(\vec{r}, E) = \sum_i \langle \vec{r} | i \rangle \delta(E - E_i) , \quad (3.62)$$

where $|i\rangle$ are the eigenstates of the system's Hamiltonian with corresponding energy eigenvalues E_i . Numerically, the usual approach to access this quantity is to approximate the delta functions by a Breit-Wigner function

$$\delta(E) \approx \frac{\epsilon}{\pi(E^2 + \epsilon^2)} \quad (3.63)$$

and choosing a numerically small value $\epsilon \rightarrow 0^+$.

When the system is opened, e.g., by attaching two leads as the case in our standard two-dimensional scattering problems, the closed system's energy levels E_i will naturally gain certain widths ϵ_i . The open boundary conditions make the problem non-hermitian and cause the energy eigenvalues E_i to become complex. In this way the width ϵ_i of each resonance will be given by the imaginary part of the energy eigenvalues according to $\epsilon_i = -2\text{Im}E_i$ and the LDOS will be

$$\tilde{\rho}(\vec{r}, E) = \sum_i \langle \vec{r} | i \rangle \frac{\epsilon_i}{\pi [(E - \text{Re } E_i)^2 + \epsilon_i^2]} . \quad (3.64)$$

Numerically, the task comes down to solving the non-hermitian eigenvalue problem for the Hamiltonian matrix H . Remember that this matrix is a huge object and solving its eigenvalue problem is time- and memory-intensive. Of course there are very efficient algorithms like the Lanczos algorithm [158] implemented in PARPACK [159] that allow for the fast calculations of those eigenvalues that are closest to the energy E at question. This approach is reasonable, as those eigenvalues that are far away from E_i will hardly contribute. Still, without any a-priori information on the resonance widths (imaginary parts of E_i) and the number of eigenstates that significantly contribute, it is always hard to be sure that the results are correct and very often the calculations have to be fine-tuned by hand.

In this section, we will use a different approach in order to access the LDOS. This method relies on an alternative definition of the LDOS

$$\tilde{\rho}(\vec{r}, E) = -\frac{1}{\pi} \text{Im Tr } \hat{\mathcal{G}}(\vec{r}, \vec{r}, E) , \quad (3.65)$$

that involves the GF $G(\vec{r}, \vec{r}', E)$. Numerically, on our usual rectangular finite differences grid, this definition allows us to write the LDOS at some slice j as

$$\vec{\rho}_j = -\frac{1}{\pi} \text{Im} \text{diag}(\mathcal{G}_{jj}) \quad , \quad (3.66)$$

where the caligraphic \mathcal{G}_{jj} stands for the $n_y \times n_y$ block of the full GF including the leads connecting slice j with itself. As this has to be evaluated at every slice of the structure, the task comes down to calculating the diagonal of the full GF which is obviously harder than evaluating surface GFs (section 3.5) or wave function pictures (section 3.6).

However, the advantages of this method are obvious: First, calculations will not depend on unphysical parameters such as the number of calculated eigenvalues of the system. In this way all contributions to the LDOS will be included automatically without worrying about approximations. Second, an iterative and fully parallel algorithm would allow for saving memory and computation time. We found such an efficient way to calculate the LDOS by iteratively using Dyson equations. As in the previous section 3.6, we are also able to parallelize the problem by the means of the PPA.

Assume once more a scattering structure that has a uniform height of n_y points and contains n_x slices. Again, two semi-infinite leads are attached to left and right.

Our algorithm for the calculation of the LDOS requires calculation of all diagonal blocks $\{\mathcal{G}_{jj}\}$ of this structure according to Eq. (3.66) (see Fig. 3.15). We assume having already calculated the surface GF G_{33} of the right lead. For convenience at later stages of our algorithm we start from the right. Starting from the right lead the structure is now put together slice-by-slice working to the left⁴. The equations are similar to those in section 3.3. One difference is that this time we only need to calculate the diagonal parts G_{jj} of the surface GFs that describe the structure from slice j to the rightmost slice at n_x . However, we need to store all these $n_y \times n_y$ matrices which represents a significant but manageable effort.

The iteration to the left hence contains n_x equally effortful steps. To find the corresponding equations we consider the upper sketch in Fig. 3.15. In the previous step we have calculated and stored the surface GF $G_{j+1,j+1}$ describing the structure from slice $j+1$ onwards to the right. In order to append the next slice j , we find the Dyson equation

$$G_{jj} = G_j^0 + G_j^0 H_I^{(j)} G_{j+1,j+1} H_I^{\dagger(j)} G_{jj} \quad . \quad (3.67)$$

Due to the definition of

$$G_j^0 = (E - H_0^{(j)})^{-1}$$

⁴ In case the system has no leads, we can alternatively start out with the GF of the last slice $G_{n_x,n_x} = (E - H_0^{(n_x)})^{-1}$.

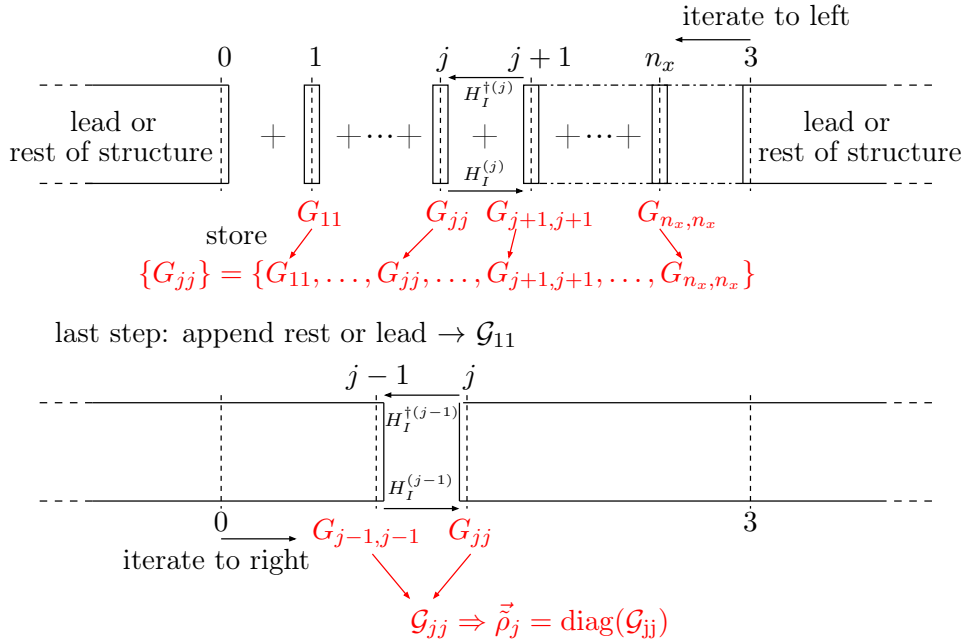


Figure 3.15.: The top panel indicates the first interaction starting from the right with the lead GF or, in the parallel calculation, the GF of the remaining structure to the right provided by the PPA. In the following each slice is appended one-by-one from right to left. At each of these steps the GF G_{jj} is calculated according to Eq. (3.68) and stored. Reaching the leftmost slice $j = 1$, the left lead (or in the parallel case the remaining structure to the left provided by the PPA) is appended and the full GF of the first slice \mathcal{G}_{11} can be evaluated using Eq. (3.70). In the following the algorithm iterates back to the right, retrieving the full GFs G_{jj} [see Eq. (3.71)] relevant for the LDOS.

we can thus calculate

$$G_{jj} = (E - H_0^{(j)} - H_I^{(j)} G_{j+1,j+1} H_I^{\dagger(j)})^{-1} \quad (3.68)$$

and also store it for later use.

Reaching slice 1 after n_x iteration steps our memory contains a set $\{G_{jj}\}$ of n_x surface GFs. We can immediately append the left lead described by the surface GF G_{00} to evaluate \mathcal{G}_{11} which already represents the first contribution to the LDOS Eq. 3.66. The corresponding Dyson equation reads

$$\mathcal{G}_{11} = G_{11} + G_{11} H_I^{\dagger(0)} G_{00} H_I^{(0)} \mathcal{G}_{11} \quad (3.69)$$

and yields

$$\mathcal{G}_{11} = (\mathbb{1} - G_{11} H_I^{\dagger(0)} G_{00} H_I^{(0)})^{-1} G_{11} \quad (3.70)$$

At this point, we can iterate back through the system starting at $j = 2$. In each of these steps, we will evaluate another contribution \mathcal{G}_{jj} of which the diagonal gives the LDOS at slice j . The situation in each such step is illustrated in the lower sketch of Fig. 3.15. The Dyson equation found from there,

$$\mathcal{G}_{jj} = G_{jj} + G_{jj} H_I^{\dagger(j-1)} \mathcal{G}_{j-1,j-1} H_I^{(j-1)} G_{jj} \quad , \quad (3.71)$$

can be directly used since the G_{jj} are known from the previous iteration to the left and $\mathcal{G}_{j-1,j-1}$ has just been calculated in the previous step. In this way one retrieves step-by-step the full LDOS according to Eq. (3.65) which can be used to calculate the total DOS by just summing over $\tilde{\rho}_j$ and all slices j .

In a next step, we again address the parallelization of this algorithm. Unfortunately each step in the iteration depends on the previous one and also the $\{G_{jj}\}$ are worthless if they do not describe the entirety of the remaining structure to the right.

At this point again the PPA provides a remedy. We assume that the PPA has been executed and each core i is assigned its module (i). Looking at the next core ($i + 1$) we already know that the PPA stored the surface GFs $\{G^{(i+1)R}\}$ there describing the structure from module $i + 1$ to the right including the right lead. This is exactly what we need for the start of our LDOS algorithm on core i for module (i). Moreover it is not even necessary to transfer all four of these surface GFs from core $i + 1$ to core i as for the LDOS iteration only $G_{11}^{(i+1)R}$ (taking the role of G_{33} in the description above) will be needed. Hence instead of starting from the right lead, the outcome of the PPA provides core (i) with the opportunity to treat the rest of the structure like a lead and start from the surface GF that is sent to it by core $i + 1$.

After the iteration to the left storing $n_x^{(i)}$ [number of slices in module (i)] GFs $\{G_{jj}\}$, we reach the left end of module (i). Again, within the PPA the GF $G_{22}^{(i-1)L}$ describing the remainder of the structure to the left has already been calculated and can be provided by core $i - 1$. In this way each core can finally calculate the LDOS of its own module entirely in parallel. The only necessary communication effort involves the exchange of $2 n_y \times n_y$ matrices among the previous and the next core.

However, this time the parallelization will not save as much time as in the new picture algorithm. We expect that the single core calculation will still be faster than the calculation on 2 cores. The reason is that, in the latter case each slice is appended twice to the geometry, once at the start of the PPA and once during the LDOS algorithm. As the two-core calculation will in addition require data exchange effort, the computation will be slower than on only one core. From this point on, however, we expect the algorithm to gain momentum and show significant speed increase on 4, 8 and 16 cores. These expectations are very nicely confirmed by the

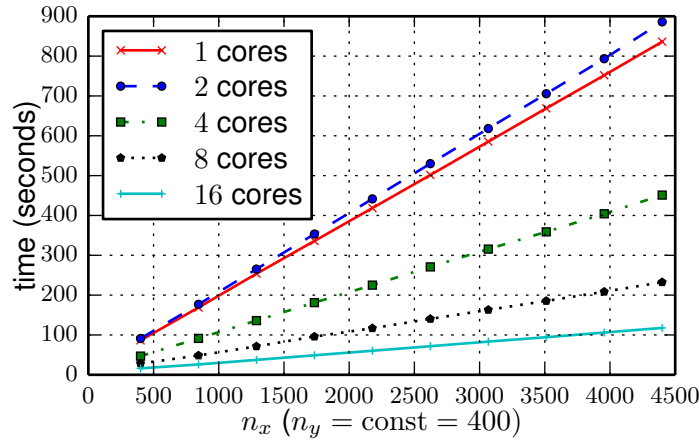


Figure 3.16.: Benchmark of the LDOS algorithm preceded by the PPA performed on 1, 2, 4, 8 and 16 cores on the VSC-3. The structures under consideration are rectangular with fixed $n_y = 400$ and the runtimes of the calculations are shown as a function of n_x . The benchmark confirms the expected behavior. While the 2-core calculation is slower than on a single core, the times decrease rapidly when more cores are used.

benchmark in Fig. 3.16.

Exemplary results of the DOS can, e.g., be found in our calculations regarding the percolating states in the topological Anderson insulator of Fig. 2.10(b). Pictures of the LDOS were presented in Fig. 2.7. The LDOS results of an upcoming paper regarding etched graphene flakes are shown in Fig. 3.17. Since the size of the numerically considered graphene flake is already comparable to the size of real samples used in experiments, we show these results as an illustrative example for the interesting applications of our new algorithm.

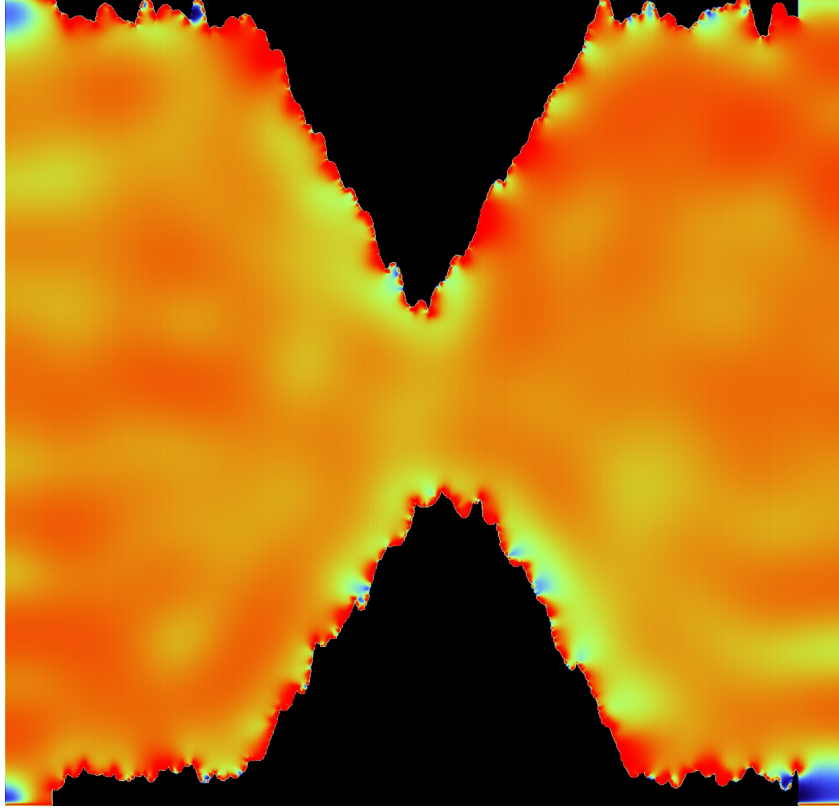


Figure 3.17.: LDOS $\tilde{\rho}(\vec{r})$ in a numerical simulation of an etched graphene flake with a constriction. Regions of high LDOS appear in red while regions of low LDOS are black. The upper boundary of the structure features graphene in arm-chair configuration. The size of the numerical grid is $n_y = 2500$ and $n_x \approx 1800$ and it thus consists of $N \approx 4.5$ million grid points. Figure adapted from Ref. [160].

3.8. Super-cell band structures

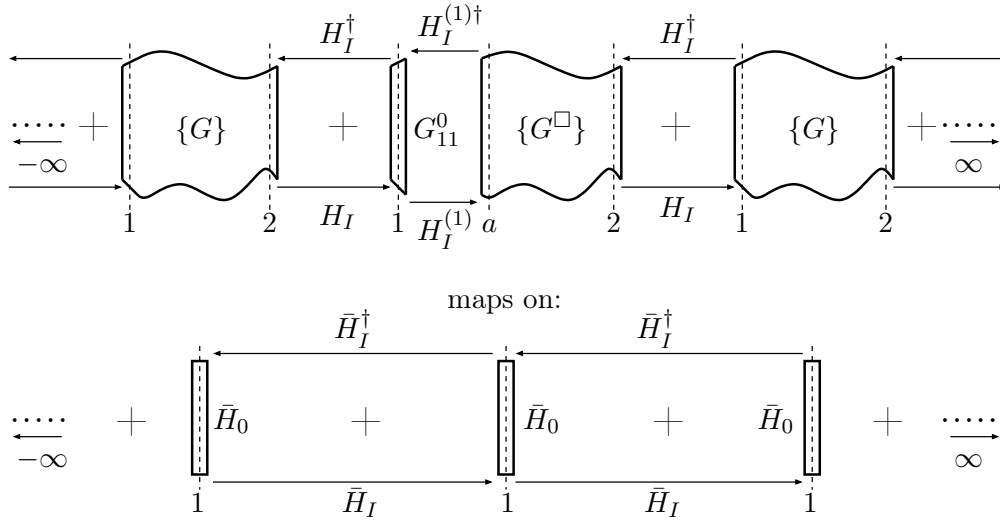


Figure 3.18.: The upper part of this figure illustrates the situation of an infinitely long lead that is composed of super-cells periodically glued together. The cell can contain disorder and arbitrarily shaped boundaries. The first slice of the cell is labelled 1, the last one labelled 2. The cell in the middle of the figure is split into its first slice and the rest described by its surface GFs $\{G^\square\}$. This procedure is part of the derivation leading to Eqs. (3.93)-(3.95). The considered super-cell can be mapped onto a single slice as illustrated in the lower part of this figure. For this procedure it is required to use effective Hamiltonian subblocks \bar{H}_0 , \bar{H}_I and \bar{H}_I^\dagger as given by Eqs. (3.93)-(3.95).

In this section, we want to consider a slightly different numerical problem that is the calculation of band structures for super-cell geometries. In section 3.2 we were interested in the numerical calculation of band structures for infinitely long systems of clean rectangular leads. Within this approach it was intrinsically assumed that the structure consists of infinitely many equal slices that are periodically glued together. To put it in different words, the unit cell of a structure consists of only a single slice. This approach, however, can be generalized to so-called super-cells: In this case the unit cell does not consist of a single slice anymore, but of a module that is continued periodically. The situation considered is sketched in the upper panel of Fig. 3.18 (note that in the middle unit cell in this sketch the first slice is cut-off just as an illustration for later purposes). In principle, Bloch's theorem does not put any restrictions on the shape of the unit cell, but only constraints that the structure has to be periodic in some way. Considerations like that can be very useful when investigating disordered systems since the unit cell in a super-cell structure

can also contain bulk disorder or arbitrarily shaped boundaries (see Fig. 3.18). As an example the band structure of a bent lead can be investigated by the methods we developed.

The question now is, how we can calculate the Bloch eigenvalues $\beta = e^{-ik_x \Delta x}$ of a periodic structure consisting of some arbitrary super-cell as a function of energy E . From this knowledge we could build the band structure $E(k_x)$ that contains information about transport and, in the case of disorder, also the influence of localization. We know that the Hamiltonian H_0^{SC} of our super-cell can be numerically represented in tri-diagonal form analogously to Eq. 3.3 by

$$H_0^{SC} = \begin{pmatrix} H_0^{(1)} & H_I^{(1)} & 0 & \dots & \dots & 0 \\ H_I^{\dagger(1)} & H_0^{(2)} & H_I^{(2)} & 0 & \dots & \vdots \\ 0 & \ddots & \ddots & \ddots & 0 & \vdots \\ \vdots & 0 & \ddots & \ddots & \ddots & 0 \\ \vdots & \dots & 0 & H_I^{\dagger(n_x-2)} & H_0^{(n_x-1)} & H_I^{(n_x-1)} \\ 0 & \dots & \dots & 0 & H_I^{\dagger(n_x-1)} & H_0^{(n_x)} \end{pmatrix}. \quad (3.72)$$

The interaction between adjacent super-cells can in this basis, that contains all the grid-points of the cell, be represented by the two matrices

$$H_I^{SC} = \begin{pmatrix} 0 & \dots & \dots & 0 \\ \vdots & \ddots & & \vdots \\ 0 & & \ddots & \vdots \\ H_I & 0 & \dots & 0 \end{pmatrix} \quad \text{and} \quad (3.73)$$

$$H_I^{\dagger SC} = \begin{pmatrix} 0 & \dots & 0 & H_I^{\dagger} \\ \vdots & \ddots & & 0 \\ \vdots & & \ddots & \vdots \\ 0 & \dots & \dots & 0 \end{pmatrix}. \quad (3.74)$$

These matrices mostly contain zeroes and only one non-zero block each that mediate the interaction between the last slice of a super-cell and the first slice of the next and vice versa. The Bloch function of the super-cell is numerically represented by a vector $\vec{\chi}$ that is defined on each grid-point of the cell and consists of vectors $\vec{\chi}_j$ each of which describes one of the cell's slices:

$$\vec{\chi} = \begin{pmatrix} \vec{\chi}_1 \\ \vdots \\ \vec{\chi}_2 \end{pmatrix}. \quad (3.75)$$

The first and last slice of the cell are labelled 1 and 2 for convenience as visualized in Fig. 3.18. With these ingredients we can formulate a Bloch equation for the periodic problem of an array of super-cells analogous to Eq. (3.14):

$$\left(H_0^{SC} + \beta^{-1}H_I^{SC} + \beta H_I^{\dagger SC}\right) \vec{\chi} = E \vec{\chi} . \quad (3.76)$$

Solving this equation directly can however be hard as the size of the matrices increases quadratically with the number of grid points in the unit cell. Additionally, one encounters problems when trying to solve the equation for fixed energy E . The solution of this problem requires doubling of the dimension of the system of equations and also involves the inversion of $H_I^{\dagger SC}$ [see Eq. (3.15)] which is clearly singular as it contains mostly zeros [see Eq. (3.74)]. In the following we will introduce a different approach for a numeric solution of this problem. For this purpose, we look at the Bloch equation (3.76) and divide the unit cell into its first slice 1 and the rest described by a Hamiltonian matrix H^\square . Analogously, the Bloch function $\vec{\chi}$ is divided into the values $\vec{\chi}_1$ at slice 1 and those at the remaining grid points represented by $\vec{\chi}^\square$. In this scheme, Eq. (3.76) reads

$$\left(\begin{array}{c|ccc} H_0^{(1)} & H_I^{(1)} & 0 & \dots & 0 & \beta H_I^\dagger \\ \hline H_I^{\dagger(1)} & & & & & \\ 0 & & & & & \\ \vdots & & & & & \\ 0 & & & & & \\ \beta^{-1}H_I & & & & & \end{array} \right) \begin{pmatrix} \vec{\chi}_1 \\ \vec{\chi}^\square \end{pmatrix} = E \begin{pmatrix} \vec{\chi}_1 \\ \vec{\chi}^\square \end{pmatrix} . \quad (3.77)$$

By only looking at the first line of this matrix equation, we find

$$H_0^{(1)} \vec{\chi}_1 + \left(H_I^{(1)} \quad 0 \quad \dots \quad 0 \quad \beta H_I^\dagger \right) \vec{\chi}^\square = E \vec{\chi}_1 , \quad (3.78)$$

while the rest of Eq. (3.77) can in compact form be expressed as

$$\begin{pmatrix} H_I^{\dagger(1)} \vec{\chi}_1 \\ 0 \\ \vdots \\ 0 \\ \beta^{-1}H_I \vec{\chi}_1 \end{pmatrix} + H^\square \vec{\chi}^\square = E \vec{\chi}^\square . \quad (3.79)$$

Solving the latter for $\vec{\chi}^\square$ yields

$$\vec{\chi}^\square = (E - H^\square)^{-1} \begin{pmatrix} \beta H_I^{\dagger(1)} \\ 0 \\ \vdots \\ 0 \\ \beta^{-1}H_I \end{pmatrix} \vec{\chi}_1 = G^\square \begin{pmatrix} H_I^{\dagger(1)} \\ 0 \\ \vdots \\ 0 \\ \beta^{-1}H_I \end{pmatrix} \vec{\chi}_1 , \quad (3.80)$$

which allows for substituting in the GF matrix

$$G^\square = (E - H^\square)^{-1}$$

describing the super-cell but with the very first slice detached. The first slice of this remaining super-cell we call a and as usual write its GF in the block form

$$G^\square = \begin{pmatrix} G_{aa}^\square & \cdots & G_{a2}^\square \\ \vdots & \ddots & \vdots \\ G_{2a}^\square & \cdots & G_{22}^\square \end{pmatrix}, \quad (3.81)$$

with only the surface GFs $\{G^\square\} = \{G_{aa}^\square, G_{a2}^\square, G_{2a}^\square, G_{22}^\square\}$ explicitly labelled. Plugging this back into Eq. (3.80) and from there into Eq. (3.78) we can eliminate the dependence on $\vec{\chi}^\square$ and replace the dependence on H^\square by the surface GFs $\{G^\square\}$:

$$\left(H_0^{(1)} + H_I^{(1)} G_{aa}^\square H_I^{\dagger(1)} + H_I^\dagger G_{22}^\square H_I + \beta^{-1} H_I^{(1)} G_{a2}^\square H_I + \beta H_I^\dagger G_{2a}^\square H_I^{\dagger(1)} \right) \vec{\chi}_1 = E \vec{\chi}_1. \quad (3.82)$$

This equation only depends on quantities situated on the first slice of the super-cell and the surface GFs of the rest. Moreover, it has the same shape as the original Eq. (3.76) but the occurring matrices are only of size $n_y \times n_y$ (with n_y the number of grid points in the first slice of the super-cell). As a result, this equation can be mapped onto an equation that only considers the Bloch-function on the first slice and is analogous to Eq. (3.14) and Eq. (3.76). This equation reads

$$\left(\bar{H}_0 + \beta^{-1} \bar{H}_I + \beta \bar{H}_I^\dagger \right) \vec{\chi}_1 = E \vec{\chi}_1. \quad (3.83)$$

For this mapping (also illustrated in the lower part of Fig. 3.18) we have used the definitions for the occurring Hamiltonian matrices \bar{H}_0 , \bar{H}_I and \bar{H}_I^\dagger describing the super-cell as an effective single slice plus the interactions with the next one. The definitions of these effective Hamiltonian subblocks are

$$\bar{H}_0 = H_0^{(1)} + H_I^{(1)} G_{aa}^\square H_I^{\dagger(1)} + H_I^\dagger G_{22}^\square H_I, \quad (3.84)$$

$$\bar{H}_I = H_I^{(1)} G_{a2}^\square H_I, \quad (3.85)$$

$$\bar{H}_I^\dagger = H_I^\dagger G_{2a}^\square H_I^{\dagger(1)}. \quad (3.86)$$

However, it appears inconvenient to use the surface GFs of a cut super-cell missing its first slice as these have no other application. It would be of great use if we could replace these with the surface GFs $\{G\}$ of the entire super-cell as these are also used for scattering problems, wave function pictures and the LDOS. To achieve this goal, we look at the middle super-cell in the upper part of Fig. 3.18 that illustrates the

situation of the cell with the first slice cut off. From this sketch we can immediately write down the Dyson equations

$$\begin{aligned} G_{12} &= G_{11} H_I^{(1)} G_{a2}^\square \quad \text{and} \\ G_{21} &= G_{2a}^\square H_I^{\dagger(1)} G_{11} \quad , \end{aligned}$$

from which directly follows

$$H_I^{(1)} G_{a2}^\square = G_{11}^{-1} G_{12} \quad \text{and} \quad (3.87)$$

$$G_{2a}^\square H_I^{\dagger(1)} = G_{21} G_{11}^{-1} \quad . \quad (3.88)$$

The remaining Dyson equations for the diagonal surface GFs are

$$G_{11} = G_{11}^0 + G_{11}^0 H_I^{(1)} G_{aa}^\square H_I^{\dagger(1)} G_{11} \quad \text{and} \quad (3.89)$$

$$G_{22} = G_{22}^\square + G_{2a}^\square H_I^{\dagger(1)} G_{11} H_I^{(1)} G_{a2}^\square \quad . \quad (3.90)$$

By multiplication with G_{11}^{-1} from the right and the definition of the GF of the decoupled first slice,

$$G_{11}^0 = (E - H_0^{(1)})^{-1} \quad ,$$

Eq. (3.89) is reshaped to yield

$$H_I^{(1)} G_{aa}^\square H_I^{\dagger(1)} = E - H_0^{(1)} - G_{11}^{-1} \quad . \quad (3.91)$$

Eq. (3.90) is multiplied with H_I from the left and H_I^\dagger from the right. By the use of Eqs. (3.87) and (3.88) we find

$$H_I^\dagger G_{22}^\square H_I = H_I^\dagger G_{22} H_I - H_I^\dagger G_{21} G_{11}^{-1} G_{12} H_I \quad . \quad (3.92)$$

Eqs. (3.87), (3.88), (3.91) and (3.92) are the desired replacements of the terms depending on $\{G^\square\}$ in Eqs. (3.84)-(3.86). Substituting these, we find the definitions of the effective Hamiltonian subblocks

$$\bar{H}_0 = E - G_{11}^{-1} + H_I^\dagger (G_{22} - G_{21} G_{11}^{-1} G_{12}) H_I \quad , \quad (3.93)$$

$$\bar{H}_I = G_{11}^{-1} G_{12} H_I \quad , \quad (3.94)$$

$$\bar{H}_I^\dagger = H_I^\dagger G_{21} G_{11}^{-1} \quad . \quad (3.95)$$

With this, we have established a method that maps the problem of a super-cell structure back onto the problem of a clean rectangular lead of constant height. The effective Hamiltonian subblocks of Eqs. (3.93)-(3.95) can be constructed entirely by the surface GFs of single super-cells. However, we have to mention that the

calculation of the band structure is still a little more complicated since one can not just solve Eq. (3.83) for fixed k_x . The reason for this is that the effective Hamiltonians intrinsically depend on the energy E . This dependence is a result of the surface GFs. Hence, one needs to solve Eq. (3.83) by calculating β for fixed E which is done by doubling the dimension of the problem analogously to Eq. (3.15).

As an example of a disordered super-cell structure, we turn towards two-dimensional topological insulators that were discussed in chapter 2. As these materials feature gapless edge states that are very resilient to disorder, we can check on this resilience by calculating a band structure of a disordered super-cell. Exemplary results are shown in Fig. 3.19. The red crosses in the plot show the original band structure of the topological system within the energy region where pure edge-transport is present. One can clearly see that the linear edge states are present in this entire energy interval. The blue crosses show the band structure of an infinitely long array of disordered super-cells under strong disorder. As expected the edge-states persist in most of the energy region and are just shifted in energy and momentum.

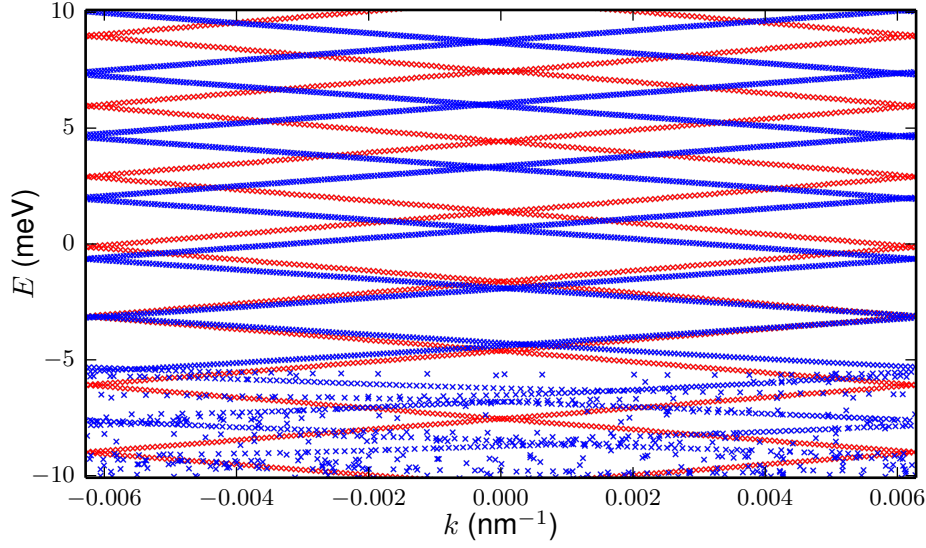


Figure 3.19.: The red crosses show the band structure of a clean two dimensional topological insulator with QW parameters $A = 364.5 \text{ nm} \cdot \text{meV}$, $B = -686.0 \text{ nm}^2 \cdot \text{meV}$, $D = -512.0 \text{ nm}^2 \cdot \text{meV}$, $m = -10.0 \text{ meV}$. The blue crosses represent the band structure for a lead consisting of quadratic, disordered super-cells of length and width $W = L = 500 \text{ nm}$. The disorder follows a uniformly random distribution with a disorder strength $U = 60 \text{ meV}$. To allow for a better comparison, the band structure of the clean lead (red crosses) is folded back into the shrunk Brillouin zone of the super-cell structure between $-\pi/L$ and $+\pi/L$. We find that the edge states indeed resist the disorder and exist also in the disorder super-cell. The grid-constants in the numerics are in both calculations set to $\Delta y = \Delta x = 5 \text{ nm}$.

3.9. Super-cell Bloch functions

In the previous section we have shown how surface GFs can be used to calculate the Bloch eigenvalues β and thereby the band structure of super-cell structures. In Eq. (3.83) we found, that for the calculation of these eigenvalues, it is sufficient to only consider a small part $\vec{\chi}_1$ that is describing only the first slice of the super-cell instead of the full eigenvector $\vec{\chi}$. However, the full Bloch eigenvector $\vec{\chi}$ is also of physical interest and should be accessible. Hence, we will try to find a method in order to also calculate the rest of the eigenvectors starting from $\vec{\chi}_1$ that is computed using Eq. (3.83). For this purpose we can start at the beginning of the derivation in the previous section at Eq. (3.76) and directly plug in Eqs. (3.75), (3.73) and

(3.74). By direct multiplication of H_I^{SC} and $H_I^{\dagger\text{SC}}$ we find

$$H_0^{\text{SC}} \begin{pmatrix} \vec{\chi}_1 \\ \vdots \\ \vec{\chi}_2 \end{pmatrix} + \begin{pmatrix} \beta H_I^{\dagger} \vec{\chi}_2 \\ 0 \\ \vdots \\ 0 \end{pmatrix} + \begin{pmatrix} 0 \\ \vdots \\ 0 \\ \beta^{-1} H_I \vec{\chi}_1 \end{pmatrix} = E \begin{pmatrix} \vec{\chi}_1 \\ \vdots \\ \vec{\chi}_2 \end{pmatrix} ,$$

which we can rearrange such that

$$\begin{pmatrix} \vec{\chi}_1 \\ \vdots \\ \vec{\chi}_2 \end{pmatrix} = (E - H_0^{\text{SC}})^{-1} \begin{pmatrix} \beta H_I^{\dagger} \vec{\chi}_2 \\ 0 \\ \vdots \\ 0 \\ \beta^{-1} H_I \vec{\chi}_1 \end{pmatrix} = G \begin{pmatrix} \beta H_I^{\dagger} \vec{\chi}_2 \\ 0 \\ \vdots \\ 0 \\ \beta^{-1} H_I \vec{\chi}_1 \end{pmatrix} . \quad (3.96)$$

In this way, again the full GF G of the super-cell has entered. By using its block-form Eq. (3.25) we can decompose Eq. (3.96) line-wise and find for the Bloch function $\vec{\chi}_j$ at some arbitrary slice j within the super-cell the relation

$$\vec{\chi}_j = G_{j1} \beta H_I^{\dagger} \vec{\chi}_2 + G_{j2} \beta^{-1} H_I \vec{\chi}_1 . \quad (3.97)$$

Evaluating this equation at $j = 1$ gives

$$\vec{\chi}_1 = G_{11} \beta H_I^{\dagger} \vec{\chi}_2 + G_{12} \beta^{-1} H_I \vec{\chi}_1 . \quad (3.98)$$

from which we find

$$\vec{\chi}_2 = \beta^{-1} \left(H_I^{\dagger} \right)^{-1} G_{11}^{-1} (\mathbb{1} - \beta^{-1} G_{12} H_I) \vec{\chi}_1 . \quad (3.99)$$

Plugging this back into Eq. (3.97) leads to the final result for the Bloch function $\vec{\chi}_j$ at each slice j

$$\vec{\chi}_j = G_{j1} G_{11}^{-1} (\mathbb{1} - \beta^{-1} G_{12} H_I) \vec{\chi}_1 + G_{j2} \beta^{-1} H_I \vec{\chi}_1 = G_{j1} \vec{\xi} + G_{j2} \vec{\eta}' . \quad (3.100)$$

This equation is of the exact same form as Eq. (3.37) that was used for the calculation of the scattering wave function, but with different definitions for

$$\vec{\xi} = G_{11}^{-1} (\mathbb{1} - \beta^{-1} G_{12} H_I) \vec{\chi}_1 , \quad (3.101)$$

$$\vec{\eta}' = \beta^{-1} H_I \vec{\chi}_1 . \quad (3.102)$$

This analogy allows us to use the picture algorithms introduced in section 3.6 also for the calculation of Bloch functions, a very handy feature.

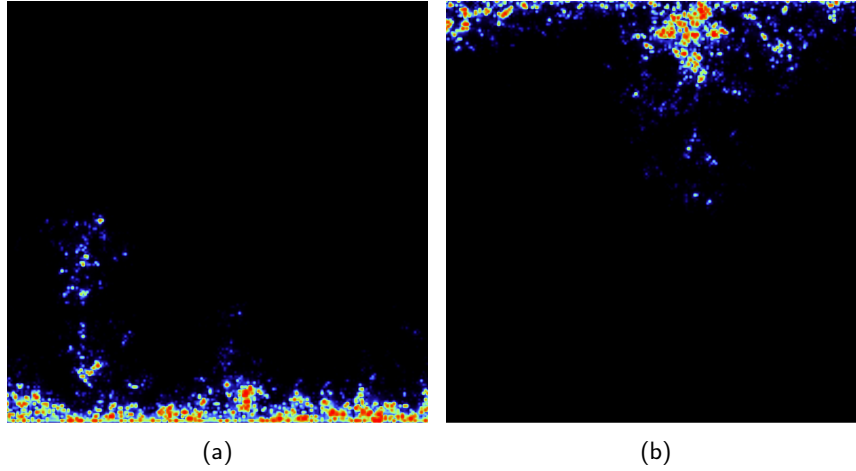


Figure 3.20.: This figure shows the Bloch functions of a disordered super-cell of two-dimensional topological insulator of length and width $L = W = 1000$ nm. The disorder follows a uniformly random distribution with amplitude (disorder strength) $U = 180$ meV. We used the parameters $A = 364.5$ nm \cdot meV, $B = -686.0$ nm² \cdot meV, $D = -512.0$ nm² \cdot meV and $m = +1.0$ meV, which is in the clean limit an ordinary insulator due to the positive topological mass $m > 0$. The Fermi energy is set to $E_F = 16$ meV. As the pictures show, the disorder, indeed, leads to a topological phase transition and the depicted effective edge states exist even in an infinitely long, disordered system that is our super-cell structure.

As an exemplary result we again look at two-dimensional topological insulators as discussed in chapter 2. In section 2.3 we investigated in detail a disorder-induced topological phase, called the topological Anderson insulator (TAI). This phase even occurs in the presence of disorder if the clean system does not feature a topologically distinct phase. This example of a topological phase transition was investigated using transport calculations through a disordered stripe of finite length as shown in Fig. 2.2(c). There, the TAI phase is identified as the green conductance plateau that occurs at strong disorder. The calculation of Bloch functions allows us to also look directly at the states of an infinitely long waveguide consisting of disordered super-cells. Indeed, the pictures in Fig. 3.20 show that the only open modes at these values of disorder and Fermi energy are counter-propagating edge-states situated at opposing edges.

Summary and outlook

In this work we investigated effects that are closely related to Anderson localization or the robustness against the latter. In a collaborative project with the University of San Antonio, Texas, we were concerned with, what we called, the single-channel regime of transport. Our numerical and experimental results validate a close relation between the single transmission eigenchannel dominant in this regime and the internal modes of the system. We showed that in this regime a single transmission eigenchannel is either formed by a single such mode or by a combination of a few modes resulting in a necklace state. By statistical means we could show that a disordered sample in the single-channel regime can be described as a one-dimensional system with a renormalized localization length, thereby providing a very simple description of such complex systems. In addition, we showed that the cross-over to the single-channel regime is unique and can be charted in terms of a well-suited statistical quantity that captures both the behavior in our two-dimensional numerics as well as in the three-dimensional microwave experiments. This cross-over could even be shown in the time-domain when the samples are excited by Gaussian pulses. For pulses with suitably chosen width, the single-channel transport through necklace states could be identified at short time-delays, whereas at large time delays single-channel transport through single long-lived localized modes could be observed. These results are fundamental for the understanding of waves in random media and provide opportunities for enhancing energy transfer through strongly-scattering systems.

Apart from Anderson localization, we investigated another wave-effect that has concerned physicists for the past 15 years, i.e., the effect of branched flow. This phenomenon occurs in disordered media in which the disorder potential is weak but smooth. Such systems develop branches along which an injected flow is guided through the medium. In particular, we asked the question how to control and utilize this effect for future applications. In an exemplary optical system we developed a method that allows for the injection of a wave in such a way that almost all the flow travels just along a single such branch. We showed that this finding is not trivial and fairly stable over a large frequency range. Although our methods rely on the scattering matrix, we found that already small parts of it are sufficient for a fair amount of control of branched flow. The amount of information that needs to be measured should thus be within experimental reach and our results might provide an important step forward in wavefront shaping and wave control.

In the second part of this thesis, we were concerned with a new class of materials that promise exciting properties in terms of transport. In such two-dimensional topological insulators, edge states that are robust against disorder and Anderson localization are present. Moreover, these edge states can even occur as a result of disorder which leads to enhanced transport properties. Our calculations show that a finite spatial correlation of the disorder potential enhances finite-size effects and may entirely suppress the aforementioned regime of quantized conductance known as the topological Anderson insulator (TAI) phase. We thereby extend previous studies in which only uncorrelated disorder potentials were considered. To describe the observed boundaries of quantized conductance theoretically, we perform a scaling analysis and adapt an existing effective medium theory to the case of spatially correlated potentials which yields quantitative agreement with our numerics. Our results suggest that for observing the topological Anderson insulator phase experimentally, it will be necessary to work with comparatively large samples (to suppress finite size effects) and with very short ranged disorder potentials as any long-range correlations may strongly suppress this topologically nontrivial phase. We speculate that spatial correlations might also be an important impediment to eliminate the bulk conductance in three-dimensional topological insulators. This would certainly constitute an interesting topic for further investigations.

In a follow-up work, we linked this phenomenon with a quantum percolation transition that we found to occur in the limit of correlated strong disorder. While the reason for the emergence of the TAI had already been understood, its breakdown could so far only be vaguely connected to a delocalization of bulk states. Here we showed that in a spatially correlated potential this delocalization is caused primarily by bulk states, that are localized when circumnavigating the hills of the disorder potential, but that become connected with each other when passing a percolation threshold. These connections and thus also the delocalization transition are consolidated by local edge states that can internally form in the disordered sample. By showing how the localized bulk states derive from flat bands in the valence band structure of the clean sample without disorder, we clarified that the same physics is at work also in the well-studied case of an uncorrelated disorder potential.

Additionally, we investigated the effects of magnetic fields on two-dimensional topological insulators. We proposed a device that could be used for basic interference experiments using the edge states of a two-dimensional topological insulator. The setup relies on building a quantum well structure in a cylindrical shape or possibly by using topological insulator thin films. By the application of two quantum point contacts (QPCs) the geometry is equivalent to a classical Mach-Zehnder interferometer which lets us observe oscillations of the transmission (conductance) as a function of Fermi energy. When applying a very weak and in-plane magnetic field through the core of the cylinder, we find that the device can in addition use the Aharonov-Bohm effect in order to serve as a spin-filter and spin-transistor. Again

the numerical results agree very well with a simple analytical model that we derived. Moreover, we could numerically demonstrate 4 possible settings of our spin-transistor. The realization of such a device would open up countless opportunities for measurements of topological insulator properties and technological applications in spin-tronics and low-power information processing.

The last chapter of this work is dedicated to various computational strategies that we implemented to make the numerics more efficient. As the numerical solution of scattering problems comes down to the calculation of surface Green's functions (GFs) of the scattering region, we were concerned with making this task as efficient as possible. While the calculation effort is already minimal in the commonly used modular recursive Green's function method, we concentrated here on an efficient parallelization of the required tasks. Since the fastest way of calculating the required surface GFs (called parallel Dyson algorithm - PDA) still leaves some of the calculation power in a parallel computation unused, we developed an algorithm (parallel permutation algorithm - PPA) that fills these gaps. While suffering from some overhead due to additional communication effort, this extra time proves well invested when, in addition to the scattering problem, scattering wave functions need to be computed. Moreover, we developed an algorithm for the efficient calculation of the local density of states. For this application, the PPA paves the way to parallelization that would otherwise not be possible. All these results are tested through by extensive benchmarks that proved our methods to allow access to larger and better-resolved systems than before.

As another numerical task we addressed the evaluation of so-called super-cell structures. Such a problem considers the task of periodically glueing together a scattering region (super-cell) to itself which results in the existence of a band structure. We found an efficient way to calculate such band structures by the use of surface Green's functions. In addition, we also showed how one can calculate the associated Bloch functions (eigenstates) in a parallel and efficient manner. For this problem we found that the PPA is once more useful since our parallel algorithm for the calculation of scattering wave functions can, with some adjustments, also be employed. Both the aforementioned applications are very useful for a better understanding and simulation of disordered system. In particular, our techniques provide access to very large systems that could not be investigated previously.

Appendix A.

Numerical Implementation of the BHZ model

A.1. Unperturbed BHZ model

The effective Hamiltonian of the BHZ model given by Eq. (2.1) includes no coupling between the spin-up and spin-down block which is why we can in a simplified numerical picture just use the upper block $h(\vec{k})$. Plugging in the explicit expressions for $\epsilon(\vec{k})$ and $d_i(\vec{k})$ as well as the Pauli-matrices into Eq. (2.2) and setting $C = 0$ yields

$$h(\vec{k}) = \begin{pmatrix} -(D+B)(k_x^2 + k_y^2) + M & A(k_x + ik_y) \\ A(k_x - ik_y) & -(D-B)(k_x^2 + k_y^2) - M \end{pmatrix}. \quad (\text{A.1})$$

In real space k_x and k_y are represented by the operators according to the Peierls relations

$$k_x \rightarrow -i \frac{d}{dx} = -i\partial_x, \quad (\text{A.2})$$

$$k_y \rightarrow -i \frac{d}{dy} = -i\partial_y \quad (\text{A.3})$$

which in combination with Eq. (A.1) leaves us with

$$h(\vec{k}) = \begin{pmatrix} (D+B)(\partial_x^2 + \partial_y^2) + M & A(\partial_y - i\partial_x) \\ A(-\partial_y - i\partial_x) & (D-B)(\partial_x^2 + \partial_y^2) - M \end{pmatrix}. \quad (\text{A.4})$$

In order to solve the Schrödinger equation defined by the above Hamiltonian $h(\vec{k})$ we need to numerically realize this operator. For this purpose we use the finite differences method described in section 3.1 and approximate the occurring derivatives by Eqs. (3.4)-(3.7).

The Hamiltonian in Eq. (A.1) raises further difficulties due to the additional (orbital) degree of freedom provided by the quantum well subbands $|E1+\rangle$ and

$|H1+\rangle$. Unlike in the case of a scalar wave function Eq. (3.2), this two-component spinor

$$\psi(x, y) = \begin{pmatrix} \psi^{E1+}(x, y) \\ \psi^{H1+}(x, y) \end{pmatrix} . \quad (\text{A.5})$$

must numerically be represented by two complex values $\psi_{i,j}^E$ and $\psi_{i,j}^H$ at each grid-point (x_i, y_j) instead of only a single one. The ordering of this components can in principle be chosen at will, however, it is preferable to preserve the tridiagonal block shape of the full Hamiltonian matrix according to Eq. (3.3) which can be guaranteed by the following arrangement for the numerical wave function vector

$$\vec{\psi} = \begin{pmatrix} \psi_{1,1}^E \\ \vdots \\ \psi_{1,n_y}^E \\ \psi_{1,1}^H \\ \vdots \\ \psi_{1,n_y}^H \\ \psi_{1,1}^E \\ \vdots \\ \vdots \\ \psi_{n_x,n_y}^H \end{pmatrix} . \quad (\text{A.6})$$

In this way the doubling of the dimension of the whole Hamiltonian matrix H from a $n_y n_x \times n_y n_x$ to a $2n_y n_x \times 2n_y n_x$ matrix translates to the block matrices H_0 and H_I being now of size $2n_y \times 2n_y$. Additionally also H_0 and H_I are split into 4 blocks of size $n_y \times n_y$ in a similar way as the Hamiltonian in Eq. (A.1), explicitly

$$H_0 = \begin{pmatrix} H_0^{11} & H_0^{12} \\ H_0^{21} & H_0^{22} \end{pmatrix} \quad \text{and} \quad (\text{A.7})$$

$$H_I = \begin{pmatrix} H_I^{11} & H_I^{12} \\ H_I^{21} & H_I^{22} \end{pmatrix} . \quad (\text{A.8})$$

Substituting the derivatives in (A.1) by the finite differences of Eqs. (3.4)-(3.7), the

elements of the $n_y \times n_y$ matrices from (A.7) can be determined to be:

$$H_0^{11} = \begin{pmatrix} -2a + M & c & 0 & \dots & 0 \\ c & -2a + M & c & \ddots & \vdots \\ 0 & \ddots & \ddots & \ddots & 0 \\ \vdots & \ddots & c & -2a + M & 0 \\ 0 & \dots & 0 & c & -2a + M \end{pmatrix}, \quad (\text{A.9})$$

$$H_0^{12} = \begin{pmatrix} 0 & g & 0 & \dots & 0 \\ -g & 0 & g & \ddots & \vdots \\ 0 & \ddots & \ddots & \ddots & 0 \\ \vdots & \ddots & -g & 0 & g \\ 0 & \dots & 0 & -g & 0 \end{pmatrix}, \quad (\text{A.10})$$

$$H_0^{21} = \begin{pmatrix} 0 & -g & 0 & \dots & 0 \\ g & 0 & -g & \ddots & \vdots \\ 0 & \ddots & \ddots & \ddots & 0 \\ \vdots & \ddots & g & 0 & -g \\ 0 & \dots & 0 & g & 0 \end{pmatrix}, \quad (\text{A.11})$$

$$H_0^{22} = \begin{pmatrix} -2d - M & f & 0 & \dots & 0 \\ f & -2d - M & f & \ddots & \vdots \\ 0 & \ddots & \ddots & \ddots & 0 \\ \vdots & \ddots & f & -2d - M & f \\ 0 & \dots & 0 & f & -2d - M \end{pmatrix} \quad (\text{A.12})$$

with

$$\begin{aligned} a &= (D + B) \left(\frac{1}{(\Delta y)^2} + \frac{1}{(\Delta x)^2} \right), \\ d &= (D - B) \left(\frac{1}{(\Delta y)^2} + \frac{1}{(\Delta x)^2} \right), \\ c &= \frac{D + B}{(\Delta y)^2}, \\ f &= \frac{D - B}{(\Delta y)^2}, \\ g &= \frac{A}{2\Delta y}, \end{aligned} \quad (\text{A.13})$$

The diagonal of H_0 (i.e. the diagonals of H_0^{11} and H_0^{22}) come from the second derivatives of Eqs. (3.6) and (3.7) which contain a term that produces an interaction of every grid-point with itself with a factor 2. As a result the diagonal elements $-2a + M$ and $-2d - M$ depend on both, Δx and Δy , quadratically. The other terms in the second derivative with respect to y (namely c and f) manifest in the secondary diagonals of H_0^{11} and H_0^{22} . The first derivative with respect to y in the off-diagonals of Eq. (A.1) results in interaction between adjacent points in y -direction [see Eq. (3.5)] and thus appears in the secondary diagonal of H_0^{12} and H_0^{21} . Analogously the subblocks of H_I (A.8) are given by

$$H_I^{11} = \begin{pmatrix} b & 0 & \dots & \dots & 0 \\ 0 & b & \ddots & \dots & \vdots \\ \vdots & \ddots & \ddots & \ddots & \vdots \\ \vdots & \dots & \ddots & b & 0 \\ 0 & \dots & \dots & 0 & b \end{pmatrix}, \quad (\text{A.14})$$

$$H_I^{12} = \begin{pmatrix} -ih & 0 & \dots & \dots & 0 \\ 0 & -ih & \ddots & \dots & \vdots \\ \vdots & \ddots & \ddots & \ddots & \vdots \\ \vdots & \dots & \ddots & -ih & 0 \\ 0 & \dots & \dots & 0 & -ih \end{pmatrix}, \quad (\text{A.15})$$

$$H_I^{21} = \begin{pmatrix} -ih & 0 & \dots & \dots & 0 \\ 0 & -ih & \ddots & \dots & \vdots \\ \vdots & \ddots & \ddots & \ddots & \vdots \\ \vdots & \dots & \ddots & -ih & 0 \\ 0 & \dots & \dots & 0 & -ih \end{pmatrix}, \quad (\text{A.16})$$

$$H_I^{22} = \begin{pmatrix} e & 0 & \dots & \dots & 0 \\ 0 & e & \ddots & \dots & \vdots \\ \vdots & \ddots & \ddots & \ddots & \vdots \\ \vdots & \dots & \ddots & e & 0 \\ 0 & \dots & \dots & 0 & e \end{pmatrix}, \quad (\text{A.17})$$

where we used the following abbreviations

$$\begin{aligned} b &= \frac{D + B}{(\Delta x)^2} , \\ e &= \frac{D - B}{(\Delta x)^2} , \\ h &= \frac{A}{2\Delta x} . \end{aligned} \tag{A.18}$$

The terms in the diagonals of H_I^{11} and H_I^{22} (namely b and e) again originate from the second derivative in the diagonal of $h(\vec{k})$ from Eq. (A.1), whereas the first derivative terms in the off-diagonals with imaginary prefactor $-i$ take effect in the diagonals of the off-diagonal blocks H_I^{12} and H_I^{21} .

A.2. Including Rashba coupling and Bulk inversion asymmetry

So far it was sufficient to only solve the spin-up block $h(\vec{k})$ Eq. (2.2) of the full effective Hamiltonian from Eq. (2.1) since the spin-down block directly follows by a time-reversal symmetry operation. Still one could also exclusively solve the spin-down block $h^*(-\vec{k})$ which means just complex conjugation and substitution of \vec{k} by $-\vec{k}$. Having a look at Eq. (A.4) we can see that this would not change entries in the diagonal since they are real and only quadratic in \vec{k} . Also in the off-diagonal this would only correspond to a substitution of $\frac{d}{dy} \rightarrow -\frac{d}{dy}$ since these are the only real and linear terms in \vec{k} . The elements of the finite differences Hamiltonian matrix resulting from the derivative with respect to y appear only in the off-diagonal sub-blocks of H_0 . Switching from $\frac{d}{dy}$ to $-\frac{d}{dy}$ will hence cause a change of sign in all the matrix elements of H_0^{12} and H_0^{21} from Eqs. (A.9)-(A.12). So numerically we can simply replace g by $-g$ in order to perform implementation of the time-reversal counterpart $h^*(-\vec{k})$.

Additional off-diagonal terms in the effective Hamiltonian Eq. (2.1) can be introduced in order to make the description more accurate (see section 2.5). The first such correction is the bulk inversion asymmetry (BIA) term which is repeated here for easier readability:

$$H_{\text{BIA}} = \begin{pmatrix} & & 0 & -\Delta \\ & 0 & \Delta & 0 \\ 0 & \Delta & & \\ -\Delta & 0 & & 0 \end{pmatrix} . \tag{2.10 revisited}$$

The second possible additional correction is the Rashba coupling term, which also is repeated here for the reader's convenience:

$$H_{\text{RC}} = \begin{pmatrix} 0 & -iR_0k_- & 0 \\ & 0 & 0 \\ iR_0k_+ & 0 & \\ 0 & 0 & 0 \end{pmatrix}. \quad (2.11 \text{ revisited})$$

As these corrections are off-diagonal in the four-band basis, a description in terms of only a single spin-block $h(\vec{k})$ Eq. (2.2) is not sufficient anymore. In this case we have to take into account also the spin-degree of freedom for both QW subbands, meaning that the spin-up (+) subbands $|E_1, +\rangle$ and $H_1, +\rangle$ are now also accompanied by spin-down (-) subbands $|E_1, -\rangle$ and $H_1, -\rangle$ making use of a four-component spinor necessary. Ordering the complex wave functions in this spinor analogously to Eq. (A.6) yields numerical matrices H_0 and H_I which both decompose into 4 blocks each of which again consists of 4 $n_y \times n_y$ blocks:

$$H_{0/I} = \left(\begin{array}{c|c} H_{0/I,\uparrow\uparrow} & H_{0/I,\uparrow\downarrow} \\ \hline H_{0/I,\downarrow\uparrow} & H_{0/I,\downarrow\downarrow} \end{array} \right) = \left(\begin{array}{cc|cc} H_{0/I,\uparrow\uparrow}^{11} & H_{0/I,\uparrow\uparrow}^{12} & H_{0/I,\uparrow\downarrow}^{11} & H_{0/I,\uparrow\downarrow}^{12} \\ H_{0/I,\uparrow\uparrow}^{21} & H_{0/I,\uparrow\uparrow}^{22} & H_{0/I,\uparrow\downarrow}^{21} & H_{0/I,\uparrow\downarrow}^{22} \\ \hline H_{0/I,\downarrow\uparrow}^{11} & H_{0/I,\downarrow\uparrow}^{12} & H_{0/I,\downarrow\downarrow}^{11} & H_{0/I,\downarrow\downarrow}^{12} \\ H_{0/I,\downarrow\uparrow}^{21} & H_{0/I,\downarrow\uparrow}^{22} & H_{0/I,\downarrow\downarrow}^{21} & H_{0/I,\downarrow\downarrow}^{22} \end{array} \right). \quad (A.19)$$

The upper left block $H_{0/I,\uparrow\uparrow}$ of H_0 as well as H_I correspond to $h(\vec{k})$ in Eq. (2.1) and are thus given by Eqs. (A.9) to (A.12) and (A.14) to (A.17) respectively. The constituents of $H_{0/I,\downarrow\downarrow}$ analogously represent $h^*(\vec{k})$ and are correspondingly numerically equal to those of $H_{0/I,\uparrow\uparrow}$ apart from a change of the parameter $g \rightarrow -g$ in $H_{0,\downarrow\downarrow}^{12}$ and $H_{0,\downarrow\downarrow}^{21}$ as compared to $H_{0,\uparrow\uparrow}^{12}$ and $H_{0,\uparrow\uparrow}^{21}$ respectively.

To include the BIA term numerically we know that the Δ -terms from Eq. (2.10) mediate an interaction between different degrees of freedom at, numerically speaking, the same point (x_i, y_i) . Thus these terms have to be diagonal and appear in the corresponding off-diagonal subblocks of $H_{0,\uparrow\downarrow}$ and $H_{0,\downarrow\uparrow}$ reading

$$H_{0,\uparrow\downarrow}^{12} = H_{0,\downarrow\uparrow}^{21} = \begin{pmatrix} -\Delta & & \\ & \ddots & \\ & & -\Delta \end{pmatrix} \quad \text{and} \quad (A.20)$$

$$H_{0,\uparrow\downarrow}^{21} = H_{0,\downarrow\uparrow}^{12} = \begin{pmatrix} \Delta & & \\ & \ddots & \\ & & \Delta \end{pmatrix}. \quad (A.21)$$

For the Rashba coupling terms of Eq. (2.11) implementation is slightly more difficult since these terms depend on $k_{\pm} = k_x \pm ik_y$ which in real space transforms into first derivatives with respect to x and y :

$$H_{\text{RC}} = \begin{pmatrix} 0 & R_0(-\partial_x + i\partial_y) & 0 \\ R_0(\partial_x + i\partial_y) & 0 & 0 \\ 0 & 0 & 0 \end{pmatrix}. \quad (\text{A.22})$$

Accordingly, the derivatives with respect to y enter in the secondary diagonal of specific subblocks of H_0 ,

$$H_{0,\uparrow\downarrow}^{11} = H_{0,\downarrow\uparrow}^{11} = \begin{pmatrix} 0 & ir_y & 0 & \dots & 0 \\ -ir_y & 0 & ir_y & \ddots & \vdots \\ 0 & \ddots & \ddots & \ddots & 0 \\ \vdots & \ddots & -ir_y & 0 & ir_y \\ 0 & \dots & 0 & -ir_y & 0 \end{pmatrix} \quad (\text{A.23})$$

with

$$r_y = \frac{R_0}{2\Delta y}. \quad (\text{A.24})$$

Analogously, the first derivatives with respect to x enter the numerical formalism in the diagonals of subblocks of H_I ,

$$H_{I,\uparrow\downarrow}^{11} = \begin{pmatrix} -r_x & 0 & \dots & \dots & 0 \\ 0 & -r_x & \ddots & \dots & \vdots \\ \vdots & \ddots & \ddots & \ddots & \vdots \\ \vdots & \dots & \ddots & -r_x & 0 \\ 0 & \dots & \dots & 0 & -r_x \end{pmatrix} \quad \text{and} \quad H_{I,\downarrow\uparrow}^{11} = \begin{pmatrix} r_x & 0 & \dots & \dots & 0 \\ 0 & r_x & \ddots & \dots & \vdots \\ \vdots & \ddots & \ddots & \ddots & \vdots \\ \vdots & \dots & \ddots & r_x & 0 \\ 0 & \dots & \dots & 0 & r_x \end{pmatrix} \quad (\text{A.25})$$

defining

$$r_x = \frac{R_0}{2\Delta x}. \quad (\text{A.26})$$

Appendix B.

Implementation of a magnetic field

B.1. The Peierls substitution

Assume a physical system described by a Hamilton operator $\hat{H}(\hat{k})$ with the wavenumber operator \hat{k} being related to the momentum operator by $\hat{p} = \hbar\hat{k}$. The usual way of including an external magnetic field \vec{B} is the minimal substitution

$$\hat{k} \rightarrow \hat{k} - \frac{e}{\hbar} \vec{A} \quad (\text{B.1})$$

with \vec{A} representing the magnetic vector potential fulfilling the relation $\text{rot} \vec{A} = \vec{B}$. An important detail is that this form of the minimal substitution is given in SI units while in atomic units the prefactor of the vector potential changes from e/\hbar to e/c . The Schrödinger equation then reads

$$\hat{H}(\hat{k} - \frac{e}{\hbar} \vec{A}) \psi(\vec{r}) = E \psi(\vec{r}) \quad . \quad (\text{B.2})$$

Numerically one could approach this problem straight forward by combining Eqs. (A.2) and (A.3) with Eq. (B.1) and in this way directly modify the spatial derivatives ∂_x and ∂_y and all their resulting terms in the finite difference approach from section 3.1. The problem with this solution is that the vector potential \vec{A} usually depends on the coordinates x and y of the geometry. Hence for large geometries the values for the components of \vec{A} can due to their positional dependence become very large and cause heavy numerical instability. A far more convenient and numerically preferable way of implementing the minimal substitution from Eq. (B.1) is in terms of the Peierls substitution. The principle of this method is to instead of mapping the effects of the external field into the Hamiltonian $\hat{H}(\hat{k})$, the wave function $\psi(\vec{r})$ is replaced by

$$\Phi(\vec{r}) = e^{-i \frac{e}{\hbar} \int_0^{\vec{r}} \vec{A}(\vec{r}') d\vec{r}'} \psi(\vec{r}) \quad . \quad (\text{B.3})$$

Using the abbreviation for the phase in the prefactor of Eq. (B.3)

$$\phi(\vec{r}) = \int_0^{\vec{r}} \vec{A}(\vec{r}') d\vec{r}' \quad (\text{B.4})$$

and the chain rule in order to investigate the action of the wavenumber operator $\hat{k} = -i\vec{\nabla}$ on this wave function $\Phi(\vec{r})$ we get

$$\hat{k} \cdot \Phi(\vec{r}) = \hat{k} \left[e^{-i\frac{e}{\hbar}\phi(\vec{r})} \psi(\vec{r}) \right] = e^{-i\frac{e}{\hbar}\phi(\vec{r})} \hat{k} \psi(\vec{r}) - i\frac{e}{\hbar} \left[\hat{k} \phi(\vec{r}) \right] e^{-i\frac{e}{\hbar}\phi(\vec{r})} \psi(\vec{r}) \quad .$$

Using

$$i\frac{e}{\hbar}[\hat{k}\phi(\vec{r})] = \frac{e}{\hbar}\vec{\nabla} \int_0^{\vec{r}} \vec{A}(\vec{r}') d\vec{r}' = \frac{e}{\hbar}\vec{A}(\vec{r})$$

this can be simplified to

$$\hat{k} \cdot \Phi(\vec{r}) = e^{-i\frac{e}{\hbar}\phi(\vec{r})} \left(\hat{k} - \frac{e}{\hbar}\vec{A} \right) \psi(\vec{r}) \quad . \quad (\text{B.5})$$

Analogously the action of every integer power \hat{k}^n of the wavenumber operator on $\Phi(\vec{r})$ yields

$$\hat{k}^n \cdot \Phi(\vec{r}) = e^{-i\frac{e}{\hbar}\phi(\vec{r})} \left(\hat{k} - \frac{e}{\hbar}\vec{A} \right)^n \psi(\vec{r}) \quad (\text{B.6})$$

and thus for every Hamiltonian $\hat{H}(\hat{k})$ that can be expressed as a converging power series in terms of \hat{k}

$$\hat{H}(\hat{k}) = \sum_{n=0}^{\infty} h_n \hat{k}^n$$

it follows that

$$\hat{H}(\hat{k}) \cdot \Phi(\vec{r}) = e^{-i\frac{e}{\hbar}\phi(\vec{r})} \hat{H} \left(\hat{k} - \frac{e}{\hbar}\vec{A} \right) \psi(\vec{r}) = E \Phi(\vec{r}) = e^{-i\frac{e}{\hbar}\phi(\vec{r})} E \psi(\vec{r}) \quad . \quad (\text{B.7})$$

This shows that the Schrödinger equation

$$\hat{H}(\hat{k}) \phi(\vec{r}) = E \phi(\vec{r}) \quad (\text{B.8})$$

for the original Hamiltonian $H(\hat{k})$ acting on the modified wave function $\phi(\vec{r})$ is after division by the Peierls phase factor in Eq. (B.7) exactly equivalent to the Schrödinger equation in terms of the minimal substitution from Eq. (B.2). With this knowledge we can rewrite Eq. (B.8)

$$\begin{aligned} \hat{H}(\hat{k}) \phi(\vec{r}) &= \hat{H}(\hat{k}) e^{-i\frac{e}{\hbar}\phi(\vec{r})} \psi(\vec{r}) = E \cdot e^{-i\frac{e}{\hbar}\phi(\vec{r})} \psi(\vec{r}) \quad \Big| \quad e^{i\frac{e}{\hbar}\phi(\vec{r})} \\ \Rightarrow \quad e^{i\frac{e}{\hbar}\phi(\vec{r})} \hat{H}(\hat{k}) e^{-i\frac{e}{\hbar}\phi(\vec{r})} \psi(\vec{r}) &= E \cdot \psi(\vec{r}) \quad , \end{aligned} \quad (\text{B.9})$$

which can be used to map the Peierls substitution from the wave function back onto an effective Hamiltonian

$$\hat{\tilde{H}}(\hat{k}, \vec{A}) = e^{i\frac{e}{\hbar}\phi(\vec{r})} \hat{H}(\hat{k}) e^{-i\frac{e}{\hbar}\phi(\vec{r})} \quad (\text{B.10})$$

acting on the original wave function $\psi(\vec{r})$ according to

$$\hat{\tilde{H}}(\hat{k}, \vec{A}) \psi(\vec{r}) = E \psi(\vec{r}) . \quad (\text{B.11})$$

All-in-all we are left with a description of the system by the effective Hamiltonian from Eq. (B.10) as an alternative to the minimal substitution from Eq. (B.1). From a numerical point of view, the phases in the transformation from Eq. (B.10) are way easier to deal with since also large values of the components of \vec{A} do not lead to numerical instabilities as they are only included in the arguments of complex numbers.

B.1.1. General numerical formalism for the Peierls substitution

In any numerical scheme the geometry will be discretized on an array of N grid points $\{\vec{r}_n\}$. Thus the wave function $\psi(\vec{r})$ is represented as a vector $\vec{\psi}$ of N components $\psi_{\vec{r}_n} := \psi_n$ standing for the values of the wave function on any of these points (see section 3.1). A linear operator such as the Hamiltonian $\hat{H}(\hat{k})$ is then represented by a matrix H with matrix elements H_{nm} that describe the coupling of the wave functions on 2 grid points \vec{r}_n and \vec{r}_m . Hence the Schrödinger equation numerically decomposes into a system of N equations

$$\sum_{m=1}^N H_{nm} \psi_m = E \psi_n \quad (\text{B.12})$$

which can be written as a matrix eigenvalue problem

$$H \vec{\psi} = E \vec{\psi} . \quad (\text{B.13})$$

In order to numerically implement an external magnetic field with vector potential $\vec{A}(\vec{r})$ we need to calculate the effective Peierls Hamiltonian from Eq. (B.10) in this numerical scheme. The operators

$$\hat{U}(\vec{r}) = e^{i \frac{e}{\hbar} \phi(\vec{r})} \quad \text{and} \quad \hat{U}^\dagger(\vec{r}) = e^{-i \frac{e}{\hbar} \phi(\vec{r})}$$

of this unitary transformation can in this discretized space be represented by the diagonal matrices

$$U = \begin{pmatrix} e^{i \frac{e}{\hbar} \phi_1} & & \\ & \ddots & \\ & & e^{i \frac{e}{\hbar} \phi_N} \end{pmatrix} \quad \text{and} \quad U^\dagger = \begin{pmatrix} e^{-i \frac{e}{\hbar} \phi_1} & & \\ & \ddots & \\ & & e^{-i \frac{e}{\hbar} \phi_N} \end{pmatrix} \quad (\text{B.14})$$

with the phases ϕ_n analogously to Eq. (B.4) given by

$$\phi_n := \phi(\vec{r}_n) = \int_0^{\vec{r}_n} \vec{A}(\vec{r}') d\vec{r}' . \quad (\text{B.15})$$

Consequently the matrix \tilde{H} describing the Hamiltonian including the external field, reads analogously to Eq. (B.10)

$$\tilde{H} = U H U^\dagger , \quad (\text{B.16})$$

which for the individual matrix elements \tilde{H}_{mn} means

$$\tilde{H}_{nm} = \sum_{i=0}^N \sum_{j=0}^N U_{ni} H_{ij} U_{jm}^\dagger = \sum_{i,j} e^{i\frac{e}{\hbar}\phi_i} \delta_{ni} H_{ij} e^{-i\frac{e}{\hbar}\phi_j} \delta_{jm} = H_{nm} \cdot e^{-i\frac{e}{\hbar}(\phi_m - \phi_n)} . \quad (\text{B.17})$$

The definitions for the phases ϕ_n from Eqs. (B.15) and (B.4) yields

$$\phi_m - \phi_n = \int_0^{\vec{r}_m} \vec{A}(\vec{r}') d\vec{r}' - \int_0^{\vec{r}_n} \vec{A}(\vec{r}') d\vec{r}' = \int_{\vec{r}_n}^{\vec{r}_m} \vec{A}(\vec{r}') d\vec{r}' . \quad (\text{B.18})$$

In summary, the Peierls transformation from Eq. (B.10) can numerically executed by transforming every matrix element H_{nm} of the original Hamiltonian by means of

$$\tilde{H}_{nm} = H_{nm} \cdot e^{-i\frac{e}{\hbar}\phi_{nm}} \quad (\text{B.19})$$

with the given Peierls phase argument ϕ_{nm} depending on the grid point positions \vec{r}_n and \vec{r}_m and on the vector potential $\vec{A}(\vec{r})$ according to

$$\phi_{nm} := \phi_m - \phi_n = \int_{\vec{r}_n}^{\vec{r}_m} \vec{A}(\vec{r}) d\vec{r} . \quad (\text{B.20})$$

B.1.2. Implementation on a finite-difference square grid

In our work we usually use the finite differences method by means of discretization of the geometry on a square grid. As already discussed in section 3.1, we can thus use an ordering of the wave function vector $\vec{\psi}$ according to Eq. (A.6). In this way the subblocks H_0 and H_I can be repeatedly used to build up the full Hamilton matrix H of the entire geometry as given in Eq. (3.3). Accordingly, the Peierls transformation from Eq. (B.10) also holds for the matrix elements of H_0 and H_I according to

$$\tilde{H}_{0,nm} = H_{0,nm} \cdot e^{-i\frac{e}{\hbar}\phi_{nm}^{(0)}} , \quad (\text{B.21})$$

$$\tilde{H}_{I,nm} = H_{I,nm} \cdot e^{-i\frac{e}{\hbar}\phi_{nm}^{(I)}} . \quad (\text{B.22})$$

The Peierls phases $\phi_{nm}^{(0)}$ and $\phi_{nm}^{(I)}$ can be calculated analogously to Eq. (B.20) using the knowledge about the geometrical positions \vec{r}_n and \vec{r}_m of the points connected by H_0 and H_I . The matrix H_0 describes the coupling between the n_y points of a

single stripe in y-direction. These points with position vectors $\vec{r}_n^{(0)}$ connected by H_0 are thus given by

$$\vec{r}_n^{(0)} = \begin{pmatrix} x_0 \\ \Delta y \cdot n \\ 0 \end{pmatrix} \quad (\text{B.23})$$

with the constant x -component x_0 within a single stripe. In order to calculate the Peierls phase arguments $\phi_{nm}^{(0)}$ for the transformation of the matrix elements $H_{0,nm}$ we have to choose a curve $\vec{r}(t)$ parameterized by the real number t along which the line integral from Eq. (B.20) is evaluated. If we use the direct connection between the two points $\vec{r}_n^{(0)}$ and $\vec{r}_m^{(0)}$ we obtain

$$\vec{r}(t) = \vec{r}_n^{(0)} + (\vec{r}_m^{(0)} - \vec{r}_n^{(0)}) \cdot t = \vec{r}_n^{(0)} + \begin{pmatrix} 0 \\ \Delta y(m-n) \\ 0 \end{pmatrix} \cdot t = \begin{pmatrix} x_0 \\ \Delta y[n + (m-n)t] \\ 0 \end{pmatrix} . \quad (\text{B.24})$$

The vector potential $\vec{A}(\vec{r})$ can thus be evaluated along such a line and will hence depend on x_0 , m , n , Δy and the parameter t :

$$\vec{A}(\vec{r}(t)) = \vec{A}(x_0, m, n, \Delta y, t) := \begin{pmatrix} A_x(t) \\ A_y(t) \\ A_z(t) \end{pmatrix} . \quad (\text{B.25})$$

The infinitesimal line element $d\vec{r}(t)$ can also by the use of Eq. (B.24) be evaluated to:

$$d\vec{r}(t) = \frac{d\vec{r}(t)}{dt} dt = (\vec{r}_m^{(0)} - \vec{r}_n^{(0)}) \cdot dt = \begin{pmatrix} 0 \\ \Delta y(m-n) \\ 0 \end{pmatrix} dt . \quad (\text{B.26})$$

In this way the Peierls phases $\phi_{nm}^{(0)}$ needed for the transformation from Eq. (B.21) can be calculated via

$$\phi_{nm}^{(0)} = \int_{\vec{r}_n^{(0)}}^{\vec{r}_m^{(0)}} \vec{A}(\vec{r}) d\vec{r} = \int_0^1 \vec{A}(x_0, m, n, \Delta y, t) \frac{d\vec{r}(t)}{dt} dt$$

which by the use of Eqs. (B.24) and (B.26) is given by

$$\begin{aligned} \phi_{nm}^{(0)} &= \int_0^1 \begin{pmatrix} A_x(t) \\ A_y(t) \\ A_z(t) \end{pmatrix} \cdot \begin{pmatrix} 0 \\ \Delta y(m-n) \\ 0 \end{pmatrix} dt \\ &= \int_0^1 A_y(t) \Delta y(m-n) dt . \end{aligned} \quad (\text{B.27})$$

The above considerations now have to be redone also for the transformation of the matrix H_I . A matrix element $H_{I,nm}$ connects two points adjacent stripes in y -direction. Hence their position vectors $\vec{r}_n^{(I)}$ and $\vec{r}_m^{(I)}$ are given by

$$\vec{r}_n^{(I)} = \begin{pmatrix} x_0 \\ \Delta y \cdot n \\ 0 \end{pmatrix} \quad \text{and} \quad \vec{r}_m^{(I)} = \begin{pmatrix} x_0 + \Delta x \\ \Delta y \cdot m \\ 0 \end{pmatrix} . \quad (\text{B.28})$$

Analogously to Eq. (B.24) we can parameterize the integration curve using

$$\vec{r}(t) = \vec{r}_n^{(I)} + (\vec{r}_m^{(I)} - \vec{r}_n^{(I)}) \cdot t = \vec{r}_n^{(I)} + \begin{pmatrix} \Delta x \\ \Delta y(m - n) \\ 0 \end{pmatrix} \cdot t = \begin{pmatrix} x_0 + \Delta x \cdot t \\ \Delta y[n + (m - n)t] \\ 0 \end{pmatrix} \quad (\text{B.29})$$

which leads to the fact that the vector potential this time also depends on Δx :

$$\vec{A}(\vec{r}(t)) = \vec{A}(x_0, m, n, \Delta x, \Delta y, t) := \begin{pmatrix} A_x(t) \\ A_y(t) \\ A_z(t) \end{pmatrix} . \quad (\text{B.30})$$

The line element is now given by

$$d\vec{r}(t) = \frac{d\vec{r}(t)}{dt} dt = (\vec{r}_m^{(I)} - \vec{r}_n^{(I)}) \cdot dt = \begin{pmatrix} \Delta x \\ \Delta y(m - n) \\ 0 \end{pmatrix} dt . \quad (\text{B.31})$$

In order to use the transformation of H_I according to Eq. (B.22), the Peierls phases $\phi_{nm}^{(I)}$ need to be obtained analogously to Eq. (B.27) yielding

$$\begin{aligned} \phi_{nm}^{(I)} &= \int_0^1 \begin{pmatrix} A_x(t) \\ A_y(t) \\ A_z(t) \end{pmatrix} \cdot \begin{pmatrix} \Delta x \\ \Delta y(m - n) \\ 0 \end{pmatrix} dt \\ &= \int_0^1 (A_x(t)\Delta x + A_y(t)\Delta y(m - n)) dt . \end{aligned} \quad (\text{B.32})$$

The transformations from Eqs. (B.21) and (B.22) given by the phase arguments from Eqs. (B.27) and (B.32) are holding generally for a numerical description in terms of a square grid and finite differences approximation. Also the choices of point position vectors along the integration line from Eqs. (B.24) and (B.29) for H_0 and H_I , respectively, are unique in this layout and together with the vector potential $\vec{A}(\vec{r})$ in a chosen gauge determine the precise form of the Peierls transformation.

B.1.3. Perpendicular magnetic field

As a first special case we consider a magnetic field $\vec{B} = B \cdot \hat{e}_z$ of strength B perpendicular in z -direction perpendicular to the 2 dimensional plane. Such a field can be generated by a vector potential

$$\vec{A}(\vec{r}) = \vec{A}(x, y, z) = \begin{pmatrix} -By \\ 0 \\ 0 \end{pmatrix}$$

which resembles the desired field

$$\vec{B} = \text{rot} \vec{A}(\vec{r}) = \begin{pmatrix} \partial_x \\ \partial_y \\ \partial_z \end{pmatrix} \times \begin{pmatrix} -By \\ 0 \\ 0 \end{pmatrix} = \begin{pmatrix} 0 \\ 0 \\ B \end{pmatrix} .$$

Since in this case $A_y(\vec{r}) = 0$ for all possible points \vec{r} we can immediately conclude according to Eq. (B.27) that all Peierls phase arguments $\phi_{nm}^{(0)}$ concerning H_0 vanish, i.e.

$$\phi_{nm}^{(0)} = 0 .$$

In the transformation for the elements of H_I the second term in Eq. (B.32) vanishes for the same reason as above, while the first term including

$$\vec{A}_x^{(I)}(t) = A_x(y = \Delta y[n + (m - n)t]) = -B\Delta y[n + (m - n)t]$$

gives

$$\begin{aligned} \phi_{nm}^{(I)} &= \int_0^1 A_x^{(I)}(t) \Delta x dt = - \int_0^1 dt \cdot B \Delta x \Delta y [n + (m - n)t] \\ &= -B \Delta y \Delta x (n + \frac{m - n}{2}) . \end{aligned} \quad (\text{B.33})$$

Usually in a finite-differences approach only points that are nearest neighbors will interact, which leads to H_I being a diagonal matrix. For those elements $H_{I,nn}$ Eq. (B.33) simplifies to

$$\phi_{nn}^{(I)} = -B \Delta y \Delta x n . \quad (\text{B.34})$$

In the special case of a two-dimensional topological insulator described by the BHZ model Eq. (2.1), also a correction to the model itself is required for a flawless description of a magnetic field (see section 2.6). This correction includes the breaking of time-reversal symmetry due to the perpendicular magnetic field and results from Zeeman-coupling in first-order perturbation theory of the effective four-band

model [121]. It is given by

$$H_{\text{zm}} = \mu_B B \begin{pmatrix} g_{E\perp} & & & \\ & g_{H\perp} & & \\ & & -g_{E\perp} & \\ & & & -g_{H\perp} \end{pmatrix} \quad (2.12 \text{ revisited})$$

and is repeated here for convenience. Due to their diagonal form, these terms do not depend explicitly on space. Numerically this means that they are only adding constant terms to the diagonal subblocks of H_0 from Eq. (A.19). In this way the corrections

$$\tilde{H}_{0,\uparrow\uparrow}^{11} = -\tilde{H}_{0,\downarrow\downarrow}^{11} = \mu_B B \begin{pmatrix} g_{E\perp} & & \\ & \ddots & \\ & & g_{E\perp} \end{pmatrix} \quad \text{and} \quad (B.35)$$

$$\tilde{H}_{0,\uparrow\uparrow}^{22} = -\tilde{H}_{0,\downarrow\downarrow}^{22} = \mu_B B \begin{pmatrix} g_{H\perp} & & \\ & \ddots & \\ & & g_{H\perp} \end{pmatrix} \quad (B.36)$$

have to be added to the subblocks $H_{0,\uparrow\uparrow}^{11}$, $H_{0,\uparrow\uparrow}^{22}$, $H_{0,\downarrow\downarrow}^{11}$ and $H_{0,\downarrow\downarrow}^{22}$ from Eq. (A.19).

B.1.4. Magnetic field in x -direction for a plane lead

For an in-plane magnetic field the Zeeman correction according to Ref. [121] is now given by

$$H_{\text{zm}} = \mu_B B \begin{pmatrix} 0 & 0 & g_{\parallel} & 0 \\ 0 & 0 & 0 & g_{\parallel} \\ g_{\parallel} & 0 & 0 & 0 \\ 0 & g_{\parallel} & 0 & 0 \end{pmatrix} \quad (2.13 \text{ revisited})$$

as already mentioned before in section 2.6. In the numerical scheme of Eq. (A.19) these corrections again only affect H_0 and read

$$\tilde{H}_{0,\uparrow\downarrow}^{11} = \tilde{H}_{0,\downarrow\uparrow}^{11} = \tilde{H}_{0,\uparrow\downarrow}^{22} = \tilde{H}_{0,\downarrow\uparrow}^{22} = \mu_B B \begin{pmatrix} g_{\parallel} & & \\ & \ddots & \\ & & g_{\parallel} \end{pmatrix} \quad (B.37)$$

which have to be added to the corresponding subblocks $H_{0,\uparrow\uparrow}^{11}$, $H_{0,\uparrow\uparrow}^{22}$, $H_{0,\downarrow\downarrow}^{11}$ and $H_{0,\downarrow\downarrow}^{22}$ from Eq. (A.19).

In order to execute the Peierls substitution for this case, we find that a suitable gauge to retrieve $B_x = \partial_y A_z - \partial_z A_y = B$ is given by $A_y = B \cdot z$ with $A_x = A_z = 0$. Trivially, in a plane two-dimensional lead, one can always choose the $z = 0$ making

the vector potential vanish in the entire x - y -plane. Correspondingly the Peierls phases according to Eqs. (B.27) and (B.32)

$$\phi_{nm}^{(0)} = \phi_{nm}^{(I)} = 0$$

all vanish.

B.1.5. Magnetic field in x -direction for a cylindrical lead

In a next step we want to implement a magnetic field again in x -direction but this time for a cylindrical lead as explained in detail in section 2.6 of the main text.

In order to find a suitable gauge potential we use the cylindrical symmetry of this envisioned geometry. While in the numerics we are limited to the two-dimensional (x, y) -plane, we can go to three-dimensional cylinder coordinates (r, ϕ, x) where the original x -axis is defined as the cylinder axis. A vector \vec{r} is then given by

$$\vec{r} = \begin{pmatrix} r \sin \phi \\ r \cos \phi \\ x \end{pmatrix} .$$

The unit vector along ϕ also corresponds to the unit vector along the y -coordinate when the original plane is mapped onto the cylindrical surface and is given by

$$\hat{e}_\phi = \frac{\partial \vec{r}}{\partial \phi} / \left| \frac{\partial \vec{r}}{\partial \phi} \right| = \begin{pmatrix} \cos \phi \\ -\sin \phi \\ 0 \end{pmatrix} = \hat{e}_{\tilde{y}} .$$

A magnetic field in x -direction is restored by a magnetic vector potential

$$\vec{A}(\vec{r}) = \frac{1}{2} Br \hat{e}_\phi = \frac{1}{2} Br \hat{e}_y$$

with r being the cylinder's radius. It can be easily verified that indeed

$$\vec{B} = \text{rot} \vec{A} = \begin{pmatrix} 0 \\ 0 \\ B \end{pmatrix} = B \cdot \hat{e}_x$$

leaving us with the desired field in x -direction. The above chosen gauge has the great advantage that it does not depend explicitly on any of the coordinates but features a non-zero but constant y -component A_y . It is thus easy to immediately find the corresponding Peierls phase arguments from Eqs. (B.27) and (B.32)

$$\phi_{nm}^{(0)} = \phi_{nm}^{(I)} = \int_0^1 A_y(t) \Delta y(m-n) dt = \frac{1}{2} Br \Delta y(m-n) . \quad (\text{B.38})$$

It is worth noting that in this way the effects on the band structure not only depend on the strength of the magnetic field but also on the radius r of the cylinder.

B.1.6. Unit conversions

In order to correctly implement the magnetic field in our BHZ model [88] we need to express the occurring prefactors, namely μ_B and $\frac{e}{\hbar}$ in units of meV (millielectronvolts) and nm (nanometers) which are the units that the other Hamiltonian parameters are given in. While μ_B is occurring in the Zeeman correction in the Hamiltonian due to the magnetic field [see Eqs. (2.12) and (2.13)], the prefactor $\frac{e}{\hbar}$ is part of the phase factor of the Peierls Hamiltonian transformation from Eq. (B.10).

The Bohr magneton μ_B is in terms of natural constants given by

$$\mu_B = \frac{e\hbar}{2m_e} = 9.27400968 \cdot 10^{-24} \frac{\text{J}}{\text{T}} .$$

Transformation of 1 Joule to the required units,

$$1 \text{ J} = 6.241509 \cdot 10^{18} \text{ eV} = 6.241509 \cdot 10^{21} \text{ meV} ,$$

yields

$$\mu_B = 9.27400968 \cdot 10^{-24} \times 6.241509 \cdot 10^{21} \frac{\text{meV}}{\text{T}} = 0.0578838 \frac{\text{meV}}{\text{T}} .$$

In the same way we have to convert the ratio of elementary charge and reduced Planck constant

$$\frac{e}{\hbar} = \frac{1.602176565 \cdot 10^{-19} \text{ C}}{1.054571726 \cdot 10^{-34} \text{ J} \cdot \text{s}} = 1.51927 \cdot 10^{15} \frac{\text{C}}{\text{J} \cdot \text{s}}$$

to units of millielectronvolts, nanometers and Tesla. For this purpose, we employ the knowledge that the unit of the electric current is

$$1 \text{ A} = 1 \frac{\text{C}}{\text{s}} ,$$

giving

$$\frac{e}{\hbar} = 1.51927 \cdot 10^{15} \frac{\text{A}}{\text{J}} .$$

Since, 1 Tesla is also given by

$$1 \text{ T} = 1 \frac{\text{J}}{\text{A} \cdot \text{m}^2} ,$$

it follows that

$$1 \frac{\text{A}}{\text{J}} = 1 \frac{1}{\text{T} \cdot \text{m}^2} = 1 \frac{1}{\text{T} \cdot 10^{18} \text{ nm}^2} = 10^{-18} \frac{1}{\text{T} \cdot \text{nm}^2} .$$

Therefore we receive the requested prefactor in the desired units as

$$\frac{e}{\hbar} = 1.51927 \cdot 10^{15} \times 10^{-18} \frac{1}{\text{T} \cdot \text{nm}^2} = 0.00151927 \frac{1}{\text{T} \cdot \text{nm}^2} .$$

Bibliography

- [1] P. W. Anderson, “Absence of diffusion in certain random lattices,” *Phys. Rev.*, vol. 109, pp. 1492–1505, 1958.
- [2] A. Peña, A. Girschik, F. Libisch, S. Rotter, and A. A. Chabanov, “The single-channel regime of transport through random media,” *Nature Communications*, vol. 5, Mar. 2014.
- [3] J. B. Pendry, “Quasi-extended electron states in strongly disordered systems,” *J. Phys. C*, vol. 20, pp. 733–742, 1987.
- [4] M. Z. Hasan and C. L. Kane, “Colloquium: Topological insulators,” *Reviews of Modern Physics*, vol. 82, pp. 3045–3067, Nov. 2010.
- [5] X.-L. Qi and S.-C. Zhang, “Topological insulators and superconductors,” *Reviews of Modern Physics*, vol. 83, pp. 1057–1110, Oct. 2011.
- [6] Y. Ando, “Topological Insulator Materials,” *Journal of the Physical Society of Japan*, vol. 82, p. 102001, Sept. 2013.
- [7] J. Li, R.-L. Chu, J. Jain, and S.-Q. Shen, “Topological Anderson Insulator,” *Physical Review Letters*, vol. 102, Apr. 2009.
- [8] C. W. Groth, M. Wimmer, A. R. Akhmerov, J. Tworzydło, and C. W. J. Beenakker, “Theory of the Topological Anderson Insulator,” *Physical Review Letters*, vol. 103, pp. 196805+, Nov. 2009.
- [9] A. Girschik, F. Libisch, and S. Rotter, “Topological insulator in the presence of spatially correlated disorder,” *Physical Review B*, vol. 88, p. 014201, July 2013.
- [10] A. Girschik, F. Libisch, and S. Rotter, “Percolating states in the topological Anderson insulator,” *Physical Review B*, vol. 91, p. 214204, June 2015.
- [11] M. A. Topinka, B. J. LeRoy, R. M. Westervelt, S. E. J. Shaw, R. Fleischmann, E. J. Heller, K. D. Maranowski, and A. C. Gossard, “Coherent branched flow in a two-dimensional electron gas,” *Nature*, vol. 410, pp. 183–186, Mar. 2001.

- [12] S. Rotter, J.-Z. Tang, L. Wirtz, J. Trost, and J. Burgdörfer, “Modular recursive Green’s function method for ballistic quantum transport,” *Physical Review B*, vol. 62, pp. 1950–1960, July 2000.
- [13] F. Libisch, S. Rotter, and J. Burgdörfer, “Coherent transport through graphene nanoribbons in the presence of edge disorder,” *New Journal of Physics*, vol. 14, p. 123006, Dec. 2012.
- [14] S. Rotter, *A Modular Recursive Green’s Function Method for Quantum Transport*. PhD thesis, Technische Universität Wien, Vienna, 1999.
- [15] S. Rotter, *Ballistic quantum transport at high energies and high magnetic fields*. PhD thesis, Technische Universität Wien, Vienna, 2003.
- [16] F. Libisch, *Electronic structure and transport in mesoscopic devices*. PhD thesis, Technische Universität Wien, Vienna, 2009.
- [17] S. M. Popoff, G. Lerosey, R. Carminati, M. Fink, A. C. Boccara, and S. Gigan, “Measuring the Transmission Matrix in Optics: An Approach to the Study and Control of Light Propagation in Disordered Media,” *Physical Review Letters*, vol. 104, p. 100601, Mar. 2010.
- [18] A. P. Mosk, A. Lagendijk, G. Lerosey, and M. Fink, “Controlling waves in space and time for imaging and focusing in complex media,” *Nat. Photon.*, vol. 6, pp. 283–292, 2012.
- [19] I. M. Vellekoop, A. Lagendijk, and A. P. Mosk, “Exploiting disorder for perfect focusing,” *Nat. Photon.*, vol. 4, pp. 320–322, 2010.
- [20] S. Popoff, G. Lerosey, M. Fink, A. Boccara, and S. Gigan, “Image transmission through an opaque material,” *Nat. Commun.*, vol. 1, p. 15, 2010.
- [21] O. Katz, E. Small, Y. Bromberg, and Y. Silberberg, “Focusing and compression of ultrashort pulses through scattering media,” *Nat. Photon.*, vol. 5, pp. 372–377, 2011.
- [22] Z. Shi and A. Z. Genack, “Transmission eigenvalues and the bare conductance in the crossover to Anderson localization,” *Phys. Rev. Lett.*, vol. 108, p. 043901, 2012.
- [23] W. Choi, Q. H. Park, and W. Choi, “Perfect transmission through Anderson localized systems mediated by a cluster of localized modes,” *Opt. Express*, vol. 20, pp. 20721–20729, 2012.
- [24] C. W. J. Beenakker, “Random-matrix theory of quantum transport,” *Rev. Mod. Phys.*, vol. 69, pp. 731–808, 1997.

- [25] O. N. Dorokhov, "On the coexistence of the localized and extended electronic states in the metallic phase," *Solid State Commun.*, vol. 51, pp. 381–384, 1984.
- [26] Y. Imry, "Active transmission channels and universal conductance fluctuations," *Europhys. Lett.*, vol. 1, pp. 249–256, 1986.
- [27] K. Frahm, "Equivalence of the Fokker-Planck Approach and the Nonlinear σ Model for Disordered Wires in the Unitary Symmetry Class," *Physical Review Letters*, vol. 74, pp. 4706–4709, June 1995.
- [28] M. E. Gertsenshtein and V. B. Vasilev, "Waveguide with random non-homogeneities and Brownian motion on the Lobachevskii plane," *Teor. Veroyatn. Primen.*, vol. 4, pp. 424–432, 1959.
- [29] J. Wang and A. Z. Genack, "Transport through modes in random media," *Nature*, vol. 471, pp. 345–348, 2011.
- [30] P. A. Mello, P. Pereyra, and N. Kumar, "Macroscopic approach to multichannel disordered conductors," *Ann. Phys.*, vol. 181, pp. 290–317, 1985.
- [31] D. J. Thouless, "Maximum metallic resistance in thin wires," *Phys. Rev. Lett.*, vol. 39, pp. 1167–1169, 1977.
- [32] E. Abrahams, P. W. Anderson, D. C. Licciardello, and T. V. Ramakrishnan, "Scaling theory of localization: absence of quantum diffusion in two dimensions," *Phys. Rev. Lett.*, vol. 42, pp. 673–677, 1979.
- [33] H. E. Türeci, A. D. Stone, L. Ge, S. Rotter, and R. J. Tandy, "Ab initio self-consistent laser theory and random lasers," *Nonlinearity*, vol. 22, pp. C1–C18, 2009.
- [34] K. Y. Bliokh, Y. P. Bliokh, V. Freilikher, A. Z. Genack, and P. Sebbah, "Coupling and level repulsion in the localized regime: from isolated to quasiextended modes," *Phys. Rev. Lett.*, vol. 101, p. 133901, 2008.
- [35] L. Labonté, C. Vanneste, and P. Sebbah, "Localized mode hybridization by fine tuning of 2d random media," *Opt. Lett.*, vol. 37, pp. 1946–1948, 2012.
- [36] J. B. Pendry, "Symmetry and transport of waves in 1d disordered systems," *Adv. Phys.*, vol. 43, pp. 461–542, 1994.
- [37] R. Landauer, "Electrical resistance of disordered one-dimensional lattices," *Philos. Mag.*, vol. 21, pp. 863–867, 1970.
- [38] D. S. Fisher and P. A. Lee, "Relation between conductivity and transmission matrix," *Phys. Rev. B*, vol. 23, pp. 6851–6854, 1981.

- [39] A. A. Abrikosov, “The paradox with the static conductivity of a one-dimensional metal,” *Solid State Commun.*, vol. 37, pp. 997–1000, 1981.
- [40] V. I. Melnikov, “Fluctuations in the resistivity of a finite disordered system,” *Fiz. Tverd. Tela (Leningrad)*, vol. 23, pp. 782–786, 1981.
- [41] J. Feilhauer and M. Moško, “Quantum and Boltzmann transport in a quasi-one-dimensional wire with rough edges,” *Phys. Rev. B*, vol. 83, p. 245328, 2011.
- [42] V. A. Gopar and R. A. Molina, “Controlling conductance statistics of quantum wires by driving ac fields,” *Phys. Rev. B*, vol. 81, p. 195415, 2010.
- [43] J. W. Goodman, *Statistical Optics*. New York, USA: Wiley, 2000.
- [44] S. Feng, C. Kane, P. A. Lee, and A. D. Stone, “Correlations and fluctuations of coherent wave transmission through disordered media,” *Phys. Rev. Lett.*, vol. 61, pp. 834–837, 1988.
- [45] P. A. Mello, E. Akkermans, and B. Shapiro, “Macroscopic approach to correlations in the electronic transmission and reflection from disordered conductors,” *Phys. Rev. Lett.*, vol. 61, pp. 459–462, 1988.
- [46] A. D. Mirlin, A. Muller-Groeling, and M. R. Zernbauer, “Conductance fluctuations of disordered wires: Fourier analysis on supersymmetric spaces,” *Ann. Phys.*, vol. 236, pp. 325–373, 1994.
- [47] E. Kogan and M. Kaveh, “Random-matrix-theory approach to the intensity distributions of waves propagating in a random medium,” *Phys. Rev. B*, vol. 52, pp. R3813–R3815, 1995.
- [48] Z. Q. Zhang, A. A. Chabanov, S. K. Cheung, C. H. Wong, and A. Z. Genack, “Dynamics of localized waves: pulsed microwave transmissions in quasi-one-dimensional media,” *Phys. Rev. B*, vol. 79, p. 144203, 2009.
- [49] S. Feng and P. Lee, “Mesoscopic conductors and correlations in laser speckle patterns,” *Science*, vol. 251, pp. 633–639, 1991.
- [50] A. Goetschy and A. D. Stone, “Filtering random matrices: the effect of incomplete channel control in multiple scattering,” *Phys. Rev. Lett.*, vol. 111, p. 063901, 2013.
- [51] H. Yu, “Measuring large optical transmission matrices of disordered media,” *Phys. Rev. Lett.*, vol. 111, p. 153902, 2013.

- [52] T. Strudley, T. Zehender, C. Blejeau, E. P. Bakkers, and O. L. Muskens, “Mesoscopic light transport by very strong collective multiple scattering in nanowire mats,” *Nat. Photon.*, vol. 7, pp. 413–418, 2013.
- [53] H. Hu, A. Strybulevych, J. H. Page, S. E. Skipetrov, and B. A. Van Tiggelen, “Localization of ultrasound in a three-dimensional elastic network,” *Nat. Phys.*, vol. 4, pp. 945–948, 2008.
- [54] Y. u. V. Nazarov, “Limits of universality in disordered conductors,” *Phys. Rev. Lett.*, vol. 73, pp. 134–137, 1994.
- [55] A. A. Chabanov, B. Hu, and A. Z. Genack, “Dynamic correlation in wave propagation in random media,” *Phys. Rev. Lett.*, vol. 93, p. 123901, 2004.
- [56] V. M. Apalkov, M. E. Raikh, and B. Shapiro, “Random resonators and pre-localized modes in disordered dielectric films,” *Phys. Rev. Lett.*, vol. 89, p. 016802, 2002.
- [57] M. P. Jura, M. A. Topinka, L. Urban, A. Yazdani, H. Shtrikman, L. N. Pfeiffer, K. W. West, and D. Goldhaber-Gordon, “Unexpected features of branched flow through high-mobility two-dimensional electron gases,” *Nature Physics*, vol. 3, pp. 841–845, Dec. 2007.
- [58] L. Kaplan, “Statistics of Branched Flow in a Weak Correlated Random Potential,” *Physical Review Letters*, vol. 89, p. 184103, Oct. 2002.
- [59] K. E. Aidala, R. E. Parrott, T. Kramer, E. J. Heller, R. M. Westervelt, M. P. Hanson, and A. C. Gossard, “Imaging magnetic focusing of coherent electron waves,” *Nature Physics*, vol. 3, pp. 464–468, July 2007.
- [60] D. Maryenko, F. Ospald, K. v. Klitzing, J. H. Smet, J. J. Metzger, R. Fleischmann, T. Geisel, and V. Umansky, “How branching can change the conductance of ballistic semiconductor devices,” *Physical Review B*, vol. 85, p. 195329, May 2012.
- [61] E. J. Heller, K. E. Aidala, B. J. LeRoy, A. C. Bleszynski, A. Kalben, R. M. Westervelt, K. D. Maranowski, and A. C. Gossard, “Thermal Averages in a Quantum Point Contact with a Single Coherent Wave Packet,” *Nano Letters*, vol. 5, pp. 1285–1292, July 2005.
- [62] E. J. Heller, L. Kaplan, and A. Dahlen, “Refraction of a Gaussian seaway,” *Journal of Geophysical Research: Oceans*, vol. 113, p. C09023, Sept. 2008.
- [63] R. Höhmann, U. Kuhl, H.-J. Stöckmann, L. Kaplan, and E. J. Heller, “Freak Waves in the Linear Regime: A Microwave Study,” *Physical Review Letters*, vol. 104, p. 093901, Mar. 2010.

- [64] L. H. Ying, Z. Zhuang, E. J. Heller, and L. Kaplan, "Linear and nonlinear rogue wave statistics in the presence of random currents," *Nonlinearity*, vol. 24, p. R67, Nov. 2011.
- [65] J. J. Metzger, R. Fleischmann, and T. Geisel, "Statistics of Extreme Waves in Random Media," *Physical Review Letters*, vol. 112, p. 203903, May 2014.
- [66] J. J. Metzger, R. Fleischmann, and T. Geisel, "Universal Statistics of Branched Flows," *Physical Review Letters*, vol. 105, p. 020601, July 2010.
- [67] B. Liu and E. J. Heller, "Stability of Branched Flow from a Quantum Point Contact," *Physical Review Letters*, vol. 111, p. 236804, Dec. 2013.
- [68] X. Ni, W.-X. Wang, and Y.-C. Lai, "Origin of branched wave structures in optical media and long-tail algebraic intensity distribution," *EPL (Europhysics Letters)*, vol. 96, p. 44002, Nov. 2011.
- [69] X. Ni, Y.-C. Lai, and W.-X. Wang, "Emergence of scaling associated with complex branched wave structures in optical medium," *Chaos: An Interdisciplinary Journal of Nonlinear Science*, vol. 22, p. 043116, Dec. 2012.
- [70] A. Brandstötter, "Branched Flow in Scattering through Disordered Media: Addressing individual Branches through Wave Control," project Thesis, Technische Universität Wien, Vienna, 2014.
- [71] F. T. Smith, "Lifetime Matrix in Collision Theory," *Physical Review*, vol. 118, pp. 349–356, Apr. 1960.
- [72] E. P. Wigner, "Lower Limit for the Energy Derivative of the Scattering Phase Shift," *Physical Review*, vol. 98, pp. 145–147, Apr. 1955.
- [73] S. Rotter, P. Ambichl, and F. Libisch, "Generating Particlelike Scattering States in Wave Transport," *Physical Review Letters*, vol. 106, p. 120602, Mar. 2011.
- [74] S. M. Popoff, G. Lerosey, M. Fink, A. C. Boccara, and S. Gigan, "Controlling light through optical disordered media: transmission matrix approach," *New Journal of Physics*, vol. 13, p. 123021, Dec. 2011.
- [75] A. A. Juárez, C. A. Bunge, S. Warm, and K. Petermann, "Perspectives of principal mode transmission in mode-division-multiplex operation," *Optics Express*, vol. 20, p. 13810, June 2012.
- [76] C. L. Kane and E. J. Mele, "Quantum Spin Hall Effect in Graphene," *Physical Review Letters*, vol. 95, Nov. 2005.

- [77] J. E. Moore and L. Balents, “Topological invariants of time-reversal-invariant band structures,” *Physical Review B*, vol. 75, p. 121306, Mar. 2007.
- [78] X.-L. Qi, T. L. Hughes, and S.-C. Zhang, “Topological field theory of time-reversal invariant insulators,” *Physical Review B*, vol. 78, p. 195424, Nov. 2008.
- [79] X.-L. Qi and S.-C. Zhang, “The quantum spin Hall effect and topological insulators,” *Physics Today*, vol. 63, no. 1, pp. 33–38, 2010.
- [80] X.-L. Qi and S.-C. Zhang, “Topological insulators and superconductors,” *arxiv.org/1008.2026*, Aug. 2010.
- [81] S.-c. Zhang, “Topological states of quantum matter,” *Physics*, vol. 1, pp. 6+, July 2008.
- [82] C. L. Kane and E. J. Mele, “A New Spin on the Insulating State,” *Science*, vol. 314, pp. 1692–1693, Dec. 2006.
- [83] G. Brumfiel, “Topological insulators: Star material,” *Nature*, vol. 466, pp. 310–311, July 2010.
- [84] M. Franz, “Solid-state physics: U-turns strictly prohibited,” *Nature*, vol. 466, pp. 323–324, July 2010.
- [85] J. E. Moore, “The birth of topological insulators,” *Nature*, vol. 464, pp. 194–198, Mar. 2010.
- [86] S. Murakami, N. Nagaosa, and S.-C. Zhang, “Dissipationless Quantum Spin Current at Room Temperature,” *Science*, vol. 301, pp. 1348–1351, May 2003.
- [87] M. Büttiker, “Edge-State Physics Without Magnetic Fields,” *Science*, vol. 325, pp. 278–279, July 2009.
- [88] B. A. Bernevig, T. L. Hughes, and S.-C. Zhang, “Quantum Spin Hall Effect and Topological Phase Transition in HgTe Quantum Wells,” *Science*, vol. 314, pp. 1757–1761, Dec. 2006.
- [89] M. König, S. Wiedmann, C. Brune, A. Roth, H. Buhmann, L. W. Molenkamp, X.-L. Qi, and S.-C. Zhang, “Quantum Spin Hall Insulator State in HgTe Quantum Wells,” *Science*, vol. 318, pp. 766–770, Nov. 2007.
- [90] A. Roth, C. Brune, H. Buhmann, L. W. Molenkamp, J. Maciejko, X.-L. Qi, and S.-C. Zhang, “Nonlocal Transport in the Quantum Spin Hall State,” *Science*, vol. 325, pp. 294–297, July 2009.

- [91] Y. Xing, L. Zhang, and J. Wang, “Topological Anderson insulator phenomena,” *Physical Review B*, vol. 84, pp. 035110+, July 2011.
- [92] A. Yamakage, K. Nomura, K. I. Imura, and Y. Kuramoto, “Disorder-Induced Multiple Transition Involving \mathbb{Z}_2 Topological Insulator,” *Journal of the Physical Society of Japan*, vol. 80, pp. 053703+, Apr. 2011.
- [93] E. Prodan, “Three-dimensional phase diagram of disordered HgTe/CdTe quantum spin-Hall wells,” *Physical Review B*, vol. 83, pp. 195119+, May 2011.
- [94] Y. Y. Zhang, R. L. Chu, F. C. Zhang, and S. Q. Shen, “Localization and mobility gap in the topological Anderson insulator,” *Physical Review B*, vol. 85, pp. 035107+, Jan. 2012.
- [95] J. Song, H. Liu, H. Jiang, Q. F. Sun, and X. C. Xie, “Dependence of topological Anderson insulator on the type of disorder,” *Physical Review B*, vol. 85, pp. 195125+, May 2012.
- [96] H. M. Guo, G. Rosenberg, G. Refael, and M. Franz, “Topological Anderson Insulator in Three Dimensions,” *Physical Review Letters*, vol. 105, pp. 216601+, Nov. 2010.
- [97] M. C. Rechtsman, J. M. Zeuner, Y. Plotnik, Y. Lumer, D. Podolsky, F. Dreisow, S. Nolte, M. Segev, and A. Szameit, “Photonic Floquet topological insulators,” *Nature*, vol. 496, pp. 196–200, Apr. 2013.
- [98] P. Titum, N. H. Lindner, M. C. Rechtsman, and G. Refael, “Disorder-Induced Floquet Topological Insulators,” *Physical Review Letters*, vol. 114, p. 056801, Feb. 2015.
- [99] B. Béri and N. R. Cooper, “ \mathbb{Z}_2 Topological Insulators in Ultracold Atomic Gases,” *Physical Review Letters*, vol. 107, pp. 145301+, Sept. 2011.
- [100] J. Billy, “Direct observation of Anderson localization of matter waves in a controlled disorder,” *Nature*, vol. 453, pp. 891–894, 2008.
- [101] J. E. Lye, L. Fallani, M. Modugno, D. S. Wiersma, C. Fort, and M. Inguscio, “Bose-Einstein Condensate in a Random Potential,” *Physical Review Letters*, vol. 95, pp. 070401+, Aug. 2005.
- [102] A. Girschik, *Mach-Zehnder interferometer based on two-dimensional topological insulators: A numerical study*. PhD thesis, Technische Universität Wien, Vienna, 2011.

- [103] H. Jiang, L. Wang, Q. F. Sun, and X. C. Xie, “Numerical study of the topological Anderson insulator in HgTe/CdTe quantum wells,” *Physical Review B*, vol. 80, pp. 165316+, Oct. 2009.
- [104] W. Li, J. Zang, and Y. Jiang, “Size effects on transport properties in topological Anderson insulators,” *Physical Review B*, vol. 84, pp. 033409+, July 2011.
- [105] F. A. B. F. de Moura and M. L. Lyra, “Delocalization in the 1d Anderson Model with Long-Range Correlated Disorder,” *Physical Review Letters*, vol. 81, pp. 3735–3738, Oct. 1998.
- [106] P. Carpena, P. Bernaola-Galvan, P. C. Ivanov, and H. E. Stanley, “Metal-insulator transition in chains with correlated disorder,” *Nature*, vol. 418, pp. 955–959, Aug. 2002.
- [107] A. E. Meyerovich and V. V. Nesvizhevsky, “Gravitational quantum states of neutrons in a rough waveguide,” *Physical Review A*, vol. 73, pp. 063616+, June 2006.
- [108] T. Kawarabayashi, Y. Ono, T. Ohtsuki, S. Kettmann, A. Struck, and B. Kramer, “Unconventional conductance plateau transitions in quantum Hall wires with spatially correlated disorder,” *Physical Review B*, vol. 75, pp. 235317+, June 2007.
- [109] J. H. Bardarson, J. Tworzydło, P. W. Brouwer, and C. W. J. Beenakker, “One-Parameter Scaling at the Dirac Point in Graphene,” *Physical Review Letters*, vol. 99, pp. 106801+, Sept. 2007.
- [110] W. Schirmacher, B. Schmid, C. Tomaras, G. Viliani, G. Baldi, G. Ruocco, and T. Scopigno, “Vibrational excitations in systems with correlated disorder,” *Phys. Status Solidi (c)*, vol. 5, no. 3, pp. 862–866, 2008.
- [111] S. Pilati, S. Giorgini, and N. Prokof’ev, “Superfluid Transition in a Bose Gas with Correlated Disorder,” *Physical Review Letters*, vol. 102, pp. 150402+, Apr. 2009.
- [112] P. Lugan, A. Aspect, L. Sanchez-Palencia, D. Delande, B. Grémaud, C. A. Müller, and C. Miniatura, “One-dimensional Anderson localization in certain correlated random potentials,” *Physical Review A*, vol. 80, pp. 023605+, Aug. 2009.
- [113] S. F. Liew and H. Cao, “Optical properties of 1d photonic crystals with correlated and uncorrelated disorder,” *Journal of Optics*, vol. 12, pp. 024011+, Jan. 2010.

- [114] Q. Li, E. H. Hwang, E. Rossi, and S. DasSarma, "Theory of 2d Transport in Graphene for Correlated Disorder," *Physical Review Letters*, vol. 107, pp. 156601+, Oct. 2011.
- [115] T. A. Sedrakyan, J. P. Kestner, and S. DasSarma, "Proposed signature of Anderson localization and correlation-induced delocalization in an $\hbar v_F$ -leg optical lattice," *Physical Review A*, vol. 84, pp. 053621+, Nov. 2011.
- [116] F. M. Izrailev, A. A. Krokhin, and N. M. Makarov, "Anomalous localization in low-dimensional systems with correlated disorder," *Physics Reports*, vol. 512, pp. 125–254, Mar. 2012.
- [117] A. Croy and M. Schreiber, "Correlation-strength-driven Anderson metal-insulator transition," *Physical Review B*, vol. 85, pp. 205147+, May 2012.
- [118] O. Dietz, H. J. Stöckmann, U. Kuhl, F. M. Izrailev, N. M. Makarov, J. Doppler, F. Libisch, and S. Rotter, "Surface scattering and band gaps in rough waveguides and nanowires," *Physical Review B*, vol. 86, pp. 201106+, Nov. 2012.
- [119] G. M. Petersen and N. Sandler, "Anticorrelations from power-law spectral disorder and conditions for an Anderson transition," *Physical Review B*, vol. 87, p. 195443, May 2013.
- [120] B. Zhou, H. Z. Lu, R. L. Chu, S. Q. Shen, and Q. Niu, "Finite Size Effects on Helical Edge States in a Quantum Spin-Hall System," *Physical Review Letters*, vol. 101, pp. 246807+, Dec. 2008.
- [121] M. König, H. Buhmann, L. W. Molenkamp, T. Hughes, C.-X. Liu, X.-L. Qi, and S.-C. Zhang, "The Quantum Spin Hall Effect: Theory and Experiment," *Journal of the Physical Society of Japan*, vol. 77, p. 031007, Mar. 2008.
- [122] L. Chen, Q. Liu, X. Lin, X. Zhang, and X. Jiang, "Disorder dependence of helical edge states in HgTe/CdTe quantum wells," *New Journal of Physics*, vol. 14, pp. 043028+, Apr. 2012.
- [123] D. Xu, J. Qi, J. Liu, V. Sacksteder, X. C. Xie, and H. Jiang, "Phase structure of the topological Anderson insulator," *Physical Review B*, vol. 85, pp. 195140+, May 2012.
- [124] K. Hashimoto, C. Sohrmann, J. Wiebe, T. Inaoka, F. Meier, Y. Hirayama, R. A. Römer, R. Wiesendanger, and M. Morgenstern, "Quantum Hall Transition in Real Space: From Localized to Extended States," *Physical Review Letters*, vol. 101, pp. 256802+, Dec. 2008.

- [125] B. Huckestein, “Scaling theory of the integer quantum Hall effect,” *Reviews of Modern Physics*, vol. 67, pp. 357–396, Apr. 1995.
- [126] R.-L. Chu, J. Lu, and S.-Q. Shen, “Quantum percolation in quantum spin Hall antidot systems,” *EPL (Europhysics Letters)*, vol. 100, pp. 17013+, Oct. 2012.
- [127] R. Zimmermann and C. Schindler, “Coherent potential approximation for spatially correlated disorder,” *Physical Review B*, vol. 80, pp. 144202+, Oct. 2009.
- [128] H. Peng, K. Lai, D. Kong, S. Meister, Y. Chen, X.-L. Qi, S.-C. Zhang, Z.-X. Shen, and Y. Cui, “Aharonov-Bohm interference in topological insulator nanoribbons,” *Nature Materials*, vol. 9, pp. 225–229, Mar. 2010.
- [129] Y.-Y. Zhang and S.-Q. Shen, “Algebraic and geometric mean density of states in topological Anderson insulators,” *Physical Review B*, vol. 88, p. 195145, Nov. 2013.
- [130] Z. Yang, F. Gao, X. Shi, X. Lin, Z. Gao, Y. Chong, and B. Zhang, “Topological Acoustics,” *Physical Review Letters*, vol. 114, p. 114301, Mar. 2015.
- [131] D. G. Rothe, R. W. Reinthaler, C.-X. Liu, L. W. Molenkamp, S.-C. Zhang, and E. M. Hankiewicz, “Fingerprint of different spin–orbit terms for spin transport in HgTe quantum wells,” *New Journal of Physics*, vol. 12, p. 065012, June 2010.
- [132] D. G. Rothe and E. M. Hankiewicz, “Tunable polarization in beam-splitter based on 2d topological insulators,” *Physical Review B*, vol. 89, Nov. 2013.
- [133] E. Novik, A. Pfeuffer-Jeschke, T. Jungwirth, V. Latussek, C. Becker, G. Landwehr, H. Buhmann, and L. Molenkamp, “Band structure of semi-magnetic Hg_{1-y}Mn_yTe quantum wells,” *Physical Review B*, vol. 72, July 2005.
- [134] R.-L. Chu, J. Li, J. K. Jain, and S.-Q. Shen, “Coherent oscillations and giant edge magnetoresistance in singly connected topological insulators,” *Physical Review B*, vol. 80, p. 081102, Aug. 2009.
- [135] L. Zehnder, “Ein neuer Interferenzrefraktor,” *Zeitschrift für Instrumentenkunde*, vol. 11, pp. 275–285, 1891.
- [136] L. Mach, “Über einen Interferenzrefraktor,” *Zeitschrift für Instrumentenkunde*, vol. 12, pp. 89–93, 1892.

- [137] Y. Ji, Y. Chung, D. Sprinzak, M. Heiblum, D. Mahalu, and H. Shtrikman, “An electronic Mach-Zehnder interferometer,” *Nature*, vol. 422, pp. 415–418, Mar. 2003.
- [138] A. Fuß, “A tunable Mach-Zehnder interferometer based on a topological insulator,” bachelor Thesis, Technische Universität Wien, Vienna, 2014.
- [139] D. Ferraro, G. Dolcetto, R. Citro, F. Romeo, and M. Sassetti, “Spin current pumping in helical Luttinger liquids,” *Physical Review B*, vol. 87, p. 245419, June 2013.
- [140] J. Maciejko, E.-A. Kim, and X.-L. Qi, “Spin Aharonov-Bohm effect and topological spin transistor,” *Physical Review B*, vol. 82, p. 195409, Nov. 2010.
- [141] F. Dolcini, “Full electrical control of charge and spin conductance through interferometry of edge states in topological insulators,” *Physical Review B*, vol. 83, p. 165304, Apr. 2011.
- [142] B. Rizzo, A. Camjayi, and L. Arrachea, “Effective tunneling processes in an interferometer of helical edge states with an antidot,” *Journal of Physics: Conference Series*, vol. 568, p. 052027, Dec. 2014.
- [143] R. Citro, F. Romeo, and N. Andrei, “Electrically controlled pumping of spin currents in topological insulators,” *Physical Review B*, vol. 84, p. 161301, Oct. 2011.
- [144] F. Romeo, R. Citro, D. Ferraro, and M. Sassetti, “Electrical switching and interferometry of massive Dirac particles in topological insulator constrictions,” *Physical Review B*, vol. 86, p. 165418, Oct. 2012.
- [145] F. Romeo and R. Citro, “Interaction effects in nonequilibrium transport properties of a four-terminal topological corner junction,” *Physical Review B*, vol. 90, p. 155408, Oct. 2014.
- [146] B. Rizzo, L. Arrachea, and M. Moskalets, “Transport phenomena in helical edge state interferometers: A Green’s function approach,” *Physical Review B*, vol. 88, p. 155433, Oct. 2013.
- [147] P. Sternativo and F. Dolcini, “Tunnel junction of helical edge states: Determining and controlling spin-preserving and spin-flipping processes through transconductance,” *Physical Review B*, vol. 89, p. 035415, Jan. 2014.
- [148] V. Krueckl and K. Richter, “Switching Spin and Charge between Edge States in Topological Insulator Constrictions,” *Physical Review Letters*, vol. 107, p. 086803, Aug. 2011.

- [149] A. Inhofer and D. Bercioux, "Proposal for an on-demand source of polarized electrons into the edges of a topological insulator," *Physical Review B*, vol. 88, p. 235412, Dec. 2013.
- [150] Y. Xing, Z.-l. Yang, Q.-f. Sun, and J. Wang, "Coherent single-spin source based on topological insulators," *Physical Review B*, vol. 90, p. 075435, Aug. 2014.
- [151] S. Sanvito, *Giant Magnetoresistance and Quantum Transport in Magnetic Hybrid Nanostructures*. PhD thesis, School of Physics and Chemistry, Lancaster University, Lancaster, 1999.
- [152] S. Sanvito, C. J. Lambert, J. H. Jefferson, and A. M. Bratkovsky, "General Green's-function formalism for transport calculations with spd Hamiltonians and giant magnetoresistance in Co- and Ni-based magnetic multilayers," *Physical Review B*, vol. 59, pp. 11936–11948, May 1999.
- [153] P. A. Lee and D. S. Fisher, "Anderson Localization in Two Dimensions," *Physical Review Letters*, vol. 47, pp. 882–885, Sept. 1981.
- [154] D. J. Thouless and S. Kirkpatrick, "Conductivity of the disordered linear chain," *Journal of Physics C: Solid State Physics*, vol. 14, p. 235, Jan. 1981.
- [155] S. Rotter, B. Weingartner, F. Libisch, F. Aigner, J. Feist, and J. Burgdörfer, "A Modular Method for the Efficient Calculation of Ballistic Transport Through Quantum Billiards," in *Large-Scale Scientific Computing* (I. Lirkov, S. Margenov, and J. Waśniewski, eds.), no. 3743 in Lecture Notes in Computer Science, pp. 586–593, Springer Berlin Heidelberg, June 2005.
- [156] P. Amestoy, I. Duff, J. L'Excellent, and J. Koster, "A Fully Asynchronous Multifrontal Solver Using Distributed Dynamic Scheduling," *SIAM Journal on Matrix Analysis and Applications*, vol. 23, pp. 15–41, Jan. 2001.
- [157] P. R. Amestoy, A. Guermouche, J.-Y. L'Excellent, and S. Pralet, "Hybrid scheduling for the parallel solution of linear systems," *Parallel computing*, vol. 32, no. 2, pp. 136–156, 2006.
- [158] C. Lanczos, "An iteration method for the solution of the eigenvalue problem of linear differential and integral operators," *J. Research of the National Bureau of Standards*, vol. 45:255, 1950.
- [159] K. Maschhoff and D. Sorensen, "P_arpack: An efficient portable large scale eigenvalue package for distributed memory parallel architectures," in *Applied*

Parallel Computing in Industrial Problems and Optimization, vol. 1184 of *Lecture Notes in Computer Science*, 1996. Editors: Jerzy Wasniewski, Jack Dongarra, Kaj Madsen, and Dorte Olesen.

- [160] B. Terrés, L. Chizhova, F. Libisch, D. Jörger, S. Engels, A. Girschik, K. Watanabe, T. Taniguchi, V. Rotkin, J. Burgdörfer, and C. Stampfer, “Size quantization of Dirac fermions in graphene quantum point contacts,” *currently under review*.
- [161] A. Girschik, A. Brandstötter, P. Ambichl, F. Libisch, and S. Rotter, “Controlling Branched Flow,” *in preparation*.
- [162] A. Girschik, F. Libisch, and S. Rotter, “A Topological Mach-Zehnder Interferometer,” *in preparation*.

Acknowledgements

At this point, I would like to thank those people without whom I would have probably not been able to complete this thesis:

- My advisor, Prof.Dr. Stefan Rotter, for his guidance, his knowledge, for many hours of helpful discussion (not exclusively on physics), for always taking as much time as necessary, for his great ideas, for his patience and for his exemplary and passionate attitude towards his profession.
- My co-advisor, Dr. Florian Libisch, for his great ideas, for his immense programming knowledge and skill that he always shared so willingly with me, for the very fruitful cooperation in improving the code he originally wrote, for the funny hours we spent at his office working on all the numerical issues and for searching and finding bugs in my algorithms.
- Prof.Dr. Ulrich Kuhl for agreeing to be referee of my thesis and also serve as examiner at the defense of this thesis.
- Prof.Dr. Andrey Chabanov from San Antonio for his ideas, his help, interesting discussions and his hospitality and very good cooking during my visit in San Antonio.
- Dr. Abe Peña for the fruitful collaboration, for measuring and analyzing the experimental data, for showing me all experimental setups and for interesting discussion during my stay at San Antonio.
- Dr. Dmitry Krimer for the perfect collaboration during the quantum theory exercises, for helpful discussions, for playing table tennis and for having a lot of fun.
- DI Jörg Doppler for originally introducing me to Python, his diligence and his good ideas.
- My project and bachelor students, Andre Brandstötter and Alexander Fuß, for the great job they did in their works which parts of this thesis are built on.

- My other colleagues, DI Philipp Ambichl, Dr. Matthias Liertzer, Dipl.-Phys. Stephan Burkhardt and DI Thomas Hisch for interesting and also funny discussions and the pleasant time we spent together in the office.
- Dr. Jan Zabloudil for his kind assistance with any questions or problems regarding the VSC.
- Dr. Christoph Lemell for solving all kinds of computer problems.
- Heike Höller and Silvia Riedler for all the administrative support.
- Big thanks also to my girlfriend, my mother and my grandmother for their consistent support over the years and their encouraging words.
- Also thanks to the rest of my family and friends for their moral support.

Finally I want to thank those, who I forgot to mention, and I apologize.

Curriculum vitae

Name: Adrian Girschik
Born: 27th of March 1985 in Vienna, Austria
Nationality: Austrian
Address: Bahnhofstraße 64-68/3
3430 Tulln
Phone: +43 1 58801 13650
E-mail: adrian.girschik@tuwien.ac.at

Education

since 11/2011	Doctoral studies in Technical Physics under the supervision of Prof.Dr. Stefan Rotter	Vienna University of Technology
10/2005 – 10/2011	Master studies in Technical Physics	Vienna University of Technology
10/2004 – 9/2005	Studies of Human Medicine	Medical University of Vienna
10/2003 – 5/2004	Basic Military Service as a medic of the Austrian army	Fliegerhorst Langenlebarn
1995 – 2003	High School	BG/BRG Tulln

List of Publications

- A. Girschik, F. Libisch, and S. Rotter, “Topological insulator in the presence of spatially correlated disorder,” *Physical Review B*, vol. 88, p. 014201, July 2013
- A. Peña, A. Girschik, F. Libisch, S. Rotter, and A. A. Chabanov, “The single-channel regime of transport through random media,” *Nature Communications*, vol. 5, Mar. 2014
- A. Girschik, F. Libisch, and S. Rotter, “Percolating states in the topological Anderson insulator,” *Physical Review B*, vol. 91, p. 214204, June 2015

- B. Terrés, L. Chizhova, F. Libisch, D. Jörger, S. Engels, A. Girschik, K. Watanabe, T. Taniguchi, V. Rotkin, J. Burgdörfer, and C. Stampfer, “Size quantization of Dirac fermions in graphene quantum point contacts,” *currently under review*
- A. Girschik, A. Brandstötter, P. Ambichl, F. Libisch, and S. Rotter, “Controlling Branched Flow,” *in preparation*
- A. Girschik, F. Libisch, and S. Rotter, “A Topological Mach-Zehnder Interferometer,” *in preparation*